Modeling of Fluid Flow in Spiral Wound Reverse Osmosis Membranes

A Dissertation

SUBMITTED TO THE FACULTY OF

UNIVERSITY OF MINNESOTA

BY

Srivathsan G

IN PARTIAL FULFILLMENT OF THE REQUIREMENTS

FOR THE DEGREE OF

DOCTOR OF PHILOSOPHY

Dr. Ephraim Sparrow

July 2013

© Srivathsan G 2013

Acknowledgements

I sincerely thank my adviser Professor Eph. Sparrow for the unconditional support, and encouragement. The moral confidence he offered me throughout the project is has no parallels. My professor, Dr. Sparrow, was available for discussion on weeknights and weekends that enabled me to work fulltime and still work full time on my PhD on weeknights and weekends.

I would like to thank Reza Ramazani-Rend and John Gorman for the CFX expertise they provided me throughout the project. More than just lab-mates, they are good friends in my life.

I here recognize and recollect the support lent by my parents. They helped me to prioritize my objectives and provided encouragement to stay focused.

Last, I would like to thank the Mechanical Engineering Department at the University of Minnesota for providing us with the computational power that enabled the simulations shown in this report, and the Dow Chemical company for providing me seeding idea for this project.

Dedication

To God and

to my dear friend, philosopher, and guide-

Eph Sparrow.

Abstract

The research performed here is motivated by the need to understand and quantify the phenomena that underlie the purification of impure water by the reverse osmosis process. Despite the fact that reverse osmosis is a well-established method of water purification, the design and implementation of the process has been based on vastly oversimplified models. Oversimplified reverse-osmosis (RO) models lead to inefficient RO element performance estimation.

Reverse osmosis is based on profoundly interacting fluid flow and mass transfer phenomena. These phenomena are modeled without approximation, and the model is implemented by numerical simulation. The numerous oversimplifications of prior models have been eliminated. In particular, the linearity that marked those models has been demonstrated to be invalid. Although the flow is laminar, it is not friction dominated. Instead, pressure drop non-linearity exists because of inertial effects. A second factor promoting non-linearity is the continuous bleeding-off of product water from the salt-containing feed stream. The flow phenomena at the entry and exit of the individual reverse osmosis elements have been clarified. The associated pressure drops were found to be remarkably small.

The simulations spanned the entire range of operating conditions of actual reverse osmosis installations. The species conservation for salt took account of both advection and diffusion. Mass transfer coefficients at the membrane surface were determined, again for all practical operating conditions. The main outcomes of the simulations were the true portrayal of the in-element pressure losses and mass transfer coefficients.

Experiments were performed to support the simulation model. The attainment of marginal levels of agreement motivated careful examination of the physical interactions of the feed spacer and the RO membrane. Upon investigation, it was found that the feed spacer penetrated into the membrane, with the outcome that the dimensions of the actual flow passage were less than that based on the dimensions of the feed spacer alone. When the simulation was repeated with the actual flow passage dimensions, good agreement was achieved between the simulations and the experimental data.

Based on the new information extracted from both the simulations and the experiments, a new methodology was developed for the accurate simulation of typical reverse osmosis elements. The new methodology supersedes that which has been standard in the past. All of the oversimplifications and omissions have been avoided in favor of a logic-based application of the underlying physical

phenomena. The outcome of the research work is a thorough understanding of the reverse osmosis desalination operation.

Table of contents

List of tables ix

List of figures x

Nomenclature xiv

Chapter 1 : REVERSE OSMOSIS OVERVIEW 1

1.1 Introduction 1

1.2 Current status of available water resources 1

1.3 Potential source for water 6

1.4 Desalination 8

1.5 Different methods of desalination 11

1.6 Comparing reverse osmosis and distillation 12

1.7 Membranes in reverse osmosis 14

1.8 Reverse osmosis as the focus of this research 17

1.9 A brief overview of reverse osmosis water treatment facility 20

1.10 A detailed overview of reverse osmosis systems 24

1.11 Brief description of the Reverse Osmosis Module 26

1.12 Description of a reverse osmosis pressure vessel 28

Chapter 2 : REVERSE OSMOSIS OVERVIEW 30

2.1 Introduction 30

2.2 Detailed description of a reverse osmosis element 30

2.3 Description of flow in spiral wound reverse osmosis element 36

2.4 Description of processes in a spiral wound element 36

2.4.1 Entry pressure drop in an element 37

2.4.2 Pressure drop in the feed spacer 38

2.4.3 Concentration polarization on the feed side 40

2.4.4 Reverse Osmosis 45

2.4.5 Exit pressure drop 49
2.4.6 Pressure drop in the permeate spacer 49
2.4.7 Net driving pressure 61
2.5 Current methods of RO element modeling 65
2.6 Insufficiencies of the current model used 74
2.7 Research work proposed 75
Chapter 3 : FEED SPACER IN CFD SIMULATION 79
3.1 Introduction 79
3.2 Geometry of the feed spacers 79
3.3 Geometry of the spacer used in simulation 81
3.4 Fluid flow and mass flow analysis 86
3.5 Mesh analysis 90
3.6 Analysis type 93
3.6.1 Laminar vs. Turbulence 93
3.6.2 Steady state vs. Transient 94
3.7 Fluid flow boundary conditions 95
3.8 Mass transfer in CFX simulation 101
3.8.1 Implementation of membrane wall boundary condition 101
3.8.2 Implementation of periodic boundary condition 103
3.9 Summary of fluid flow and mass transfer boundary conditions 112
3.9.1 Volume domain 112
3.9.2 Feed spacer opening 112
3.9.3 RO membrane boundary condition 113
3.10 Post processing of output from simulations 113
Chapter 4 : CFX SIMULATION RESULTS 118
4.1 Introduction 118

4.2 Results of feed spacer pressure drop from simulations 118
4.3 Analysis of feed spacer pressure drop 120
4.3.1 Correlation of pressure drop results 124
4.4 Analysis fluid flow through the feed spacers 130
4.5 Results of feed spacer mixing 137
4.5.1 Correlation of mass transfer results 140
4.6 Analysis of mass transport in the feed spacers 144
4.7 Pressure drop factor and the Sherwood number in simulation 148
Chapter 5 : EXPERIMENTS 149
5.1 Introduction 149
5.2 Experiments to measure feed spacer pressure drop 149
5.2.1 Cleaning 150
5.2.2 The RO elements and test preparation 151
5.2.3 Experiment and data acquisition 151
5.2.4 Theory of feed spacer deformation during membrane fabrication 157
5.3 Experiments to measure the mixing created by the feed spacer 160
5.3.1 Understanding the response of the membrane to the feedwater pH 162
5.3.2 Understanding the response of membrane to feedwater concentration 165
5.3.3 Understanding the effect of feed spacer on mass transfer 168
5.4 Conclusion 173
Chapter 6 : ENTRY AND EXIT PRESSURE DROP 174
6.1 Introduction 174
6.2 Discussion of the geometry 174
6.3 Boundary conditions 176
6.4 Results and discussion 177
6.4.1 Entry pressure drop 177

6.4.2 Exit pressure drop 181
6.5 Conclusion 185
Chapter 7 : NEW RO SIMULATION METHOD 186
7.1 Introduction 186
7.2 Method of RO discretization 186
7.3 Required user input and its nomenclature 190
7.4 Identification of notation used in the simulation algorithm 191
7.5 Simulation initialization 192
7.6 Simulation algorithm 192
7.7 Simulation post processing 197
7.8 Multi-element pressure vessel 198
7.9 Comparison of results and conclusions 201
Chapter 8 : SUMMARY AND FUTURE WORK 203
8.1 Introduction 203
8.2 Summary 203
8.3 Conclusion 205
8.4 Future work 207
References 209
Appendix A 215

List of tables

Table 1-1: Percentage of population with access to safe drinking water 3
Table 1-2: Range of Energy Use of different Desalination Technologies 12
Table 2-1: Input conditions for the pressure vessel 69
Table 2-2: Property of feedwater used in simulation 70
Table 3-1: Example of geometric similarity in feed spacers 81
Table 3-2: Dimensions of feed spacers used for the CFD simulation 83
Table 3-3: Heat transfer-Mass transfer Analogy 90
Table 3-4: Analysis of the μ_t/μ. Ratio (Driving pressure = 100Pa) 94
Table 4-1: Flow pressure-drop analysis 20-mil spacer 118
Table 4-2: Flow pressure-drop analysis 25-mil spacer 119
Table 4-3: Flow pressure-drop analysis 30-mil spacer 119
Table 4-4: Flow pressure-drop analysis 35-mil spacer 120
Table 4-5: The value of pressure drop parameters 125
Table 4-6: Revised values of pressure drop parameters 127
Table 4-7: Analysis of fit for the parametric pressure drop equation 129
Table 4-8: Mass transfer results for 20-mil spacer 137
Table 4-9: Mass transfer results for 25-mil spacer 137
Table 4-10: Mass transfer results for 30-mil spacer 138
Table 4-11: Mass transfer results for 35-mil spacer 138
Table 4-12: The value of pressure drop parameters 141
Table 4-13: Analysis of fit for the parametric Sherwood Number equation 143
Table 5-1: Results from feed spacer pressure drop experiment 152
Table 5-2: Data from feed spacer concentration polarization experiment 170
Table 5-3: Experimentally calculated concentration polarization 171
Table 5-4: Experimentally observed Sherwood number 172
Table 7-1: User input for RO simulations 190
Table 7-2: Table for notation used in simulation algorithm 191

List of figures

Figure 1.1: Areas of physical and economic water scarcity 4
Figure 1.2: Population density of the world (1994) 5
Figure 1.3: Percentage of households in major cities connected to water and sewers 6
Figure 1.4: Distribution of earth's water supply 6
Figure 1.5: Average composition of seawater 7
Figure 1.6: Distribution of seawater surface salinity in Practical Salinity Unit [PSU] 7
Figure 1.7: Schematic diagram of a desalination system 9
Figure 1.8: The theoretical minimum energy for desalting seawater as a function of pure water recovery 10
Figure 1.9: The qualitative description of the capital costs and energy consumption 10
Figure 1.10: Breakdown of desalination processes 12
Figure 1.11: Size distribution of particles and corresponding modes of separation 15
Figure 1.12: Description of osmosis in action 18
Figure 1.13: A schematic of a reverse osmosis facility 20
Figure 1.14: Schematic of a reverse osmosis system 25
Figure 1.15: Various arrangements of RO pressure vessels in a RO module 27
Figure 1.16: RO modules with many pressure vessels 28
Figure 1.17: cross-section of a pressure vessel with three membrane elements 28
Figure 2.1: Cutaway view of a spiral RO element 30
Figure 2.2: Cross section of a reverse osmosis membrane 31
Figure 2.3: Inserting a spacer in a membrane 32
Figure 2.4: Schematic of the direction of the feedwater over the Membrane and feed spacer 32
Figure 2.5: The construction of leaves that forma an element 33
Figure 2.6: Cutaway section of a leaf in SPRO 34
Figure 2.7: Spiral wound RO element showing leaves before winding 35
Figure 2.8: Flow of feedwater and permeate inside an element 36
Figure 2.9: Process flowchart of product water 37
Figure 2.10: Picture of a scroll of an element 38
Figure 2.11: Mass transfer boundary layer 41
Figure 2.12: Salt concentration profile 42
Figure 2.13: A conceptual diagram of the product water tube and the permeate spacer 51
Figure 2.14: Schematic of pressure drop in permeate spacer 59

Figure 2.15: Pressure vessel containing three elements 65
Figure 2.16: Qualitative graph showing current method used for modeling RO pressure vessel 67
Figure 2.17: Flowchart describing the method used to simulate element performance 72
Figure 2.18: Quantitative graph showing element performance in the pressure vessel 73
Figure 2.19: Proposed model for RO pressure vessel 78
Figure 3.1: Woven and non-woven feed spacer 79
Figure 3.2: Plan view of a two layer feed spacer 80
Figure 3.3: Typical feed spacer and the *repeating unit* used for simulation 82
Figure 3.4: Modeling of the feed spacer strand 82
Figure 3.5: Appearance of a typical feed spacer under a microscope 83
Figure 3.6: 20-mil feed spacer (Feed spacer 1) 84
Figure 3.7: 25-mil feed spacer (Feed spacer 2) 84
Figure 3.8: 30-mil feed spacer (Feed spacer 3) 85
Figure 3.9: 35-mil feed spacer (Feed spacer 4) 85
Figure 3.10: Close-up view of the inflation layers and the remaining mesh used in spacer simulation 90
Figure 3.11: Mesh analysis of 20-mil feed spacer 91
Figure 3.12: Mesh analysis of 25-mil feed spacer 92
Figure 3.13: Mesh analysis of 30-mil feed spacer 92
Figure 3.14: Mesh analysis of 35-mil feed spacer 93
Figure 3.15: Plot of mass flowrate as a function of time 95
Figure 3.16: Boundaries were periodic boundary condition is used 96
Figure 3.17: The pair of boundaries across with the pressure-difference driving the flow is applied . 96
Figure 3.18: Boundary where the RO membranes is simulated 97
Figure 3.19: Inlet location in the upstream of the feed flow 98
Figure 3.20: Velocity profile used at the inlet (a) shown in Figure 3.19 99
Figure 3.21: Outlet opening located downstream of the flow 99
Figure 3.22: Pictorial representation of the boundary conditions used ($v \neq 0$) 100
Figure 3.23: Comparison of no-slip wall and real membrane wall boundary conditions 100
Figure 3.24: Picture showing the direction of flow along the x-axis 104
Figure 4.1: Dependence of the feed velocity on the driving pressure difference 121
Figure 4.2: Pressure drop/velocity vs. velocity 122
Figure 4.3: Pressure drop factor vs. Reynolds number 123
Figure 4.4 Log-log graph of Pressure drop factor vs. Reynolds number 124

Figure 4.5: Plot of simulation data and the correlation equation 126
Figure 4.6: Plot of simulation data and the correlation equation (b = -1) 128
Figure 4.7: Pattern of seed-points used for the simulation of the streamlines 130
Figure 4.8: The two planes used to generate the vector diagrams 131
Figure 4.9: Streamline and vector diagrams for a 20-mil spacer Re = 61 132
Figure 4.10: Streamline and vector diagrams for a 20-mil spacer Re = 467 133
Figure 4.11: Streamline and vector diagrams for a 35-mil spacer Re = 89 134
Figure 4.12: Streamline and vector diagrams for a 35-mil spacer Re = 463 135
Figure 4.13: Flow patterns though the feed spacers at different Reynolds numbers 136
Figure 4.14: Percentage of mass flowing parallel to feed spacer strands 136
Figure 4.15: Plot of Sherwood number as a function of Reynolds number 139
Figure 4.16: Plot of Stanton number as a function of Reynolds number 139
Figure 4.17: Simulation data and the curve fit 142
Figure 4.18: Distribution of local Sherwood number Re = 65 (35-mil spacer) 144
Figure 4.19: Distribution of local Sherwood number Re = 365 (35-mil spacer) 145
Figure 4.20: Distribution of local Sherwood number 20-mil spacer, Re = 107 146
Figure 4.21: Distribution of local Sherwood number 25-mil spacer, Re = 92 146
Figure 4.22: Distribution of local Sherwood number 30-mil spacer, Re = 116 147
Figure 4.23: Distribution of local Sherwood number 35-mil spacer, Re = 143 147
Figure 5.1: Schematic of the RO system used in the experiments 150
Figure 5.2: Pressure drop factor vs. Reynolds number 154
Figure 5.3: Pressure drop factor vs. Reynolds number (log-log graph) 154
Figure 5.4: Pressure drop v. Reynolds Number from day 1 elements 155
Figure 5.5: Pressure drop v. Reynolds Number from all four day averages 155
Figure 5.6: Pressure drop vs. Reynolds Number with updated $X = 17.5$ 157
Figure 5.7: Figure of feed spacer and the support points 157
Figure 5.8: Schematic for feed spacer compression estimation 158
Figure 5.9: Layout of the flat cell apparatus used to measure concentration polarization 162
Figure 5.10: Effect of pH on the membrane salt rejection 163
Figure 5.11: Representative chemical structure of commercial polyamide RO membranes 165
Figure 5.12: Mode of hydrolysis by RO membrane in acidic and basic feedwater conditions 165
Figure 5.13: Effect of feedwater concentration on *Membrane B value* 168

Figure 5.14: Layout of the flat-cell apparatus used to measure concentration polarization with feed spacer 169
Figure 5.15: Comparison of the Sherwood number between experiment and simulation 173
Figure 6.1: Diagram of the CFX simulation domain 174
Figure 6.2: Diagram of a spiral RO element (a), modeled as concentric annuli (b) and simulated as a wedge (c) 175
Figure 6.3: Diagram of the mesh used in the simulation 175
Figure 6.4: Simulation domain and the boundary conditions 176
Figure 6.5: Plot of entry pressure drop and the feed flow velocity 177
Figure 6.6: Pressure contour diagram of entry pressure drop of 50 Pa 178
Figure 6.7: Simulated streamlines of the flow entering the RO vessel 178
Figure 6.8: Radial variation of feedwater axial velocities in the feed spacers 179
Figure 6.9: Picture showing the location of lines where pressure and velocity changes are plotted .. 180
Figure 6.10: Axial pressure variations at different radial positions for flow entering the RO element 180
Figure 6.11: Axial velocity variations at different radial positions for flow entering the RO element 181
Figure 6.12: Plot of exit pressure drop and the feed flow velocity 182
Figure 6.13: Comparing the magnitudes of inlet and exit pressure drops 182
Figure 6.14: Streamlines of the flow exiting the RO element 183
Figure 6.15: Pressure variations at different radial positions for flow exiting the RO element 184
Figure 6.16: Velocity variations at different radial positions for flow exiting the RO element 184
Figure 7.1: Diagram of a typical half of a leaf 186
Figure 7.2: Discretization of the membrane sheet in an RO element 187
Figure 7.3 : Diagram of the half-leaf with arrows showing feed and permeate flow directions 188
Figure 7.4: Diagram showing the faces and the edges 189
Figure 7.5: Isometric view of the faces and edges 189
Figure 7.6: Pictorial representation of flow in the permeate spacer in each discrete element 195
Figure 7.7: Description of the approximation made in the simulation. 196
Figure 7.8: Quantitative graph showing element performance in the pressure vessel 200
Figure 7.9: Element performance graph that compares the two simulation results 202

Nomenclature

Symbol	Description	Units
a	Pressure drop coefficient	
a_1	Darcy Coefficient in Forchheimer model	
A	*Membrane A value*	$[M]^{-1}[L]^{3}[T]^{1}$
A_x	Area of cross section on the *repeating unit* where the flow enters	$[L]^2$
A_{memb}	Area of cross section of the membrane in the *repeating unit*	$[L]^2$
AA	*Membrane A*ctive area of the membrane	$[L]^2$
AA_{leaf}	Active area of the leaf	$[L]^2$
b	Pressure drop exponent (old pressure drop factor expression)	
b_1	Forchheimer coefficient in Forchheimer model	
B	*Membrane B value*	$[L][T]^{-1}$
C	Concentration of salt in fluid flow	$[M][L]^{-3}$
C_{bulk}	Bulk concentration of the feed flow	$[M][L]^{-3}$
$C_{permeate}$	Concentration of the permeate water produced	$[M][L]^{-3}$
C_{wall}	Concentration of the feedwater near the membrane surface	$[M][L]^{-3}$
ΔC	Concentration difference across the *repeating unit*	$[M][L]^{-3}$
C_P	Specific heat	$[L]^2[T]^{-2}[\theta]^{-1}$
CP	Concentration polarization	
d_h	Hydraulic diameter	[L]
d_{hp}	Thickness of the permeate spacer	[L]
d_{feed}	Thickness of the feed spacer	[L]
D	Molecular diffusion coefficient of salt in water	$[L]^2[T]^{-1}$
f	Pressure drop factor	$[L][T]^{-1}$
$\dot{G}_x$	Gibbs free energy flowrate of species x	$[M][L]^2[T]^{-2}$
h	Heat transfer coefficient	$[M][T]^{-3}[\theta]^{-1}$
H	Permeate spacer pressure drop constant	$[M][L]^{-5}[T]^{-1}$
J	Permeate flux of product water flowing through the membrane	$[L][T]^{-1}$

Symbol	Description	Units
J_s	Salt flux passing through the membrane into the product water	$[M][L]^{-2}[T]^{-1}$
k	Thermal conductivity	$[M][L][T]^{-3}[\theta]^{-1}$
K	Mass transfer coefficient	$[L][T]^{-1}$
l	Length of the spacer *repeating unit*	[L]
L	Length of the element	[L]
L_{leaf}	Length of the permeate spacer leaf	[L]
$\dot{m}$	Mass flowrate of feedwater entering the *repeating unit*	$[M][L]^{-2}[T]^{-1}$
M	Concentration multiplication factor	
NDP	Net Driving pressure	$[M][L]^{-1}[T]^{-2}$
Nu	Nusselt number	
p	Static pressure of fluid flow	$[M][L]^{-1}[T]^{-2}$
ΔP	Pressure drop across the *repeating unit*	$[M][L]^{-1}[T]^{-2}$
P_{drop}	Pressure drop per unit length-Pressure gradient (scalar)	$[M][L]^{-2}[T]^{-2}$
P_{feed}	Feed pressure around the membrane	$[M][L]^{-1}[T]^{-2}$
P_{perm}	Permeate pressure around the membrane	$[M][L]^{-1}[T]^{-2}$
$P_{permeate}$	Pressure of the permeate in the product water tube	$[M][L]^{-1}[T]^{-2}$
ΔP_{memb}	Static pressure difference across the membrane	$[M][L]^{-1}[T]^{-2}$
$\ddot{q}$	Volumetric heat source/sink term	$[M][L]^{-1}[T]^{-3}$
Q_{feed}	Volumetric flowrate of feedwater	$[L]^3[T]^{-1}$
$Q_{permeate}$	Volumetric permeate flowrate	$[L]^3[T]^{-1}$
rec	Percentage recovery of product water from feedwater	
Re	Reynolds number	
$\dot{S}_{gen}$	Rate of entropy generation	$[M][L]^2[T]^{-2}[\theta]^{-1}$
Sc	Schmidt number	
Sh	Sherwood number	

Symbol	Description	Units
SP	Salt passage	
St	Stanton number	
t	Time	[T]
T	Temperature	[θ]
v	Velocity of fluid flow	$[L][T]^{-1}$
v_{feed}	Bulk velocity of the feedwater through the feed spacer	$[L][T]^{-1}$
v_{memb}	Velocity of membrane flow near the membrane wall	$[L][T]^{-1}$
v_p	Velocity of permeate water through the permeate spacer	$[L][T]^{-1}$
v_x	Velocity in x direction	$[L][T]^{-1}$
$\dot{V}$	Volumetric flowrate of feedwater entering the *repeating unit*	$[L]^3[T]^{-1}$
$\dot{W}$	Work of separation of salt from water	$[M][L]^2[T]^{-2}$
X	dimensionless spacer *geometry factor*	
α	Thermal diffusivity	$[L]^2[T]^{-1}$
Γ	Concentration Factor	
μ	Dynamic viscosity	$[M][L]^{-1}[T]^{-1}$
Π	Osmotic pressure of water	$[M][L]^{-1}[T]^{-2}$
Π_{feed}	Osmotic pressure of feedwater near the membrane wall	$[M][L]^{-1}[T]^{-2}$
$\Delta\Pi_{memb}$	Osmotic pressure difference across the membrane	$[M][L]^{-1}[T]^{-2}$
Π_{perm}	Osmotic pressure of permeate around the membrane	$[M][L]^{-1}[T]^{-2}$
$\Pi_{permeate}$	Osmotic pressure of permeate in the product water tube	$[M][L]^{-1}[T]^{-2}$
ρ	Density	$[M][L]^{-3}$
σ	Mass flux of salt transported from the membrane wall to bulk flow	$[M][L]^{-2}[T]^{-1}$
$\ddot{\sigma}$	Volumetric mass (salt) source/sink term	$[M][L]^{-3}[T]^{-1}$

Chapter 1 : REVERSE OSMOSIS OVERVIEW

1.1 Introduction

Water is an important essential elixir of life. Although two thirds of the earth's surface is covered by water in its various forms, there are not sufficient, continuous and reliable sources of fresh drinking water available when and where needed for about three billion people around the world. Even the naturally available potable water is often contaminated by human activity. Drinking water availability today, far from being pure may contain some two hundred deadly commercial chemicals. Add to that bacteria, viruses, organic and inorganic minerals, thereby giving rise to a chemical cocktail that is unsuitable (if not deadly) for human consumption. In the year 2000 alone, unsafe water mortality amounted to 80 million years of lost life [1]. The human body, being primarily water, requires sufficient daily water replacement in order to function efficiently. Treatment of natural fresh water has now become necessary for human consumption. Furthermore, with rising population and increasing per-capita requirement of fresh water, attention has been turned to the sea as a source of available water for subsequent processing and purification. Certain municipalities around the world are also extracting fresh water from effluent water or sewer water.

Separation of impurities from water is an indispensable part of water purification. Separation technology is not only confined to water purification but also an indispensable part of downstream operations in chemical, petrochemical, biochemical, and several other process industries. Efficient separations process technologies are essential to minimize waste and conserve energy. To perform separation processes efficiently, it is necessary to understand the science behind the process. Various separation processes can be accomplished by exploiting the differences between the media to be separated: size, shape, vapor pressure, solubility, chemical activity, etc.

1.2 Current status of available water resources

Water shortage in the United States is not as critical as it is in other parts of the world. Notwithstanding this, there are feuds over water sharing, for example between Arizona and California [2][3]. In such situations, the problem is expected to be resolved through negotiations in the courtroom. If the focus is shifted to a global perspective, the terms dramatically change.

There are several principle manifestations of global water shortage problems:

a) Inadequate access to safe drinking water for about 900 million people [4]
b) Inadequate access to domestic water for approximately three billion people [5]
c) Groundwater over drafting leading to diminished agricultural yields [6]
d) Overuse and pollution of water resources harming biodiversity [7]
e) Waterborne diseases and pandemic [7]
f) Extended drought [7]
g) Flood damage to existing infrastructure causing short-term potable water scarcity [7]
h) Regional conflicts over scarce water resources sometimes resulting in warfare [7]

The World Bank reported that 90 countries now have water shortages that threaten health and economies. More than three billion people, fifty percent of the world population, have no access to clean water or sanitation. In this context, it cannot be expected that water conflicts will be amicably resolved. More than a dozen nations receive most of their water from rivers that cross borders of neighboring countries viewed as hostile. Although water crises are closely related to regional tensions, history shows that water has brought people together many times. Acute conflicts over water are far less than the record of cooperation [8][9] .In contrast, regional instability was brought about when there was an absence of institutions to co-operate in regional collaboration [10].

The situation becomes even more grave and personal when the water scarcity comes down to the availability of safe drinking water. Over 1.1 billion people are still without access to safe drinking water. The coverage remains low, especially in poor rural areas of Africa and informal peri-urban settlements. In many developing countries, water problems have grown more severe due to unplanned industrialization. Dangerous levels of arsenic in groundwater have emerged in several Asian countries over the decade making available natural water unsuitable for consumption. Table 1-1 [11] shows the percentage of population with access to safe drinking water.

Table 1-1: Percentage of population with access to safe drinking water

Percentage of Population with access to safe drinking water											
	1990	2000		1990	2000		1990	2000		1990	2000
Sub-Saharan Africa			**Middle East/North Africa**			**South Asia**			**CEE/CIS**		
Mauritius	100	100	Cyprus	100	100	Maldives	-	100	Belarus	-	100
Comoros	88	96	Djibouti	-	100	Bangladesh	94	97	Bulgaria	-	100
Botswana	93	95	Lebanon	-	100	Pakistan	83	90	Slovakia	-	100
Gabon	-	86	Egypt	94	97	Nepal	67	88	Hungary	99	99
South Africa	86	86	Jordan	97	96	Regional average	72	85	Russian Federatior	-	99
Zimbabwe	78	83	Saudi Arabia	-	95	India	68	84	Ukraine	-	98
Côte d'Ivoire	80	81	Iran	-	92	Sri Lanka	68	77	Yugoslavia	-	98
Burundi	69	78	Algeria	-	89	Bhutan	-	62	Albania	-	97
Lesotho	-	78	Regional average	82	87	Afghanistan	-	13	Moldova, Rep.	-	92
Senegal	72	78	Palestinian Terr.	-	86				Kazakhstan	-	91
Namibia	72	77	Iraq	-	85	**Latin America/Caribbean**			Regional average	-	91
Cape Verde	-	74	Morocco	75	80	Barbados	-	100	Uzbekistan	-	85
Ghana	53	73	Syria	-	80	Saint Lucia	-	98	Turkey	79	82
C. African Rep.	48	70	Tunisia	75	80	Uruguay	-	98	Georgia	-	79
Tanzania	38	68	Sudan	67	75	Bahamas	-	97	Azerbaijan	-	78
Mali	55	65	Libya	71	72	Dominica	-	97	Kyrgyzstan	-	77
Zambia	52	64	Yemen	-	69	Costa Rica	-	95	Tajikistan	-	60
Benin	-	63	Oman	37	39	Grenada	-	95	Romania	-	58
Gambia	-	62				Guyana	-	94			
Nigeria	53	62	**East Asia/Pacific**			Chile	90	93	**Industrialized countries**		
Niger	53	59	Cook Islands	100	100	Belize	-	92	Andorra	-	100
Cameroon	51	58	S. Korea,	-	100	Guatemala	76	92	Australia	100	100
Kenya	45	57	Niue	100	100	Jamaica	93	92	Austria	100	100
Malawi	49	57	Singapore	100	100	Colombia	94	91	Canada	100	100
Mozambique	-	57	Tonga	-	100	Cuba	-	91	Denmark	-	100
Sierra Leone	-	57	Tuvalu	-	100	Panama	-	90	Finland	100	100
Regional average	53	57	Samoa	-	99	Trinidad & Tobago	91	90	Malta	100	100
Guinea-Bissau	-	56	Korea, Rep.	-	92	Honduras	83	88	Monaco	-	100
Togo	51	54	Vanuatu	-	88	Mexico	80	88	Netherlands	100	100
Uganda	45	52	Philippines	87	86	Brazil	83	87	Norway	100	100
Congo	-	51	Thailand	80	84	Dominican Rep.	83	86	Slovenia	100	100
Guinea	45	48	Palau	-	79	Regional average	82	86	Sweden	100	100
Madagascar	44	47	Indonesia	71	78	Ecuador	71	85	Switzerland	100	100
Eritrea	-	46	Viet Nam	55	77	Bolivia	71	83	United Kingdom	100	100
Congo, Dem. Rep.	-	45	Regional average	71	76	Venezuela	-	83	United States	100	100
Equatorial Guinea	-	44	China	71	75	Suriname	-	82	Regional average	100	100
Burkina Faso	-	42	Myanmar	-	72	Peru	74	80			
Rwanda	-	41	Solomon Islands	-	71	Paraguay	63	78			
Angola	-	38	Mongolia	-	60	El Salvador	66	77			
Mauritania	37	37	Kiribati	-	48	Nicaragua	70	77			
Chad	-	27	Fiji	-	47	Haiti	53	46			
Ethiopia	25	24	Papua New Guinea	40	42						
			Lao People's Dem.	-	37						
			Cambodia	-	30						

Many arid and semi-arid countries face shortage of water due to lack of natural resources, especially the Arab world. Arab countries pay increasing attention and interest to water resources because of their growing economies, growing standard of living, and increasing populations. These countries

continuously invest towards the development of available resources and providing large amounts of water supplies to urban centers, villages, farms and other users. However, the limited water resources, and the need to balance economic and social development resulted in the emergence of an imbalance between the available water resources and demand. Figure 1.1 [12] show the distribution of physical and economical water scarcity.

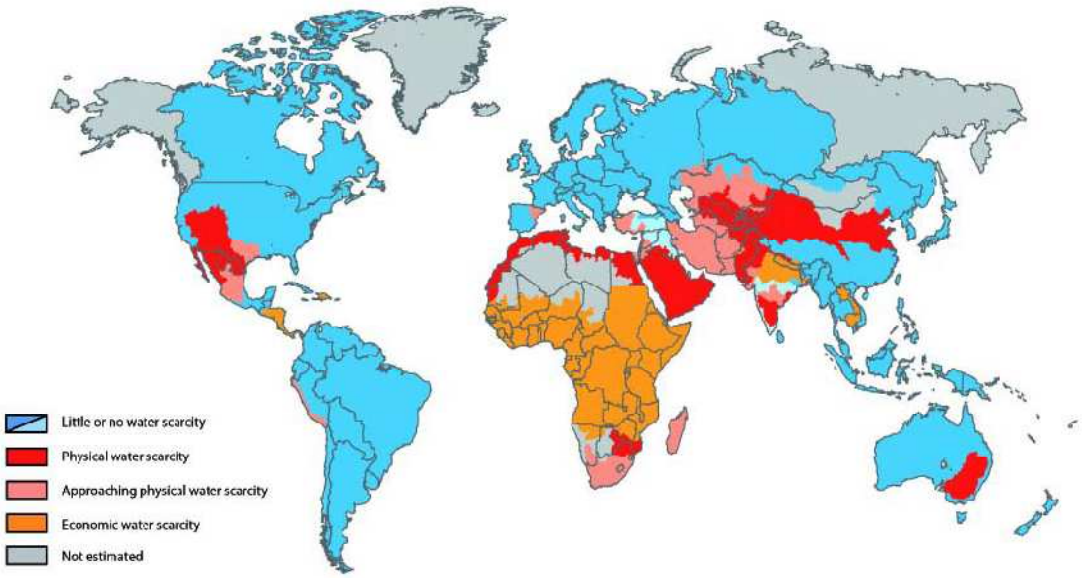

Figure 1.1: Areas of physical and economic water scarcity

The situation of water shortage is not only confined to poor countries in Africa or arid regions of Arabia but also is prominent in developing countries endowed with natural water resources. Many places in India face water shortage because of large populations. Cities, such as Chennai (the author's hometown), Tamil Nadu (India), have enough water resources to sustain a population of three million. Nevertheless, when the cities grow, the available water supply is not enough, and a water shortage is created. Especially in summer, 5.5 million people in Chennai suffer and will have to adjust to infrequent and insufficient supply of domestic water. Water is transported by trucks to supply the city of Chennai from other parts of the country. This also causes collateral issues because, by transporting water from other areas to the cities, the other areas run short of water for their regional use. This state of affairs led to the installation of the biggest seawater desalination plant in India that can supply 100 million liters of domestic water to two million people per day. Such a situation is not just confined to the city of Chennai. Similar situations exit in other parts of the world too, with large populations greater than which the natural resources can support. Figure 1.2 [13] shows the

population density distribution of the world. Thus, poverty, industrialization, lack of natural resources, and population explosion are a few of the many factors that contribute to water problems [14].

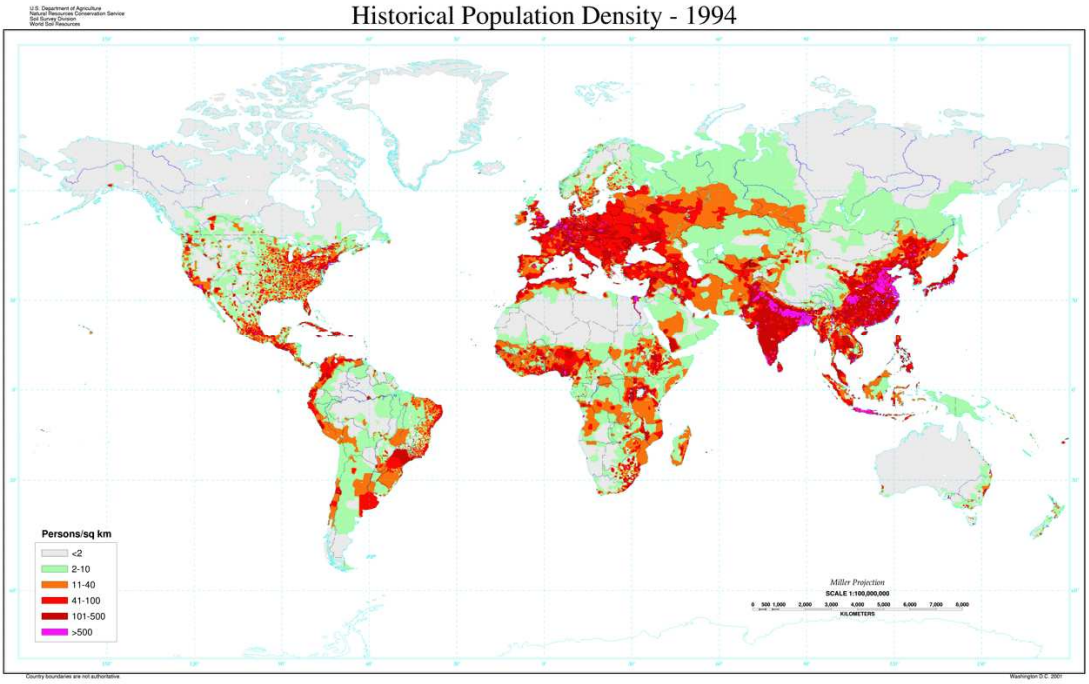

Figure 1.2: Population density of the world (1994)

Water problems are not confined just to water availability. Human activity produces a great deal of wastewater, and this wastewater should be processed before being released into the environment. Water supply system, sewer systems, and sewer treatment facilities are essential to eliminate water problems. This situation is good in developed continents in Europe and North America. The situation is worse in developing nations. Large fraction of households, even in the major cities of developing nations, do not have access to sewers. Furthermore, up to 90% of the developing world's waste is still discharged untreated into local rivers and streams [15][16] Figure 1.3 shows the percentage of households in major cities connected to water and sewers.

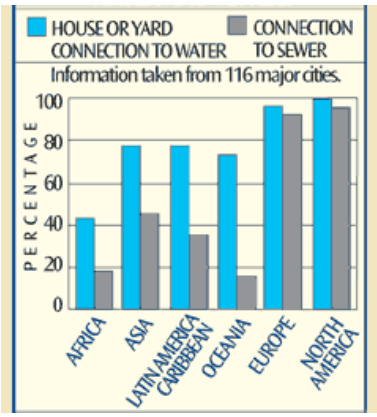

Figure 1.3: Percentage of households in major cities connected to water and sewers

1.3 Potential source for water

About 71% of earth's surface is covered with water. A total of 1.4 billion cubic kilometers of water is available on earth. Unfortunately, as shown in Figure 1.4 [17], 97.5% of that is found in the seas. This water is not useful for human consumption.

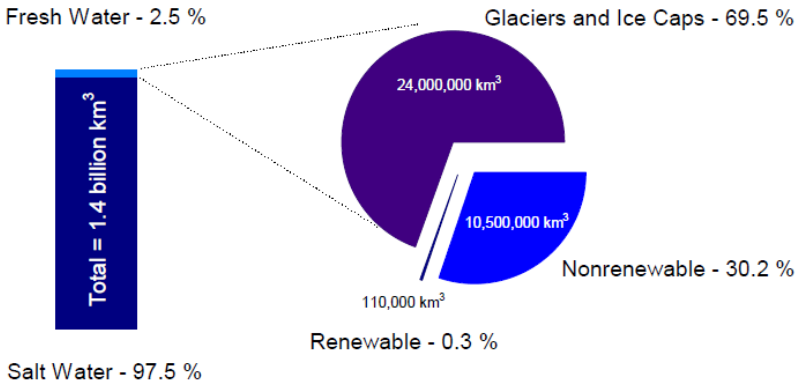

Figure 1.4: Distribution of earth's water supply

Just as the English poet, Samuel Taylor Coleridge wrote in his poem -- *The Rime of the Ancient Mariner*- there is "Water, water, everywhere, not any drop to drink". Seawater is available with a salt concentration that is excessive for human consumption - about 3.5% by weight of dissolved salts (35000 ppmw salt). Human blood has the salinity equivalent of 0.9% (~9000 ppmw). Therefore, seawater is unsuitable for consumption as it worsens the salt balance of the body. Therefore,

seawater must be processed to produce fresh water. Figure 1.5 [18] shows the average composition of the seawater.

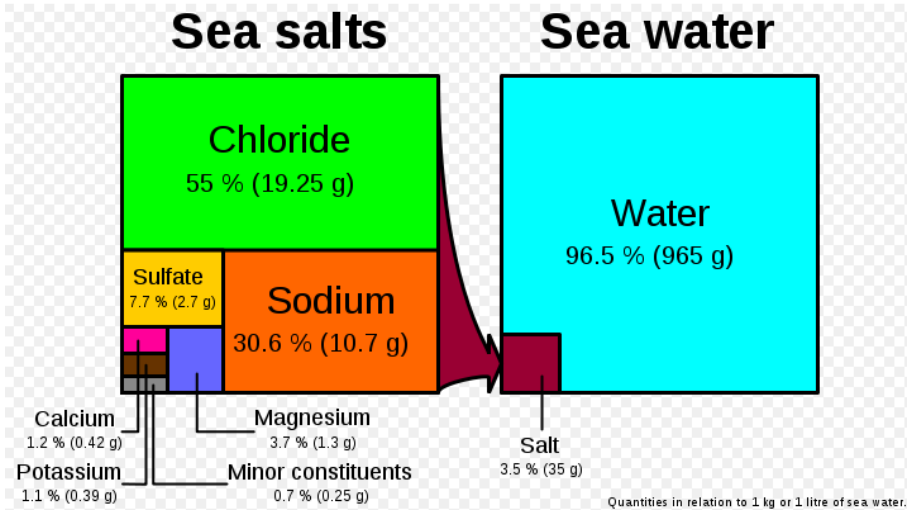

Figure 1.5: Average composition of seawater

Furthermore, the salinity distribution of seawater is not constant around the world. Climate, ocean current, river discharge, and seawater temperature affect the salinity of seawater from one region to another. Figure 1.6 [19] shows the salinity distribution of seawater.

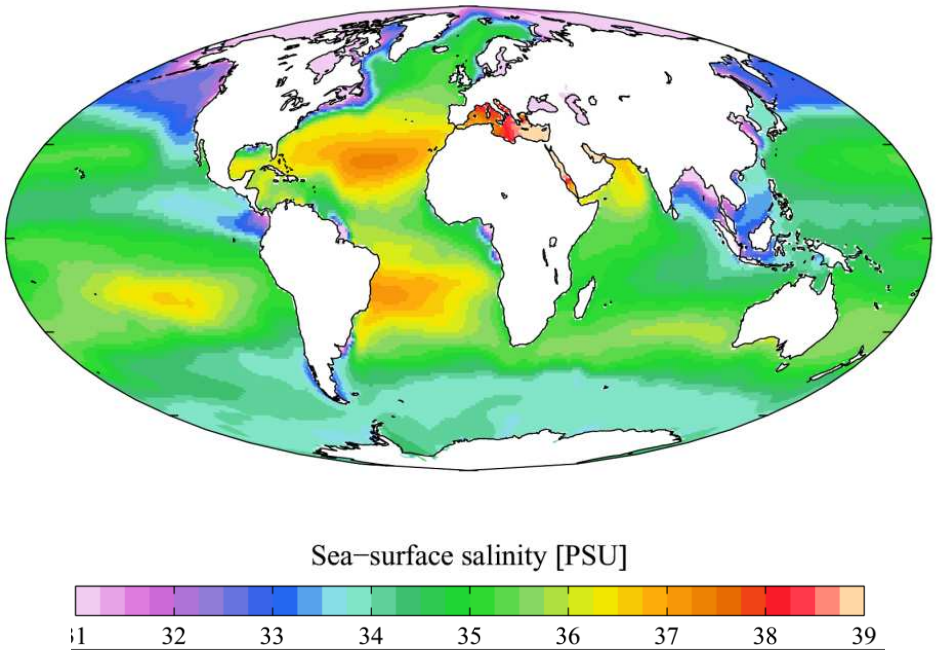

Figure 1.6: Distribution of seawater surface salinity in Practical Salinity Unit [PSU]

The remaining 2.5% is available as fresh water. To add to the complexity of the situation, almost 70% of the available fresh water is found in glaciers and ice caps. Only a small fraction, 30%, is available as lakes, rivers, ground water, etc. Like fossil energy resources, most of this water has accumulated over time and cannot be considered renewable. The global water cycle accounts for the only naturally renewable source of fresh water, that is, precipitation that occurs over land (about 110,300 km^3/year) [20].

It is environmentally malignant to tap into the non-renewable sources of water, and the renewable sources of fresh water may be too expensive to tap and distribute, or may turn out to be just not enough with growing human demand.

Other renewable natural bodies of water can be a potential source of water. However, most sources are not sufficiently salinity free to be suitable for consumptions. For this reason, these water sources are called brackish water. The word *brackish* comes from the Middle Dutch root "brak," meaning "salty". Technically, brackish water contains between 0.5 and 30 grams of salt per liter—more often expressed as 0.5 to 30 parts per thousand (ppt or ‰). Thus, the designation brackish covers a wide range of salinity regimes.

Hence, salt must be removed from many naturally occurring sources of water. In light of this situation, there is a concerted effort for desalination as a sustainable source of fresh water.

1.4 Desalination

Water available in nature has high salt content. To use the available sea or brackish water, the available water must be processed by a desalination system to produce pure water. The theoretical minimum energy for reversible desalination of seawater is a little less than three kJ/kg_water [21]. Although this value can be arrived at in a number of ways, it is perhaps easiest to think of the minimum requirement as the Gibbs free energy change associated with the process of salt dissolution. It is important to note that in a reversible process, dissolution and desalination deals with the same amount of energy. This energy change is linked to any number of physical characteristic, including salinity, boiling point elevation, freezing point depression, and osmotic potential (or pressure). Work is necessary to separate the salt from available water. Figure 1.7 shows a schematic of a desalination system.

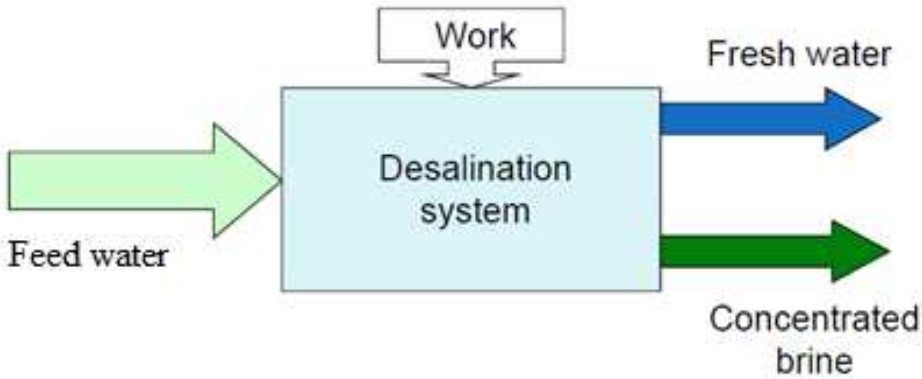

Figure 1.7: Schematic diagram of a desalination system

The rate of work of separation $\dot{W}$ is given by

$$\dot{W} = \left[\left(\dot{G}\right)_{Concentrate} + \left(\dot{G}\right)_{Freshwater}\right] - \left(\dot{G}\right)_{Feedwater} + T\dot{S}_{gen} \tag{1.1}$$

where $\left(\dot{G}\right)_{Concentrate}$, $\left(\dot{G}\right)_{Freshwater}$, and $\left(\dot{G}\right)_{Feedwater}$ are the Gibbs free energy flowrate of concentrated brine, fresh water and feedwater respectively, and $T\dot{S}_{gen}$ is the loss due to irreversibility. $\dot{S}_{gen}$ is the rate of entropy generation in the water desalination process.

From Equation (1.1), it is very clear that the work for separation is a function of the salt concentration in the feedwater, the percent of feedwater that is recovered as pure water, and the salt concentrations of pure and concentrated brine. It is clear that as the recovery of purewater is increased, the remaining solution becomes ever more concentrated, thereby further elevating the $\left(\dot{G}\right)_{Concentrate}$. Thus, as the recovery increases, the energy required to perform the operation must also increase. The relationship between recovery and the theoretical minimum energy for seawater (35000 ppmw Nail) desalting is shown qualitatively in Figure 1.8.

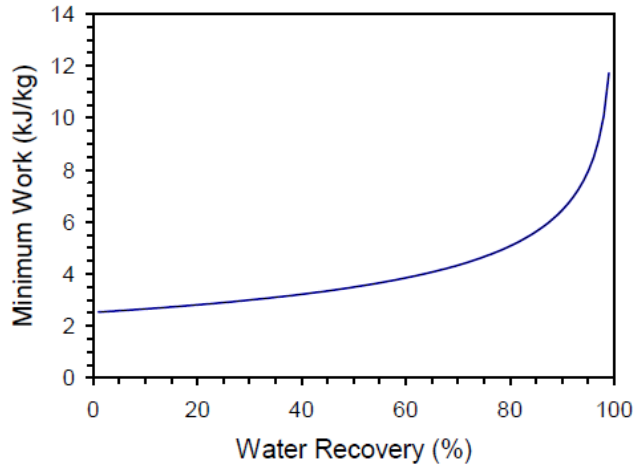

Figure 1.8: The theoretical minimum energy for desalting seawater as a function of pure water recovery

It is not practical to conduct desalination at theoretically ideal conditions. For that matter, no process can operate at perfect efficiency if it were to be spontaneous. Furthermore, design considerations teach us that systems operating with nearly perfect energy efficiency (near thermodynamic reversibility) will be large, and will therefore have high capital costs. Conversely, processes that use energy less efficiently can be smaller and will thus tend to have lower capital costs. Consequently, for most practical applications, there is a tradeoff between capital costs and energy costs. This tradeoff should be handled astutely to create an optimum plant design yielding a minimum total operating cost (here the cost of pure water). [22][23].

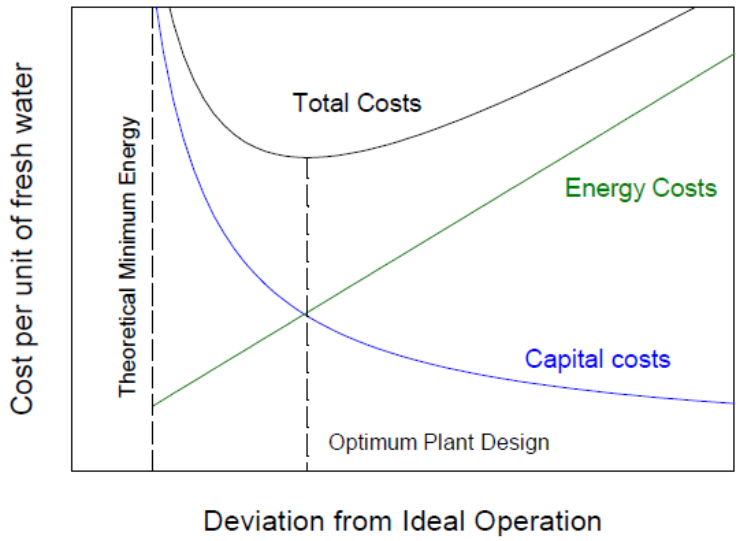

Figure 1.9: The qualitative description of the capital costs and energy consumption

Figure 1.9 [24] shows two important curves - the capital cost curve and the energy cost curve. The minimum point of the total cost curve is the optimum-plant-design curve. To identify the location of the optimum plant design, it is necessary to predict the capital cost curve and the energy cost curve accurately. The two curves can be predicted correctly only if the desalination system can be modeled accurately. The aim of this doctoral work is to improve significantly the understanding of the reverse osmosis (RO) desalination system and to provide an improved model to help predict the optimum plant design for the system.

1.5 Different methods of desalination

The principal desalination techniques are

- Membrane techniques
    - Reverse osmosis
    - Electrodialysis
    - Capacitive deionization
- Phase change techniques (distillation)
    - Multi-stage flash evaporation (MSF)
    - Multi-effect distillation (MED or MEE)
    - Vapor compression distillation
    - Solar thermal distillation
- De-Ionization

Among the aforementioned methods of desalination, distillation and reverse-osmosis are the two major and preferred means. Especially in the US, reverse osmosis is the most preferred method to desalination as shown in Figure 1.10 [25].

.

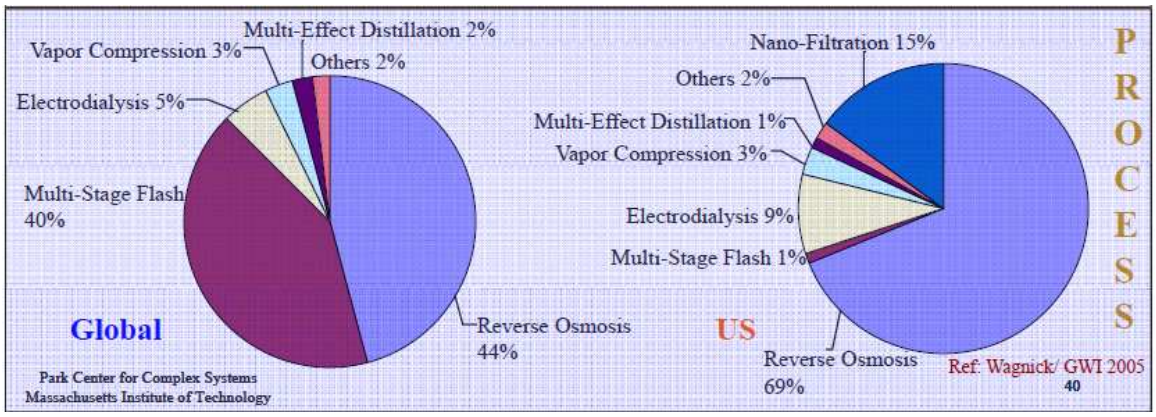

Figure 1.10: Breakdown of desalination processes

Both distillation and reverse osmosis have their advantages and disadvantages. The first difference comes in the form of energy used in desalination. Table 1-2 [26] shows the range of energy required for various desalination techniques.

Table 1-2: Range of Energy Use of different Desalination Technologies

Technology	Energy Use kJ/kg
Multiple Stage Flash (Distillation)	95-299
Multiple Effect Distillation (Distillation)	95-275
Vapor Compression (Distillation)	14-120
Reverse Osmosis (Seawater)	11-61
Reverse Osmosis (brackish water)	7.2-11
Electro Deionization (Brackish)	0.4-4

1.6 Comparing reverse osmosis and distillation

It may be apparent from Table 1-2 that distillation requires more energy per kilogram of desalinated water than do the other methods. This information requires some explanation. Distillation uses energy in the form of heat (low quality energy) whereas reverse osmosis uses energy in the form of work (higher quality energy). Distillation is very practical where energy is available in the form of heat. Not all locations have easy access to heat energy. The cost of heat energy from burning fuel is

considerably lower than the cost of work energy e.g., electricity. Therefore, in practice, distillation and reverse osmosis cost similarly.

The capital installation cost for a distillation plant is high, but the operational cost consists of regular maintenance plus the cost of the heat energy. Often, distillation plants are combined with a fossil fuel power plant to maximize energy utilization. Therefore, heat, which might have otherwise been rejected to the environment, is used for desalination (practically free). Distillation plants function well with relatively poor quality feedwater. Therefore, in distillation, the feedwater needs to be pretreated to a lower quality than in the case of reverse osmosis, which amounts to a lower expense in the case of distillation. Heat exchangers in a distillation plant can become fouled, but the frequency of interventional maintenance and the severity of fouling are higher in a RO plant. The RO plant has to be stopped periodically for cleaning. The running cost of and RO desalination plant is very high. In addition to energy, RO plant operating cost includes replacing RO filtering units (RO elements).

RO plants can be installed wherever there is access to raw feedwater. This advantage makes RO process viable and more frequently used around the worlds than distillation. There is no chemical addition so the effluent is safe and can be returned to the environment without any significant post-treatment operations. Reverse osmosis plants have a very small geographical and environmental footprint. They have a modular design and can be readily expanded and resized as the need arises. RO process is capable of producing water free of dissolved gaseous and volatile impurities. In contrast, distillation plants require extensive planning and infrastructure modification for installation and expansion, and the produced water is not free from volatile impurities. These advantages of the RO technology and the ever-improving RO-membrane technology make reverse osmosis stand out as the single most important method to remove dissolved impurities from water.

Distillation is not commonly used for brackish water desalination. The reverse osmosis process is the prominent means of desalination of brackish water. Brackish water reverse osmosis technology removes salt, organic materials, and other dissolved contaminants from water. It can also reject bacteria, sugars, proteins, particles, dyes, and other constituents that have a molecular weight of greater than 150-250 Da.. Reverse osmosis is also capable of selectively removing divalent cations like calcium and magnesium, which cause hard water.

Other than purifying naturally occurring water for human use, RO systems are used around the world for purifying water for the food and beverage industries, in hospitals, in agriculture to alter soil

salinity, in hotels and resorts, in pharmaceutical industries, for water bottling and ice making, in industrial boilers, in pharmaceuticals, in car wash and in many more applications.-

1.7 Membranes in reverse osmosis

The heart of the reverse osmosis processes is membranes. Membrane technologies have been established as a very effective and commercially attractive option for water separation and purification process. Membrane-based water purification processes are currently competitive relative to older techniques like distillation or ion exchange because membrane techniques work without the addition of chemicals (used in ion exchange), with low initial capital expense (relative to distillation), and in a compact modular design (relative to distillation). Given the fact that there is a shortage of pure drinking water, that there is a recurring energy crisis, and uncontrolled population growth in the world, the study of membrane separation processes for water purification is now more important than ever [27].

The word membrane originates from the Latin word *membrana,* which means a skin. In its common usage, membrane refers to a skin-like material that separates two media and precludes their direct contact. Membranes are generally permeable or semi-permeable, often synthetic (except in biological entities) thin polymeric solids that restrict motion of certain species and pass other media selectively. A membrane can be defined as a barrier that separates two multi-species entities that restricts and regulates transport of various species across its thickness in the presence of various driving forces. Membrane separation process, like all separation processes that operate on a given raw material, produce a product depleted in certain components and another that is enriched (concentrated). The important point to be noted with respect to the definition of a membrane is that it is defined by what it does (function) and not by what it is. Therefore, it does not matter if the membrane is homogeneous or heterogeneous, solid or liquid, symmetric or asymmetric, neutral or bipolar; all that matters about the membrane is the function it performs

Membrane function can be categorized based on its separation mechanism, which include <u>size exclusion</u>, <u>solubility and diffusivity</u>, and <u>electric charge</u> [28]. These mechanisms can be elucidated as follows:

a) Size-exclusion membrane separation includes: micro-filtration, ultra-filtration, and nano-filtration

b) Solubility and diffusivity membrane separation includes reverse osmosis, gas separation, and pervaporation.

c) Charge membrane separation includes electrodialysis and electro-deionization.

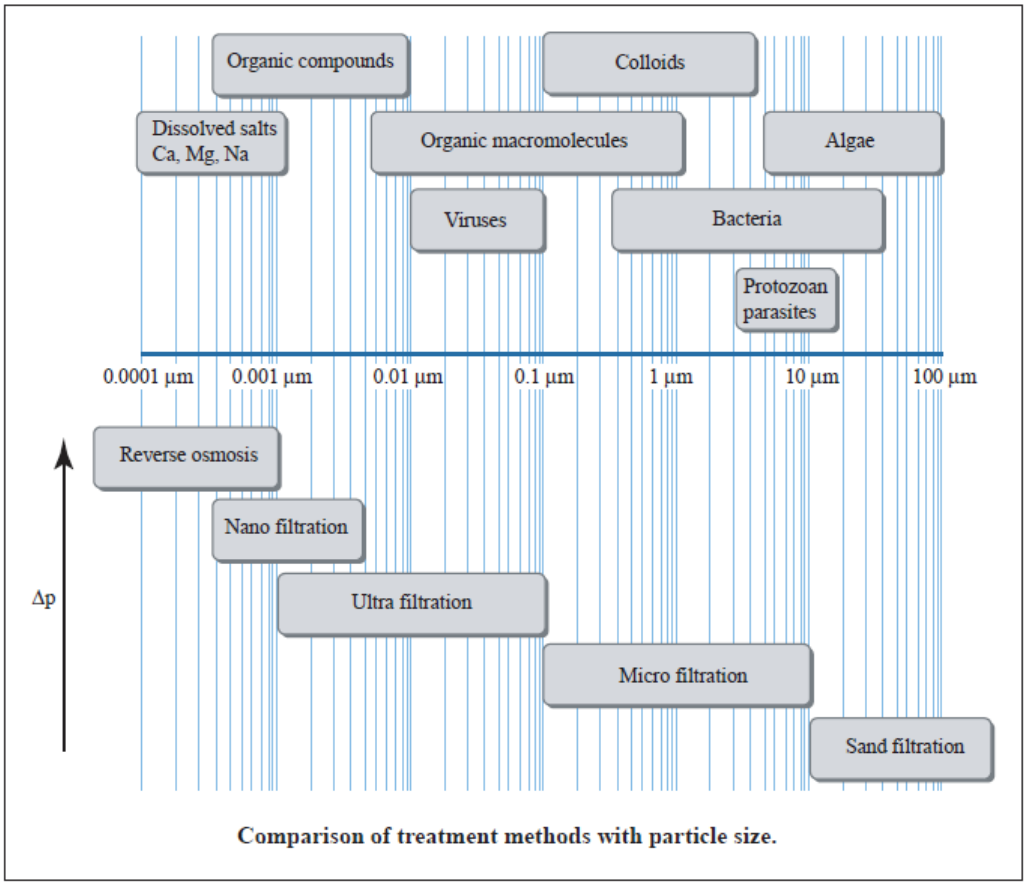

Figure 1.11: Size distribution of particles and corresponding modes of separation

These various methodologies may be further elucidated. Amongst filtration methods, microfiltration membranes consist of the large size pores (0.1-10µm) as compared to ultra-filtration membranes (1-100 nm) and nano-filtration (0.5-1 nm). The microfiltration process is used in initial pretreatment of RO feedwater. Ultrafiltration membranes are classified by the molecular weight cutoff and by nominal pore size. This type of membrane is commonly used in separation of macro-molecular solutes and of colloidal material from micro-molecular solutes and solvents. The applications of these membranes include concentration of proteins/enzymes for the pharmaceutical and biomedical industries, the food and dairy industries, the paper and pulp industries, etc [29]. Nanofiltration processes use membrane with a pore size ranging 0.5 to 1 nm. Nanofiltration is used to separate

relatively small organic compounds and high molecular weight ions from solvents. The application areas for nanofiltration cover purification of sugar from acids, salts from dyes, water treatment, sulphate separation, electroplating, etc. [30]. Purification of water base on size is shown in Figure 1.11

Reverse osmosis membranes can essentially separate all solutes species, both inorganic and organic, from the solution. The particle size range for separation is approximately 0.1 – 0.5 nm. Reverse osmosis finds it application in water purification such as desalination of brackish and seawater, wastewater treatment, and production of ultra-pure water for the semiconductor industry. Other application of reverse osmosis includes concentration of solutions for food products, pharmaceutical solutions, and chemical streams. [31]

Gas separation processes using gas permeation membranes (non-porous membranes) essentially depend on the differences in permeability and diffusivity of the gaseous components. Gas permeation membranes find their major applications in the chemical and petrochemical industries such as separation and recovery of hydrogen from refinery gas, purification of natural gas, separation of oxygen and nitrogen from air, dehydration of gases, methane recovery from biogas, etc [32]

A third type of membrane process that exhibits a solution-diffusion mechanism is pervaporation. This process is applied in separation of liquid-liquid azeotropes with relatively small difference in volatility. Applications that use this process include dehydration of ethanol, acetic acid, removal of ethanol for fermentation products, etc.

The electrodialysis process is used to transport salt ions from one solution to another through an electrodialysis ion-exchange membrane under the influence of an applied electric field. During this separation process, a charged molecule may selectively be exchanged for another charged molecule. The ion-exchange groups incorporated in the semi-permeable barrier material allow the passage of either positively or negatively charged ions while excluding the passage of ions of opposite charge. These semi-permeable barriers are commonly known as electrodialysis membranes. This process is performed in an electrodialysis cell. Electrodialysis cells are different from reverse-osmosis, distillation, and other membrane-based-process separations in that dissolved species are removed from the feed stream rather than the reverse. As the electrodialysis method removes the salt ions from the solution, electrodialysis offers the practical advantage of much higher feed recovery in many applications such as small-scale brackish water and seawater desalination, drinking water production,

waste water reuse, demineralization in boiler applications, glycol desalting and glycerin purification.[33][34].

Electro-deionization (EDI) is another process that uses membranes that separate species based on the charge that they possess. In EDI, an electrode is used to ionize water molecules and to separate dissolved ions (impurities) from water by means of a charge-selective membrane. EDI is a continuous and chemical-free process for removing ionized and ionizable species from the feedwater using DC power. It is typically used to polish reverse osmosis (RO) permeate (remove ions from solution to parts per billion purity) and to replace conventional mixed-bed ion exchangers, which eliminates the need to store and handle hazardous chemicals used for resin regeneration and associated waste neutralization requirements [35].

1.8 Reverse osmosis as the focus of this research

In this thesis work, the focus is on reverse osmosis systems. The word osmosis comes from the word endosmose (1830s) "inward passage of a fluid through a porous septum," from French endo- "inward" + Greek osmos "a thrusting, a pushing," or "to push, to thrust,". Osmosis is a natural phenomenon. It is the spontaneous flow of liquid from a dilute solution of to a more concentrated solution. For the case described in this thesis, the solvent is water and the solute is common salt. Figure 1.12 shows the effect of osmosis. The flow of solvent across the membrane raises the level of the solution in the funnel as shown in the figure. The hydrostatic pressure developed is called the Osmotic pressure. Works by Y. Luo [36] and Jamaluddin [37] show more detailed work on osmotic pressure calculations.

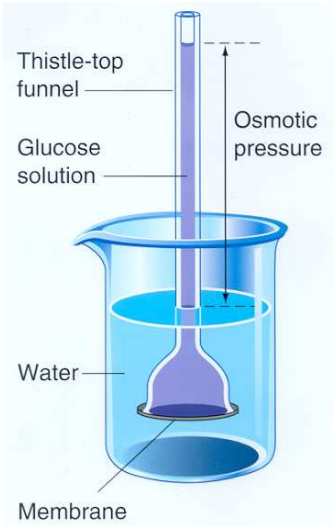

Figure 1.12: Description of osmosis in action

Reverse Osmosis is the process of separating water from a high-salt concentration solution by increasing the pressure on high-salt-concentration side over and above the osmotic pressure difference between the two sides to force water to flow into the dilute solution. It is reverse of the natural osmosis process, hence reverse osmosis.

Brackish water (1000-5000 ppmw salt) and seawater (32000-35000 ppmw salt) can be purified to produce pure water. In addition to desalination, reverse osmosis water processing techniques are used for rainwater pre-treatment. Rainwater collected from storm drains is purified by reverse osmosis and used for landscape irrigation and industrial cooling, as a solution to the problem of water shortages. In industry, reverse osmosis removes minerals from boiler water at power plants where the water is boiled and condensed repeatedly. It must be as pure as possible so that it does not leave deposits on the machinery (fouling) or cause corrosion. The deposits inside or outside the boiler tubes may result in under-performance of the boiler, bringing down its efficiency and resulting in poor steam production, hence poor power production at the turbine.

It is also used to clean effluent and brackish groundwater. The effluent in larger volumes (more than 500 cubic-meters per day) should be treated in an effluent treatment plant first, and then the clear effluent is subjected to a reverse osmosis system. The process of reverse osmosis can also be used for the production of deionized water. Because of its lower mineral content, RO water is often used in car washes during the final vehicle rinse to prevent water spotting on the vehicle. Reverse osmosis

water also enables the car wash operators to reduce the demands on the vehicle drying equipment, such as air blowers.

RO processes for water purification do not require thermal energy. Flow through RO systems can be regulated by a high-pressure pump. The recovery of purified water depends upon various factors including membrane sizes, membrane pore size, temperature, operating pressure, and membrane surface area.

In addition to water treatment, reverse osmosis is a more economical operation for concentrating food liquids (such as fruit juices) than are conventional heat-treatment processes. Research has been performed on using reverse osmosis to concentrate orange juice and tomato juice. Its advantages include a lower operating cost and the ability to avoid heat-treatment processes, thereby making it suitable for heat-sensitive substances like the protein and enzymes found in most food products.

Reverse osmosis is extensively used in the dairy industry for the production of whey protein powders and for the concentration of milk to reduce shipping costs. In whey applications, the whey (liquid remaining after cheese manufacture) is concentrated with RO from 6% total solids to 10–20% total solids before UF (Ultrafiltration) processing. The UF retentate can then be used to make various whey powders, including whey protein isolate used in bodybuilding formulations. Additionally, the UF permeate, which contains lactose, is concentrated by RO from 5% total solids to 18–22% total solids to reduce crystallization and drying costs of the lactose powder. Although use of the process was once avoided in the wine industry, it is now widely understood and used. An estimated 60 reverse osmosis machines were in use in Bordeaux, France in 2002. Known users include many of the elite class growths (Kramer) such as Château Léoville-Las Cases in Bordeaux. Many maple syrup producers have started using reverse osmosis to remove water from sap before being further boiled down to syrup. The use of reverse osmosis allows approximately 42-54% of the water to be removed from the sap, reducing energy consumption and exposure of the syrup to high temperatures. Microbial contamination and degradation of the membranes has to be monitored to ensure safe and hygienic process.

1.9 A brief overview of reverse osmosis water treatment facility

Figure 1.13 shows a schematic of a simple reverse osmosis facility [38] consisting of:

1. pre-treatment
2. reverse osmosis system
3. water preparation
4. reject water handling

The feedwater from the environment is treated for macroscopic impurities and chemical incompatibility in the pretreatment system. The pretreated feedwater is passed through the RO system to remove solutes. The purified RO water is further processed and prepared in water preparation module for storage, distribution, and use. The water rich with impurities is treated by reject water handling operation before disposing safely back to the environment. The following explains each module in detail.

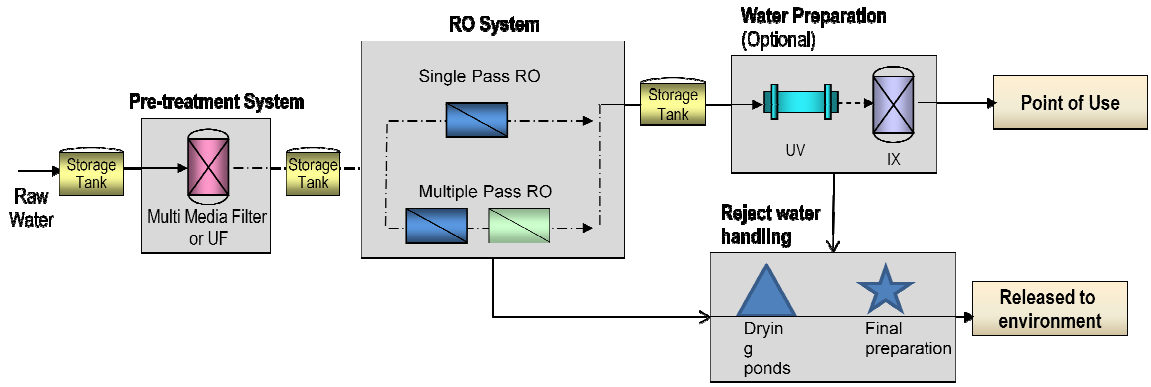

Figure 1.13: A schematic of a reverse osmosis facility

1. Pretreatment

Pretreatment of raw water is necessary to avoid fouling and clogging of membranes due to suspended solids and colloids. The more common foulants are silica, iron, calcium carbonate, calcium sulphate, strontium sulphate, barium sulphate, and heavy metals. It is also important to recognize the presence of dissolved gasses such as oxygen, carbon dioxide, hydrogen sulphide, etc., and other volatile inorganic compounds. The membrane performance is also sensitive to many

reductive and oxidative reactants in water. These compounds react with the membrane, alter its chemistry, and thereby reduce its performance over time. Membranes are sensitive to the raw water composition and are affected by the variations in the composition and contaminants over time. Therefore, the raw water quality and the pretreatment process are to be monitored regularly, frequently, and carefully [39].

One of the means to characterize water quality is to measure its turbidity. Turbidity is a measure of cloudiness in water. The more turbid the water, the murkier it is. Turbidity can be caused by soil erosion, waste discharge, urban runoff, bottom feeders like carp that stir up sediments, household pets playing in the water, and algal growth. High water turbidity correlates to high fouling capability. Standard turbidity measurements are inadequate to detect the fouling potential of water. Water potential for fouling is characterized by the *Silt Density Index (SDI)*. This index measures the rate at which a 0.45-micrometer filter is plugged when subjected to a constant water pressure of 206.8 kPa (30 psi) (Pohland 1981). Typically, spiral wound reverse osmosis systems will need an SDI less than 5, and hollow fiber reverse osmosis systems will need an SDI less than three [40] . In these kinds of systems, deep well waters (with a typical SDI of three) could be used directly from the source. If fed from surface waters (with a typical SDI greater than six), the water will need to be pretreated before use. Seawater desalination plants utilizing reverse osmosis systems also need very efficient filtering due to the typically high but variable SDI of seawater.

The maximum allowable temperature range for optimum membrane performance is 45°C for most operations. The water must be cooled, especially in hot regions, to operable temperatures before processing. The pH value of water should be between 4 and 11. Any higher pH or any lower pH cause the water to degenerate the membrane. Most RO operations are more efficient at high pH. Hence, to improve efficiency and to increase the salt rejection, sodium hydroxide (caustic soda) and zinc phosphate are added to water to increase and adjust the pH to approximately eight. Some membranes are sensitive to oxidizing agents like chlorine; therefore, chlorine has to be removed from water before application in a RO process.

In many pretreatment plants, water is chemically treated to remove biological materials. Biological materials may provide necessary conditions for microbial growth in a RO membrane. Water is chlorinated to kill many biological foulants and subsequently the water is de-chlorinated for RO use. Chlorine is an oxidizing agent and chlorine can react with the RO Membrane and deteriorate its

performance. The chlorination-de-chlorination operation requires a large facility and thus increases the complexity of the RO operation.

Other pre-treatment operation is softening of feedwater by addition of sulfuric acid and sodium hexametaphosphate to convert enough of the bi-carbonates to carbonate ions and carbonic acid thereby preventing the scaling of the membrane. Hydrogen sulphide and carbon di-oxide gases are removed from the product by degasification and aeration.

Another prominent pretreatment operation is to remove suspended impurities. Suspended impurities accumulate over time in the RO system, clog the water passages, foul, and reduce the efficiency of the system. Sedimentation tanks, pressure filters, and micro filters are used to remove suspended impurities. Use of ultra-filtration (UF) techniques in water pretreatment is gaining popularity because they have a very small geographical footprint. UF is capable of removing suspended, biological, and large macromolecules and colloids from water. The disadvantage of UF is that the filters need to be cleaned, maintained, and replaced periodically. With improving UF technology, and with the increase in the cost of land, and other resources presently used for water-pretreatment, Ultra-filtration is becoming a staple part of RO water pretreatment to remove suspended solids that can clog the RO system. The pretreatment operation is necessary to ensure safe, reliable, and long operation life of RO systems.

2. Reverse Osmosis system

Reverse osmosis accounts for 95-99% of water purification. The RO process has relatively lower energy requirements since the separation is entirely in the liquid phase. Removal of solutes from water depends on the quality of the raw-water, the pretreatment technique, and membrane quality. Marginally pretreated water causes the RO to have a deteriorating performance over time, and periodic cleaning is necessary. Frequent cleaning interrupts water production and hence increases the cost of the product water.

Higher solute concentrations in water require higher operating pressures for water separation. This means higher energy requirements, which leads to higher operating cost. For seawater, the applied pressure usually varies between 700 to 1000 psi, whereas for brackish water, it is generally between 100 to 300 psi. At the end of the process, the reject or the concentrate water (that contains the rejected solute) leaves the RO pressure vessel at 30 to 60 psi less than the operating pressure. Pressure recovery devices installed in the system help to repossess the energy contained in reject

stream [41]. The RO system consists of a high-pressure pump, RO units (elements), pressure recovery devices, and water handlers. The RO system will be described in detail in later sections.

3. Water Preparation

Water preparation is the process where the RO product water is processed for its appropriate applications. It involves all the water treatment processes that take place downstream of the reverse osmosis plant system. Water preparation is also known as post treatment. Post-treatment processes often include disinfection using suitable biocides, pH adjustment, and possibly the addition of suitable corrosion inhibitors.

For example, drinking water has to be replenished with necessary minerals for human consumption. Drinking water is also aerated to replenish necessary oxygen. Domestic water is chlorinated to sterilize the water from the source to the point of use. In that regard, 0.3 mg/L of sodium hypochlorite is added to the product water to guarantee the preservation of the obtained quality until the point of use. Ion exchange, electrodionization, and many other methods are also used in water polishing. Water, after preparation and processing is transported and stored until the time of use.

4. Reject water handling

The rejected water contains a high concentration of solute and it should be disposed off safely and without major impact to the environment. Greater product recovery produces reject with higher concentration. If the RO operation were to run at 50% recovery, the reject water would be approximately twice as salt concentrated as that of feedwater. The concentration of the salt in the rejected water is a function of the percentage of feedwater recovered and the percentage of solute rejected by the RO process. This salt concentration in the rejected water is characterized by

$$M = \frac{1-rec(SP)}{1-rec} \quad \textbf{(1.2)}$$

where M is the concentration multiplication factor or concentration factor. This factor is multiplied by the concentration of salt in the feedwater to calculate the concentration of the rejected water.

Recovery rec is represented in fraction. Recovery is the volume fraction of the feedwater that is recovered as product water. Recovery is also known as *conversion*.

Salt passage SP is the fraction of salt in the feedwater that is passed on to the product water.

If the concentration of solute in the rejected water is very low, then the rejected water may be discharged to sanitary sewers since the contribution of salinity from the reject to the sewer would be negligible [42]. For very-large-recovery RO operations, the reject water can be discharged into the sea. For inland cities short of fresh water supply, the quality of brine discharged may be much larger because the desalted water may be the only source of water supply. In that case, evaporation ponds may be used for brine disposal. The water evaporated from the pond can be condensed to achieve 100% recovery. The solute left behind in solid form will be treated as solid waste and can be handled accordingly.

1.10 A detailed overview of reverse osmosis systems

Figure 1.14 shows a detailed schematic of a reverse osmosis system. A Reverse osmosis system consists of

1. Reverse osmosis module
2. High pressure pumps and recirculation pumps
3. Pressure exchange system for energy recovery
4. Feedwater lines
5. Product water lines
6. Concentrate lines

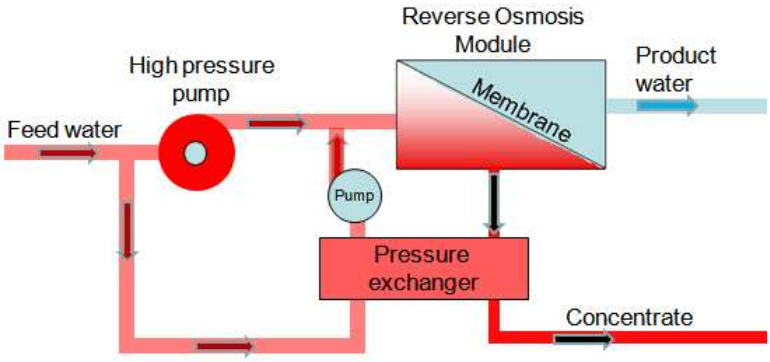

Figure 1.14: Schematic of a reverse osmosis system

Feedwater that enters the RO system as shown in Figure 1.14 is pumped to RO operating pressure. A high-pressure pump and/or a pressure exchanger (a pressure recovering device) is used to pump the feedwater into the operating pressures. This high-pressure water is pumped through the RO module to produce the pure product water and the reject water concentrated with solute. In case of large RO plants, the energy stored in the reject water is recovered. The following sections give a detailed explanation of each component.

1. Reverse osmosis module

Study of the *Reverse osmosis module* is the key focus of this research. In the reverse osmosis module, the feedwater is separated to two streams- a) product water (permeate) containing very low concentration of solute and b) concentrate containing very high solute concentration. A detailed description and explanation of the reverse osmosis module is conveyed in section described later in the report.

2. High pressure pump

The *high-pressure pump* raises the pressure of available water high enough to enable reverse osmosis to occur. For example, seawater has an osmotic pressure of around 400 psi or 28 bar. Therefore, to enable reverse osmosis to occur the high-pressure pump raises the pressure of the feedwater to over 400 psi. In most seawater RO plants, the feedwater pressure is raised to about 800 psi to enable high volume transformation. In case of brackish water, the RO operating pressure is anywhere between 100 and 400psi. Recirculation pumps (shown as pump in Figure 1.14) are used, where economics allow, to aid the high-pressure pump.

3. Pressure exchanger

The *pressure exchanger* or pressure recovery device recovers exergy (exergy is available energy) from the concentrate stream. The concentrate stream is wastewater and it is usually discarded. In RO, the concentrate stream exits the RO system at the RO operating pressure. In most RO systems, this pressurized flowing water is used to turn turbines. The work from the turbine is used either to generate electricity or to pressurize the feedwater. The use of high-pressure concentrate to pressurize the feedwater reduces the power requirement for the high-pressure pump to run the RO system. As energy to power the pumps is one of the significant costs of running a RO plant, pressure exchangers help to improve the efficiency of the RO water treatment plant.

4. Feedwater

The *feedwater* refers to the water entering the reverse osmosis system. This water is generally the product of the water pretreatment process. The feedwater containing dissolved impurities (like salt, organic, and small biological substances).

5. Product water (Permeate)

The *product water* is the useful product of the reverse osmosis system. The solute and impurities in the feedwater is removed to create the product water. The product water is sent to water preparation unit for further processing.

6. Concentrate

The *concentrate* is the waste byproduct of the reverse osmosis system. When pure permeate is recovered from the feed stream, the remaining portion of the feed stream becomes concentrated with impurities (solute) and is known as the concentrate. The concentrate is rejected and sent to reject-water handling unit for safe disposal.

1.11 Brief description of the Reverse Osmosis Module

The RO system is made up of one or several RO pressure vessels as shown in Figure 1.15. When the feedwater is passed through one vessel after the other, each vessel is considered as a stage. The product from these stages can be further processed to create double pass filtration. Figure 1.15 shows examples of single-stage and triple-stage filtration, double-pass filtration and double-pass filtration with three stages in each pass.

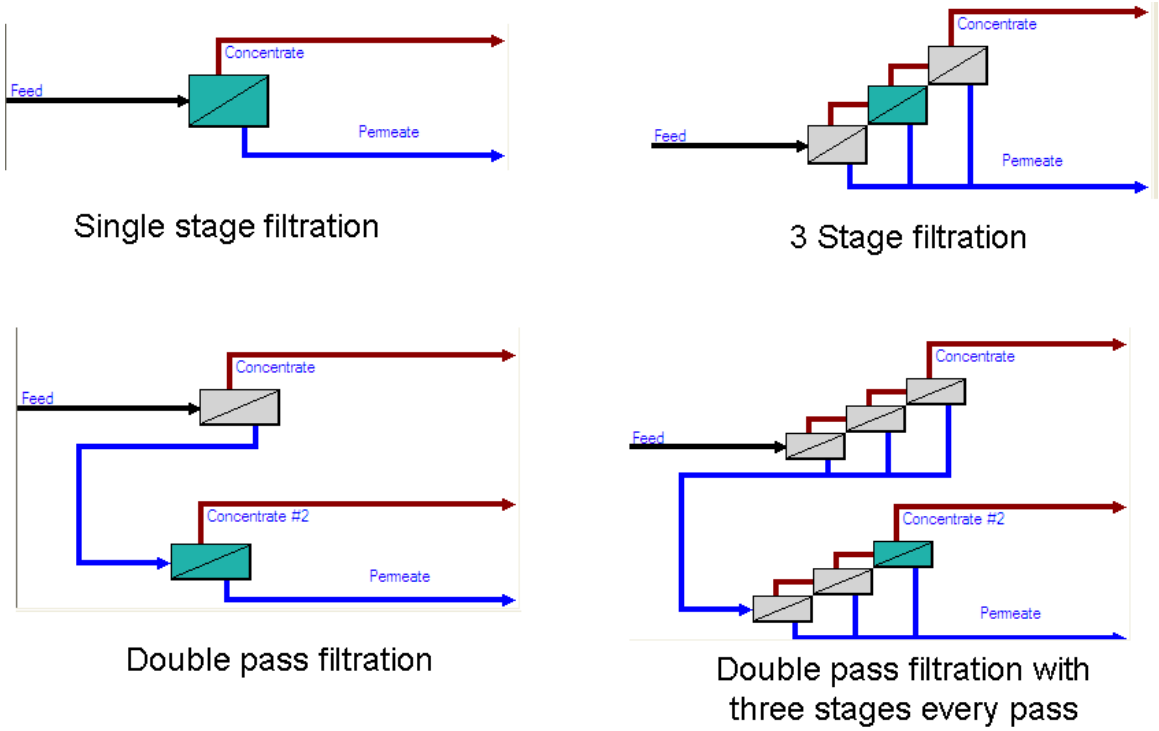

Figure 1.15: Various arrangements of RO pressure vessels in a RO module

In Figure 1.15, every represents a RO pressure vessel.

In large RO plants, many hundreds of modules are arranged to operate parallel to one another. Modules that are arranged parallel to one another are called trains. A very large-scale RO plant consists of hundreds of RO trains Figure 1.16 (courtesy Veolia advertisement) shows an example of a large-scale reverse osmosis system with hundreds of RO trains.

Figure 1.16: RO modules with many pressure vessels

1.12 Description of a reverse osmosis pressure vessel

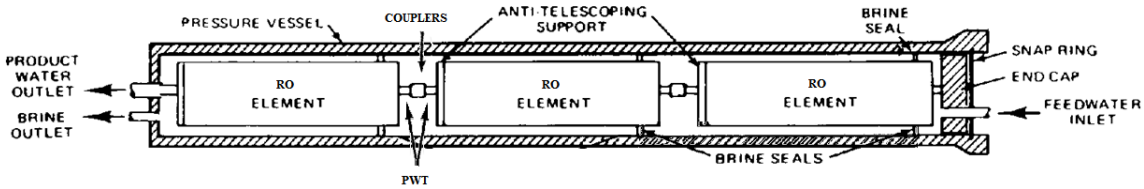

Figure 1.17: cross-section of a pressure vessel with three membrane elements

A common pressure vessel as shown in Figure 1.17 [43] is made up of a fiberglass shell. For dairy and food applications, the pressure vessel is made from stainless steel. The pressure vessel contains many spiral wound reverse osmosis elements (RO elements), up to eight in some applications. For illustrative purposes, a pressure vessel with three elements is shown in Figure 1.17

The spiral wound elements come in many standard lengths up to 40 inches (1 meter) and the diameters of the elements generally vary from 2.5 inches to up to 16 inches. A very common size for an element used in industrial water purification is eight inches (20 cm) in diameter and 40 inches (1 meter) in length. When many elements are placed in a pressure vessel, male o-ring connectors (couplers) connect the product water tube (PWT) in each element to the product tube of the next element. This inter-connection allows all permeate to exit the pressure vessel in either direction (Figure 1.17 shows permeate collected only on the left side). Typically, one end of the product tube is capped and the other is open to allow product water to exit in one direction. The couplers have o-

rings to prevent high-pressure feedwater from passing into the product tube. The water from the product water tubes is collected through the product water outlet as shown in Figure 1.17.

As seen in the figure, each element has a brine seal located on the outside of the anti-telescoping cap. It is critical that this brine seal is always placed on the feedwater inlet side of the element. This seal prevents the feedwater from going around the element rather than through it. A set of specific-purpose adaptors are used on either end of the array of elements with one end that has a modification that enables the elements to be inserted into or removed out of the pressure vessel. This end has the snap ring and the end cap as noted in the figure. The other end has the provision to collect the permeate water (product water) from the pressure vessel. Both these adaptors have provisions to let high-pressure feedwater in and let high-pressure concentrate water out of the pressure vessel. These adaptors also enable sealing on both sides of the pressure vessel to maintain high pressure.

Chapter 2 : REVERSE OSMOSIS OVERVIEW

2.1 Introduction

In this chapter, The RO element is systematically broken down to its constituent components. A detailed analysis of the calculation method currently used in the RO industry to simulate an RO element is presented. Later, inconsistencies of the method currently used are elaborated. Finally, the focus of this research dissertation is stated.

2.2 Detailed description of a reverse osmosis element

The separation of feedwater into pure water (product water or permeate) and reject (concentrate) occurs in the RO element. The RO element consists of a semi permeable membrane that allows the passage of pure water but prevents the passage of dissolved matter and ions. Extraction of pure water from feedwater increases the concentration of dissolved matter in the residual feedwater. This residual feedwater is variously designated as reject, reject water, or concentrate. The most common form of RO element is a spiral wound RO element. Figure 2.1 shows the construction of such an element.

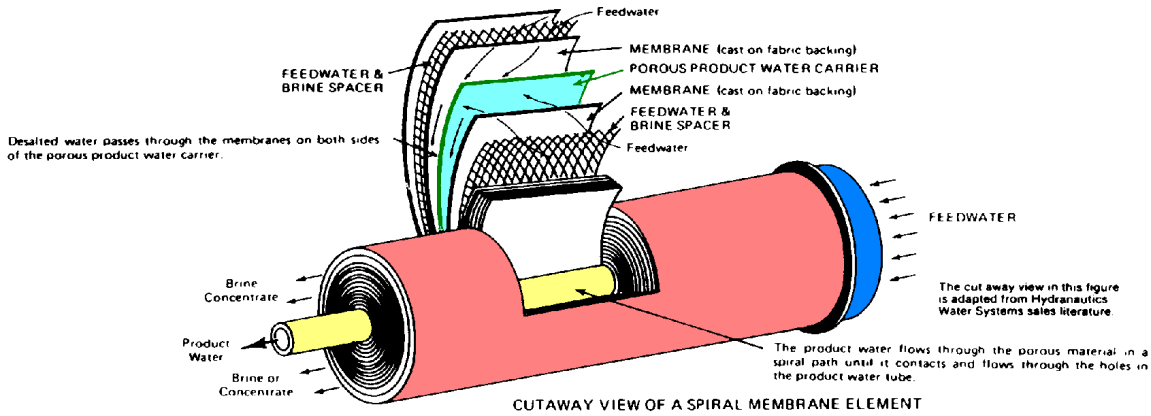

Figure 2.1: Cutaway view of a spiral RO element

The semi-permeable flat sheet membrane is the most important functional part of the element. Flat sheet reverse osmosis membranes are made from automated casting equipment. Most RO membranes are made from polyester (polyethylene terephthalate PET) fabric web, coated with a micro-porous polysulfone (PS) support layer. The web and the PS layer provide additional support to the top 0.1-0.2 micron-thick polyamide semi-permeable membrane functional layer. The top polyamide barrier functional layer performs the actual separation to purify the water. The functional layer consists of proprietary polymeric material [44]. This functional semi-permeable membrane is formed on the polysulfone support base by interfacial polymerization of monomers containing amines and carboxylic acids-chloride functional groups. This layer helps to reject salt yet enable water to flow through the membrane. This three-layer composite makes a durable flat sheet RO membrane that is installed in each spiral wound element. Figure 2.2 shows a cut cross section of a reverse osmosis membrane.

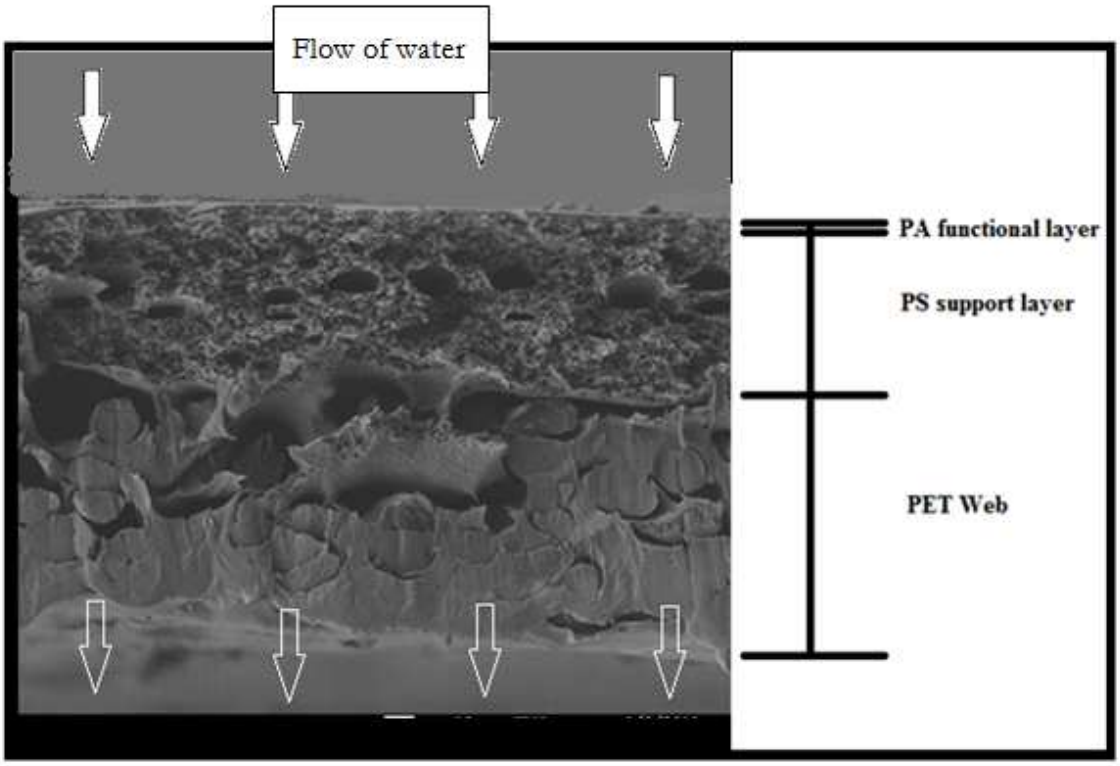

Figure 2.2: Cross section of a reverse osmosis membrane

Each membrane flat sheet is then combined with a feed channel spacer. The membrane is folded and the feed channel spacer is inserted into each fold as shown in Figure 2.3.

Figure 2.3: Inserting a spacer in a membrane

The feed spacers are made of netting materials. They provide space between the membrane sheets for uniform flow to occur. The spacers also promote mixing in the flow. The mixing helps to reduce the concentration polarization build up over the membrane layer when product water is separated from the feedwater. Concentration polarization is a result of concentration gradient is created by molecules that cannot pass through the membrane. Figure 2.4 shows a diagram of the flow of feedwater over the membrane surface and the feed spacer. The combination of the membrane and the feed spacer is called a leaf.

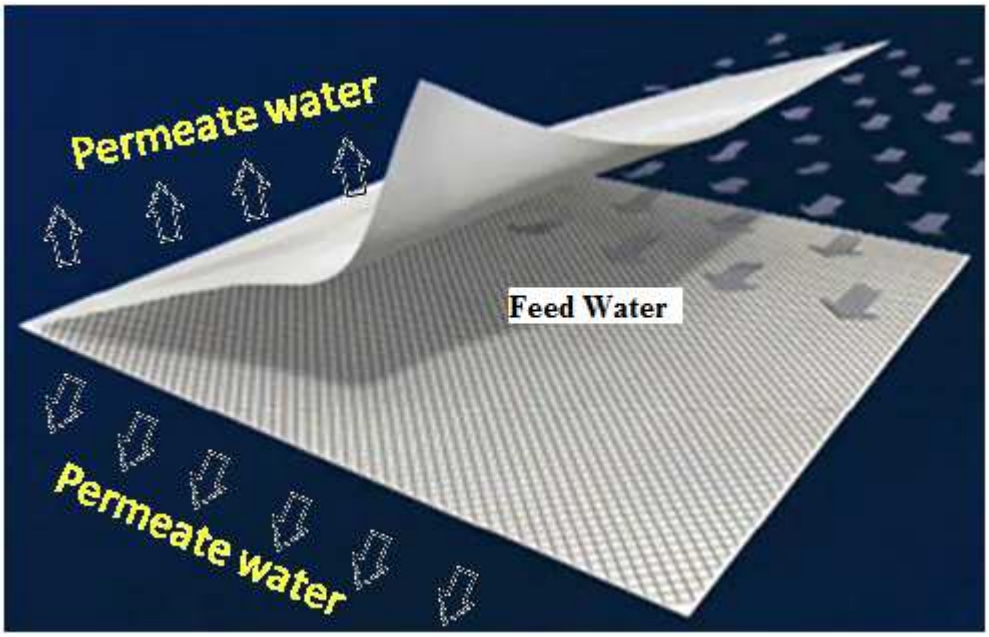

Figure 2.4: Schematic of the direction of the feedwater over the Membrane and feed spacer

An element is made up of leaves. Some small, purpose-specific elements carry a single leaf, but most large commercial reverse osmosis elements carry more than one leaf. Water flows through the feed

spacer, permeates across the membrane, and exits through the other side of the membrane as shown in Figure 2.4.

The permeate water created in the membrane is collected in the permeate spacer. A permeate spacer is a sheet of tricot fabric inserted between leaves on the backside of the membrane to promote the collection and transportation of permeate water to the product water tube. The permeate spacer, also known as tricot, should be able to withstand the high differential pressures of RO operation without collapsing. The surface of the permeate spacer must be smooth to prevent intrusion of the membrane into the permeate spacer. The tricot is connected to the product water tube. The product water tube has holes that enable the permeate water to enter it from the permeate spacer.

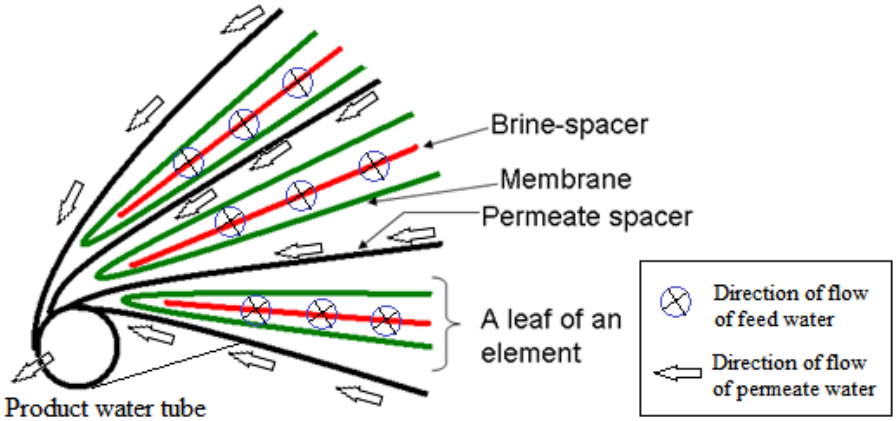

Figure 2.5: The construction of leaves that forma an element

Figure 2.5 shows the arrangement of leaves, permeate spacer, and product water tube (PWT) in an element. It also shows the direction of flow of the feed and the permeate water.

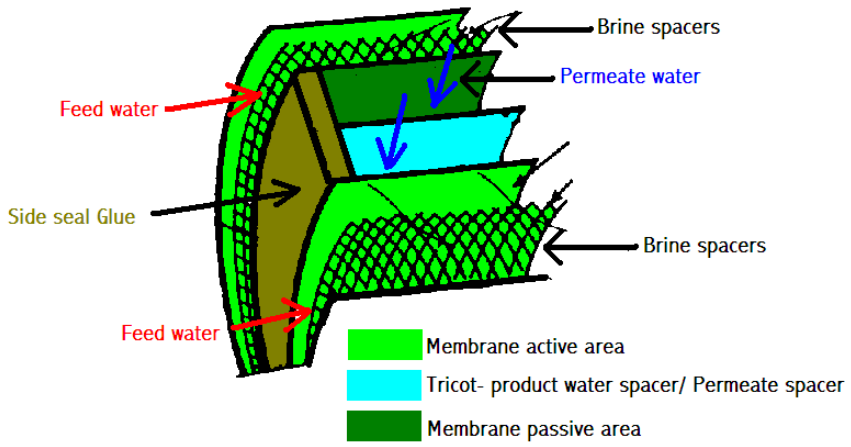

Figure 2.6: Cutaway section of a leaf in SPRO

The leaves are glued along each of the three exposed sides. This prevents the advective flow of feedwater from the feed channel (brine spacer) directly into the permeate channel. Figure 2.6 shows the location of the glue and the method by which the glue prevents the feedwater from mixing with the product water.

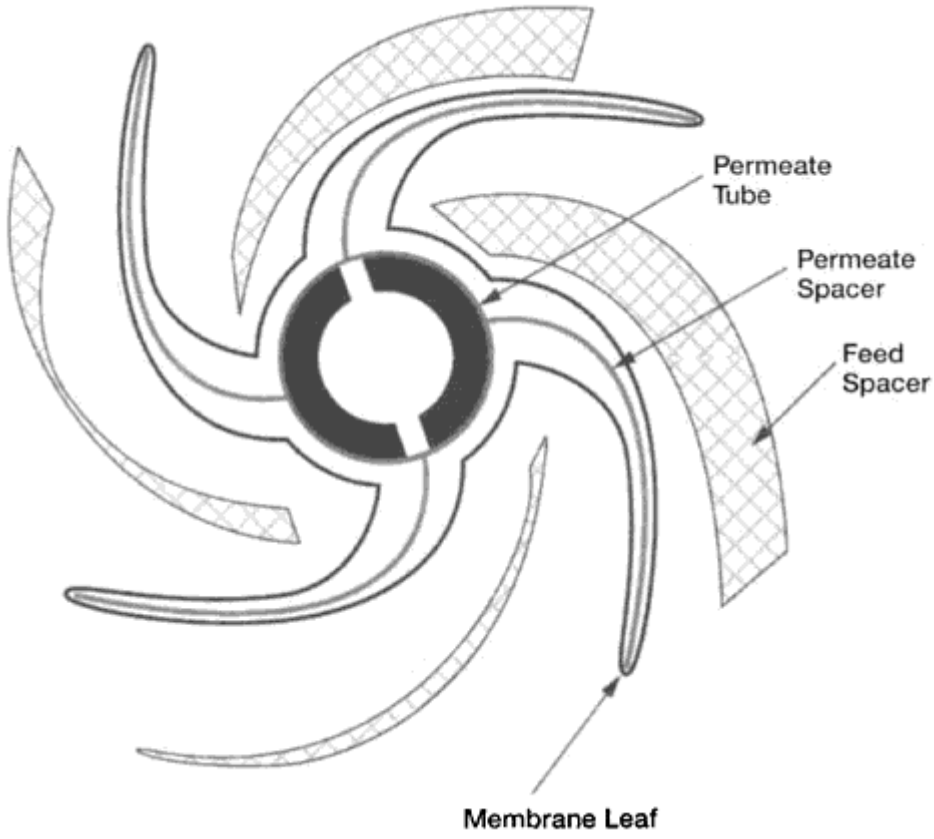

Figure 2.7: Spiral wound RO element showing leaves before winding

The array of leaves and the permeate spacers are then rolled around the core product water tube to make the spiral wound element. Figure 2.7 [45] shows the arrangement of the leaves and the permeate spacer. Anti-telescoping devices are installed on the ends of the spiral wound element to prevent the spiral from telescoping during high volumetric flowrate of the feedwater. With the back of the membrane completely sealed on the edges of the permeate spacer by the side seal glue, the feedwater is forced to enter through the feed channel spacer. The feedwater flows over the polyamide functional layer of the membrane. Clean water or permeate passes through the membrane surface into the permeate channel. This flow is driven by the reverse osmosis operating pressure. The permeate water flows in a spiral direction to the center of the element and is collected in the core tube (product water tube/permeate tube).

2.3 Description of flow in spiral wound reverse osmosis element

To reiterate, the objective of this doctoral work is to understand the fluid-flow processes in a reverse osmosis pressure vessel in order to achieve improved water management. This section introduces the various phenomena that take place in a reverse osmosis element when the water is processed.

Figure 2.8 shows the water flow pattern in a SPRO (Spiral wound reverse osmosis) element. Feedwater flows through the feed spacer and across/past the membrane. The pressure difference between the feed side and the permeate side drives a small fraction of the flow through the membrane. The permeate trickles through the permeate spacer (tricot) en route to the product water tube, from where it exits the element.

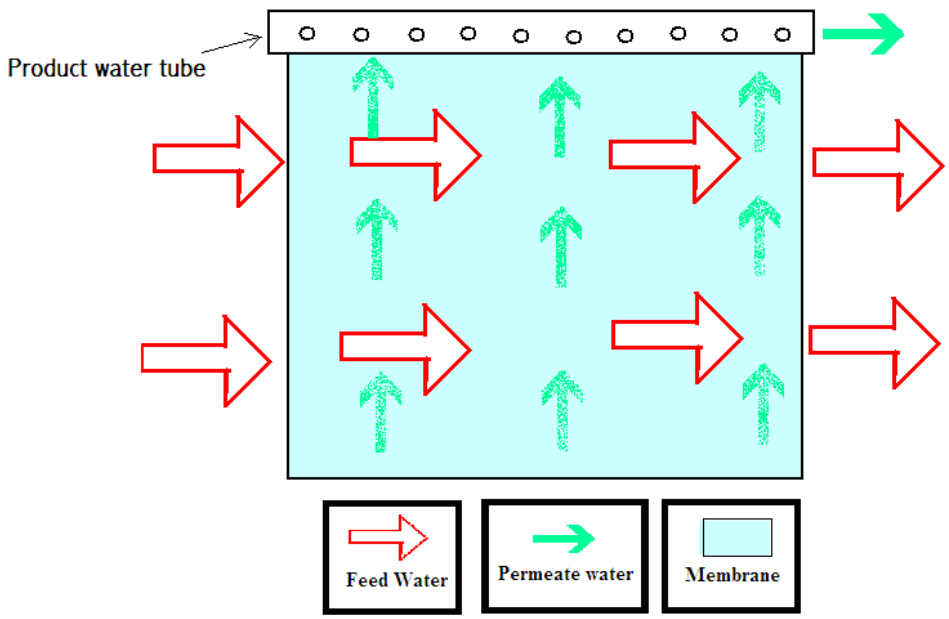

Figure 2.8: Flow of feedwater and permeate inside an element

2.4 Description of processes in a spiral wound element

A block diagram displaying the flow path of the feedwater through the various processing sites that lead to the production of the product water is presented in Figure 2.9.

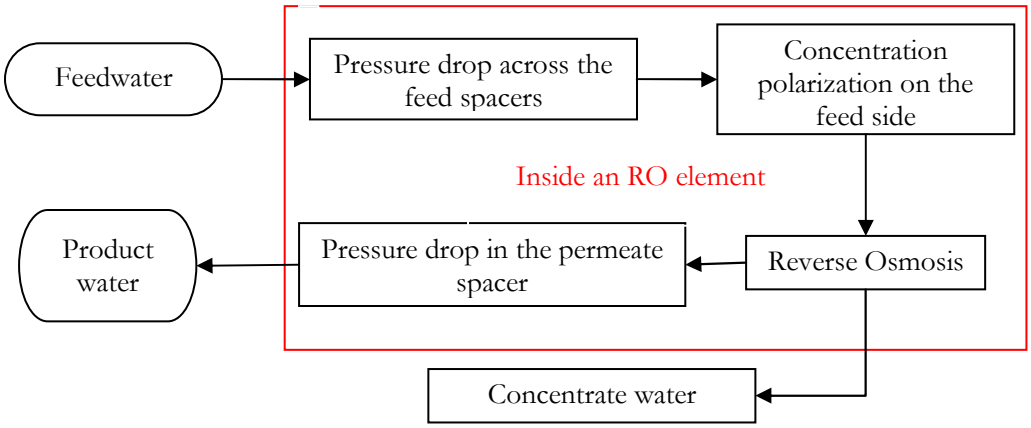

Figure 2.9: Process flowchart of product water

The successive events that occur along the path of feedwater flow are:

1. Entry of feedwater into an element
2. Pressure drop of the feedwater as it flows end-to-end along the element
3. Concentration polarization near the membrane as the permeate is extracted from the feedwater
4. Reverse osmosis
5. Exit of concentrate water with increased salt concentration from the element
6. Drop in pressure of the permeate water as it trickles along the permeate spacer

2.4.1 Entry pressure drop in an element

When the feedwater enters the element from the RO pressure vessel, significant pressure drop occurs because the flow cross section is markedly diminished from that of the plenum to that of the spaces provided by the feed-spacers. These spaces can be seen in Figure 2.10, which is a photograph of the scroll-like geometry of an element. The feedwater from the plenum enters the annular spaces delineated by the feed spacer. It appears that this significant pressure drop has not been identified in the published literature. The determination of the magnitude of this pressure drop is one of the goals of the proposed research.

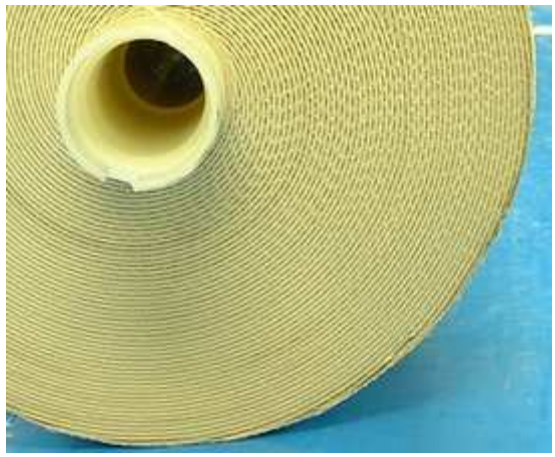

Figure 2.10: Picture of a scroll of an element

2.4.2 Pressure drop in the feed spacer

A feed spacer is a net/mesh that creates open space to allow feed/reject water to pass over the membrane. The feed spacer also helps to mix the feedwater and thereby reduces the concentration polarization in the feed channel. An ideal spacer would increase mixing and yet keep the pressure drop low along the membrane [46][47][48].

A net type spacer as shown in Figure 3.1 has been found to be most effective in this regard [49]. Several research works have been performed in the search for the ideal net geometry [50][51][52][53]. As the feedwater flows along the feed spacer, it experiences a pressure drop due to both inertial and frictional losses. This trend is opposed by the pressure rise associated with the deceleration of the flow caused by defection of part of the feed, which passes through the membrane and becomes the permeate. The net of these opposing tendencies is a pressure drop.

The pressure drop per unit length P_{drop} of the feed spacer can be written as

$$P_{drop} = \frac{\delta P}{\delta L} \tag{2.1}$$

where δP is the pressure drop across the length δL , and L is the length of the element along the axis (length traveled by the feed flow across the element).

The non-dimensional form of velocity represented by the Reynolds number is defined as

$$\mathrm{Re} = \frac{\rho . v_{feed} . d_h}{\mu} \tag{2.2}$$

where v_{feed} is the bulk feed velocity of the flow through the feed spacer, and d_h is the hydraulic diameter of the flow through the feed spacer (twice the thickness of the feed spacer). The bulk velocity varies along the length of the element.

It is well established that the pressure drop is a function of Reynolds number. For values of this Reynolds numbers greater than 1, a suitable representation is

$$P_{drop} = a_1 V + b_1 V^2 \tag{2.3}$$

where a_1 is the Darcy factor and b_1 is the Forchheimer factor. If the permeability-based Reynolds number is less than one, the quadratic term is absent.

The equation used in the industry to model the pressure drop across the feed spacer is

$$P_{drop} = f . \left(\frac{1}{2} \rho v_{feed}{}^2 \right) . \frac{1}{d_h} \tag{2.4}$$

where the *pressure drop factor* f is given by

$$f = a.\mathrm{Re}^{b} \tag{2.5}$$

It will be demonstrated here that the pressure drop depends on

1. the velocity of the flow through the feed spacer
2. the geometry of the feed spacer

As permeate is continuously recovered from the element, the velocity of the flow though the feed spacer decreases, as does the momentum. This reduction in momentum contributes to an increase in pressure. The pressure drop across the element due to dissipative losses in the feed spacer is in the order of few pounds per square inch. For a change in momentum to cause a significant raise in pressure, the change in feedwater flow velocities should be in the order for few meters per second. The maximum flow of feedwater permissible for safe operation in an RO element is 50 cm/sec. Therefore, the rise in pressure is insignificant compared to the pressure drop due to flow through the feed spacer.

2.4.3 Concentration polarization on the feed side

The extraction of pure water across the membrane creates a mass transfer boundary layer. The mass transfer boundary layer refers to a layer in the immediate neighborhood of the feed side of the membrane, where there is high salt concentration gradient [54]. A conceptual diagram of the mass transfer boundary layer is displayed in Figure 2.11 as a red zone about the membrane. The accumulation of high concentrated feedwater near the membrane is known as *concentration polarization*.

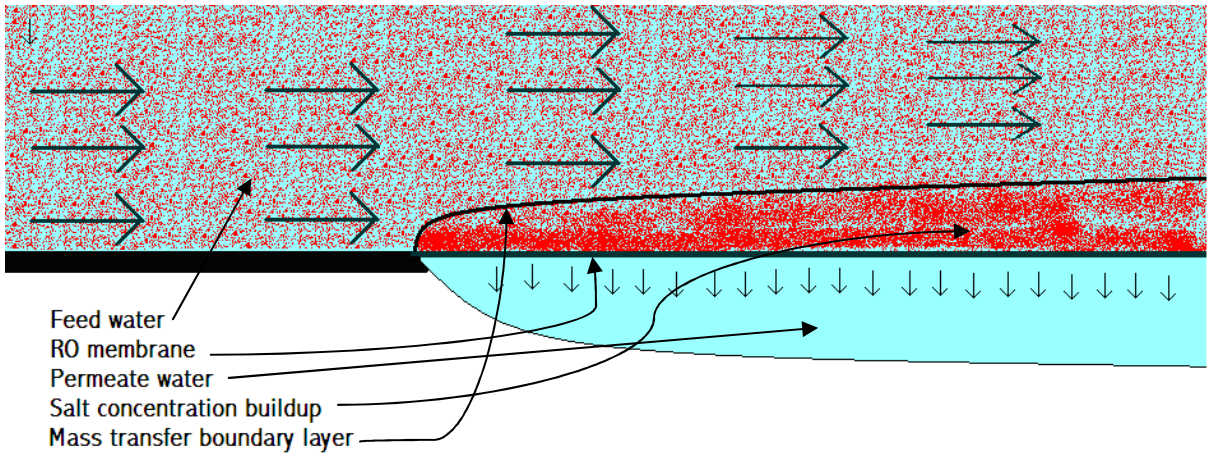

Figure 2.11: Mass transfer boundary layer

In reverse osmosis membranes, as pure water is extracted from the system, salt is left behind on the feed side of the membrane. This leads to salt accumulations or concentration polarization characterized by higher values of salt concentration near the membrane surface compared to that in the bulk of the feed solution. This difference in concentration drives diffusive mass transfer of salt from a higher concentration to a lower concentration. Figure 2.11 illustrates the reason for concentration polarization and the mass transfer boundary layer.

Concentration polarization *CP* is defined as

$$CP = \frac{C_{wall}}{C_{bulk}} \tag{2.6}$$

where C_{wall} is the wall-adjacent concentration, and C_{bulk} is the bulk concentration of the salt in the feed stream. The salt concentration of the feedwater near the membrane surface is very important since reverse osmosis occurs across the membrane. Figure 2.12 shows pictorially the difference between the bulk concentration and the feed concentration.

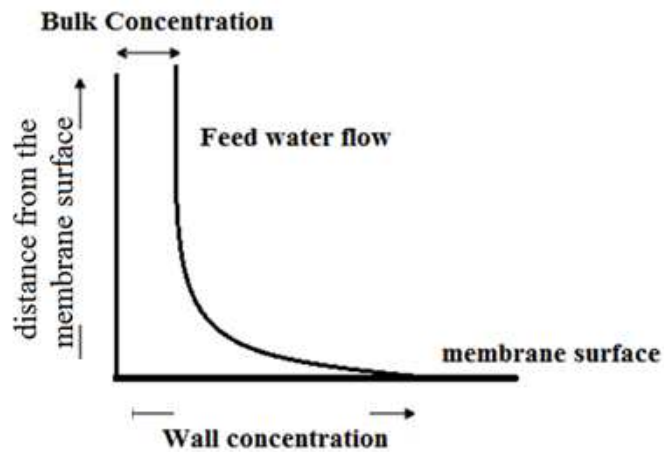

Figure 2.12: Salt concentration profile

The continuous flow of permeate through the membrane increases the concentration polarization. This process is termed advection. Mass transfer of salt from the membrane surface to the bulk is driven by a concentration gradient (molecular diffusion). Considerable research has been performed to improve the understanding of the concentration boundary layer and the concentration polarization in a reverse osmosis element [54][55][56][57]. The two processes noted in the foregoing tend to balance the buildup of salt at the surface of the membrane and gives rise to a steady-state concentration polarization on the membrane surface.

The transport of salt on the feedwater side of the membrane can be represented by the mass transfer coefficient K. The mass transfer coefficient is analogous to the heat transfer coefficient, although it has different units. The mass transfer coefficient K is defined as

$$K = \frac{\sigma}{(C_{wall} - C_{bulk})} \tag{2.7}$$

where σ is the mass of salt transported per unit area (mass flux) from the membrane surface to the bulk feed flow.

A dimensionless form of the mass transfer coefficient is the Sherwood number Sh, which is analogous to the Nusselt number Nu for heat transfer. It represents the ratio of advective to diffusive mass transport.

$$Sh = \frac{K.d_h}{D} \tag{2.8}$$

where D is the binary molecular diffusion coefficient of salt (NaCl) in water.

Much effort has been expended in the past to estimate concentration polarization in the feed spacers. Work by K.K. Lau et al. [59] has dealt with the effect of spacing between the strands that constitute the spacer in reducing the concentration polarization by advective mixing. The same group has also worked on experimental and numerical modeling of spacers with different strand geometries [60]. L. Song [61] and V. Geraldes [62] discuss the effect of various feed spacer geometric properties on mixing and pressure drop estimation.

The well-established analogy between heat and mass transfer enables the transformation of the correlation between the Nusselt, Reynolds, and Prandtl numbers to be used to represent mass transfer.

That representation is

$$Sh = c\,\mathrm{Re}^{d}\, Sc^{\frac{1}{3}} \tag{2.9}$$

The quantity Sc is the Schmidt number that is directly analogous to the Prandtl number. The Schmidt number is defined as

$$Sc = \frac{\mu}{\rho D} \tag{2.10}$$

It is the ratio of the kinematic viscosity of the fluid to the mass diffusion coefficient. The constants c and d in Equation (2.9) are determined by the geometry of the feed spacer. One of the aims of this work is to determine the c and d values by means of numerical simulation as a function of the feed spacer geometry.

For a flow between two parallel plates (in the absence of a feed spacer), the concentration polarization is given by the works of T.K. Sherwood [58]. Sherwood uses the concentration factor Γ to calculate wall concentration. The concentration factor is defined as

$$\Gamma = \frac{C_{wall} - C_{permeate}}{C_{bulk} - C_{permeate}} \tag{2.11}$$

where C_{wall} is the wall-adjacent salt concentration, C_{bulk} is the feed bulk and $C_{permeate}$ is the concentration of salt in the permeate water.

The concentration factor is evaluated as

$$\Gamma = e^{\frac{J}{K}} \tag{2.12}$$

where the quantity J is the permeate flux, also known as the velocity of the permeate flow passing through the membrane (normal to the membrane surface). It may also be regarded as the volumetric flow per unit area (flux). The ratio of J to the mass transfer coefficient K is dimensionless.

2.4.4 Reverse Osmosis

Osmosis is the spontaneous flow of water from a dilute solution of salt in water to a more concentrated solution of salt in water. Reverse osmosis is the process of extraction of pure water from the feed solution by increasing the pressure on the side of high salt concentration. The net driving pressure (NDP) drives the flow through the membrane. The net driving pressure refers to the difference between the feed pressure and the osmotic pressure. The net driving pressure is the measure of the actual driving pressure available to force the water through the membrane. Equation (2.13) gives a mathematic representation of the NDP.

Every RO membrane is characterized by its *Membrane A* and *Membrane B value*s [63]. *Membrane A value* is the membrane's pure water permeability coefficient. *Membrane B value* is the membrane's salt permeability coefficient. Even though reverse osmosis membranes are capable of extracting multi-solute contaminated solvent, [64][65] for simplicity sake a single-solute model is pursued though the rest of the research work. The solute used is NaCl and the solvent used is water. The fluid pressure drives the water flow from the region of higher pressure to the region of lower pressure. In contrast, the osmotic pressure drives the flow from the region of low salt concentration to the region of higher salt concentration. For reverse osmosis to work, the applied fluid pressure should be greater than the osmotic pressure difference between the permeate and the feedwater. Thus, the total pure water flux is given by:

$$J = A.(\Delta P_{memb} - \Delta\Pi_{memb}) \qquad \textbf{(2.13)}$$

This equation is a *de facto* definition of *Membrane A value-* A which is equivalent to the membrane's pure water permeability coefficient. (This is a membrane property)

J is the volumetric flux of pure water across membrane (volume/area-second)

ΔP_{memb} is the static pressure difference across the membrane (feed pressure - permeate pressure)

$\Delta\Pi_{memb}$ is the osmotic pressure difference across the membrane

= osmotic pressure on the feed side – osmotic pressure on the permeate side

A rudimentary modified Van't Hoff's osmotic pressure equation is used to calculate the Osmotic pressure (Source: The Dow Chemical Company).

$$\Pi = 0.255 \, .T \, .C \tag{2.14}$$

where Π is measured in Pascal, T is measured in Kelvin, and C is measured in parts per million by weight.

Many commercially available RO modeling software use Pitzer model [66] , Davis model [67] , or a polynomial fit to calculate the Osmotic Pressure.

$\Delta P_{memb} - \Delta\Pi_{memb}$ is the net driving pressure across the membrane (NDP).

$$NDP = \Delta P_{memb} - \Delta\Pi_{memb} \tag{2.15}$$

$$J = A.NDP \tag{2.16}$$

If the NDP is positive, water flow occurs from the feed side to the permeate side; otherwise, the water flow occurs from the permeate side to the feed side. ΔP is assumed to be the feed pressure when the permeate back pressure is defined as zero gauge pressure. Permeate back pressure is the hydrostatic pressure of the permeate water. A detailed definition of NDP is given later in this chapter under Equation (2.37).

The *B value* of the membrane is the salt permeability coefficient, which is also a membrane property.

$$J_s = B.(C_{wall} - C_{permeate}) \quad \textbf{(2.17)}$$

where J_s is the salt flux (in mass per second per unit area), $C_{permeate}$ is the concentration of salt on the permeate side, and C_{wall} is salt concentration adjacent to the membrane wall on the feed side. The unit for *Membrane B value* is in volume flowrate in a given area per second. In American RO industry, the *Membrane B value*s is given in gallons per square foot per day (GFD).

The *Membrane A* and *B value*s are a function of operating temperature, feed pressure, and feed salt concentration [68][69].

The salt passage SP of the membrane is the ratio of the salt concentration in the permeate to the salt concentration in the bulk feed. It describes the quantity of salt, as a percentage, which passes through the reverse osmosis membrane into to the permeate stream.

$$SP = \frac{C_{permeate}}{C_{bulk}} \quad \textbf{(2.18)}$$

The concentration polarization of a flat plate channel is given by substituting the concentration factor in

$$CP = \Gamma(1 - SP) + SP \quad \textbf{(2.19)}$$

Salt passage SP for any membrane is defined in the following section.

The parameters defined in the foregoing paragraphs will now be manipulated to arrive at various useful relationships in the following

$$C_{wall} = CP.C_{bulk} \tag{2.20}$$

$$C_{permeate} = \frac{J_s}{J} \tag{2.21}$$

$$J_s = J.SP.C_{bulk} \tag{2.22}$$

Therefore, substituting for J_s from Equation (2.17) and dividing by C_{bulk} and incorporating in Equation (2.22)

$$J.SP.C_{bulk} = B.C_{bulk}(CP - SP) \tag{2.23}$$

Cancellation of C_{bulk} on both sides leads to

$$B = \frac{J.SP}{(CP - SP)} \tag{2.24}$$

and rearrangement yields

$$SP = \frac{B.CP}{J + B} \tag{2.25}$$

The value of J is given in Equation (2.13)

From Equation (2.25) and Equation (2.18)

$$C_{permeate} = \frac{B.CP}{J+B}.C_{bulk} \tag{2.26}$$

2.4.5 Exit pressure drop

When the reject water exits the reverse osmosis element, it exits the brine spacer and enters the pressure vessel plenum. This process involves a drop in the pressure of the feedwater. This drop in pressure is known as the exit pressure drop. One of the aims of the doctoral research work is to calculate the pressure drop associated with RO concentrate exiting the RO element.

2.4.6 Pressure drop in the permeate spacer

The permeate water enters the permeate side of the membrane and travels along the permeate spacer (tricot) to the permeate water tube. The pressure drop along the permeate spacer is a function of the Reynolds number. The flow through the permeate spacer is laminar. It is well established that the friction factor for laminar flow through any constant area conduit (e.g., the permeate spacer) is inversely proportional to the Reynolds number as follows:

$$f = \frac{Const}{\mathrm{Re}} \tag{2.27}$$

$$f = const.\frac{\mu}{\rho.v_p.d_{hp}} \tag{2.28}$$

where μ is the dynamic viscosity, v_p is the velocity of the flow in the permeate channel, d_{hp} is the thickness of the permeate spacer, and ρ is the density.

The pressure drop through the permeate channel when the permeate water flows along the x-direction is given by

$$\frac{\partial P_{perm}}{\partial x} = \frac{1}{2}\rho v_p^{\ 2}.f.\frac{1}{2.d_{hp}} \tag{2.29}$$

where P_{perm} is the pressure of the permeate water at location x along the permeate spacer (refer Figure 2.13).

Substitution of the definition of f in Equation (2.29) yields

$$\frac{\partial P_{perm}}{\partial x} = const.\frac{v_p.\mu}{d_{hp}^{\ 2}} \tag{2.30}$$

For a specified geometry of the permeate spacer and for a given permeate medium, the only variable in Equation (2.30) is the velocity v_p of flow through the permeate spacer.

Since $\frac{\mu}{d_{hp}^{\ 3}}$ is a constant,

$$\frac{\partial P_{perm}}{\partial x} = H.v_p.d_{hp} \tag{2.31}$$

where H is another constant of proportionality.

Equation (2.31) is universal for all laminar flows. This can be regarded as a constitutive equation in that it relates an outcome to its cause. Specifically, the volumetric flowrate is the outcome, and the pressure gradient is the cause. In this light, Equation (2.31) is in the same category as Fourier's law of conduction and Fick's law of mass diffusion [70].

The following section describes the method used to estimate the permeate spacer pressure drop. Figure 2.13 shows a representative picture of a permeate spacer and a product water tube.

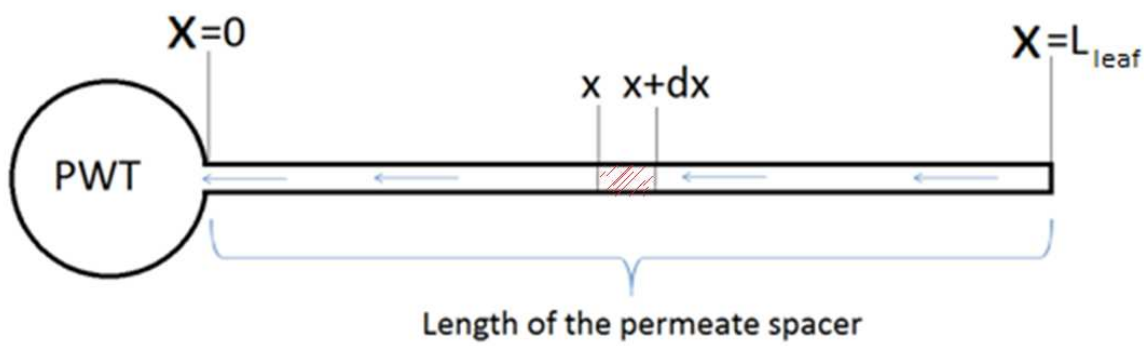

Figure 2.13: A conceptual diagram of the product water tube and the permeate spacer

Consider a small element of length dx at a distance x from the edge of the product water tube (PWT) on the permeate spacer. By applying conservation of mass around the small element (the shaded region)

$$v_p(x).L.d_{hp} = 2.J(x).dx.L + v_p(x+dx).L.d_{hp} \tag{2.32}$$

where L is the length of the element, which is also the width of the permeate spacer, $v_p(x)$ is the velocity of the permeate water flowing through the permeate spacer at point x. $J(x)$ is the flux of product water entering from the permeate spacer through the membrane. The value of $J(x)$ is obtained from Equation (2.13). In simple terms, Equation (2.32) states that the volume of water flowing at location x is the sum of volume of flowing in location $x+dx$ and the product water permeating into the permeate spacer from two sides of the spacer.

Substituting Equation (2.31) and Equation (2.13) in Equation (2.32) and canceling w on both RHS and LHS of the equation

$$\frac{1}{H}\frac{\partial P_{perm}}{\partial x}\bigg|_{x} = 2.A(\Delta P_{memb} - \Delta\Pi_{memb}).dx + \frac{1}{H}\frac{\partial P_{perm}}{\partial x}\bigg|_{x+dx} \tag{2.33}$$

ΔP_{memb} is defined as the pressure difference between the feed side P_{feed} and the permeate side P_{perm} of the membrane:

$$\Delta P_{memb} = P_{feed} - P_{perm} \tag{2.34}$$

$\Delta\Pi_{memb}$ is defined as the osmotic pressure difference between the feed side Π_{feed} and the permeate side Π_{perm} of the membrane:

$$\Delta\Pi_{memb} = \Pi_{feed} - \Pi_{perm} \tag{2.35}$$

Substituting Equation (2.34) in Equation (2.33)

$$\frac{1}{H}\frac{\partial P_{perm}}{\partial x}\bigg|_{x} = 2.A((P_{feed} - P_{perm}) - (\Pi_{feed} - \Pi_{perm})).dx + \frac{1}{H}\frac{\partial P_{perm}}{\partial x}\bigg|_{x+dx} \tag{2.36}$$

It may be noted that P_{perm} and Π_{perm}, can vary as a function of x and all the other terms are constant as a function of x. The quality of product water produced from the membrane is assumed not to change along the length of the permeate spacer, Π_{perm} is constant. The only variable is P_{perm}.

The net driving pressure NDP of a membrane is define as

$$NDP = (P_{feed} - P_{permeate}) - (\Pi_{feed} - \Pi_{permeate}) \tag{2.37}$$

where $P_{permeate}$ and $\Pi_{permeate}$ are permeate hydrostatic pressure and osmotic pressure at the product water tube PWT.

$$P_{permeate} = P_{perm}(x = 0) \tag{2.38}$$

$$\Pi_{permeate} = \Pi_{perm}(x = 0) \tag{2.39}$$

As in most RO applications $P_{permeate}$ is zero because raising the pressure of the permeate water is counterproductive to RO operations. Therefore pressure of the permeate water at distance x from the product water tube can be written as

$$P_{perm}(x) + P_{permeate} \tag{2.40}$$

Similarly the osmotic pressure of permeate water at distance x from the product water tube can be written as

$$\Pi_{perm}(x) + \Pi_{permeate} \tag{2.41}$$

As osmotic pressure is assumed to be invariant along the distance x

$$\Pi_{perm}(x) = 0 \qquad \forall x \in [0, L] \tag{2.42}$$

The Equation (2.36) can be rearranged as

$$-\frac{1}{H}\frac{\partial^2 P_{perm}}{\partial x^2}\bigg|_x = 2.A((P_{feed} - P_{perm}(x) - P_{permeate}) - (\Pi_{feed} - \Pi_{perm}(x) - \Pi_{permeate})) \tag{2.43}$$

Substituting Equation (2.37) and Equation (2.42) in Equation (2.33)

$$-\frac{1}{H}\frac{\partial^2 P_{perm}}{\partial x^2}\bigg|_x = 2.A(NDP - P_{perm}(x)) \tag{2.44}$$

The negative sign in the LHS of Equation (2.43) is rearranged as

$$\left.\frac{\partial^2 P_{perm}(x)}{\partial x^2}\right|_x = 2.AH\,(P_{perm}(x) - NDP) \tag{2.45}$$

To simplify this form of equation, the dependent variable is transformed by defining a new variable θ as

$$\theta(x) = P_{perm}(x) - NDP \tag{2.46}$$

where, since NDP is assume to be constant in an RO element (shown explicitly in Figure 2.16)

$$\frac{d\theta(x)}{dx} = \frac{dP_{perm}(x)}{d(x)} \tag{2.47}$$

further

$$\frac{d^2\theta(x)}{d^2x} = \frac{d^2P_{perm}(x)}{d^2(x)} \tag{2.48}$$

Substituting Equation (2.48) and (2.46) in (2.45)

$$\frac{\partial^2 \theta(x)}{\partial x^2} = 2.AH\,\theta(x) \tag{2.49}$$

The Equation (2.49) is of the form $\frac{\partial^2 y}{\partial x^2} = m^2 y$

The constants in the RHS of the Equation (2.49) can be substituted as

$$m = \sqrt{2.AH} \tag{2.50}$$

$$\frac{\partial^2 \theta(x)}{\partial x^2} = m^2 \theta(x) \tag{2.51}$$

Equation (2.51) is a linear-homogenous-second order differential equation with constant coefficients. Its general solution is of the form

$$\theta(x) = C1e^{mx} + C2e^{-mx} \tag{2.52}$$

To evaluate the constant C1 and C2 of Equation (2.52), it is necessary to specify appropriate boundary conditions. One such boundary condition may be specified in terms of the pressure of the permeate water at the product water tube (x = 0). Permeate water pressure at x = 0 is zero.

$$\theta(0) = -NDP \tag{2.53}$$

The other known boundary condition is at ($x = L_{leaf}$). At the tip of the permeate spacer sheet, the velocity of the flow of permeate water through the spacer is zero.

$$v_p(L_{leaf}) = 0 \tag{2.54}$$

From Equation (2.54) and Equation (2.31)

$$\left.\frac{\partial P_{perm}}{\partial x}\right|_{x=L_{leaf}} = 0 \quad \text{or} \quad \left.\frac{\partial \theta}{\partial x}\right|_{x=L_{leaf}} = 0 \tag{2.55}$$

Substituting Equation (2.55) and Equation (2.53) in Equation (2.52)

$$C1 + C2 = -NDP \tag{2.56}$$

$$C1e^{mL_{leaf}} - C2e^{-mL_{leaf}} = 0 \tag{2.57}$$

Solving for C1 and C2 and after some manipulation [71]

$$\frac{\theta(x)}{-NDP} = \frac{\cosh\left(m\left(L_{leaf} - x\right)\right)}{\cosh\left(mx\right)} \tag{2.58}$$

From Equation (2.58) and Equation (2.46)

$$\frac{P_{perm}(x) - NDP}{-NDP} = \frac{\cosh\left(m\left(L_{leaf} - x\right)\right)}{\cosh(mx)} \tag{2.59}$$

By rearranging Equation (2.59) and substituting of m

$$P_{perm}(x) = NDP\left[1 - \frac{\cosh\left(\sqrt{2.A.H}\left(L_{leaf} - x\right)\right)}{\cosh\left(\sqrt{2.A.H}\,(x)\right)}\right] \tag{2.60}$$

From Figure 2.13, it may be observed that the total quantity of product water entering the product water tube from the permeate spacer $Q_{permeate}$ can be defined as

$$Q_{permeate} = v_p.L.d_{hp}\Big|_{x=0} \tag{2.61}$$

From Equation (2.61) and Equation (2.31)

$$Q_{permeate} = \frac{1}{H}\frac{\partial P_{perm}}{\partial x}\Bigg|_{x=0}.L \tag{2.62}$$

Substituting for $P_{perm}(x)$ from Equation (2.60) in Equation (2.62)

$$Q = \sqrt{\frac{2.A}{H}}.NDP.\tanh(\sqrt{2.A.H}\,L_{leaf}).L \tag{2.63}$$

The volumetric rate of permeate-flow into the product water tube PWT is given by Equation (2.63).

The impact of resistance offered by the permeate spacer on the rate of product water produced can be quantified by an efficiency term. The efficiency of the membrane is defined as the ratio of the rate of product water produced when the permeate spacer offers resistance to the rate of product water produced when the permeate spacer offers no resistance as shown in Figure 2.14

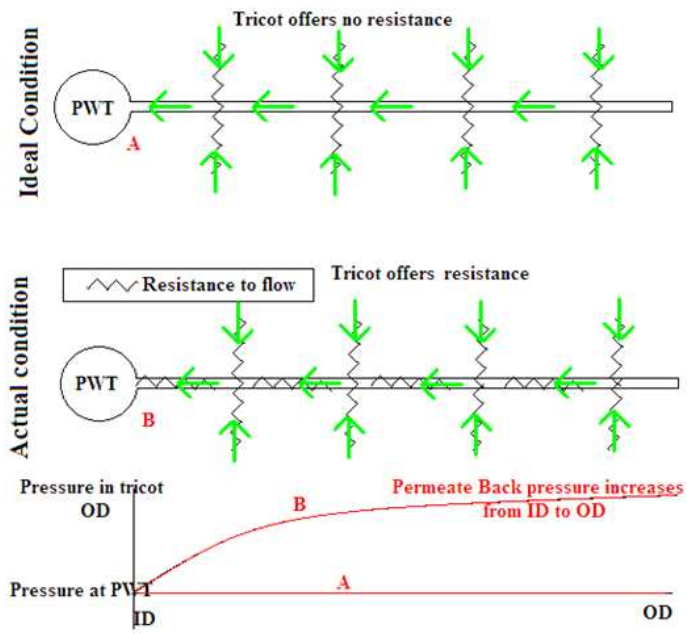

Figure 2.14: Schematic of pressure drop in permeate spacer

The volume of permeate produced when the permeate spacer offers no resistance can be obtained from Equation (2.63) by substituting H = 0.

$$Q_{ideal} = \lim_{H \to 0} \sqrt{\frac{2.A}{H}}.NDP.\tanh(\sqrt{2.A.H}\,L_{leaf}).L \tag{2.64}$$

$$Q_{ideal} = 2.A.NDP.L.L_{leaf} \tag{2.65}$$

It may be observed that the total active area of the membrane that is feeding permeate water to the permeate spacer is the product of the length of the Membrane and the width of the membrane. Further, there is membrane feeding permeate water to the permeate spacer from the two sides of the permeate spacer. Therefore the total active area AA_{leaf} of the membrane is

$$AA_{leaf} = 2.L.L_{leaf} \tag{2.66}$$

The efficiency of the permeate spacer is the defined as the ratio of the actual volumetric flowrate through the permeate spacer to the ideal flow through the permeate spacer (no backpressure/resistance to flow in the tricot)

$$\eta = \frac{Q_{permeate}}{Q_{ideal}} \tag{2.67}$$

$$\eta = \frac{\tanh(\sqrt{2.A.H}\,.L_{leaf})}{\sqrt{2.A.H}\,.L_{leaf}} \tag{2.68}$$

Substituting Equation (2.68) and Equation (2.66) in Equation (2.63) and extending the solution to all the leaves in the RO element.

$$Q_{permeate} = \eta.AA.NDP.A \tag{2.69}$$

where η is the efficiency, AA is the active area of the whole RO element, A is the *Membrane A value* and NDP is the net driving pressure, and $Q_{permeate}$ is the actual permeate flowrate.

Figure 2.14 illustrates both the situations where the pressure change in the tricot is insignificant (ideal condition) and significant (actual condition).

2.4.7 Net driving pressure

A definition of the NDP is provided in the previous section in Equation (2.37). The net driving pressure varies along the length of the membrane. The variation of a property along the length of the element is different from the variation along the length of the permeate spacer (discussed in the foregoing section). In simulation methods currently used in the industry, the an average of properties are used to calculate the average NDP (refer Figure 2.16)

$$NDP\Big|_{average} = (P_{feed}\Big|_{average} - P_{permeate}\Big|_{average}) - (\Pi_{feed}\Big|_{average} - \Pi_{permeate}\Big|_{average}) \tag{2.70}$$

where

$P_{feed}\Big|_{average}$ is the feed pressure averaged along the length of the element

$P_{permeate}\Big|_{average}$ is the pressure of the permeate is product water tube averaged along the length of the element

$\Pi_{feed}\Big|_{average}$ is the feed osmotic pressure of the feed along the wall of the element averaged along the length of the element

$\Pi_{permeate}\Big|_{average}$ is the osmotic pressure of the permeate is product water tube averaged along the length of the element

Therefore, the average pressure in the feed spacer is

$$P_{feed}\Big|_{average} = P_{feed}\Big|_{inlet} - \frac{P_{drop}}{2}.L \tag{2.71}$$

$P_{feed}\Big|_{inlet}$ is the pressure of the feedwater that is entering the element. P_{drop} is the pressure gradient defined in Equation (2.4) and L is the length of the element.

$\Pi_{permeate}\Big|_{average}$ and $P_{permeate}\Big|_{average}$ does not vary along the length of the permeate product water tube appreciably.

$\Pi_{feed}\Big|_{average}$ is calculated from the membrane wall concentration. As the feedwater wall concentration varies along the length of the element, an average of the wall concentration is used to calculate the osmotic pressure. Therefore from Equation (2.20)

$$C_{wall}\Big|_{average} = CP.C_{bulk}\Big|_{average} \tag{2.72}$$

where

$C_{wall}\Big|_{average}$ is the average concentration of the feedwater near the membrane wall

$C_{bulk}\Big|_{average}$ is the average bulk concentration of the feedwater

CP is the concentration polarization described in Equation (2.19)

As the feed flows through the spacer, the permeate water with lower concentration is recovered, and the concentration of the feed flow increases and a straight line is used to model the variation of concentration across the length of the element (refer Figure 2.16c.). The concentration of the feedwater (concentrate) that exits the RO element is given by conserving the mass of salt entering and leaving the element.

$$C_{bulk}\Big|_{outlet} = C_{bulk}\Big|_{inlet}\left(\frac{Q_{feed}\Big|_{inlet} - Q_{permeate}.SP}{Q_{feed}\Big|_{outlet}}\right) \tag{2.73}$$

where

$C_{bulk}\Big|_{outlet}$ is the bulk concentration of the feedwater exiting the element (aka concentrate)

$C_{bulk}\Big|_{inlet}$ is the bulk concentration of the feedwater entering the element

$Q_{feed}\Big|_{inlet}$ is the volumetric flowrate of feedwater entering the element

$Q_{feed}\Big|_{outlet}$ is the volumetric flowrate of feedwater exiting the element

$Q_{permeate}$ is the volumetric flowrate of the permeate produced in the element

and SP is the salt passage from Equation (2.18)

By law of conservation of flow of water around the element

$$Q_{feed}\Big|_{outlet} = Q_{feed}\Big|_{inlet} - Q_{permeate} \tag{2.74}$$

The fraction of permeate water recovered in an element is given by

$$rec = \frac{Q_{permeate}}{Q_{feed}\big|_{inlet}} \tag{2.75}$$

Dividing the numerator and the denominator in Equation (2.73) by $Q_{feed}\big|_{inlet}$

$$C_{bulk}\big|_{outlet} = C_{bulk}\big|_{inlet}\left(\frac{1 - rec.SP}{1 - rec}\right) \tag{2.76}$$

Thereby, the effective bulk feedwater concentration is given by the average of the inlet and the outlet feedwater bulk concentration.

$$C_{bulk}\big|_{average} = C_{bulk}\big|_{inlet}\left(\frac{2 - rec.(1 + SP}{2.(1 - rec)}\right) \tag{2.77}$$

And from Equation (2.72)

$$C_{wall}\big|_{average} = CP.C_{bulk}\big|_{inlet}\left(\frac{2 - rec.(1 + SP}{2.(1 - rec)}\right) \tag{2.78}$$

The osmotic pressure $\Pi_{feed}\big|_{average}$ in Equation (2.70) is calculated from $C_{wall}\big|_{average}$

$P_{permeate}\big|_{average}$ in large RO plants is calculated from flow losses that are unique to every RO plant's plumbing and is assumed as zero unless specified.

$\Pi_{permeate}\Big|_{average}$ is calculated from the concentration of product water produced in the element. The concentration of the permeate is estimated from Equation (2.26)

The approximations made in determining the standard net driving pressure may become significant when the feed pressure or the concentration varies non-linearly across the element. One of the main aims of this research work is to minimize the approximations made and improve the method of estimating the standard net driving pressure.

2.5 Current methods of RO element modeling

For modeling an RO pressure vessel, consider a pressure vessel containing three reverse osmosis RO elements (hereafter called RO elements or elements) as shown in Figure 2.15. The snap ring and the end cap seen at the right-hand end of the figure enable the opening and closing of the pressure vessel. It is through this opening that the elements are inserted into the pressure vessel.

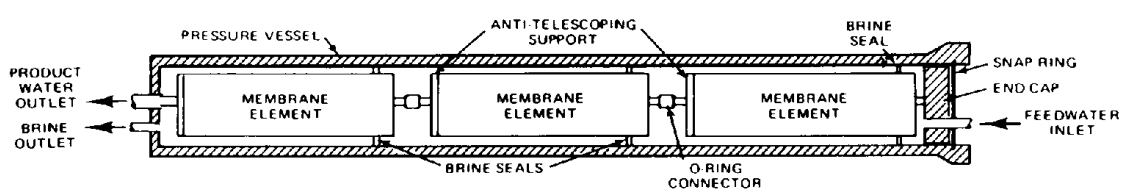

Figure 2.15: Pressure vessel containing three elements

When the elements are inserted one by one, two elements are connected by the product water tube with the help of an o-ring connector also known as a coupler, as shown in Figure 2.15. The coupler connector helps to prevent the feedwater from mixing with the product water in the product water tube. The feedwater enters the pressure vessel through a port at one of its ends. This feedwater is pumped at a high pressure. It fills the pressure vessel, but it is prevented from bypassing any of the elements by the brine seals. The feedwater is forced to enter the element through the scroll.

The current understanding of the physical phenomena occurring in a RO pressure vessel is depicted in Figure 2.16 (b)-(e). The pressure-related events can be described as follows:

1. The incoming high-pressure feedwater is forced to enter the first element through the scroll of the element as described in the foregoing sections.

2. The pressure of the feedwater drops as it flow across the first element

3. The feedwater exits the first element through the other end of the scroll and fills the pressure vessel between the downstream of the brine seal of the first element and the brine seal of the second element.

4. The high-pressure of the feedwater forces it to flow from the pressure vessel into the middle element.

5. The pressure drop processes that occur in the middle and the last element are identical to that which occurs in the first element.

The aforementioned pressure drop pattern is illustrated in Figure 2.16(b).

As the feedwater is forced through an element over the membrane, the permeate passes through the membrane and through the permeate spacer into the product water tube. Removal of low-salinity product increases the salt concentration in the residual feedwater. The variation of the salt concentration of the feedwater along the length of the pressure vessel is illustrated in Figure 2.16(c). As the concentration in the feedwater increases, its osmotic pressure increases. Therefore, the net driving pressure (NDP) changes as depicted in Figure 2.16(d).

The pressure, concentration, and the NDP are assumed to vary linearly across each element as exhibited in Figure 2.16 (b)-(d). The horizontal red lines shown in Figure 2.16 (b)-(d) represent the average value of pressure, concentration, and NDP. The average values of the NDP are plotted separately in Figure 2.16 (e).

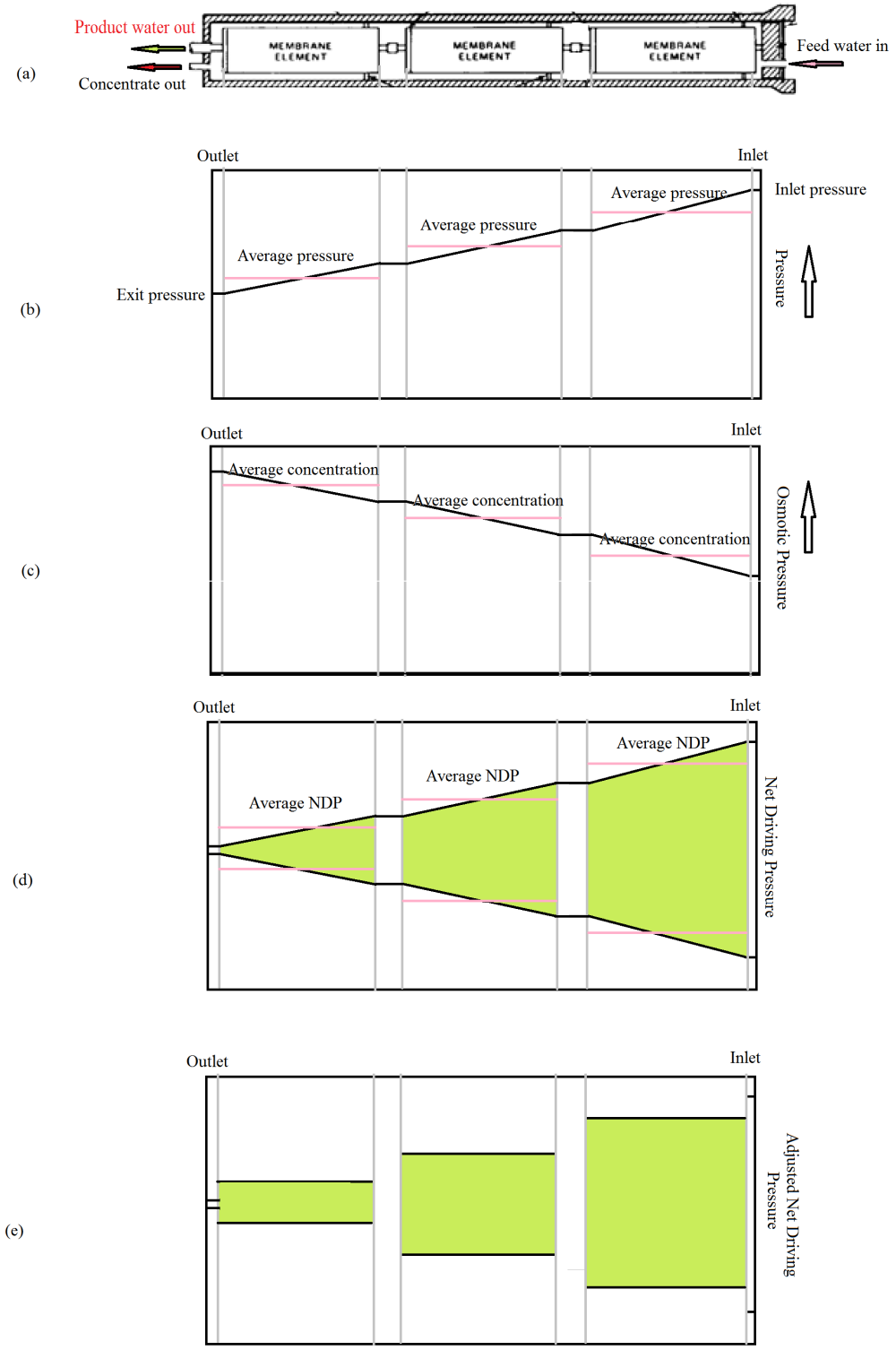

Figure 2.16: Qualitative graph showing current method used for modeling RO pressure vessel

For the purpose of simulation, the following information about the element and the element arrangement configuration are accepted from the user initiating the simulation:

1. The property of the membrane
    a. the membrane water permeability (*Membrane A value*)
    b. the membrane salt permeability (*Membrane B value*)
    c. Thickness of the membrane
2. The property of the RO element
    a. length of the RO element
    b. number of leaves in the RO element
    c. geometry of the feed spacer
        i. strand diameter
        ii. strand angle
        iii. spacer thickness
        iv. feed spacer pressure drop coefficient (a and b from (2.4))
        v. feed spacer mixing coefficient (c and d from (2.9))
    d. property of the permeate spacer
        i. hydrodynamic resistance
        ii. Thickness
    e. ID of the product water tube
    f. type of inter-element interconnect
3. The pressure of the feedwater entering the Pressure vessel containing the RO element

4. Flowrate of feedwater

5. Concentration of the feedwater

6. Temperature of the feedwater

It may be observed that Figure 2.16 is a qualitative graph. A quantitative graph Figure 2.18 is plotted based on the user input. In the following, the current industry method to model elements is portrayed.

Table 2-1: Input conditions for the pressure vessel

Membrane A value	0.09 GFD/psi
Membrane B value	0.085 GFD
Area of the element AA	400 ft^2
Thickness of the membrane	7-mil
Length of the RO element	40 inches
Number of leaves in the RO element	25
Length of each leaf	30 inches
Feed spacer thickness	33-mil
Feed spacer strand angle	90°
Permeate spacer hydrodynamic resistance	30 psi-sec/in^3
Permeate spacer thickness	11-mil
OD of the product water tube	1.5 inches
Feedwater pressure entering the pressure vessel	250 psi
Feedwater flowrate	9.5 liters per minute
Feedwater salt concentration	2000 ppmw NaCl
Temperature of the feedwater	25°
a- Pressure factor coefficient	140
b- Pressure factor exponent	-0.6
c- Sherwood number coefficient	0.37
d- Sherwood number exponent	0.58

The properties of feedwater used in the simulation are shown in Table 2-2.

Table 2-2: Property of feedwater used in simulation

Dynamic viscosity	8.899E-4 kg/m/sec
Density of water	997 kg/m^3
Diffusion coefficient of salt in water	1.5E-9 m^2/sec

The pressure of the feedwater exiting the element is calculated iteratively.

For the first iteration, the average bulk velocity of the feedwater through the feed spacer is calculated from the feed flowrate. Given the number of leaves in the element is 25 and the spacer thickness is 33-mil and the length of the leaf is 30 inches

Average flow velocity is calculated as $\frac{9.5LPM}{33mil \times 30inches}$ = 24 cm/sec

The corresponding Reynolds number of the flow is calculated as 467 (using (2.2))

The exit velocity calculated from Equation (2.74) and Equation (2.75) is 21 cm/sec.

The Reynolds number at the exit of the element is 397

The average Reynolds number of the element is 432

The pressure drop across the first element is calculated as 10.4 psi (using (2.4))

The pressure of feedwater after passing through the first element is (250-17.34) = 239.6 psi.

The average feed pressure is calculated as 244.78 psi (using Equation (2.71))

The concentration polarization is calculated iteratively using Equations (2.12) and Equation (2.19).The initial values for salt passage and concentration polarization are assumed as zero to calculate the net driving pressure. The NDP is used to correct the CP and SP. The iteration is performed until the CP and SP stabilize. The final values for CP and SP are 1.25 and 0.34%.

Using Equation (2.73), the concentration of the feedwater exiting the first element is 2347 ppmw NaCl.

The rate of concentrate water exiting the first element is 8.1 lpm.

The rate of permeate water produced in the first element is 1.4 lpm.

The quality of permeate water produced in the first element is 11 ppmw NaCl.

The flowchart in Figure 2.17 shows pictorially the processes adopted to calculate the performance of the first element in the pressure vessel. These calculations are repeated for the second and the third element shown in the pressure vessel in Figure 2.15.

The quality of permeate exiting the pressure vessel is calculated from the mass average of permeate concentration exiting each element. From the simulations, the quality of permeate exiting element 2 and element 3 are 14.2 ppmw and 18.6 ppmw NaCl. The flowrate of permeate produced in element 2 and element 3 are 1.27 lpm and 1.15 lpm respectively, The quality and flowrate of permeate produced in the pressure vessel is 14.38 ppmw NaCl at 3.85 lpm.

The calculation methods described so far is shown in a flow chart (Figure 2.17) for easy understanding.

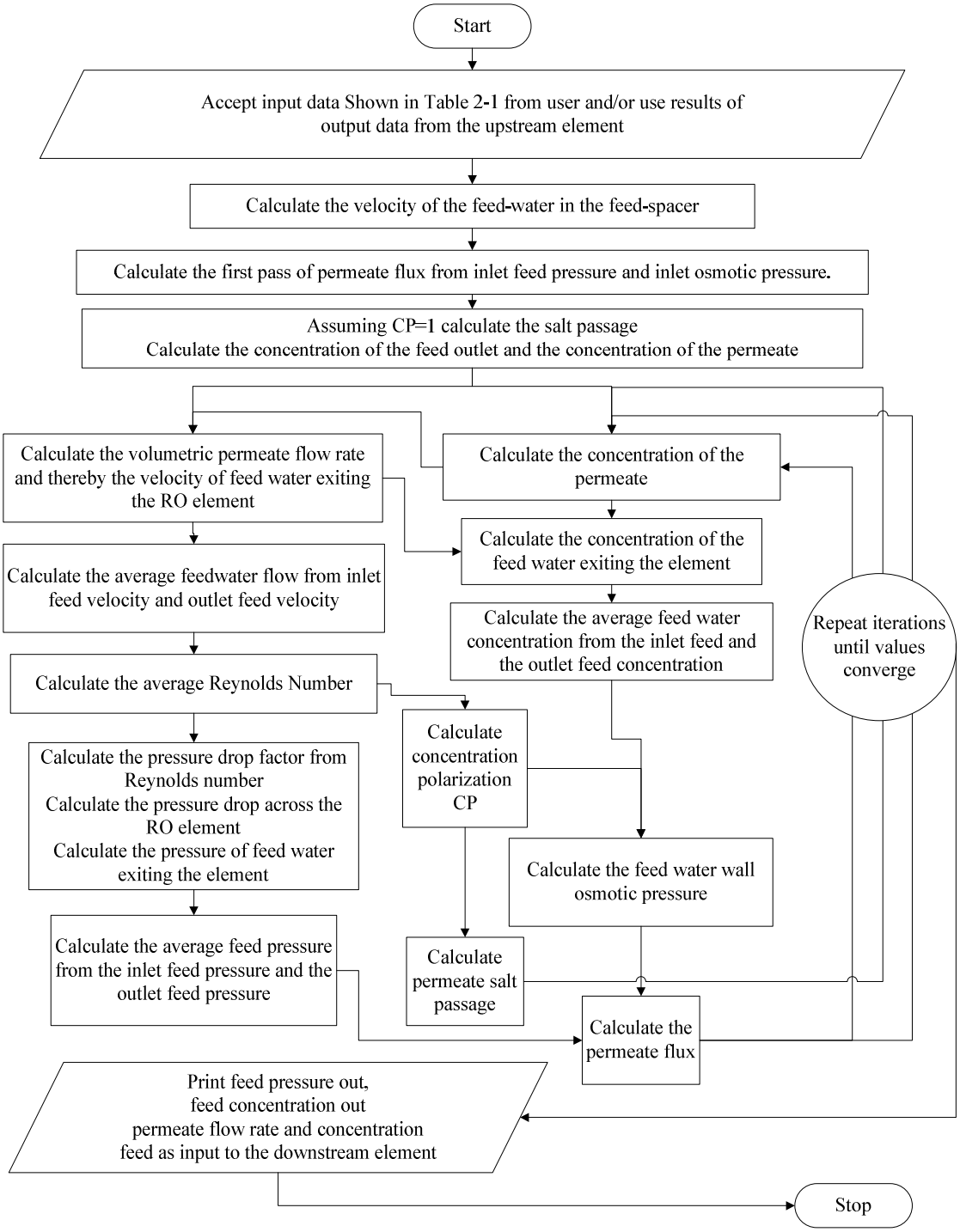

Figure 2.17: Flowchart describing the method used to simulate element performance

For the inlet conditions specified in Table 2-1, the quantitative element performance graph is shown in Figure 2.18, which is the quantitative graph of Figure 2.16.

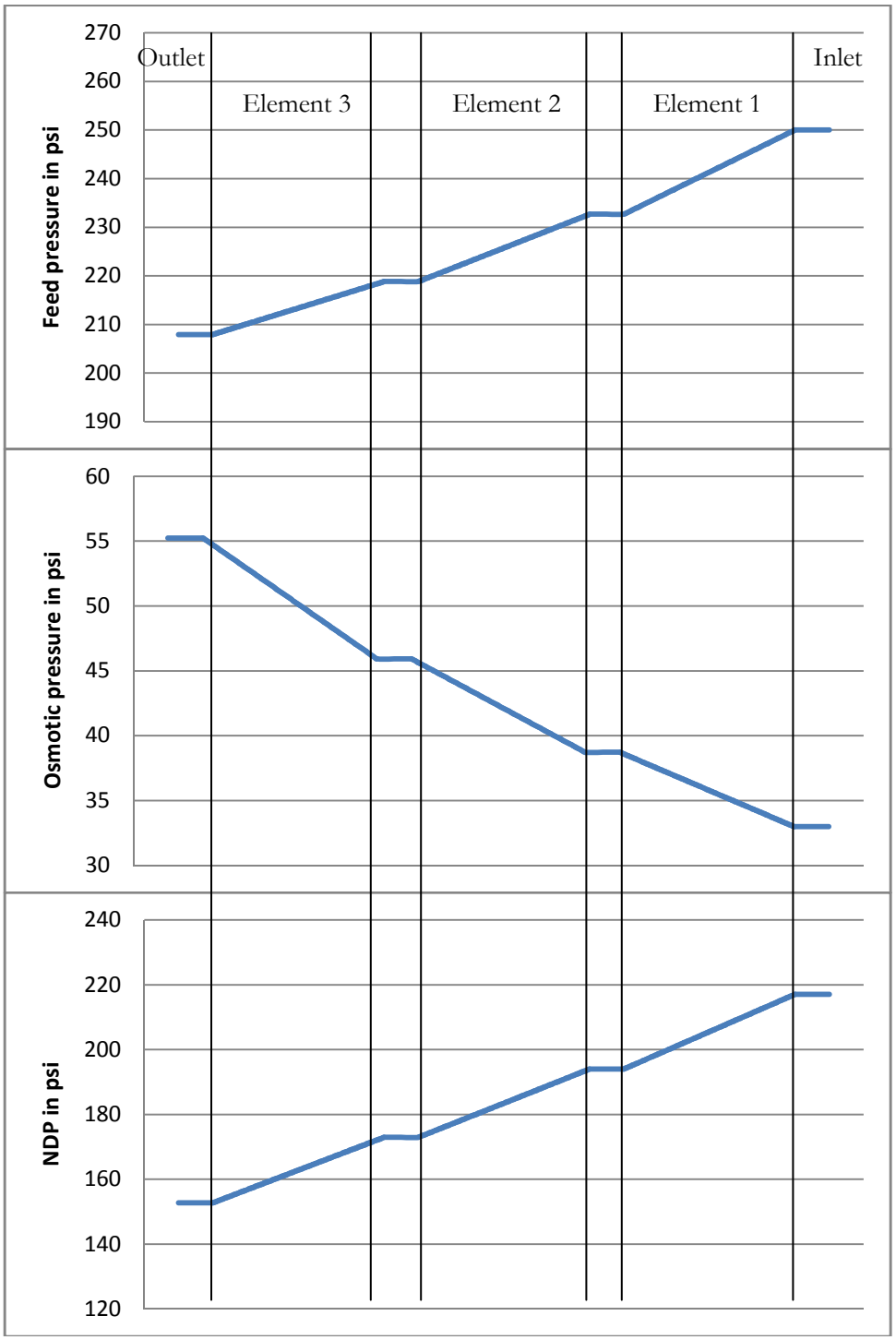

Figure 2.18: Quantitative graph showing element performance in the pressure vessel

2.6 Insufficiencies of the current model used

The just-described current model departs from reality in a number of important ways, the most significant of which will be described shortly. As background, it may first be useful to review certain phenomena that give rise to pressure variations. There are three main causes of pressure variations:

a) friction internal to the fluid and also due to fluid-wall interactions

b) acceleration or deceleration

c) inertial losses

Friction and inertial events always cause parasitic (irreversible) pressure losses. Inertial losses are connected with processes such as uncontrolled mixing, flow recirculation, and eddy. On the other hand, acceleration and deceleration are, in principle, reversible processes. All of these processes occur in an RO pressure vessel.

1. When the feedwater enters an element via the scroll, it experiences a change of cross section and of direction. The resulting pressure losses are parasitic and are not accounted for in current models.

2. Within any element, permeate is extracted with a consequent reduction of the mass flow-rate of the feedwater. The extracted permeate amounts to about 15-20% of the feedwater flow. Consequently, the mass flowrate of the feed flow varies in the stream-wise direction, so that fully developed flow cannot be achieved by the feedwater. This outcome precludes a linear variation of the pressure between the inlet and exit of an element, thereby negating the present model.

3. The key factor that must be taken into account for modeling the flow described in (2) is the continuous changing of the velocity profile in the stream-wise direction. These changes have two critical ramifications: (a) changes of the wall-fluid interactions due to the changing slope of the velocity profile at the wall and (b) changes in the momentum flowrate that accompanies changes of the shape of the velocity profile. When these factors are taken into account, the stream-wise pressure variation in an element must be non-linear.

4. The process described in (1) is reversed when the feedwater leaves an element and enters the pressure vessel, giving rise to related, but not identical, pressure losses that are completely unaccounted for in current models.

5. Further, the premise that the pressure gradient across the element is a linear function of velocity should be verified.

6. The product water flux across the membrane is a function of the net driving pressure (NDP). The non-linearity of the end-to-end pressure variation in the feedwater within an element will have a direct effect on the NDP. Furthermore, since the flow-pressure drop relation for the product flow across the element is non-linear, the impact of the feedwater pressure non-linearity must be predicted from first from first principles and cannot be "fixed" by use of a rule of thumb.

7. The non-linearity in NDP across the membrane introduces a non-linearity in permeate recover across the membrane, which in turn introduces a non-linearity in feedwater salt concentration variation across the element.

8. Most current membrane models assume invariant *Membrane A* and *Membrane B value*s across the element. However, this assumption ignores reality. The *Membrane A value* - decreases with an increase in pressure due to compaction and decreases with increase in concentration due to osmotic effects. While the *Membrane B value* increases with an increase in pressure due to convective transport. Therefore, due to these realities alone, the rate of permeate recovery must vary along the length of the membrane. If element averages are used for feed pressure, *Membrane A* and *B value*s, and concentration, the errors in the current model are exacerbated.

The root cause of the insufficiencies listed in the foregoing can be traced to the gross nature of nature of the model. A more exact and detailed model will be set forth in the detailed proposal that follows.

2.7 Research work proposed

The following are the key features of the proposed thesis.

1. Modeling of the fluid flow and pressure variations along the length of an element, with special emphasis on the entry and exit pressure drops (Figure 2.19 b). This includes

a. Providing a parametric functional relationship between the entry pressure drop and the feedwater flowrate, based on simulation.

b. Providing a parametric functional relationship between the exit pressure drop and the reject water flowrate, based on simulation.

c. Providing a parametric function that relates the geometry of the feed spacer, the velocity of the feedwater flow over the feed spacer, and the pressure drop per unit length across the element by numerical simulation.

d. Identification of the mechanism of pressure drop within each element by means of comparisons between the Darcy and Forchheimer models, the choice depending on the Reynolds number of the membrane flow.

2. A critical outcome of task (1) will be the demonstration that the currently used model of a linear pressure drop across the element is unrealistic.

3. Another major result of task (1) is the determination of the variation of the feedwater salt concentration within each element (Figure 2.19 c).

    a. This task includes understanding the phenomenon of concentration polarization

    b. Providing a parametric function that relates the geometry of the feed spacer, the velocity of the feedwater flow over the feed spacer, the permeate flux through the feed spacer, and the concentration polarization over the membrane.

4. A corollary of task (2) and (3) will be the determination of the correct net driving pressure for separation (Figure 2.19 d)

5. Since the fluid flow and pressure variations within each element in the pressure vessel cannot be the same, the interactions between individual elements will have to be taken into account. This will involve an iterative process to determine the parameters involved.

6. An outcome of tasks (3-5) will be the accurate prediction of RO separation performance of the entire pressure vessel and the corresponding overall pressure drop.

7. The methodology underlying the simulation is discretization of an element into a number of small discrete sections deployed along the axial direction. (Figure 2.19 e)

8. Devise and implement an experimental method to be used to obtain more accurate *Membrane A* and *B value*s, than have been available in the past, as a function of RO operating conditions.

9. Make use of the new knowledge about fluid flow, pressure drop, and separation rate to build an encompassing design algorithm.

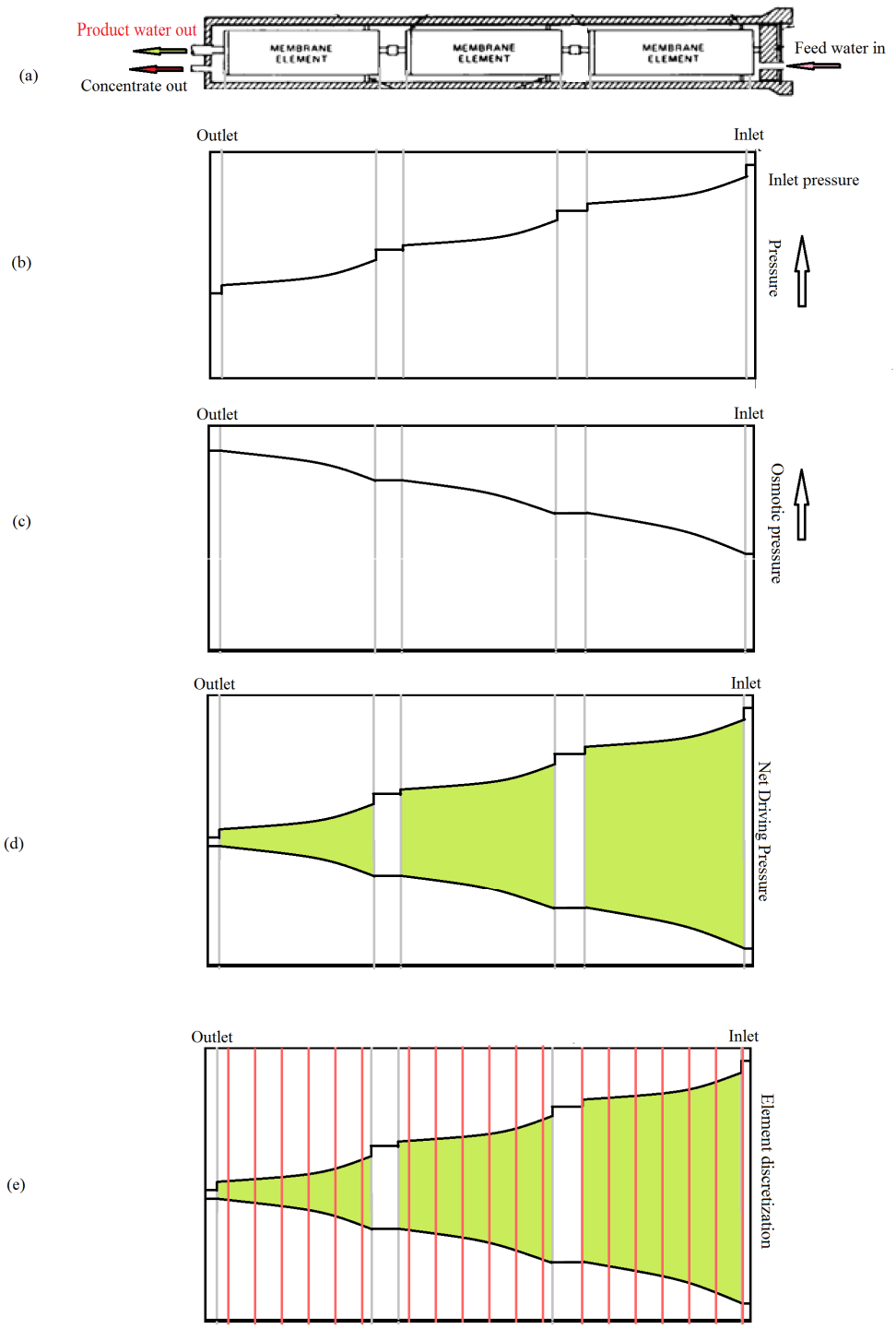

Figure 2.19: Proposed model for RO pressure vessel.

Chapter 3 : FEED SPACER IN CFD SIMULATION

3.1 Introduction

The focus of this chapter is to describe the approach used to describe the flow of feedwater through the feed spacer. A Computational Fluid Dynamics (CFD) simulation is formulated and implemented to simulate the fluid flow with mass transfer in three-dimensional narrow channels containing non-woven feed spacers.

3.2 Geometry of the feed spacers

First, only non-woven feed spacer fibers are evaluated in this work because the geometry of most feed spacers used in practical RO elements is non-woven. Figure 3.1 [72] shows the difference between woven and non-woven fibers. Second, only 90º strand angles are considered in this report. Third, even though feed spacers are available in different geometries, only the simple two-layer-strand, symmetric spacer is examined because it is the most common type of feed spacer utilized in most commercial RO elements.

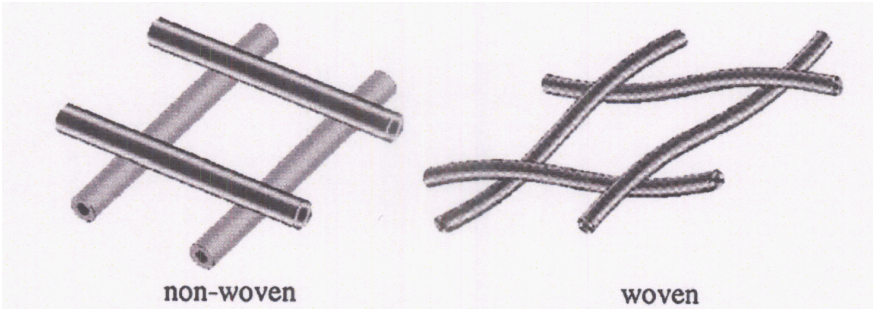

Figure 3.1: Woven and non-woven feed spacer

The cases considered here consist of simple two-layer-strand-symmetric spacers. A simple two-layer-strand, symmetric spacer (simple spacer) refers to feed spacers made from overlaying one layer of parallel spacer strands over the other. The inter strand spacing is reported in strands per inch. Further, the direction of flow is parallel to the angle bisector of the angle formed by the two-strand layer as shown in the Figure 3.2.

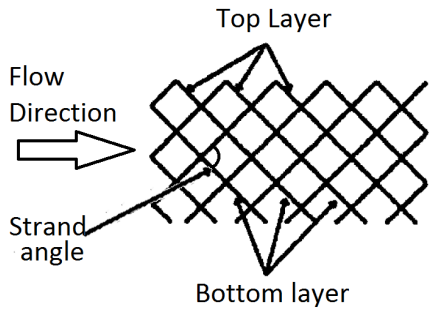

Figure 3.2: Plan view of a two layer feed spacer

The geometrical specifications necessary to define commercially available simple spacers are:

1. Spacer thickness
2. Strand diameter
3. Strand spacing
4. Strand angle

In most simple spacers, the spacer thickness is equal to twice the strand diameter as the two strands are stacked one on top of the other. In this investigation, the strand angle is maintained constant at 90° and the strand spacing and the spacer thickness are varied. Geometric similarity and non-dimensional numbers are used to generalize the results and reduce the number of independent calculations.

Two objects are said to be geometrically similar if both the objects have the same shape and one object can be obtained from the other by uniform scaling (enlarging or shrinking). In the example shown in Table 3-1, *Spacer 1* and *Spacer 2* are geometrically similar because *Spacer 1* can be obtained by uniformly doubling the size of *Spacer 2*.

Table 3-1: Example of geometric similarity in feed spacers

Spacer 1		Spacer 2	
Spacer thickness	**40-mil**	Spacer thickness	**20-mil**
Strand diameter	**20-mil**	Strand diameter	**10-mil**
Strand spacing	**0.2 inch**	Strand spacing	**0.1 inch**
Strand angle	**90°**	Strand angle	**90°**

With the use of geometric similarity, any spacer geometry with a strand angle 90° can be scaled to a spacer with fixed strand spacing and varying spacer thickness. To accommodate all the sizes of spacers encountered, the strand spacing is fixed at 0.1 inch (100-mil) and the spacer thickness is varied [20-, 25-, 30-, and 35-mil].

For the simulations, a 3-D model of the flow channel is generated, and a commercial CFD code (ANSYS CFX-14.0) is used to solve for the steady state fluid flow and mass transport inside the feedwater channel. Fimbres et al [73] have shown that neither gravity nor density variations will have a significant effect on the solutions obtained. ANSYS CFX-14.0 applies the finite-volume method to discretize the governing partial differential Navier-Stokes equations and the equations of mass conservation. It uses a coupled solver where both continuity and momentum transport equations are treated as a single system and solved simultaneously.

3.3 Geometry of the spacer used in simulation

3D models require high memory usage; therefore, a representative spatially periodically *repeating unit* is simulated instead of the entire feed-spacer screen. The representative, periodically, *repeating unit* selected for simulation is shown in Figure 3.3.

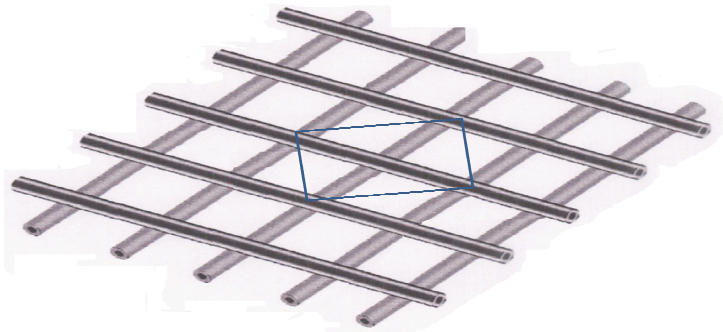

Figure 3.3: Typical feed spacer and the *repeating unit* used for simulation

In this case, spatially periodic boundary conditions are used on all four sides of the feed spacer. Figure 3.4 shows the geometry of the strand used for simulation. To prevent singularity error in the simulation, the spacer strand is assumed to dig into the membrane. If the spacer strand were to meet the membrane tangentially, the line contact between the strand and the membrane would causes singularity error. Thus in the simulations model, the strand diameter is chosen to be greater than half the channel width. This is the reason why the strand is not represented as a complete cylinder in Figure 3.4. Further, close examination of the feed spacer under a microscope (Figure 3.5) shows that the plastic deforms around the point where two strands meet. This deformation is approximated as a cylinder in the CFD simulation.

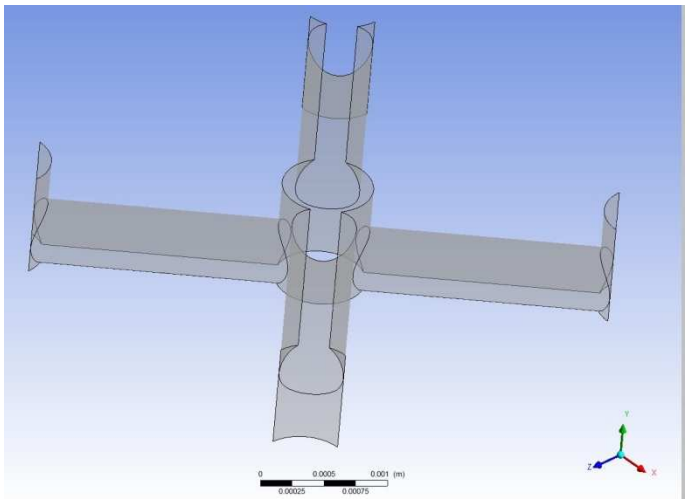

Figure 3.4: Modeling of the feed spacer strand

Figure 3.5: Appearance of a typical feed spacer under a microscope

To enable the use of geometric similarity and to create a generalized solution for spacers of different geometry, four representative feed-spacer geometries were chosen.

The geometric specifications for the four geometries chosen are shown in Table 3-2

Table 3-2: Dimensions of feed spacers used for the CFD simulation

Feed spacer	Spacer thickness (mil)	Distance between strands (mil)	Radius of the strand (mil)	Radius of center cylinder (mil)
1	20	100	5.71	8.11
2	25	100	7.14	10.14
3	30	100	8.57	12.17
4	35	100	10	14.20

Figures 3.6 to 3.9 show all the four geometries used to simulate a feed spacer.

When a feed spacer used in an RO application does not coincide with any of the four geometries mentioned in Table 3-2, the results for that spacer geometry is interpolated from the result from the simulation. For example, the results for a 28-mil spacer with 111-mil inter strand spacing will be similar to a 25-mil spacer ($\frac{28}{111}.100 =$ 25.2-mil exact) with 100-mil inter strand spacing.

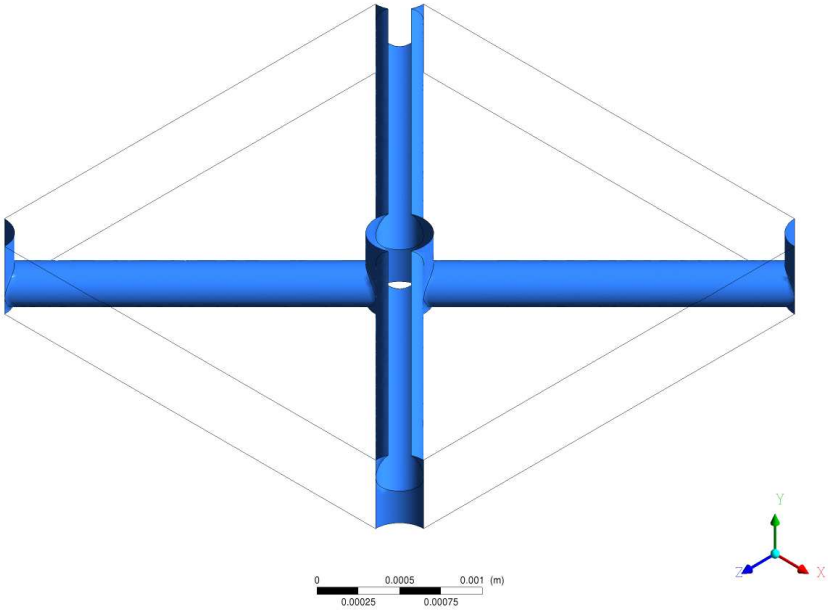

Figure 3.6: 20-mil feed spacer (Feed spacer 1)

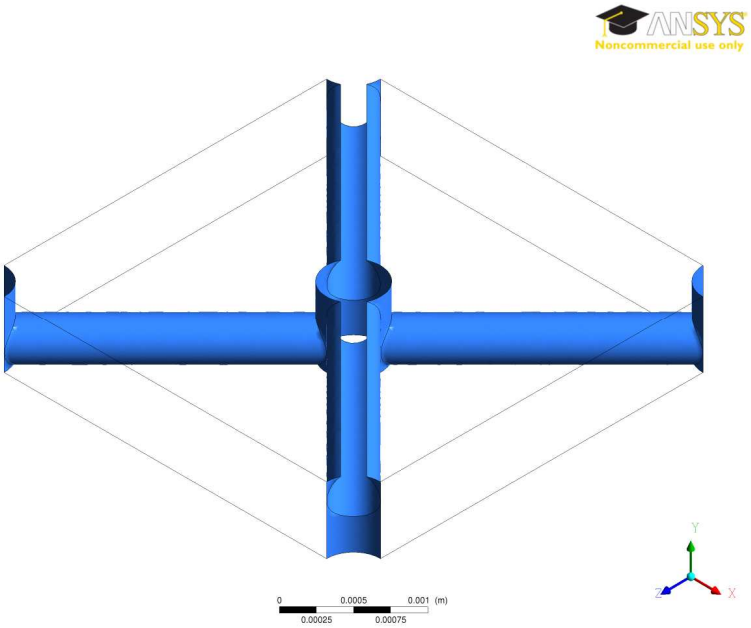

Figure 3.7: 25-mil feed spacer (Feed spacer 2)

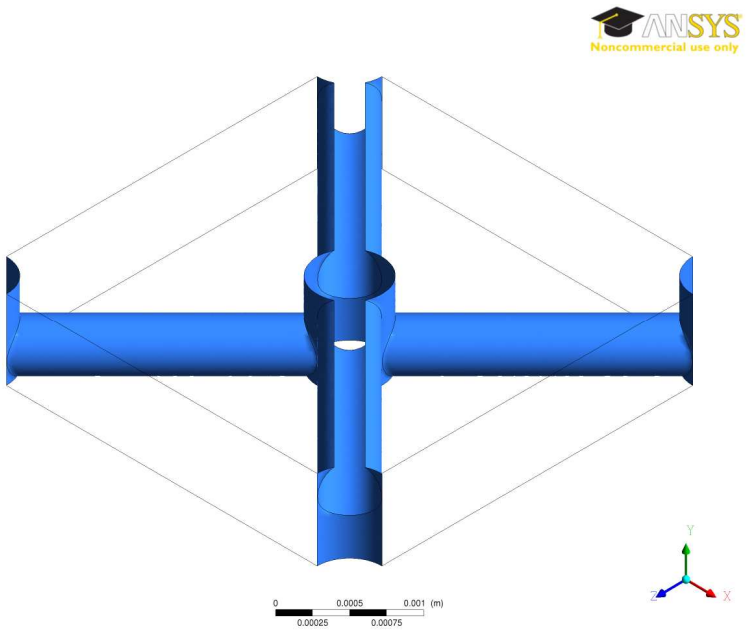

Figure 3.8: 30-mil feed spacer (Feed spacer 3)

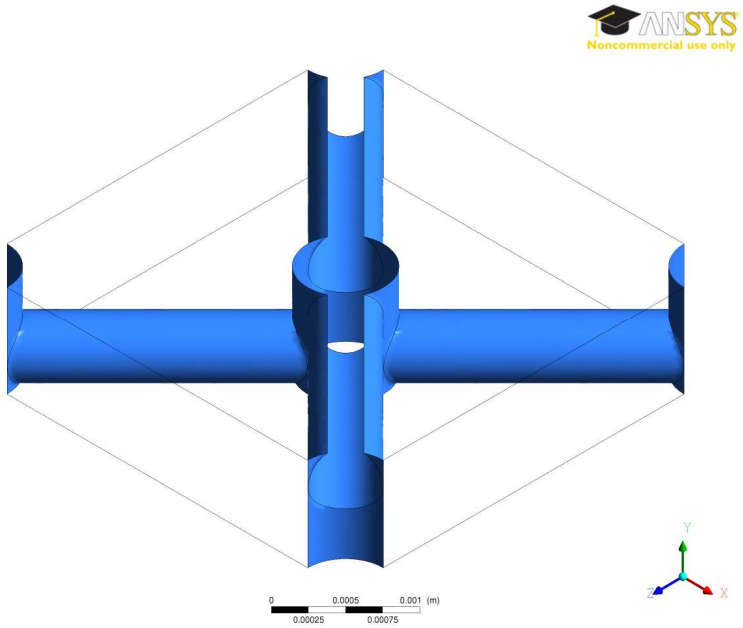

Figure 3.9: 35-mil feed spacer (Feed spacer 4)

3.4 Fluid flow and mass flow analysis

ANSYS CFX-14 was used to simulate the fluid flow and mass transfer in the feed spacer. The mass transfer of salt through the feedwater in the feed spacer is simulated as a thermal problem using the heat and mass transfer analogy. CFX is a commercially available computational fluid dynamics solver. It solves for mass, momentum and heat transfer equations iteratively.

The mass transfer equations are also referred to as the continuity equation.

$$\frac{\partial \rho}{\partial t} + \nabla.(\rho \vec{v}) = 0 \tag{3.1}$$

where ρ is the density of the fluid, t is the time, $\vec{v}$ is fluid flow velocity vector. The right hand side of the equation is zero as mass can neither be created nor be destroyed.

As the fluid flow is incompressible, the density is invariant. As there is no volumetric fluid source or sink, $\dot{m}$ is assumed zero. The removal of permeate water along the walls of the membrane is dealt as a special case.

$$\nabla.\vec{v} = 0 \tag{3.2}$$

The momentum conservation of the feedwater fluid flow is governed by the Navier-Stokes equation. Navier-Stokes equation is a derived from Newton's second law that relate force to acceleration.

$$\rho \frac{d}{dt}\vec{v} = -\nabla p + \mu \nabla^2 \vec{v} \tag{3.3}$$

where p is the static pressure, μ is the dynamic viscosity (the loss component of fluid flow), and $\vec{v}$ is the fluid flow velocity in vector form. The density is out of the differential because the density is invariant in the flow through feed spacer.

$\frac{d}{dt}\vec{v}$ is the complete differential of velocity by time-acceleration. It consists of two components- the unsteady acceleration and the convective acceleration.

$$\rho\left(\frac{\partial}{\partial t}\vec{v}+\vec{v}.\nabla\vec{v}\right)=-\nabla p+\mu\nabla^2\vec{v} \tag{3.4}$$

CFX uses Equation (3.4) to solve for an unsteady case. For a steady state simulation, $\frac{\partial}{\partial t}\vec{v}\rightarrow 0$

Mass transfer in fluid flow is governed by a mass conservation equation. This equation's constitutive equation is the Fick's law.

$$\frac{d}{dt}C=D.\nabla^2 C \tag{3.5}$$

where C is the concentration of solute (the species) in solvent given by mass of solute in the volume of solvent and D is the binary mass diffusion coefficient of the solute in solvent.

The left hand side of the equation shows the temporal dissipation of the species in solvent (advection) and the right hand side of the equation shows the spatial dissipation of said species (diffusion). As species is neither created nor destroyed, the LHS is equal to the RHS. In special cases where a species is added to the system on the boundary, a species-generation-rate term $\ddot{\sigma}$ is added to the RHS.

$$\frac{d}{dt}C = D.\nabla^2 C + \ddot{\sigma} \tag{3.6}$$

Similar to mass transfer heat transfer in fluid flow is governed by a specialized energy conservation equation Fourier law.

$$\rho.C_P.\frac{d}{dt}T = k.\nabla^2 T + \ddot{q} \tag{3.7}$$

where C_P is the specific heat capacity, T is the temperature, k is thermal diffusivity, and $\ddot{q}$ is the volumetric heat source/sink.

Equation (3.7) does not take into account the viscous dissipation of heat.

In both the equations $\frac{d}{dt}$ has an unsteady term and a convective term. Therefore, Equation (3.6) and Equation (3.7) can be rewritten as

$$\frac{\partial}{\partial t}C + \vec{v}.\nabla C = D.\nabla^2 C + \ddot{\sigma} \tag{3.8}$$

$$\frac{\partial}{\partial t}T + \vec{v}.\nabla T = \frac{k}{\rho C_P}.\nabla^2 T + \frac{\ddot{q}}{\rho C_P} \tag{3.9}$$

If the concentration is assumed to be invariant as a function of time,

$$\vec{v}.\nabla C = D.\nabla^2 C + \ddot{\sigma} \tag{3.10}$$

Similarly

$$\vec{v}.\nabla T = \frac{k}{\rho C_P}.\nabla^2 T + \frac{\ddot{q}}{\rho C_P} \tag{3.11}$$

$$\vec{v}.\nabla T = \alpha.\nabla^2 T + \frac{\ddot{q}}{\rho C_P} \tag{3.12}$$

where

$$\alpha = \frac{k}{\rho C_P} \tag{3.13}$$

where α is the thermal diffusivity.

The mass transfer is calculated by the very commonly used heat transfer and mass transfer analogy. From Equation (3.10) and Equation (3.11), one can observe the similarity the two equations have with each other. The temperature is analogous the concentration. The binary mass diffusion coefficient is analogous to the thermal diffusivity.

Table 3-3: Heat transfer-Mass transfer Analogy

Heat Transfer	Mass transfer
Temperature T	Concentration C
Heat transfer coefficient h	Mass transfer coefficient K
Thermal diffusivity α	Binary diffusion coefficient D
Thermal conductivity k	Binary diffusion coefficient D
Prandtl number Pr	Schmidt number Sc
Nusselt number $= \frac{hd_h}{k}$	Sherwood number $= \frac{Kd_h}{D}$

3.5 Mesh analysis

3D modeling of a feed spacer requires a very dense mesh. To enable the mesh to capture mass transfer near the membrane without significant numerical error or artifact, an array of inflation-layers is created around the spacer strands and at the membrane surface. Figure 3.10 shows an example of an inflation layer array.

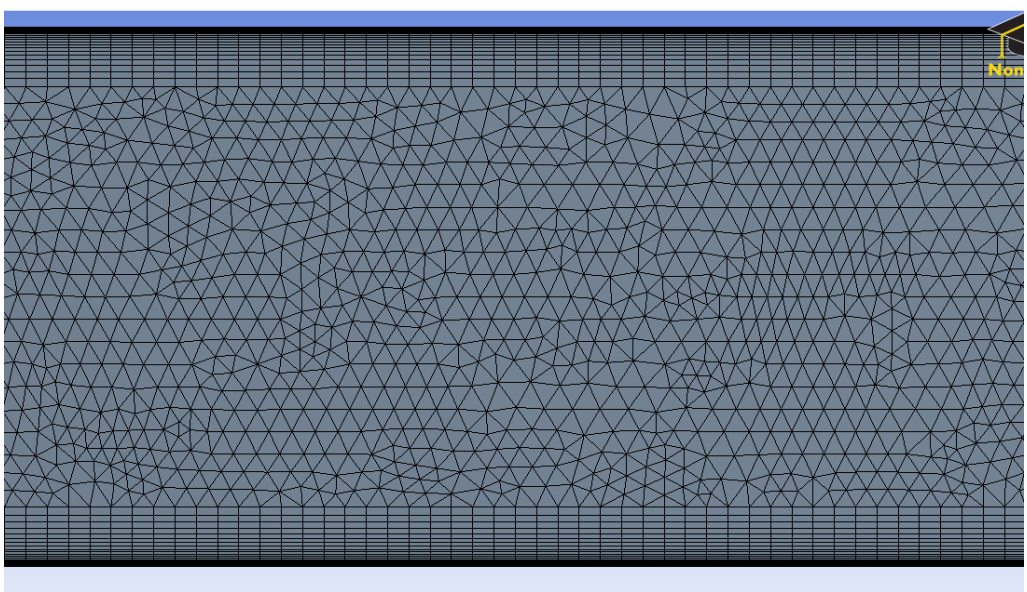

Figure 3.10: Close-up view of the inflation layers and the remaining mesh used in spacer simulation

Further, to ensure that the mesh is fine enough to yield reliable results yet not so fine, that it exceeds the available computational resources, a mesh independence study was conducted. For this purpose, two mesh densities were considered. The results from the mesh that is accepted for the final simulations are compared with those from finer mesh. The mesh independence study was carried out for a laminar flow model.

Low density Mesh	High Density Mesh
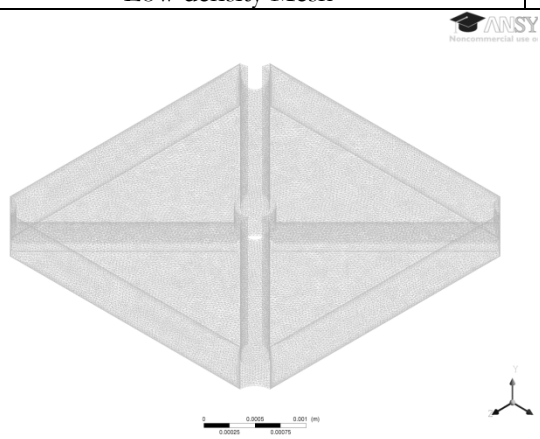	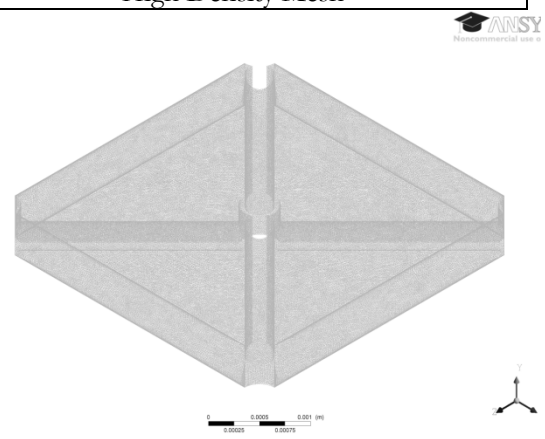
Nodes : 1,280,459 Elements: 401,145	Nodes : 1,676,224 Elements: 5,544,641
Applied pressure driving the flow: 100 Pa	
Mass flowrate in x direction: 2.49E-4 kg/sec	Mass flowrate in x direction: 2.51E-4 kg/sec
Percentage change in mass flowrate: 0.75%	

Figure 3.11: Mesh analysis of 20-mil feed spacer

Low density Mesh	High Density Mesh
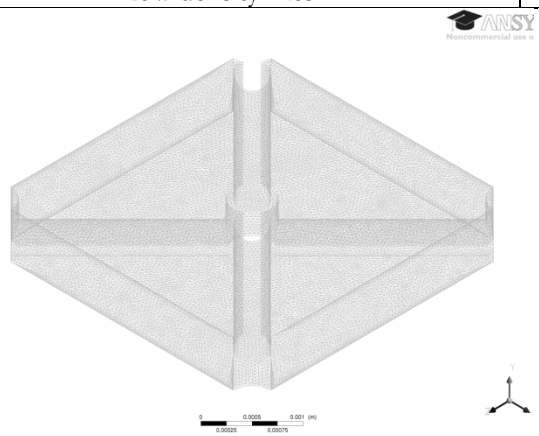	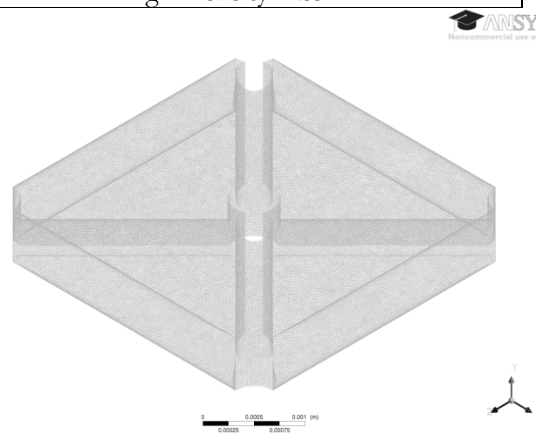
Nodes : 318,831 Elements: 1,115,964	Nodes : 1,010,626 Elements: 3,612,361
Applied pressure driving the flow: 100 Pa	
Mass flowrate in x direction: 3.26E-4 kg/sec	Mass flowrate in x direction: 3.28E-4 kg/sec
Percentage change in mass flowrate: 0.61 %	

Figure 3.12: Mesh analysis of 25-mil feed spacer

Low density Mesh	High Density Mesh
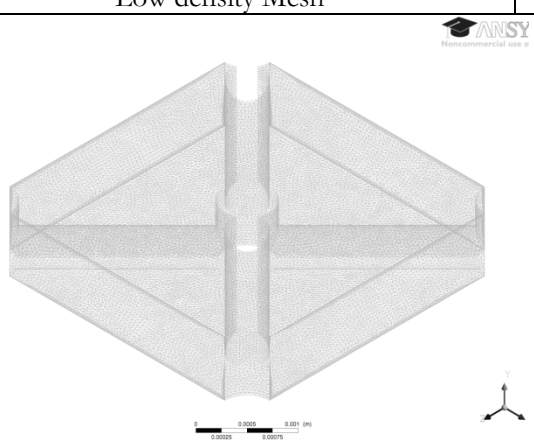	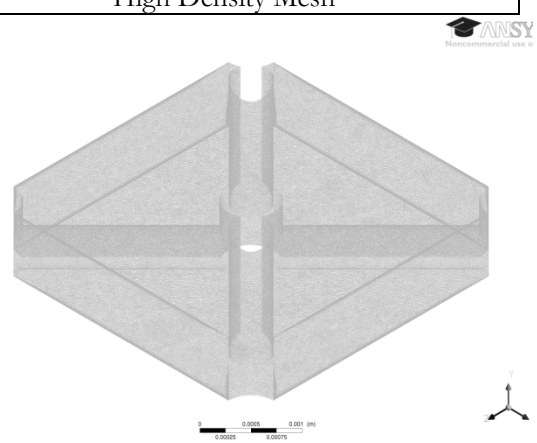
Nodes : 330,630 Elements: 1,142,661	Nodes : 2,545,387 Elements: 9,050,793
Applied pressure driving the flow: 100 Pa	
Mass flowrate in x direction: 3.90E-4 kg/sec	Mass flowrate in x direction: 3.88E-4 kg/sec
Percentage change in mass flowrate: 0.51 %	

Figure 3.13: Mesh analysis of 30-mil feed spacer

Low density Mesh	High Density Mesh
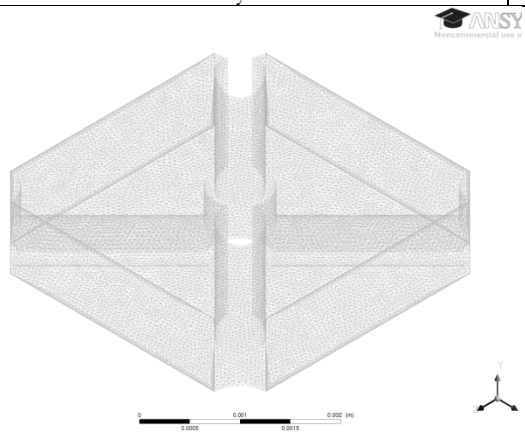	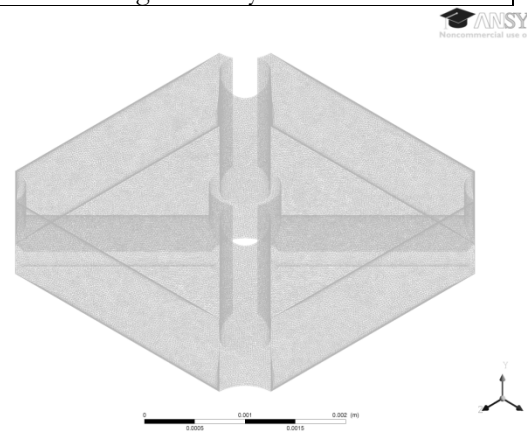
Nodes : 205,441 Elements: 689,011	Nodes : 1,575,838 Elements: 5,472,538
Applied pressure driving the flow: 100 Pa	
Mass flowrate in x direction: 4.68E-4 kg/sec	Mass flowrate in x direction: 4.65E-4 kg/sec
Percentage change in mass flowrate: 0.64 %	

Figure 3.14: Mesh analysis of 35-mil feed spacer

3.6 Analysis type

3.6.1 Laminar vs. Turbulence

To calculate the mesh independence a simple laminar, steady state assumption was made. Notwithstanding that, the following exercise was conducted to ensure that the flow dealt with here is laminar and steady. To analyze the situation, the flow domain was solved using *shear stress turbulence model* (SST) [74][75]. That model is used because the Reynolds number of the participating flow is very low, lower than the accepted transition number for internal flows (2300). The hydraulic-diameter Reynolds number calculated based on the spacer thickness is less than 1000. In the SST-based simulation, the value of the turbulent eddy viscosity μ_t was compared with the dynamic viscosity μ in the ratio μ_t/μ. If the ratio is much less than one, then the flow is largely laminar. Table 3-4 shows the results of this study for a driving pressure of 100 Pa.

Table 3-4: Analysis of the μ_t/μ. Ratio (Driving pressure = 100Pa)

Spacer Geometry	Reynolds Number	Eddy viscosity (Pa.s)	Dynamic viscosity (Pa.s)	Fraction of turbulence
1	176	4.57E-30	8.89E-4	0.00%
2	238	3.55E-26	8.89E-4	0.00%
3	295	6.05E-32	8.89E-4	0.00%
4	367	lower than machine epsilon	8.89E-4	0.00%

It is clear from the results shown in Table 3-4 that the fluid flow in the feed spacer is laminar.

3.6.2 Steady state vs. Transient

The flow through the feed spacer need not be steady. The bumpiness caused by the feed spacer strands will cause vortex shedding, and flow with vortex shedding will be unsteady. Even though the flow through the feed spacer is inherently unsteady, all analyzes of flow through feed spacers reported in the literature have assumed steady state. Here, the flow through the feed spacer is solved as both a steady-state problem and as a transient problem. The results obtained by the two methods are compared. If the flow is *macroscopically* steady, then the results from the steady state analysis and the transient analysis will yield comparable results. The initial condition for the transient flow is the simulation result obtained by solving the flow through the feed spacer in steady state.

For the transient analysis, the flow through the feed spacer was simulated for 0.2 seconds with a pressure difference driving the flow of 100 Pa. A simulation time of 0.2 sec is chosen because: for a pressure drop of 100 Pa, the bulk velocities of the flow through the spacers are 15.5, 16.7, 17.3, and 18.4 cm/sec for 20-, 25-, 30-, and 35-mil spacers respectively. The length of the *repeating unit* is 0.00359 m ($100\sqrt{2}$ mil). Therefore the times taken by the flow to traverse completely the length of the *repeating unit*s are- 0.023, 0.021, 0.020, and 0.019 sec for 20-, 25-, 30-, and 35-mil spacers respectively.

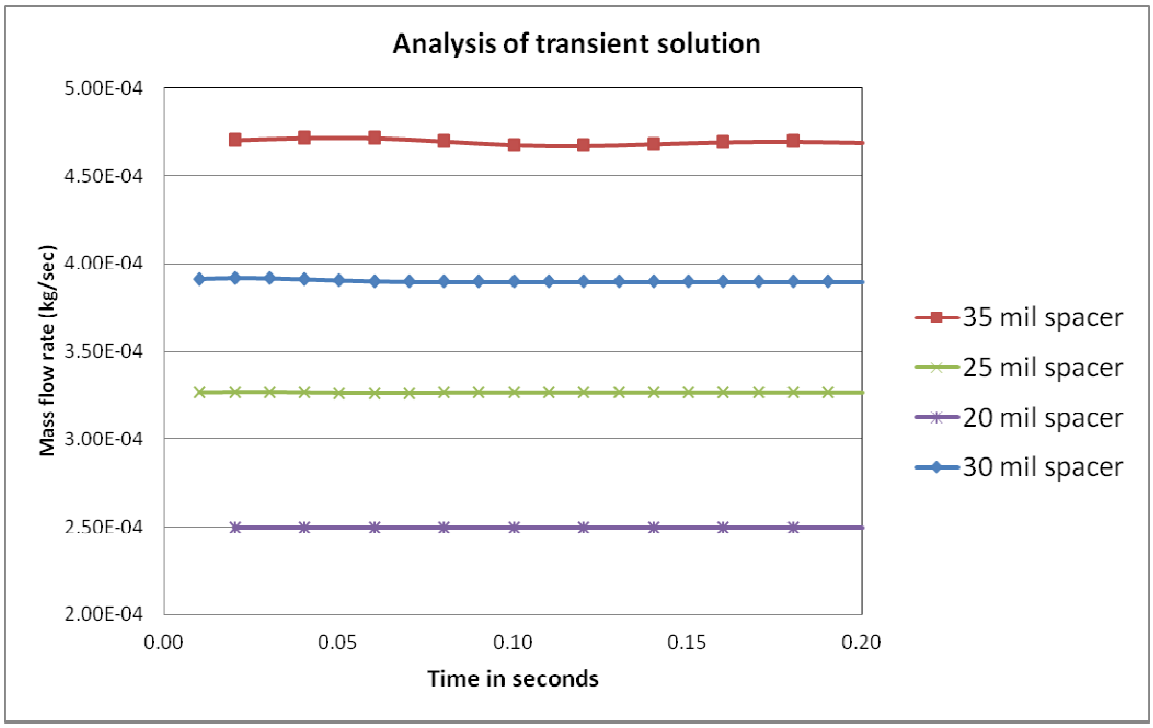

Figure 3.15: Plot of mass flowrate as a function of time

From Figure 3.15, it is seen that there is little or no change in the mass flowrate with time. The maximum percentage changes in mass flowrate for the 20-, 25-, 30-, and 35-mil screens are 0.03, 0.128, 0.477, and 0.977% respectively. The overall maximum change is less than 1%.

3.7 Fluid flow boundary conditions

Spatially periodic boundary conditions are used [76][77] in the simulation. Figure 3.16 (a) and (b) show the two sides where periodic boundary condition is used for the simulation. A zero pressure gradient is applied along the z-direction. This is shown in Figure 3.16 (b) by a two-headed arrow.

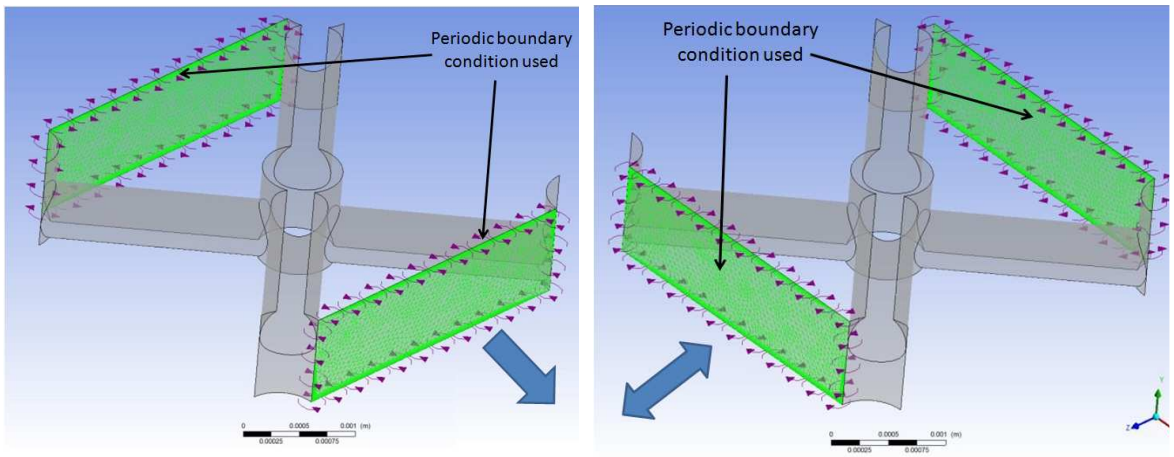

(b)

(a)

Figure 3.16: Boundaries were periodic boundary condition is used

A pressure difference is applied across one particular periodic boundary pairs to drive the flow of feedwater along the x-axis. The arrow in Figure 3.17 shows the direction of the pressure gradient. The two boundaries across which the pressure gradient is applied are shown in green. The wall boundary condition is applied on the strands that comprise the feed-spacer and on the membrane surfaces that comprise the top and bottom of the feed spacers.

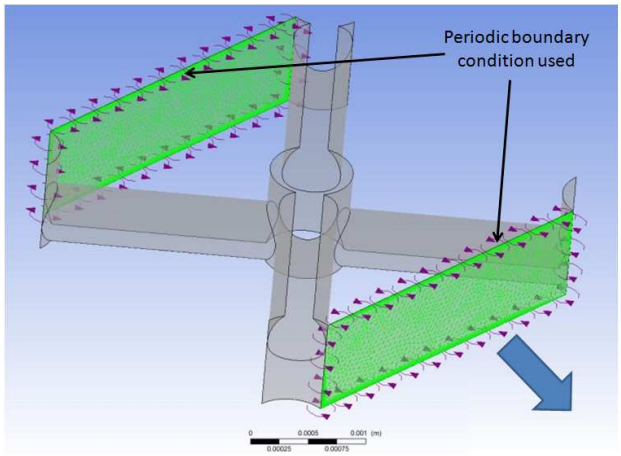

Figure 3.17: The pair of boundaries across with the pressure-difference driving the flow is applied

The membrane, shown in Figure 3.18, is simulated by a wall (no-slip) boundary condition. This is an approximation because the velocity of fluid flow near the wall of the membrane is not exactly zero. The velocity of the fluid flow along the wall of the membrane is given by the permeate flux through the membrane.

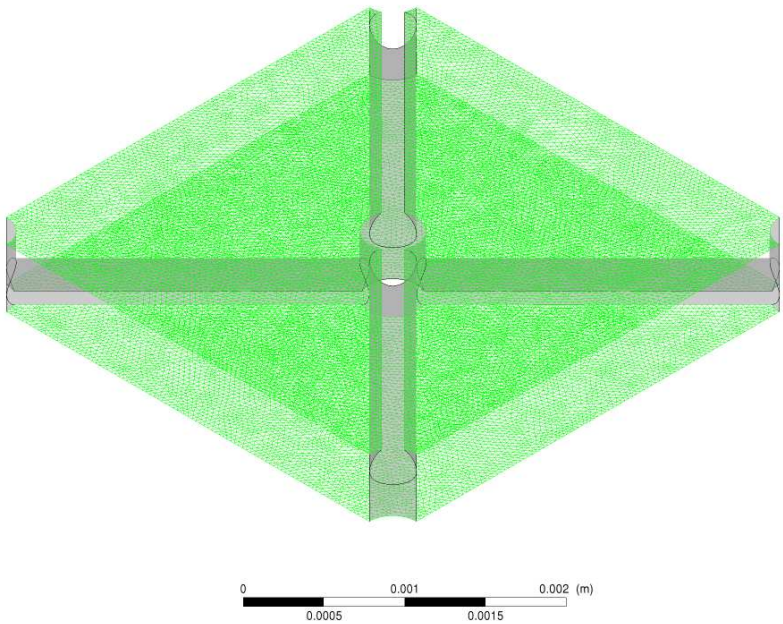

Figure 3.18: Boundary where the RO membranes is simulated

The rate of permeate flux through the membrane is obtained from Equation (2.16). J_w in Equation (2.16) has the units of velocity though it is expressed in gallons per square-foot per day GFD. One GFD is equal to 4.72E-7 meters per second m/s is

For elements with a typical permeate flux of 25 GFD, the value of wall velocity v_{memb} across the membrane is 1.18E-5 m/sec. This flow velocity across the membrane is insignificant compared to the cross flow velocity of the feedwater through the feed spacer ($v_{feed} = 15$ cm/sec). A rough calculation puts the cross flow velocity of feedwater through the feed spacer v_{feed} to be tens of thousands of times greater than the cross membrane permeate flow velocity v_{memb}.

To confirm through simulation that the trans-membrane velocity v_{memb} indeed has insignificant impact on the overall simulation results, a simulation was performed on a 20-mil feed spacer

geometry with trans-membrane velocity v_{memb} of 2E-5 m/sec (flowing outwards). It is theoretically impossible to establish a periodic boundary condition along the direction of the bulk feed flow (the x-axis) of the membrane because, the mass of water entering and leaving the periodically coupled domains are not the same. To overcome the above-mentioned problem, a simulation was initially run with no-slip boundary conditions on the membrane walls ($J = 0$ and $v_{memb} = 0$). For this case, a periodic boundary condition was used along the direction of the bulk feed flow (x-axis). A pressure difference driving the flow $\Delta P = 100$ Pa was applied across the *repeating unit*. The CFX code was solved until the residuals of mass and momentum converged to less than 1E-6. The velocity profile for the inlet region, shown in Figure 3.19, was obtained from this converged solution. The contour diagram of the velocity profile is shown in Figure 3.20. This velocity profile is used as the inlet conditions for the subsequent simulation where a non-zero traverse flow condition is imposed on the membrane surface ($J \neq 0$ and $v_{memb} = 2E-5$ (flowing out)). A periodic boundary condition is imposed across the z direction (The direction perpendicular to the bulk feed floe direction). An opening condition is imposed along downstream side of the *repeating unit* (shown in Figure 3.21). The opening-entrainment boundary condition allows the fluid to flow any direction and is unconstrained. The complete boundary condition detail is shown in Figure 3.22

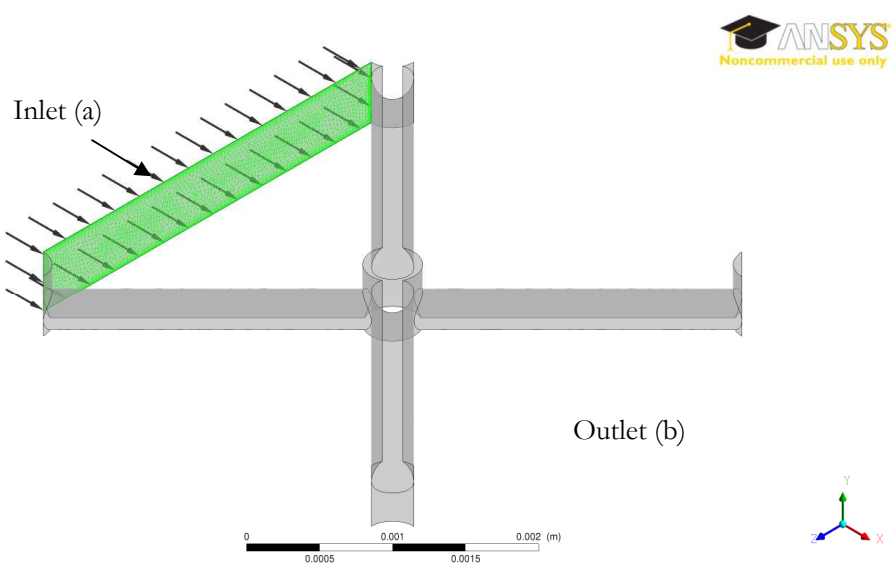

Figure 3.19: Inlet location in the upstream of the feed flow

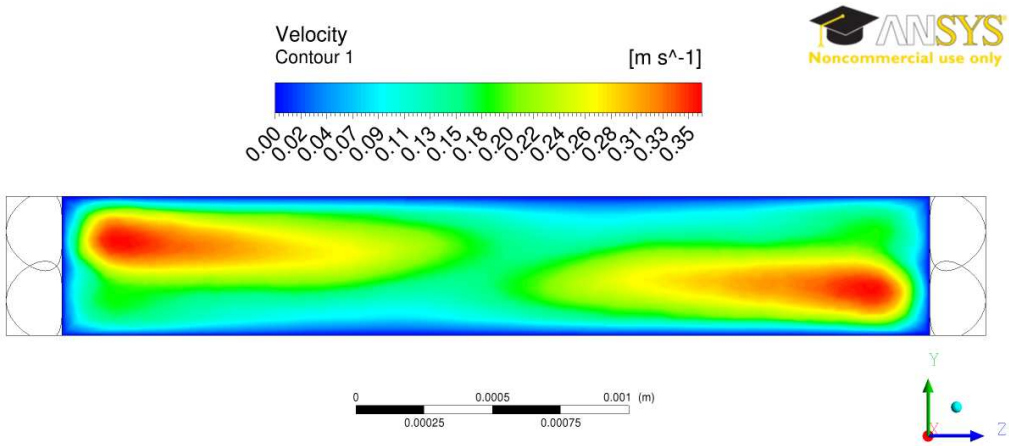

Figure 3.20: Velocity profile used at the inlet (a) shown in Figure 3.19

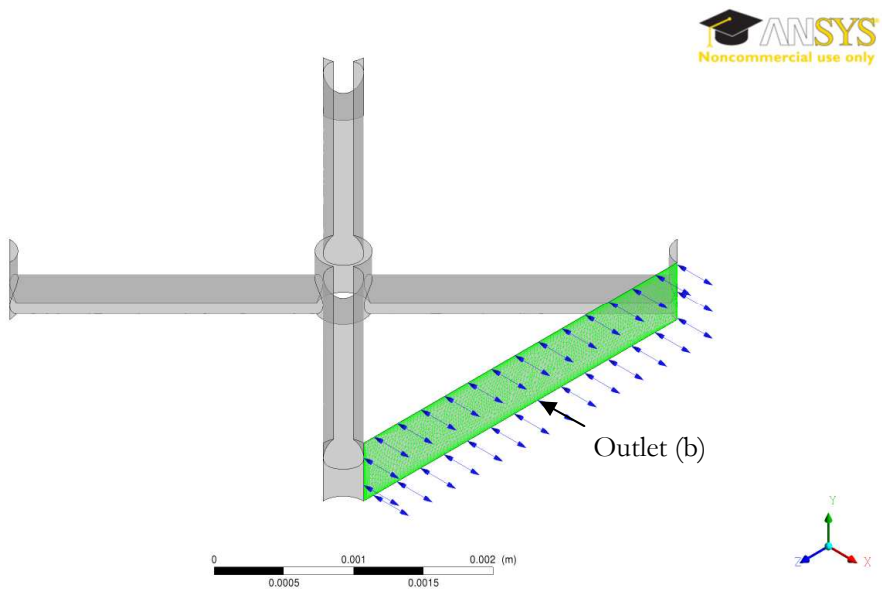

Figure 3.21: Outlet opening located downstream of the flow

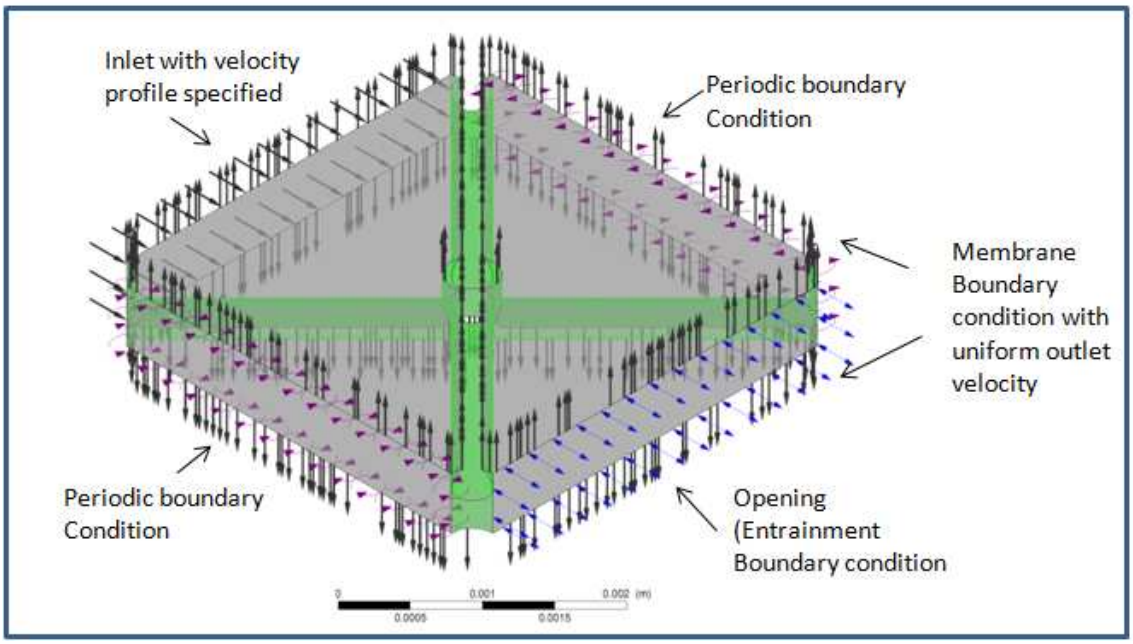

Figure 3.22: Pictorial representation of the boundary conditions used ($v \neq 0$)

With no-slip membrane boundary condition	**With v_{memb} = 2E-5m/sec membrane condition**
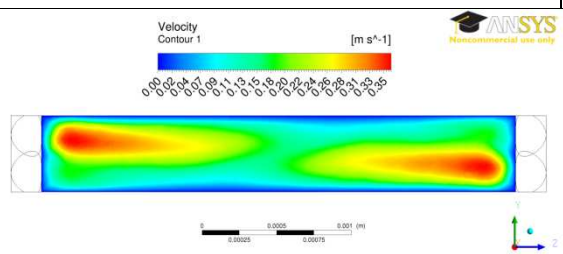	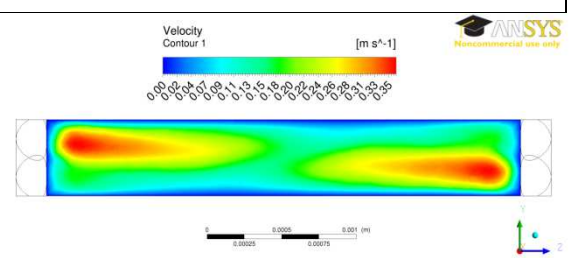
Velocity profile of the downstream opening (b)	Velocity profile of the downstream opening (b)
Mass flow outlet = 0.0002757 kg/sec	Mass flow outlet = 0.0002753 kg/sec
No significant change in flow pattern observed and the change in mass flowrate is 0.15%	

Figure 3.23: Comparison of no-slip wall and real membrane wall boundary conditions

Figure 3.23 shows the comparison in the results between no-slip wall conditions and the real wall conditions that would exist on the membrane boundary. The change in mass flowrate entering and exiting the *repeating unit* is insignificant (<0.5%) which in turn results in the difference between the solution of the two simulated conditions also insignificant.

3.8 Mass transfer in CFX simulation

The mass transport occurring in the feed spacer is simulated as a heat transport. ANSYS CFX-14.0 does not have the capability to solve heat transfer problems that involve periodic boundary condition. When the permeate devoid of salt is removed from the feedwater through the membrane, the salt that is rejected by the membrane is left on the feed side of the membrane. The process of removing purewater alone from the feedwater stream increases the concentration of salt in feedwater along the direction of the feed flow. This gradual increase in feedwater concentration along the direction of the feed flowrate is periodic similar to the pressure drop along the feed flow direction. This phenomenon is represented in CFX simulation as an increase in temperature along the direction of the flow. As CFX 14.0 is incapable of solving a periodic boundary condition, a method adopted by Patankar and Sparrow [78] is used to solve the periodic boundary condition.

3.8.1 Implementation of membrane wall boundary condition

For all the mass transfer simulations, a permeate flux of 30 GFD is assumed to flow across the membrane. The feedwater concentration is set at 2000 ppmw NaCl. 2000 ppmw is represented as 2000 K in the CFX simulation. The salt passage of the membrane is set at zero (100% rejection). The set concentration of the feedwater, the permeate flux across the membrane, or the salt passage through the membrane is irrelevant as only the Sherwood number of the flow is calculated as a result from the simulation.

The accumulation of salt on caused by the permeate flowrate is given by

$$\sigma = J.C_{bulk} \tag{3.14}$$

where σ is the mass of salt accumulated on the membrane surface per unit area (Mass flux of salt), J is the permeate flux and C_{bulk} is the bulk concentration of the feedwater.

The concentration of the salt in the feed channel is assumed to be in steady state. Therefore, the salt left behind on the membrane wall should be transported into the bulk stream by diffusion and advection. As the velocity of the feedwater on the membrane wall is not significant to transport this salt by advection, the salt is transported by diffusion alone. The diffusion of the salt is driven by the salt spatial concentration gradient. The value of spatial concentration gradient is given by $\dot{\sigma}$

$$D.\frac{d}{dt}C\Big|_{Membrane\,wall} = \dot{\sigma} \tag{3.15}$$

where D is the binary mass transfer coefficient of salt in water. C is the concentration of salt in water.

From Equation (3.14) and Equation (3.15),

$$\frac{d}{dt}C\Big|_{Membrane\,wall} = \frac{J.C_{bulk}}{D} \tag{3.16}$$

To simulate the mass transfer of salt in the feed stream caused by pure water permeate being extracted from the feedwater, the concentration gradient of the salt in the membrane wall is set at $\frac{J_w.C_{bulk}}{D}$.

This boundary is simulated as a constant heat flux condition on the membrane wall.

$$\frac{d}{dt}T\Big|_{Membrane\ wall} = \frac{\dot{q}}{k} \tag{3.17}$$

where $\dot{q}$ is the heat flux on the membrane surface.

3.8.2 Implementation of periodic boundary condition

As CFX-14.0 does not have the method to implement periodic boundary condition involving mass transfer. The periodic boundary condition is simulated by implementing a special variable that varies as a function of concentration in the feed spacer.

The feed spacer consists of repeating geometric element shown in Figure 3.3. Just as the pressure drops along the length of the feed spacer, the concentration of the feedwater increases along the length of the feed spacer. To solve mass transport as heat transport, ANSYS requires the temperature profile on the two boundaries that constitute the periodic boundary condition identical. As the walls that constitute the RO membrane in the simulation domain has a constant mass flux boundary condition that continuously increases the concentration of the feed flow, the concentration profile of the two boundaries will not be identical. Rather, the two boundaries will have a concentration profile that differs from each other by a constant value. This constant value determined by the flowrate of the feedwater and the flux on the membrane.

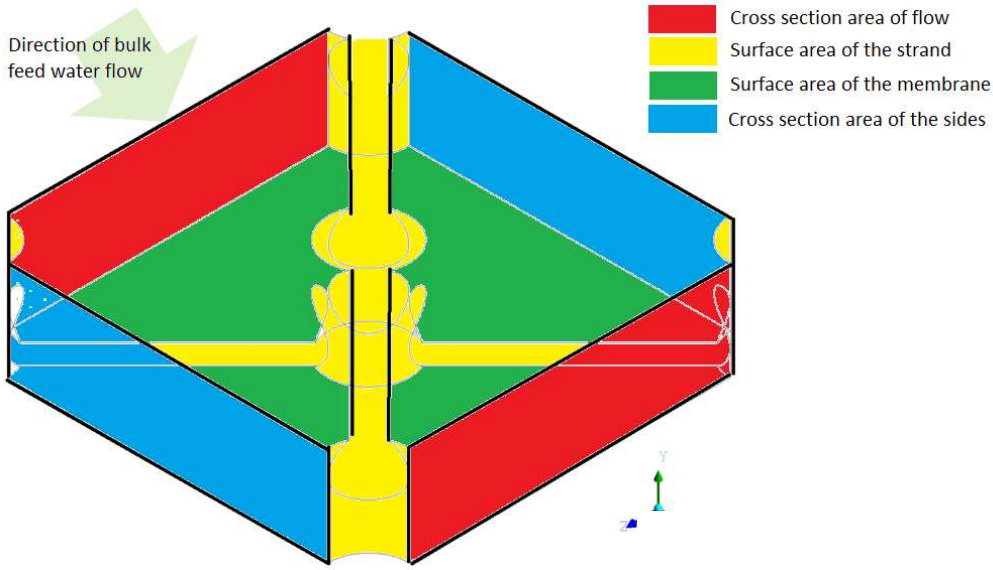

Figure 3.24: Picture showing the direction of flow along the x-axis

Let $\dot{m}$ be the mass of feedwater entering the and leaving the *repeating unit*, then the volumetric flowrate of feedwater entering and leaving the *repeating unit* is given by

$$\dot{V} = \frac{\dot{m}}{\rho} \tag{3.18}$$

where ρ is the density of the feedwater.

Let σ be the mass flux on the RO membrane surface, and A_{memb} be the area of the RO membrane surface. Then the increase in bulk concentration across one *repeating unit* is given by

$$\Delta C = \frac{\sigma . A_{memb}}{\dot{V}} \tag{3.19}$$

Let A_x be the cross section area of the flow (the area, whose area vector is parallel to the pressure gradient and x-axis). The dimensions of A_x is given by

$$A_x = d_{feed}.W \tag{3.20}$$

where d_{feed} is the thickness of the feed spacer and W is the width of the feed spacer *repeating unit*.

The surface area of the membrane A_{memb} is given by

$$A_{memb} = l.W \tag{3.21}$$

where l is the length of the membrane. In the simulation domain, l is the length of the *repeating unit* along which the feedwater flows. As the strand spacing in the simulation is set at 100-mil, the length l for the simulation is 141.42-mil.

The volume flowrate $\dot{V}$ can be broken into

$$\dot{V} = d_{feed}.W.v_{feed} \tag{3.22}$$

where v_{feed} is the bulk velocity of the feedwater flow though the feed spacer.

Substituting Equation (3.22) and Equation (3.21) in Equation (3.19)

$$\Delta C = \frac{\sigma . l . W}{d_{feed} . W . v_{feed}} \tag{3.23}$$

$$\Delta C = \frac{\sigma . l}{d_{feed} . v_{feed}} \tag{3.24}$$

The flow of feedwater though the feed spacer develops into a periodic flow due to the periodic nature of the feed spacer geometry, however, there is an entry length associated with the development of periodic nature of the flow. The periodicity of fluid flow property in the feed spacer leads to the periodic nature of the buildup of concentration along the direction of the feed flow.

$$C(x+l, y, z) = C(x, y, z) + \Delta C \qquad \text{for all } x \in [0, L-l] \tag{3.25}$$

where $C(x, y, z)$ is the concentration of the feedwater at location (x, y, z), x is a variable that determines the position along the x axis (the direction of feedwater flow), y and z are variables that determines the positions along the y and z axis, L is the total length of the feed spacer flow channel as against l being the length of the *repeating unit*. l is also known as the length of periodicity.

In a thermal fluid flow problem, this property of a periodic flow is expressed as

$$T(x+l, y, z) = T(x, y, z) + \Delta T \qquad \text{for all } x \in [0, L-l] \tag{3.26}$$

where $T(x, y, z)$ is the temperature of the fluid flow at location (x, y, z).

ΔT is given by

$$\Delta T = \frac{\dot{q}.l}{\rho.C_P.v_{feed}.d_{feed}} \tag{3.27}$$

The periodic boundary condition is invoked in the CFX simulation by introducing a new variable for concentration $\tilde{C}(x, y, z)$ that varies along the *repeating unit* as

$$\tilde{C}(x, y, z) = C(x, y, z) - \Delta C.\frac{x}{l} \qquad \text{for all } x \in [0, l] \tag{3.28}$$

$\tilde{C}(x, y, z)$ is defined only for the *repeating unit* that is chosen for the simulation. (x, y, z) can be any position that is defined within the simulation domain. The new variable for concentration carries a unique property that the value of concentration at $(x = l, y, z)$ is the same as the value at $(x = 0, y, z)$

$$\tilde{C}(x = l, y, z) = \tilde{C}(x = 0, y, z) \tag{3.29}$$

This property enables the implementation of periodic boundary condition in CFX simulation where a new variable $\tilde{T}(x, y, z)$ is defined as

$$\tilde{T}(x, y, z) = T(x, y, z) - \Delta T.\frac{x}{l} \qquad \text{for all } x \in [0, l] \tag{3.30}$$

Implementing this new variable in the governing Equation (3.10) and Equation (3.12)

In the mass transfer governing equation

$$\vec{v}.\nabla\left(\tilde{C}+\Delta C.\frac{x}{l}\right)=D.\nabla^2\left(\tilde{C}+\Delta C.\frac{x}{l}\right)+\sigma \tag{3.31}$$

As there is not volumetric mass add $\sigma = 0$ and by earranging the terms

$$\vec{v}.\nabla\tilde{C}+\frac{\Delta C}{l}\left(\vec{v}.\nabla x\right)=D.\nabla^2\tilde{C}+D\frac{\Delta C}{l}.\nabla^2 x \tag{3.32}$$

as $\nabla^2 x = 0$ an

$$\vec{v}.\nabla\tilde{C}+\frac{\Delta C}{l}\left(\vec{v}.\nabla x\right)=D.\nabla^2\tilde{C} \tag{3.33}$$

Equation (3.3) should be analysed in three coordinate directions x, y, and z.

$$v_x\frac{\partial\tilde{C}}{\partial x}+v_y\frac{\partial\tilde{C}}{\partial y}+v_z\frac{\partial\tilde{C}}{\partial z}+\frac{\Delta C v_x}{l}=D\left(\frac{\partial^2 C}{\partial x^2}+\frac{\partial^2 C}{\partial y^2}+\frac{\partial^2 C}{\partial z^2}\right) \tag{3.34}$$

where v_x, v_y, and v_z are the velocities components of feedwater along the x, y, and the z axis.

Rearranging Equation (3.34)

$$v_x \frac{\partial \tilde{C}}{\partial x} + v_y \frac{\partial \tilde{C}}{\partial y} + v_z \frac{\partial \tilde{C}}{\partial z} = D\left(\frac{\partial^2 \tilde{C}}{\partial x^2} + \frac{\partial^2 \tilde{C}}{\partial y^2} + \frac{\partial^2 \tilde{C}}{\partial z^2} \right) - \frac{\Delta C v_x}{l} \tag{3.35}$$

Because of the new implementation of the new variable $\tilde{C}$, a volumetric mass flow sink term $\frac{\Delta C v_x}{l}$ is introduced.

The implementation of the new variable $\tilde{C}$ also affects the boundary conditions.

The feed spacer strand does not take part in the mass transfer process like the membranes do. This means the gradient of concentration on the feed spacer strand should be zero. The gradient is zero because, the feed spacer strands have a no-slip flow conditions and no mass is either added or removed on the surface.

$$D.\left.\frac{\partial C}{\partial n}\right|_{wall} = 0 \tag{3.36}$$

where n is the unit vector normal to the surface.

By substituting $\tilde{C}$ in Equation (3.36)

$$D.\left.\frac{\partial}{\partial n}\left(\tilde{C} + \Delta C.\frac{x}{l} \right)\right|_{wall} = 0 \tag{3.37}$$

$$D.\frac{\partial}{\partial n}\tilde{C}+D.\frac{\partial}{\partial n}\Delta C.\frac{x}{l}\bigg|_{wall}=0 \tag{3.38}$$

$$D.\frac{\partial}{\partial n}\tilde{C}+\frac{D.\Delta C}{l}(\hat{n}.\hat{x})\bigg|_{wall}=0 \tag{3.39}$$

By moving the constant term to the right side of the equation a constant heat flux of $\frac{D.\Delta C}{l}(\hat{n}.\hat{x})$ is added on adiabatic surfaces. For RO membrane surfaces where mass transfer takes place $\frac{D.\Delta C}{l}(\hat{n}.\hat{x})+\dot{\sigma}$ of mass flux is added as the boundary conditions.

To summarize, A volumetric mass sink of $\frac{\Delta C v_x}{l}$ is implemented where v_x is the velocity of feedwater flowing in the x-direction (direction of pressure gradient).

The strands have a mass transfer of $\frac{D.\Delta C}{l}(\hat{n}.\hat{x})$ or $\frac{D.\Delta C}{l}\cos\theta$ where θ is the angle made by the surface vector with the x-axis. As the membranes make 90 degree with the x-axis $\cos\theta = 0$, therefore a flux of $\dot{\sigma}$ is implemented.

The above mass transfer equations are represented as heat transfer equation in CFX as

$$\vec{v}.\nabla\tilde{T}+\frac{\Delta T}{l}(\vec{v}.\nabla x)=\alpha.\nabla^2\tilde{T} \tag{3.40}$$

where the heat sink is given by $\frac{\Delta T}{l}(\vec{v}.\nabla x).\rho.C_p$ or $\frac{\Delta T v_x}{l}.\rho.C_P$

where ΔT is given by Equation (3.27), where v_{feed} is the bulk velocity given by

$$v_{feed} = \frac{\int_y \int_z v_x(x,y,z).dy.dz \Big|_{x=0}}{A_x} \tag{3.41}$$

where A_x of the equation is calculated from CFX using the CFX function calculator. The value of W is not the width of the simulation domain because, some parts of the simulation domain in the entrance and exit is blocked by the feed spacer strand.

The length of the *repeating unit* l is 141.42-mil or 0.003592 meters.

The value of heat flux $\dot{q}$ is set at one W/m². This value is immaterial as only the Sherwood number is noted as the output of the simulation.

The boundary condition for the feed spacer strand is given by

$$\phi = k.\frac{\Delta T}{l}\left(\hat{n}.\hat{x}\right) \tag{3.42}$$

where ϕ is the area heat flux, k is substituted as

$$k = D.\rho.C_p \tag{3.43}$$

where D is mass diffusivity of salt in water 1.5E-9 m²/sec, ρ is density of water set at 997 kg/m³ and C_p of water set at 4181 J/kg/K. and $(\hat{n}.\hat{x})$ is the cosine of the angle, the area vector of the strand makes with the x-axis.

3.9 Summary of fluid flow and mass transfer boundary conditions

3.9.1 Volume domain

Water at 25ºC is used as the medium. The dynamic viscosity of water is set at 8.899E-4 kg/m/sec. The thermal conductivity of water is changed to $D.\rho.C_p$ where the binary molecular diffusion coefficient D is set at 1.5E-9 m/sec, density ρ is set at 997 kg/m3, and specific heat capacity C_P is set at 4181 J/kg/K

A volumetric heat sink is established where

$$\ddot{q} = \frac{\dot{q}}{d_{feed}} . \frac{v_x}{v_{feed}} . \tag{3.44}$$

where $\dot{q}$ is set arbitrarily at unit value of 1W/m² and is set constant depending on the geometry that is used in the simulation. There are four different geometries used with d_{feed} at 20-, 25-, 30-, and 35-mil.

v_x is the velocity at location (x, y, z) obtained from the interim solution after every iteration solved by the CFX. v_{feed} is given by the Equation (3.41). The value of v_{feed} is updated every iteration by CFX.

3.9.2 Feed spacer opening

As shown in Figure 3.17, a periodic boundary condition for flow is set between the two boundaries and the flow is driven by pressure difference set by the user. The pressure difference varies from 10 Pascal to 400 Pascal. The pressure difference used for simulation are shown in Table 4-1 to Table 4-4

The other two openings that constitute the sides of the feed spacer flow, shown in Figure 3.24 in blue color, also have a periodic boundary condition with no pressure difference.

The strands of the feed spacer, shown as thick blue lines in Figures 3.6 through 3.9 carries a no-slip wall boundary condition. The heat flux on the wall is set as

$$\phi = D.\frac{\dot{q}}{v_{feed}.d_{feed}}\left(\hat{n}.\hat{x}\right) \tag{3.45}$$

where $\left(\hat{n}.\hat{x}\right)$ is the cosine of the angle the strand makes with the x-axis. As feed spacer strands are completely encapsulated inside the simulation domain, the area integral of ϕ over all the feed spacer strand surface is zero. This no heat is added or removed by the strands in whole.

3.9.3 RO membrane boundary condition

A no-slip wall fluid boundary condition is set and the boundaries that simulate the RO membrane. A heat flux of $\dot{q}$ is set on the membrane boundary surface to simulate the removal of water and the deposition of salt on the membrane surface. As discussed earlier, the value of $\dot{q}$ is set at unity.

3.10 Post processing of output from simulations

The simulations are run until the residuals reached 1E-6 for the flow and 1E-5 for the thermal parameters. The mass flowrate across the cross section area of flow $\dot{m}$ (shown in Figure 3.24) is noted as an observation.

The bulk velocity v_{feed} is calculated by

$$v_{feed} = \frac{\dot{m}}{\rho A_x} \tag{3.46}$$

where A_x as discussed earlier is the area of cross section of the flow calculated from the CFX function calculator.

The hydraulic diameter of the channel d_h is calculated similar to that of a parallel plate channel.

$$d_h = 2 \times spacerthickness \tag{3.47}$$

The Reynolds number is calculated from the hydraulic diameter

$$\mathrm{Re} = \frac{\rho . v_{feed} . d_h}{\mu} \tag{3.48}$$

where μ is the viscosity of the feedwater.

The *pressure drop factor f* is calculated from the applied pressure difference.

$$f = \frac{d_h}{l} \frac{2\Delta P}{\rho . v_{feed}^{\ 2}} \tag{3.49}$$

The Sherwood number of the flow is calculated from the area average temperature of the RO membrane boundary condition and the volumetric average temperature of the simulation domain.

The area average temperature of the RO membrane boundary is calculated from the CFX function calculator using the following formula.

$$T_{area\ average}\Big|_{Membrane} = \frac{\iint_{RO\ membrane} T(x, y, z).dx.dz}{A_{RO\ membrane}} \tag{3.50}$$

The volume average temperature of the simulation domain is calculated from the CFX function calculator using the following formula.

$$T_{volume\ \ average}\Big|_{Domain} = \frac{\iiint_{CFX\ \ domain} T(x,y,z).dx.dy.dz}{V_{CFX\ \ simulation\ \ domain}} \tag{3.51}$$

The Sherwood number is similar to Nusselt number. The Nusselt number Nu is defined as

$$Nu = \frac{h.d_h}{k} \tag{3.52}$$

where k is thermal diffusivity coefficient of the conduction coefficient and the heat transfer coefficient h is given by

$$h = \frac{\dot{q}}{T_{area\ \ average}\Big|_{Membrane} - T_{volume\ \ average}\Big|_{Domain}} \tag{3.53}$$

where $\dot{q}$ is the heat flux per unit area

Substituting Equation (3.53) in Equation (3.52). The Nusselt number is given by

$$Nu = \frac{\dot{q}.d_h}{k.\left(T_{area\ \ average}\Big|_{Membrane} - T_{volume\ \ average}\Big|_{Domain}\right)} \tag{3.54}$$

The value of k is given by Equation (3.43).

The Nusselt number calculated is the Sherwood number for mass transfer of the flow from dimensionless similarity.

$$Sh = Nu \tag{3.55}$$

The Sherwood number is used to calculate the concentration polarization.

The concentration polarization, defined in Equation (2.6), is calculated from the Sherwood number.

Substituting Equation (2.7) and Equation (3.14) in Equation (2.8)

$$Sh = \frac{J.C_{bulk}.d_h}{D.(C_{wall} - C_{bulk})} \tag{3.56}$$

Dividing the numerator and the denominator of the RHS by C_{bulk} and substituting Equation (2.6)

$$Sh = \frac{J.d_h}{D.(CP - 1)} \tag{3.57}$$

Rearranging the terms

$$CP = 1 + \frac{J.d_h}{D.Sh} \tag{3.58}$$

The Equation (3.58) is valid for cases where the salt passage SP of the membrane in 0. For case with finite salt passage the concentration polarization is given by

$$CP = 1 + \frac{J.d_h}{D.Sh}(1 - SP) \tag{3.59}$$

Another parameter that will help to determine the mixing property in the feed spacer is the mass transfer Stanton number. The Stanton number arises in the consideration of the geometric similarity of the momentum boundary layer and the mass transfer boundary layer, where it can be used to express a relationship between the shear force at the wall (due to viscous drag) and the total mass transfer at the wall (due to molecular diffusion). The Stanton number St is given by dividing the Sherwood number by the Reynolds number and the Schmidt number.

$$St = \frac{Sh}{\mathrm{Re}.Sc} \tag{3.60}$$

Chapter 4 : CFX SIMULATION RESULTS

4.1 Introduction

The results from the CFD simulations are presented and discussed in this chapter. A detailed analysis of the effect of feedwater flow on pressure drop along the length of the RO element is provided. Further, an exposition of the mixing that the feed spacer provides to reduce the concentration polarization is given. The streamlines of the feedwater flow through the feed spacers are displayed to illustrate the complexity of the flow.

4.2 Results of feed spacer pressure drop from simulations

A total of 84 simulations were conducted on various feed spacer geometries to simulate the fluid flow and verify the same for mesh independence and time-scale independence of the results. Tables 4-1 to 4-4 show the main practical results of the fluid flow simulations. The Reynolds number and the *pressure drop factor* are defined by Equations (3.48) and (3.49) respectively. The driving pressure difference is applied across a single *repeating unit*. The display of the *repeating unit* is shown in Figure 3.4).

Table 4-1: Flow pressure-drop analysis 20-mil spacer

20-mil spacer				
Driving pressure difference (Pa) [INPUT]	**Mass flow (kg/sec) [OUTPUT]**	**Reynolds number**	**Feed velocity (m/sec)**	**Pressure drop factor**
25	8.64E-05	61	0.054	4.93
50	1.51E-04	107	0.094	3.24
75	2.04E-04	144	0.126	2.66
100	2.49E-04	176	0.155	2.37
150	3.27E-04	231	0.203	2.06
300	5.12E-04	362	0.318	1.68
450	6.61E-04	467	0.410	1.52

To enable the simulation of the flow in the 20-mil spacer to a Reynolds number of up to 400, the range of driving pressure difference for a 20-mil spacer is increased to 450 Pa. The feed velocity is the representative bulk velocity of the feedwater in the feed spacer. The realistic feed flow velocities in a feed spacer is around 5-15 cm/sec

Table 4-2: Flow pressure-drop analysis 25-mil spacer

25-mil spacer				
Driving pressure difference (Pa) [INPUT]	**Mass flow (kg/sec) [OUTPUT]**	**Reynolds number**	**Feed velocity (m/sec)**	**Pressure drop factor**
10	6.05E-05	44	0.031	7.36
15	8.49E-05	62	0.044	5.61
25	1.27E-04	92	0.065	4.20
50	2.07E-04	151	0.106	3.13
75	2.71E-04	198	0.139	2.74
100	3.26E-04	238	0.167	2.53
150	4.19E-04	306	0.215	2.30

Table 4-3: Flow pressure-drop analysis 30-mil spacer

30-mil spacer				
Driving pressure difference (Pa) [INPUT]	**Mass flow (kg/sec) [OUTPUT]**	**Reynolds number**	**Feed velocity (m/sec)**	**Pressure drop factor**
10	7.59E-05	57	0.034	7.54
15	1.05E-04	79	0.046	5.96
25	1.53E-04	116	0.068	4.62
50	2.49E-04	189	0.110	3.49
75	3.25E-04	246	0.144	3.08
100	3.90E-04	295	0.173	2.86
150	5.03E-04	380	0.222	2.58

Table 4-4: Flow pressure-drop analysis 35-mil spacer

35-mil spacer				
Driving pressure difference (Pa) [INPUT]	**Mass flow (kg/sec) [OUTPUT]**	**Reynolds number**	**Feed velocity (m/sec)**	**Pressure drop factor**
10	8.26E-05	65	0.032	9.41
13	1.13E-04	89	0.045	6.50
17	1.38E-04	108	0.054	5.73
25	1.83E-04	143	0.072	4.80
50	3.04E-04	238	0.119	3.49
75	3.95E-04	309	0.155	3.10
100	4.68E-04	367	0.184	2.93
150	5.92E-04	463	0.233	2.75

To enable the simulation of low Reynolds number (Re = 50) flow in a 35-mil spacer, the driving pressure difference is reduced to 10 Pa. Though a feed flow of 3 cm/sec is unrealistic, this flow regime is simulated and analyzed to present a complete comprehensive analysis.

From an inspection of these tables, it can be seen that the range of driving pressure differences is not the same for all the spacers. Rather, the values of the driving pressure drop were selected to provide a desired range of the Reynolds number.

4.3 Analysis of feed spacer pressure drop

In general, the tables show that the feed velocity increases monotonically with increasing values of the driving pressure difference. In contrast, the *pressure drop factor*, which includes the quantity $1/v^2$, decreases.

The results conveyed in the foregoing tables are given clearer meaning when displayed in graphical form, and Figures 4.1 through 4.4 have been prepared for this purpose. Figure 4.1 shows the relationship between the driving pressure difference and the feed velocity for all of the feed spacers.

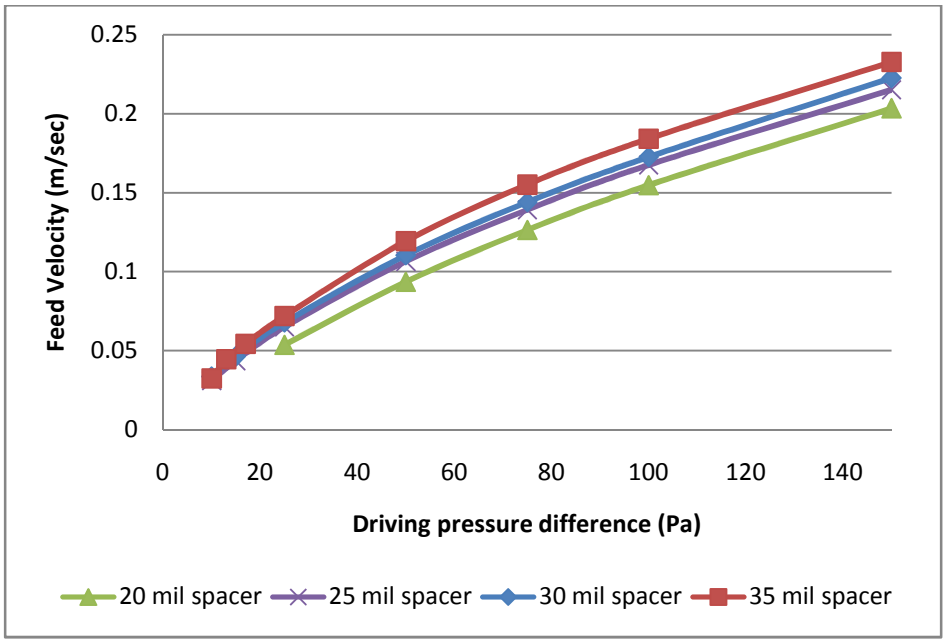

Figure 4.1: Dependence of the feed velocity on the driving pressure difference

Inspection of the figure reveals that the feed velocity increases with increasing values of the driving pressure difference. The rate of increase is greatest at the lower values of the driving pressure difference but diminishes as the driving pressure difference increases. At the higher values of the driving pressure difference, a nearly linear relationship sets in. Further examination of the figure shows that higher values of the feed velocity are achieved with increasing spacer size. The spread among the feed velocity magnitudes is greatest at the higher driving pressure differences.

The specification of the driving pressure is tantamount to specifying the pressure gradient along the feedwater flow in the feed spacer. The pressure gradient P_{drop} is calculated from

$$P_{drop} = \frac{\Delta P}{l} \tag{4.1}$$

where ΔP is the driving pressure difference and l is the length of the *repeating unit*. The value of l is 0.00359 meters.

In Equation (2.3), it was hypothesized that the pressure drop along the feed spacer will have both linear and quadratic terms. That representation is designated as the Forchheimer model. To investigate the conformity of the simulation data to the Forchheimer model, a graph of $\frac{P_{drop}}{v_{feed}}$ vs. v_{feed} may be plotted for all the feed spacers and is displayed in Figure 4.2. The resulting straight lines appearing in the figure verify that the pressure drop results for the individual spacers conform to the model. Least-squares linear equations representing the results are listed beneath the figure.

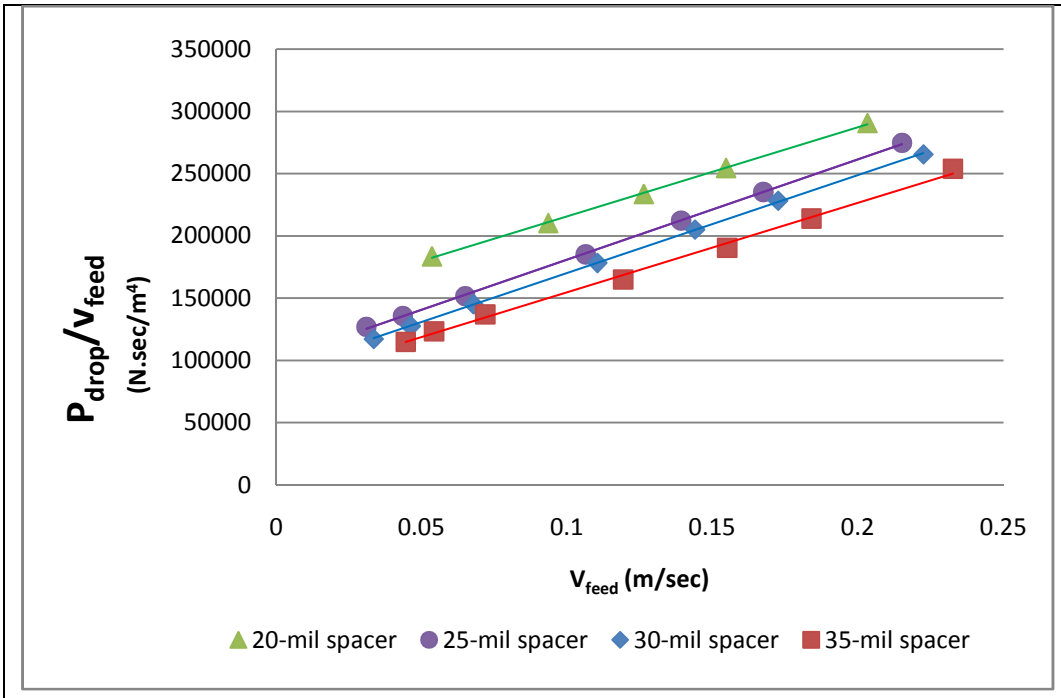

20-mil spacer	$P_{drop} = 143962.v_{feed} + 716607.v_{feed}^{2}$
25-mil spacer	$P_{drop} = 100248.v_{feed} + 805689.v_{feed}^{2}$
30-mil spacer	$P_{drop} = 91288.v_{feed} + 787396.v_{feed}^{2}$
35-mil spacer	$P_{drop} = 82643.v_{feed} + 718928.v_{feed}^{2}$
where P_{drop} is measured in N/m³ and v_{feed} is measured in m/sec	

Figure 4.2: Pressure drop/velocity vs. velocity

The existence of a slope and an adequate straight-line fit adds credibility to the claim that that Forchheimer model is more appropriate to evaluate the feed spacer pressure drop than a mere exponential model (Equation (2.4))

In Figure 4.3, the non-dimensional *pressure drop factor* f is plotted as a function of Reynolds number. Note that the factor includes the square of the velocity in its denominator, so that $f = C_3 + \frac{C_4}{\mathrm{Re}}$. Clearly, at small Re, the second term dominates, while for large Re, the constant term dominates. The data of Figure 4.3 is also presented in a log-log format in Figure 4.4, but the re-plot does not provide further insights.

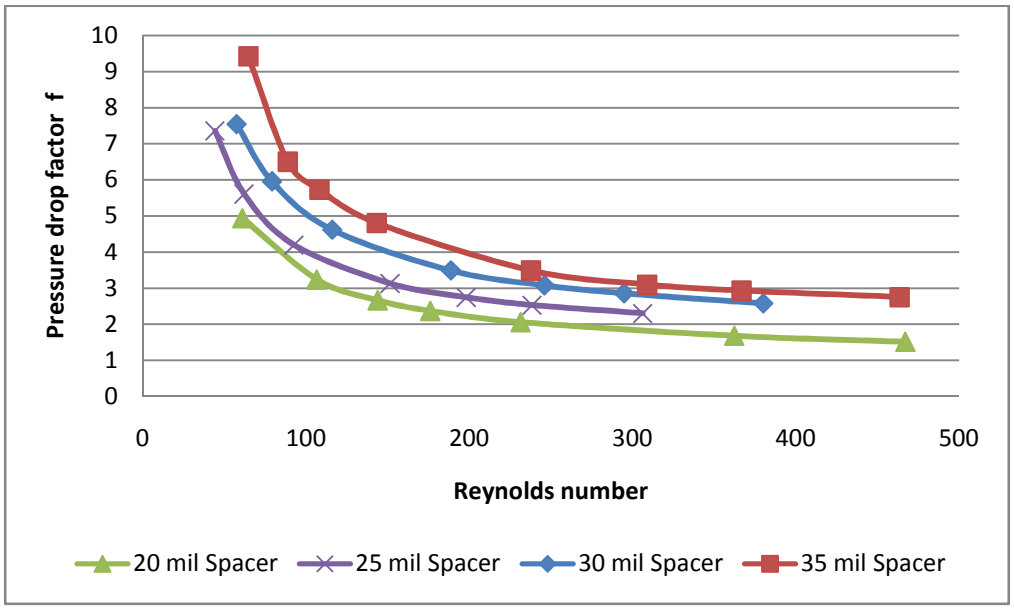

Figure 4.3: Pressure drop factor vs. Reynolds number

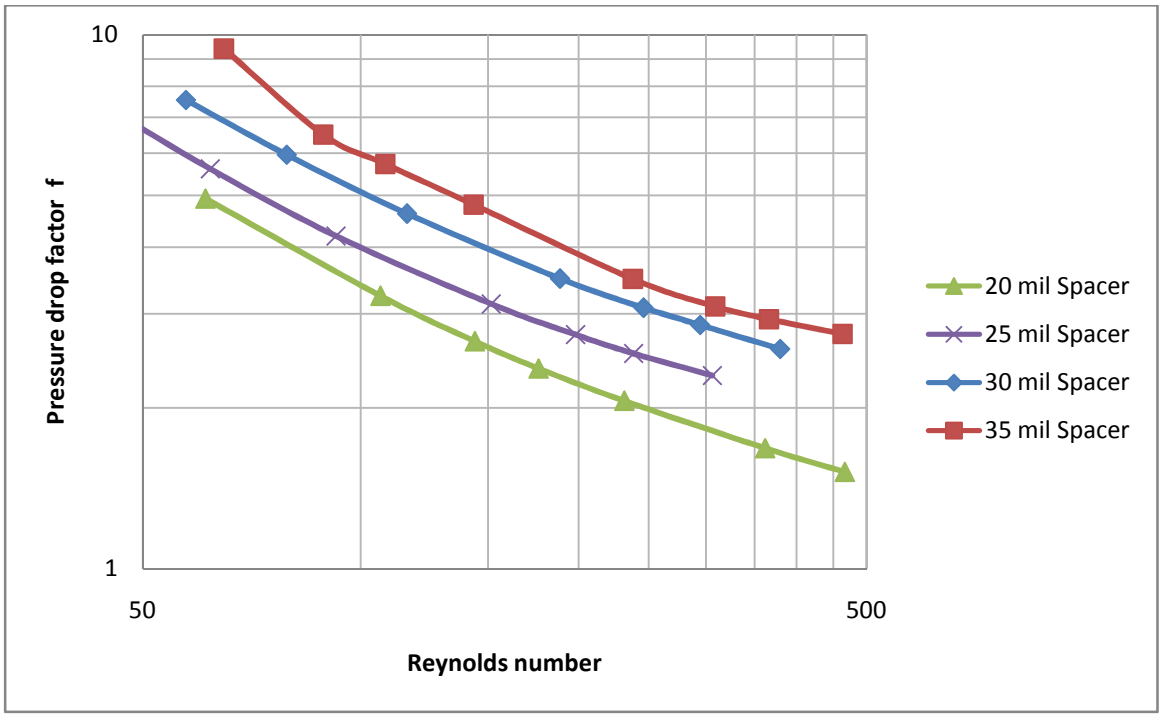

Figure 4.4 Log-log graph of Pressure drop factor vs. Reynolds number

4.3.1 Correlation of pressure drop results

The key goal of this section is to analyze the information portrayed in Figure 4.3 and to correlate it in a compact manner. The proposed correlation model is shown in Equation (4.2).

$$f = \left[a\left(\frac{\mathrm{Re}}{\alpha}\right)^{b} - \beta \right] X^{\gamma} \tag{4.2}$$

where a, b, α, β, and γ are parameters that relate the pressure drop to the Reynolds number for any simple feed spacer with a strand angle of 90°, and X is a dimensionless spacer *geometry factor* given by

$$X = \frac{thickness\ \ of\ \ the\ \ spacer}{space\ \ between\ \ the\ \ strands} \tag{4.3}$$

a is Reynolds number coefficient

b is Reynolds number exponent

α is Reynolds number scaling factor

β is constant correction factor

γ is the *geometry factor* exponent

The parameters a , b , α, β, and γ were varied to fit the data shown in portrayed in Figure 4.3.The resulting values of a , b , α, β, and γ are

Table 4-5: The value of pressure drop parameters

a	Reynolds number coefficient	1719
b	Reynolds number exponent	-0.935
α	Reynolds number scaling factor	0.657
β	constant correction factor	-5.77
γ	*geometry factor* exponent	1.182

so that

$$f = \left[1719 \left(\frac{\mathrm{Re}}{0.657} \right)^{-0.935} + 5.77 \right] X^{1.182} \tag{4.4}$$

This equation has been plotted in Figure 4.5 along with the numerical data, and very good agreement is in evidence.

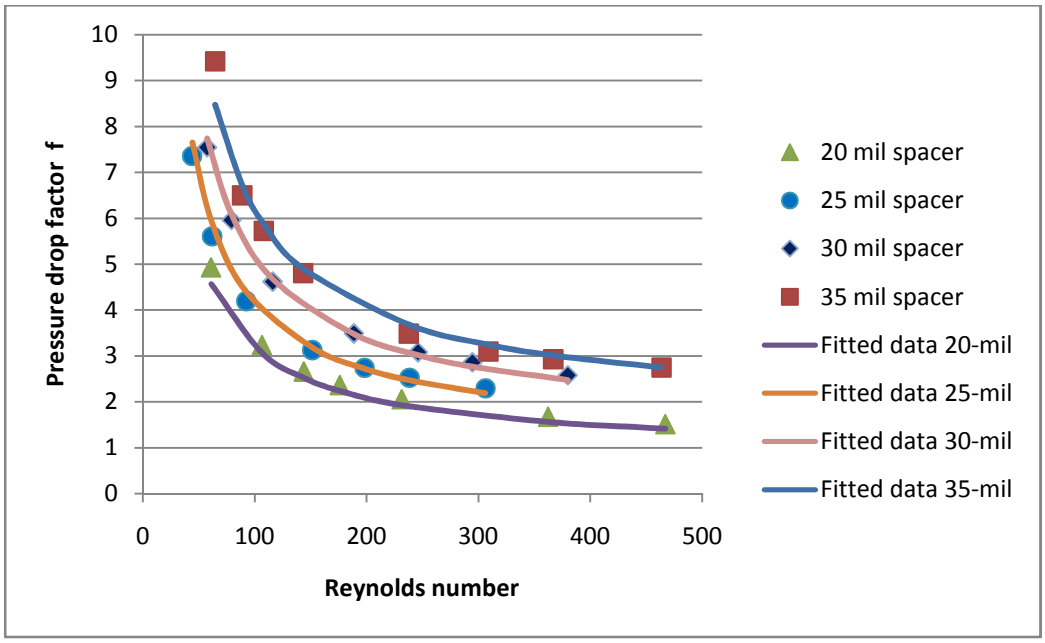

Figure 4.5: Plot of simulation data and the correlation equation

With the Equation (4.4), the pressure-drop-factor across any 90° feed spacer can be determined.

It may be observed that the exponent b of the Reynolds number is -0.935 ≈ -1.0. The exponent of (-1) has a significance because $\frac{1}{\text{Re}}$ corresponds to the friction term (Darcy term) in the Forchheimer model.

Another observation is that value of the constant correction or the zero correction for the *pressure drop factor* βX^{γ} is the Forchheimer coefficient.

Finally, were the Reynolds number exponent to be approximated to the nearest whole number as $b = -1$, the two additive terms in Equation (4.4) would represent the Darcy and Forchheimer coefficients. Therefore, an effort was made to solve for a, α, β, and γ while keeping $b = -1$.

The new values for a , α, β, and γ are

Table 4-6: Revised values of pressure drop parameters

a	Reynolds number coefficient	1719
α	Reynolds number scaling factor	0.868
β	constant correction factor	-9.33
γ	*geometry factor* exponent	1.19

so that the new equation for the *pressure drop factor* f is given by

$$f = \frac{1493}{\mathrm{Re}} X^{1.19} + 6.60 X^{1.19} \tag{4.5}$$

where $\frac{1493}{\mathrm{Re}} X^{1.19}$ is the Darcy Coefficient and $6.60 X^{1.19}$ is the Forchheimer coefficient.

when this equation is plotted in Figure 4.6, it is evident that the modified correlating equation is as good a representation as was the original correlation.

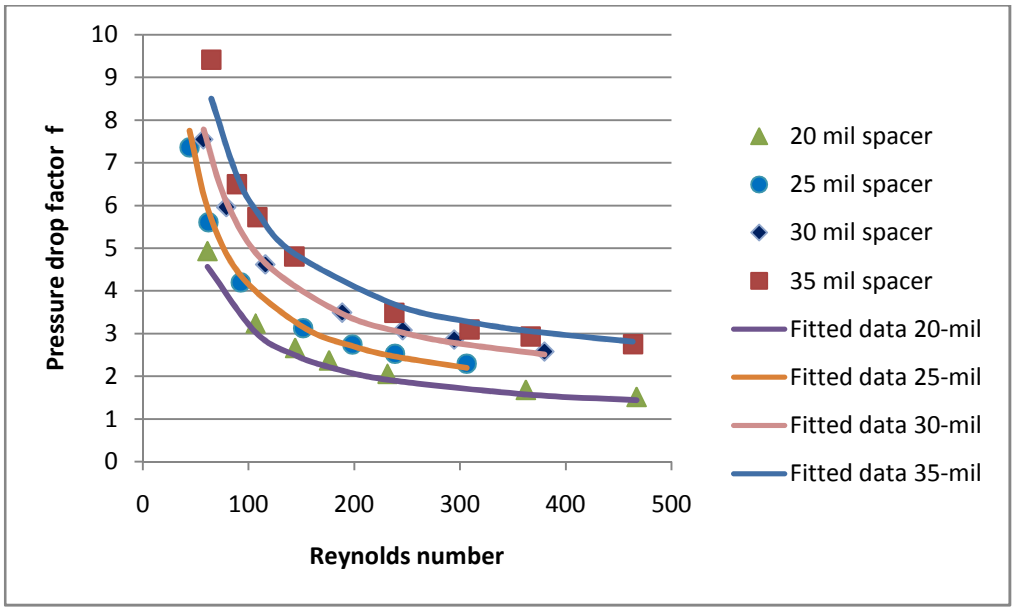

Figure 4.6: Plot of simulation data and the correlation equation (b = -1)

The fit of the correlation equation to the data is discussed in Table 4-7.

Equation (4.5) is an important parametric equation for pressure drop that will contribute to the modeling of feedwater flow through 90° feed spacer in Chapter 7.

Table 4-7: Analysis of fit for the parametric pressure drop equation

Feed spacer geometry	Reynolds Number	Pressure drop coefficient f		Fractional deviation	Coefficient of determination R^2
		from CFX simulation	From parametric equation		
20-mil	61	4.93	4.57	0.07	0.97
	107	3.24	3.03	0.06	
	144	2.66	2.50	0.06	
	176	2.37	2.22	0.06	
	231	2.06	1.92	0.07	
	362	1.68	1.58	0.06	
	467	1.52	1.44	0.05	
25-mil	44	7.36	7.75	(0.05)	0.99
	62	5.61	5.89	(0.05)	
	92	4.20	4.36	(0.04)	
	151	3.13	3.16	(0.01)	
	198	2.74	2.71	0.01	
	238	2.53	2.47	0.02	
	306	2.30	2.20	0.04	
30-mil	57	7.54	7.78	(0.03)	1.00
	79	5.96	6.08	(0.02)	
	116	4.62	4.64	(0.01)	
	189	3.49	3.46	0.01	
	246	3.08	3.02	0.02	
	295	2.86	2.78	0.03	
	380	2.58	2.51	0.03	
35-mil	89	6.50	6.71	(0.03)	0.97
	108	5.73	5.84	(0.02)	
	143	4.80	4.88	(0.01)	
	238	3.49	3.69	(0.06)	
	309	3.10	3.27	(0.06)	
	367	2.93	3.06	(0.04)	
	463	2.75	2.81	(0.02)	

4.4 Analysis fluid flow through the feed spacers

The feedwater flow through the feed spacer is a very bumpy one. The feed spacers are like tripwires that try to generate mixing of the feed flow. As the feed flow velocities and the spacer thicknesses are very small, the feed flow is laminar. Even though the flow of feedwater is laminar, there is intense mixing that helps to transport excess salt from the membrane surface to the bulk of the feed flow. This process helps to reduce concentration polarization near the membrane surface. The feedwater flow through the feed spacer is best understood by observing the streamlines and the vector diagrams.

To generate the streamlines, the seed points patterned in a rectangular grid are used to trace the feedwater flow. The seed points are located on each vertices of the rectangular grid shown in the Figure 4.7

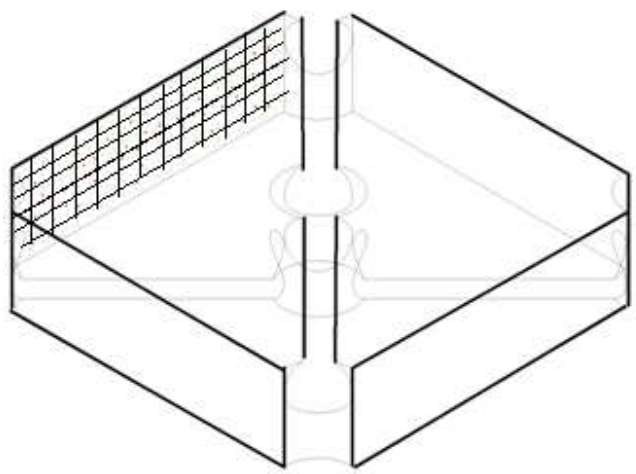

Figure 4.7: Pattern of seed-points used for the simulation of the streamlines

The vector plots are generated from two planes, the planes are shown in Figure 4.8.

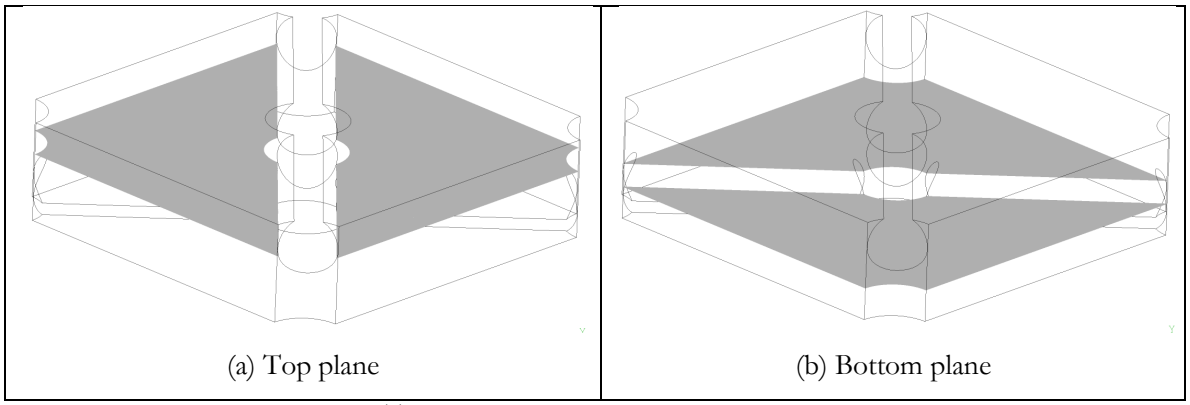

(a) Top plane (b) Bottom plane

Figure 4.8: The two planes used to generate the vector diagrams

Two planes are chosen to plot the vector diagrams because the top strand and the bottom strand of the feed spacer crisscross the membrane in two directions. The vector diagrams from these two planes will help to capture the flow pattern in these two locations. The following results show the streamlines and vector diagrams for 20-mil and 35-mil spacers at low and high Reynolds number. In the pictures portrayed (Figures 4.9 through 4.12), the direction of the pressure gradient is from the left side to the right side of the page.

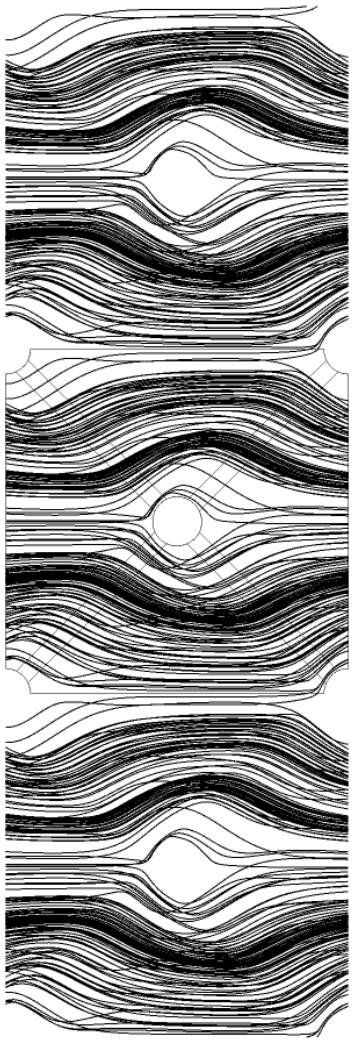

a) Streamlines

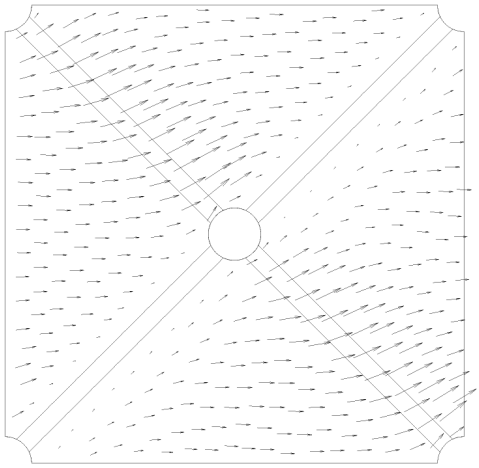

b) Vector diagram through the top plane

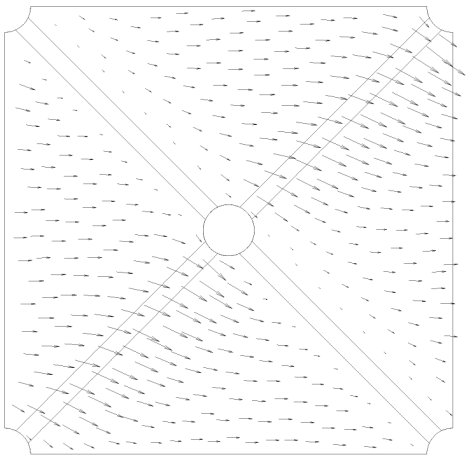

c) Vector diagram through the bottom plane

Figure 4.9: Streamline and vector diagrams for a 20-mil spacer Re = 61

It may be observed from Figure 4.9, that at a low Reynolds number, the direction of the feedwater flow is parallel to pressure gradient and the flow in the top plane is similar to the flow in the bottom plane.

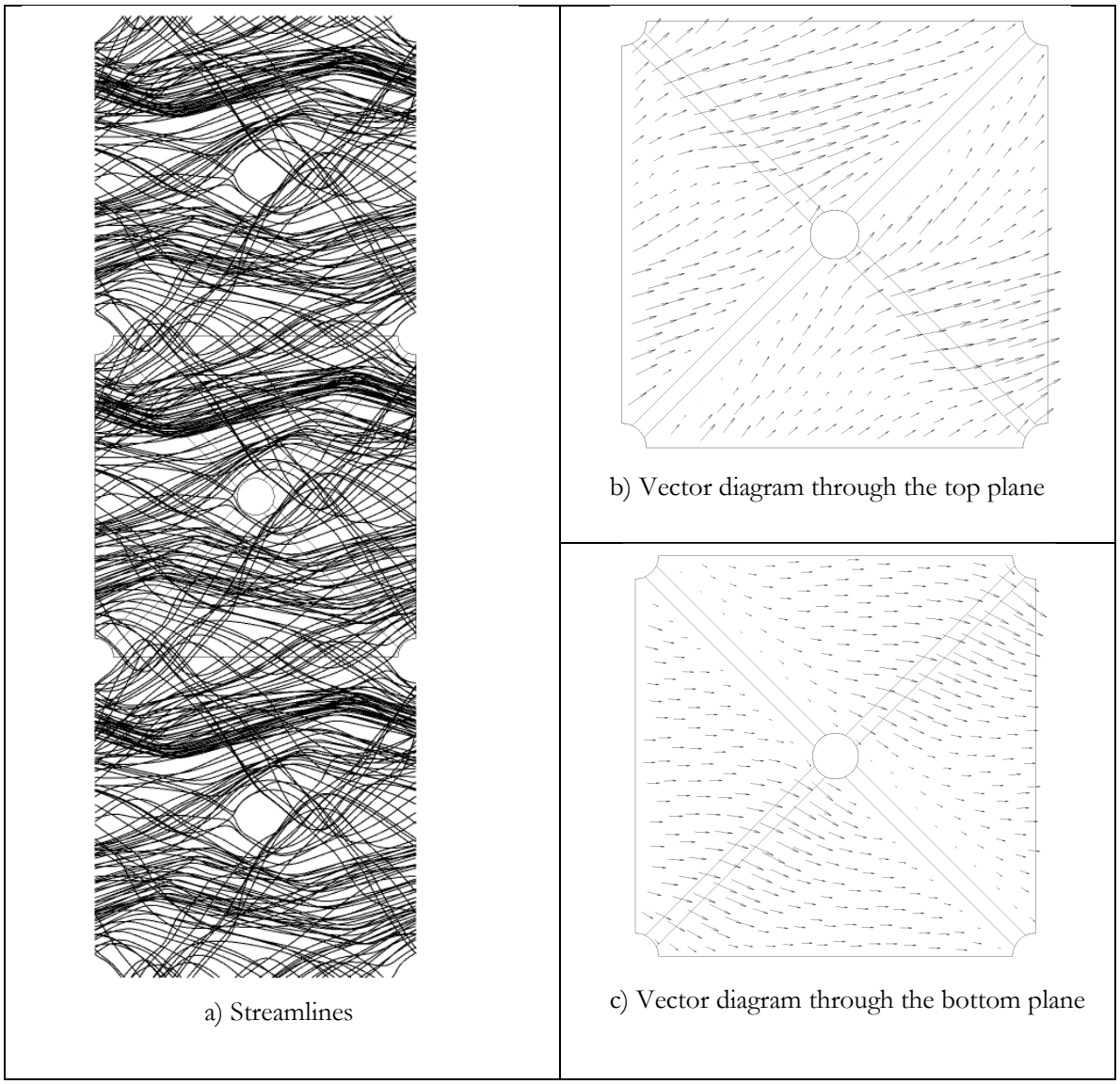

Figure 4.10: Streamline and vector diagrams for a 20-mil spacer Re = 467

From Figure 4.11, it is seen that at a high Reynolds number, the direction of the feedwater flow is at a 45° angle with the pressure gradient and is parallel to the feed spacer strand. Moreover, the bulk direction of feedwater in the top plane is perpendicular to the direction of the feed flow in the bottom plane. This claim is more evident from the crisscrossing pattern found in the streamline picture.

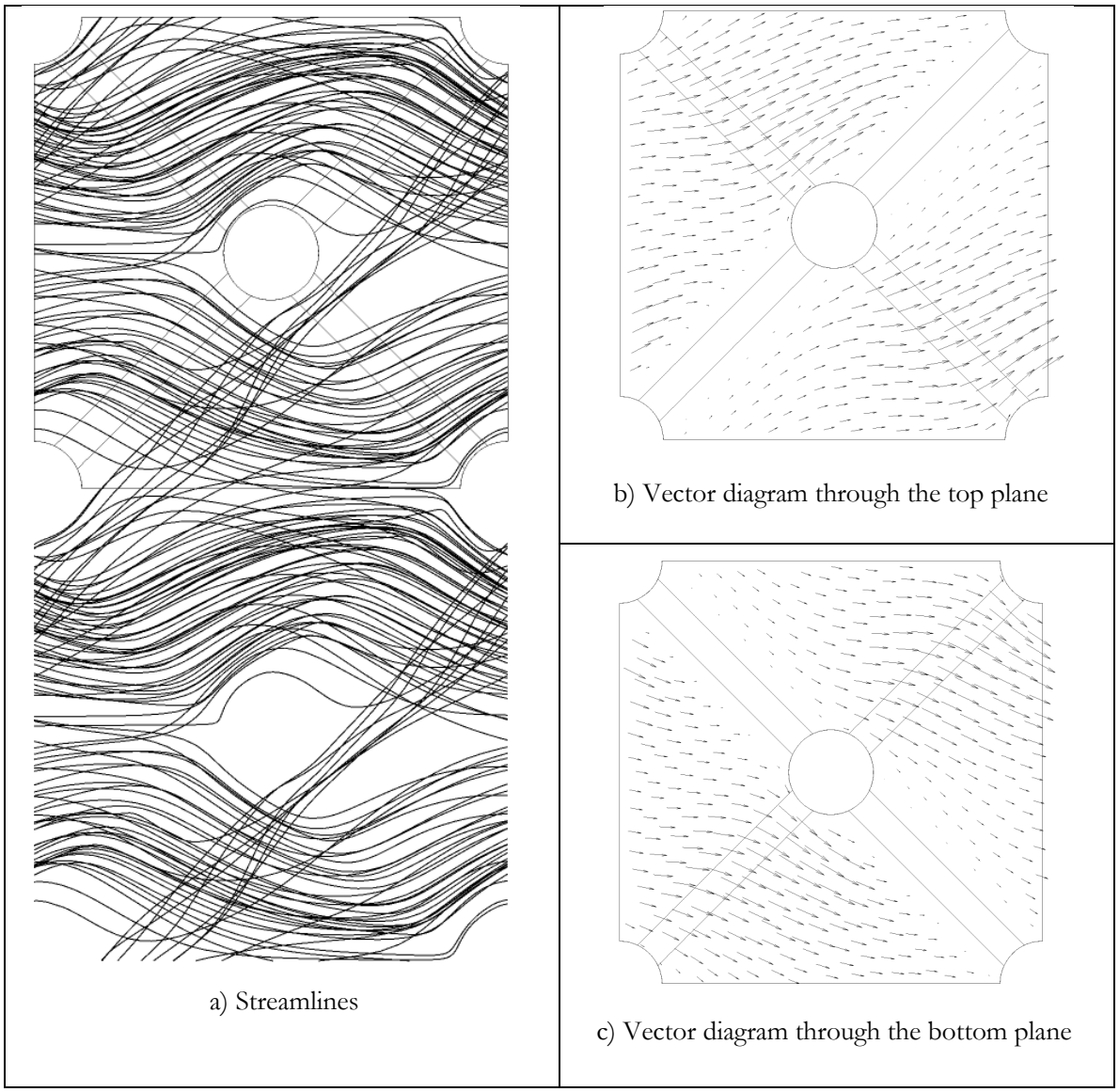

Figure 4.11: Streamline and vector diagrams for a 35-mil spacer Re = 89

Figure 4.11 shows the streamlines and vector diagrams for a 35-mil feed spacer for a low Reynolds number. It may be observed that with the except for a few streamlines, most of the streamlines flow parallel to each other and to the pressure gradient. This flow pattern is similar to the flow pattern that is observed in the 20-mil spacer (Figure 4.9). Similar observations were made in 25-mil and 30-mil spacers (not shown in the document).

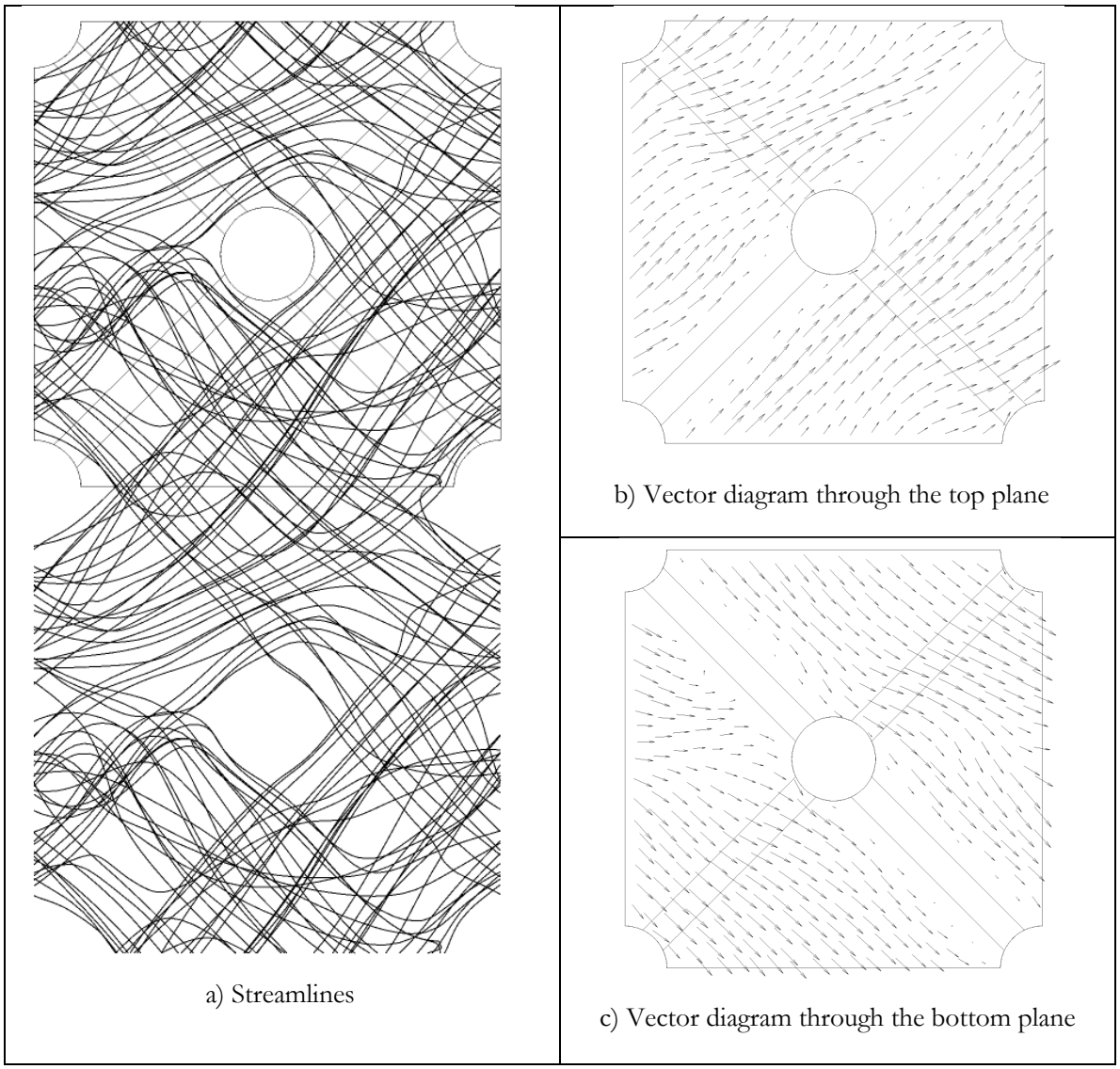

Figure 4.12: Streamline and vector diagrams for a 35-mil spacer Re = 463

Figure 4.12 shows the streamlines and the vector diagrams for the 35-mil spacer. Similar to the 20-mil spacer (shown in Figure 4.10), the streamlines appear in the crisscross pattern. The streamlines run parallel to the feed spacer strands. This can be observed in the vector diagram at the two planes. In addition to the vector diagrams, the crisscrossing of the streamlines adds evidence to the claim.

The general observation that can be made from Figures 4.9 to 4.12 is that at low Reynolds numbers, the feedwater flows in the direction of the applied pressure gradient and at higher Reynolds numbers, the feedwater flows parallel to the feed spacer strands. This outcome is summarized pictorially in Figure 4.13

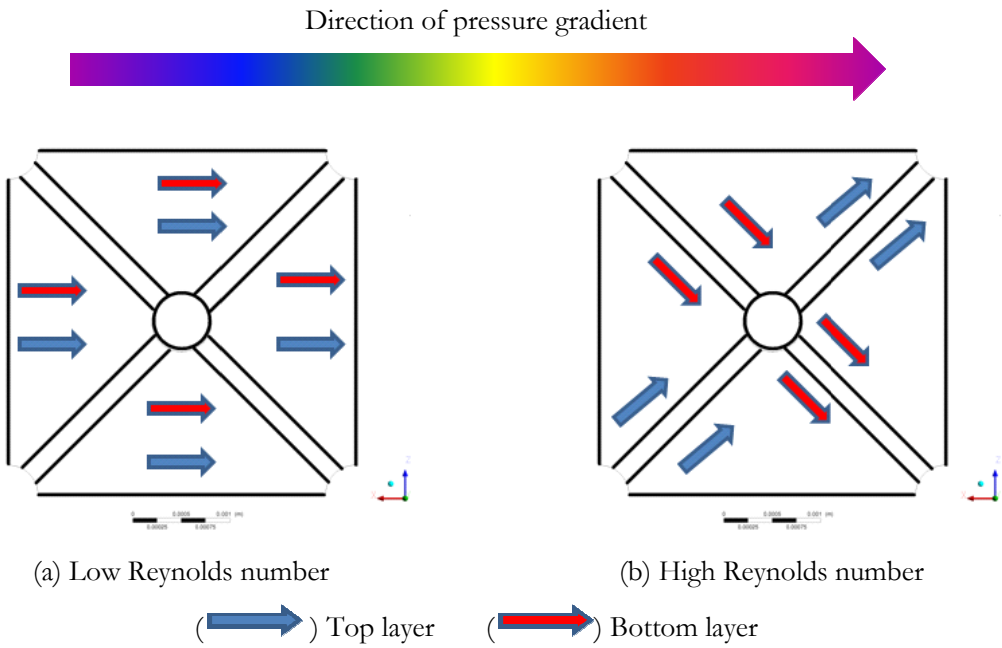

Figure 4.13: Flow patterns though the feed spacers at different Reynolds numbers

To quantify these findings, the percentage of the mass flowing parallel to the feed spacer strands to the total mass flowing across the feed spacer is plotted as a function of the Reynolds number in Figure 4.14

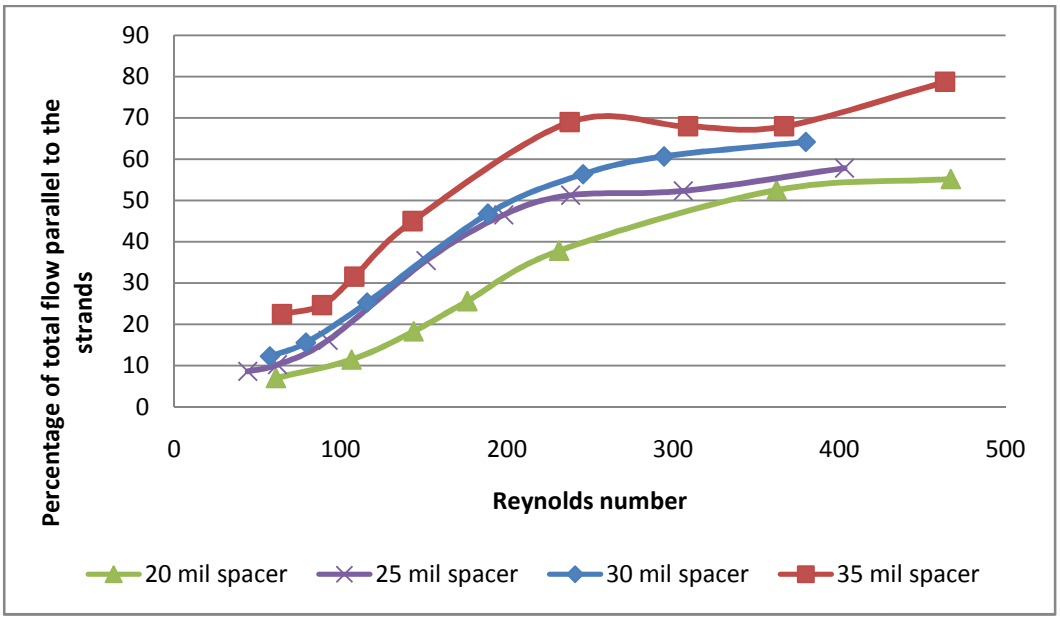

Figure 4.14: Percentage of mass flowing parallel to feed spacer strands

4.5 Results of feed spacer mixing

Eighty-four simulations were conducted on the feed spacer geometries to simulate the feed spacer mixing and the effect it has on the concentration polarization and the mass transport properties. Analyses similar to those done for pressure drop determination were done to verify the mesh independence and time scale independence.

Table 4-8: Mass transfer results for 20-mil spacer

20-mil spacer			
Driving pressure difference (Pa) [INPUT]	**Reynolds number**	**Sherwood Number**	**Stanton Number**
25	61	74	2.03E-03
50	107	86	1.35E-03
75	144	101	1.17E-03
100	176	108	1.02E-03
150	231	130	9.40E-04
300	467	229	1.06E-03

Table 4-9: Mass transfer results for 25-mil spacer

25-mil spacer			
Driving pressure difference (Pa) [INPUT]	**Reynolds number**	**Sherwood Number**	**Stanton Number**
10	44	74	2.77E-03
25	92	116	2.09E-03
50	151	152	1.67E-03
75	198	191	1.61E-03
100	238	222	1.55E-03
150	306	272	1.48E-03

Table 4-10: Mass transfer results for 30-mil spacer

30-mil spacer			
Driving pressure difference (Pa) [INPUT]	**Reynolds number**	**Sherwood Number**	**Stanton Number**
10	57	76	2.21E-03
25	116	128	1.85E-03
50	189	180	1.59E-03
75	246	226	1.53E-03
100	295	264	1.49E-03
150	380	319	1.40E-03

Table 4-11: Mass transfer results for 35-mil spacer

35-mil spacer			
Driving pressure difference (Pa) [INPUT]	**Reynolds number**	**Sherwood Number**	**Stanton Number**
10	65	98	2.53E-03
25	143	120	1.40E-03
50	238	156	1.10E-03
75	309	192	1.03E-03
100	367	200	9.10E-04

It may be recollected that in the previous section, to estimate the pressure drop across the feed spacer for a given flow, a known pressure gradient was applied and the flow across the spacer was simulated. Similarly, to estimate the mass transport property of the flow, a known mass transport condition was applied on the membrane interface. The CFX simulation yielded the results for the area average membrane wall concentration and the volume average feedwater bulk concentration. The Sherwood number was calculated substituting the area average membrane wall concentration and the volume average feedwater bulk concentration in Equation (3.56).

The Stanton number is given by Equation (3.60).

To provide another perspective for the mass transfer results, the numerical data from Table 4-8 to Table 4-11 have been plotted in Figures 4.15 and 4.16.

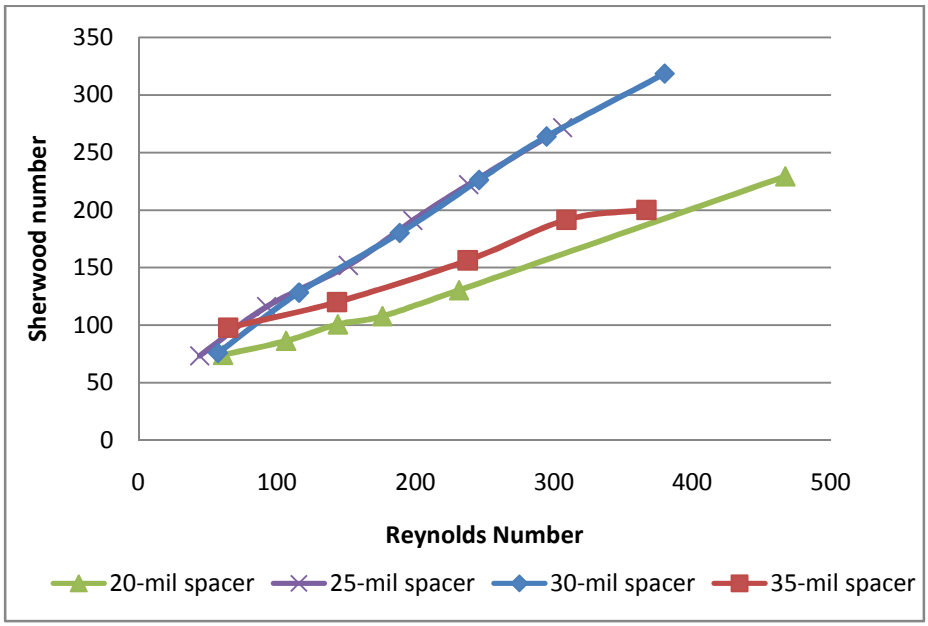

Figure 4.15: Plot of Sherwood number as a function of Reynolds number

A dimensionless representation of the mass transfer coefficient alternative to the Sherwood number is provided by the Stanton number in Figure 4.16.

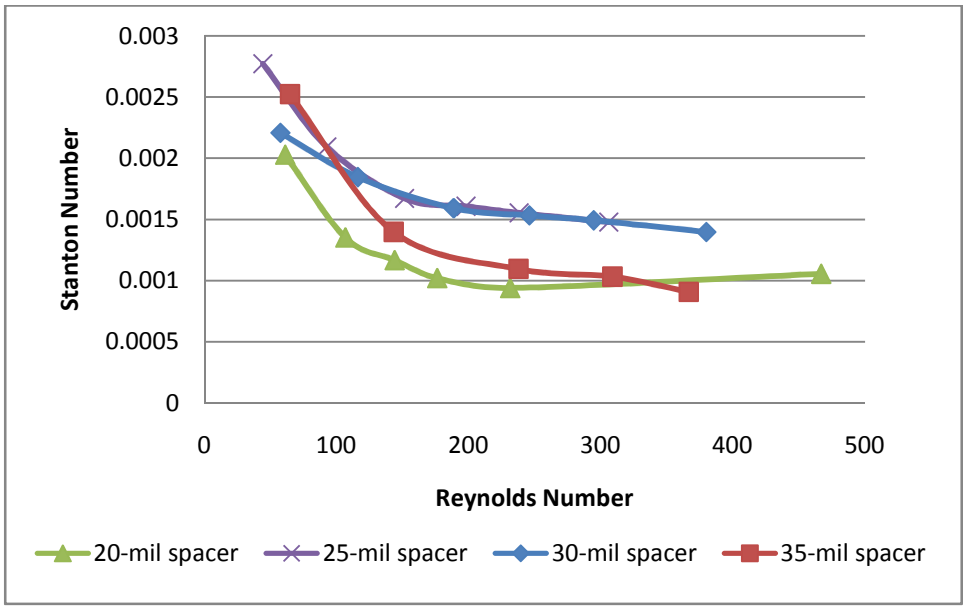

Figure 4.16: Plot of Stanton number as a function of Reynolds number

Inspection of Figure 4.15 indicates that the Sherwood number increases with the increasing value of Reynolds number, on the other hand, the Stanton number (Figure 4.16) decreases with increasing Reynolds number and approaches a constant value at higher Reynolds numbers.

It may be observed that from Figure 4.15 that the 20-mil and the 35-mil spacers have a lower slope of Sh vs. Re compared to the 25-mil and 30-mil spacers. Similar observations can be made from Figure 4.16, too. This indicates the existence of a non-monotonic relation between the *geometry factor* and the Sherwood number.

4.5.1 Correlation of mass transfer results

In this section, the Sherwood number results will be correlated by a single equation of the form

$$Sh = a\left[\left(\frac{\mathrm{Re}}{\alpha}\right)^{b} - \beta\right] Sc^{\frac{1}{3}}\left[\bar{e}X^{2} + \bar{f}X + \bar{g}\right] \tag{4.6}$$

where a, b, α, β, $\bar{e}$, $\bar{f}$, and $\bar{g}$ are constants that are chosen to make the Equation (4.6) fit the curve.

Sh is the Sherwood Number

Re is the Reynolds number

Sc is the Schmidt number a

and X is *geometry factor* described in Equation (4.3)

Equation (4.6) is similar to Equation (2.9), the differences being- that a Reynolds number scaling factor α and a constant correction factor β are introduced. The *geometry factor* is represented as a quadratic equation because, it is believed that the response of the Sherwood number to the *geometry factor* is not monotonic based on the observation from the Figure 4.15. The constant correction factor is introduced because it is expected that a non-zero Sherwood number can exist for zero Reynolds number. The Reynolds number scaling factor is introduced to accommodate the special flow geometry of the feed spacer in comparison to an internal flow through a pipe.

The parameters a , b , α, β, $\bar{e}$, $\bar{f}$ - are varied to fit the data portrayed in Figure 4.15. The resulting values are tabulated in Table 4-12.

Table 4-12: The value of pressure drop parameters

a	Reynolds number coefficient	0.52
b	Reynolds number exponent	0.65
α	Reynolds number scaling factor	0.71
β	constant correction factor	1.36
$\bar{e}$	Quadratic coeff. geom. factor	-78.66
$\bar{f}$	Linear coeff. geom. factor	43.85
$\bar{g}$	Constant coeff. geom. factor	-4.84

Thus, the correlating equation for the Sherwood number is given by

$$Sh = \left[-41.X^2 + 22.85.X - 2.52\right]\left[\left(\frac{\mathrm{Re}}{0.71}\right)^{0.65} - 1.36\right].Sc^{\frac{1}{3}} \tag{4.7}$$

This equation is plotted along with the original data points in Figure 4.17

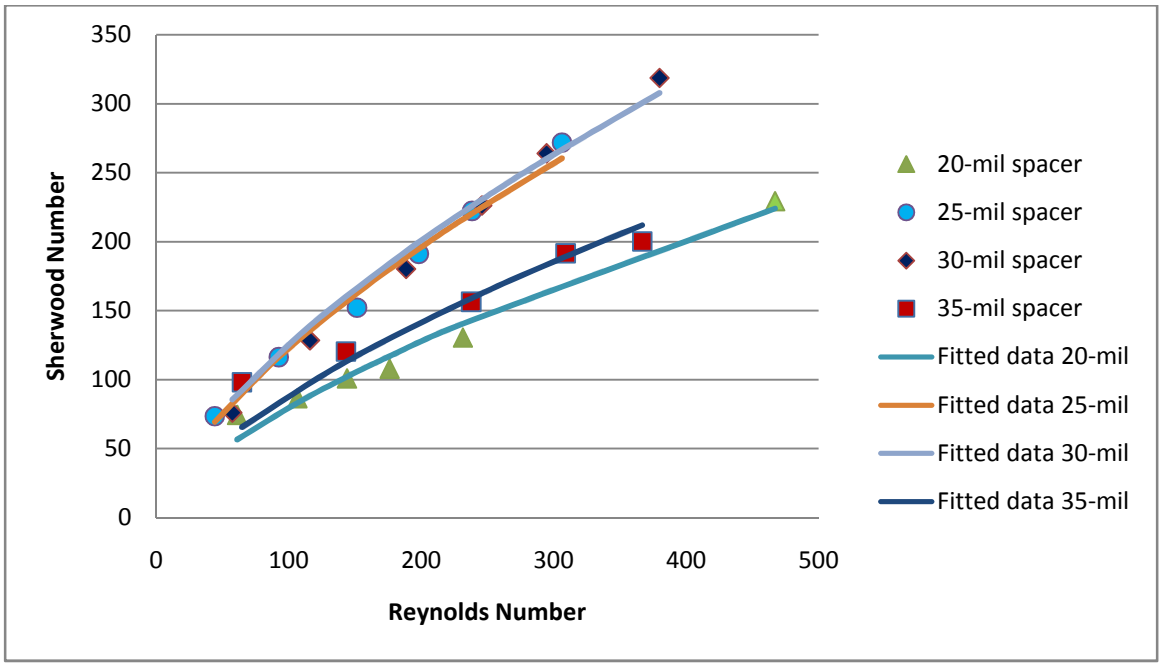

Figure 4.17: Simulation data and the curve fit

The fit of the correlation is demonstrated in detail in Table 4-13.

Table 4-13: Analysis of fit for the parametric Sherwood Number equation

Feed spacer geometry	Reynolds Number	Sherwood Number Sh		Fractional deviation	Coefficient of determination R^2
		from CFX simulation	From parametric equation		
20-mil	61	74.32	56.63	0.24	0.97
	107	86.44	83.21	0.04	
	144	100.79	102.08	(0.01)	
	176	107.85	116.97	(0.08)	
	231	130.45	140.47	(0.08)	
	467	229.33	223.88	0.02	
25-mil	44	73.51	69.32	0.06	0.99
	92	116.21	116.20	0.00	
	151	152.00	162.57	(0.07)	
	198	191.15	194.77	(0.02)	
	238	222.23	220.42	0.01	
	306	271.65	260.42	0.04	
30-mil	57	76.00	85.40	(0.12)	0.98
	116	128.44	138.87	(0.08)	
	189	180.18	192.96	(0.07)	
	246	226.21	230.48	(0.02)	
	295	264.00	259.98	0.02	
	380	318.64	307.76	0.03	
35-mil	65	98.04	65.53	0.33	0.91
	143	120.28	113.04	0.06	
	238	156.43	158.89	(0.02)	
	309	191.62	189.21	0.01	
	367	200.14	212.01	(0.06)	

From Table 4-13, it is observed that the R^2 value is greater than 0.9 suggesting a satisfactory fit.

Equation (4.7) can be used to predict accurately the Sherwood number for the flow through any 90° feed spacer. This equation will be used in Chapter 7 to estimate the concentration polarization in the feed spacers in RO elements.

The Sherwood number for any Reynolds number has maxima at a particular *geometry factor*. This *geometry factor* can be identified by differentiating the quadratic term and equating it to zero.

$$-82.X + 22.85 = 0 \tag{4.8}$$

$$X = 0.278 \tag{4.9}$$

Therefore, the ideal *geometry factor* to generate the maximum mass transfer mixing and minimize the concentration polarization is given by $X = 0.278$.

4.6 Analysis of mass transport in the feed spacers

The Sherwood number discussed so far is the area-averaged Sherwood number. The local Sherwood number is calculated by substituting the local mass transfer coefficient in Equation (2.8). The local Sherwood number is calculated by substituting the local membrane wall concentration in Equation (3.56). The mass transfer is not uniform across the whole area of the membrane. Figures 4.18 and 4.19 show the distribution of local Sherwood number on the membrane surface at a low Reynolds number of 65 and high Reynolds number of 365 on a 35-mil spacer.

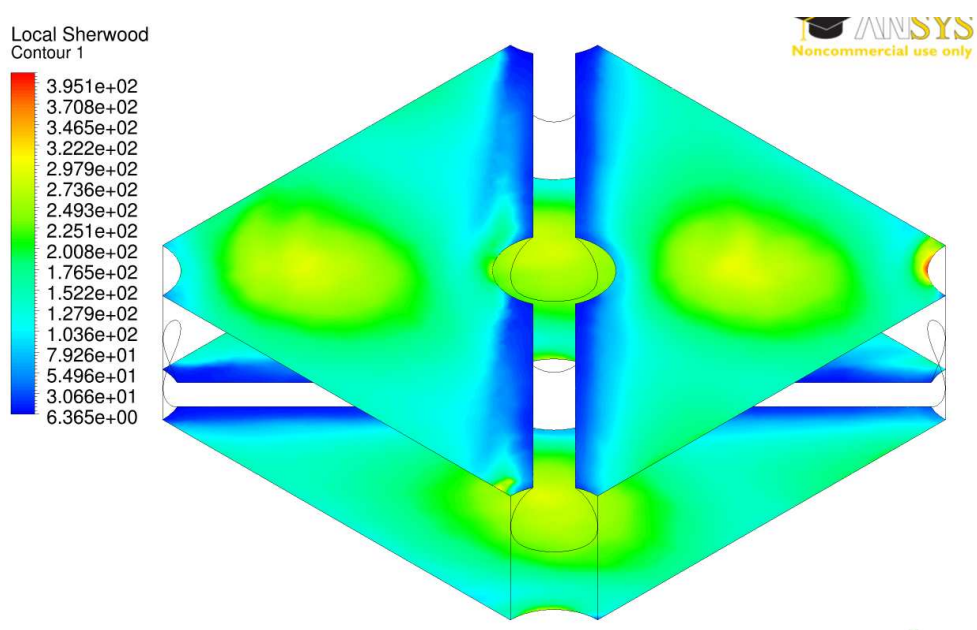

Figure 4.18: Distribution of local Sherwood number Re = 65 (35-mil spacer)

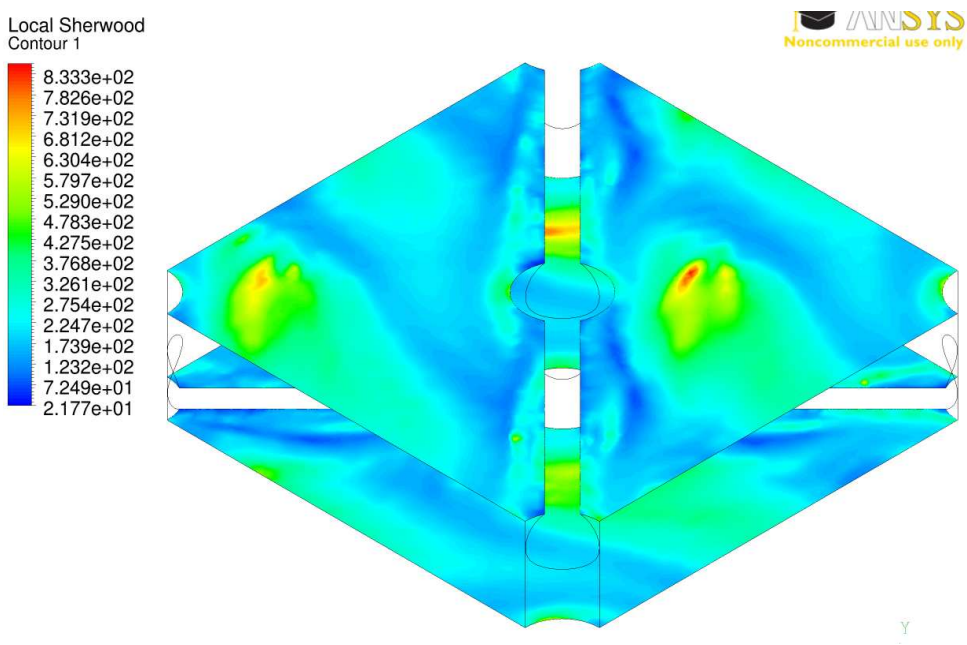

Figure 4.19: Distribution of local Sherwood number Re = 365 (35-mil spacer)

The distribution of local Sherwood number gives a quantitative estimation of the local concentration polarization as described in the Equation (3.59). The areas with high Sherwood numbers have low concentration polarization and vice versa.

It may be observed that the membrane area located opposite to the strand has the highest local Sherwood number. At the lower Reynolds number, the local Sherwood number near the region where the strand meets the membrane is very low in comparison to that for the higher Reynolds number. The recirculation zones observed behind the strand at the lower Reynolds number can contribute to this occurrence. When the flow transitions from the lower Reynolds number to the higher Reynolds number as shown in Figure 4.13, the dead zones caused by recirculation of feed flow is no longer existent.

At any Reynolds number, the local Sherwood number is lower at regions where the strands meet the membranes.

Figures 4.20 to 4.23 show the distribution of the local Sherwood numbers for 20-mil to 35-mil spacers for Reynolds number of approximately 100. These figures were plotted to show that the general observation made in the earlier paragraph still holds good even for different geometries.

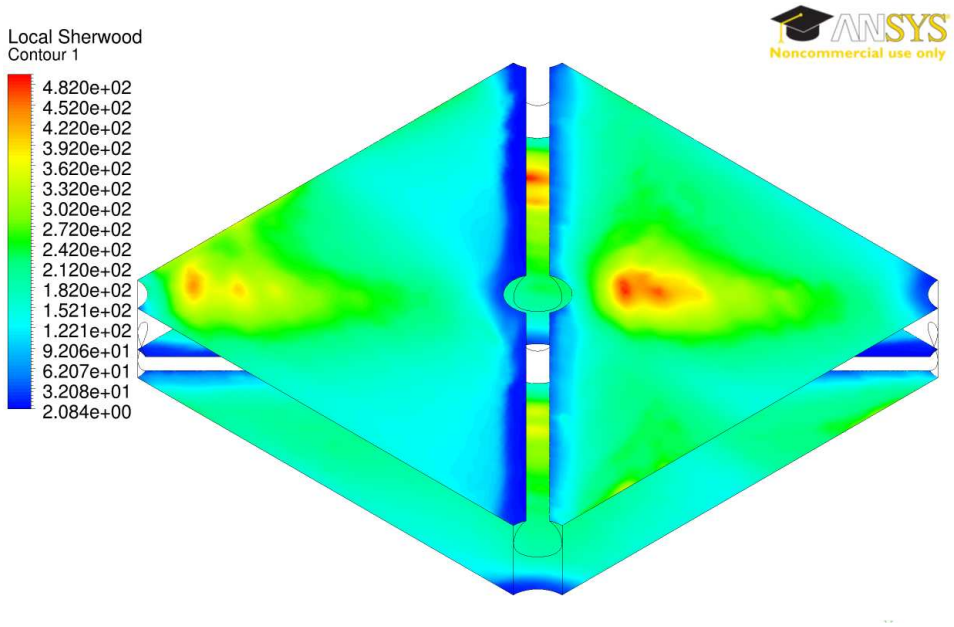

Figure 4.20: Distribution of local Sherwood number 20-mil spacer, Re = 107

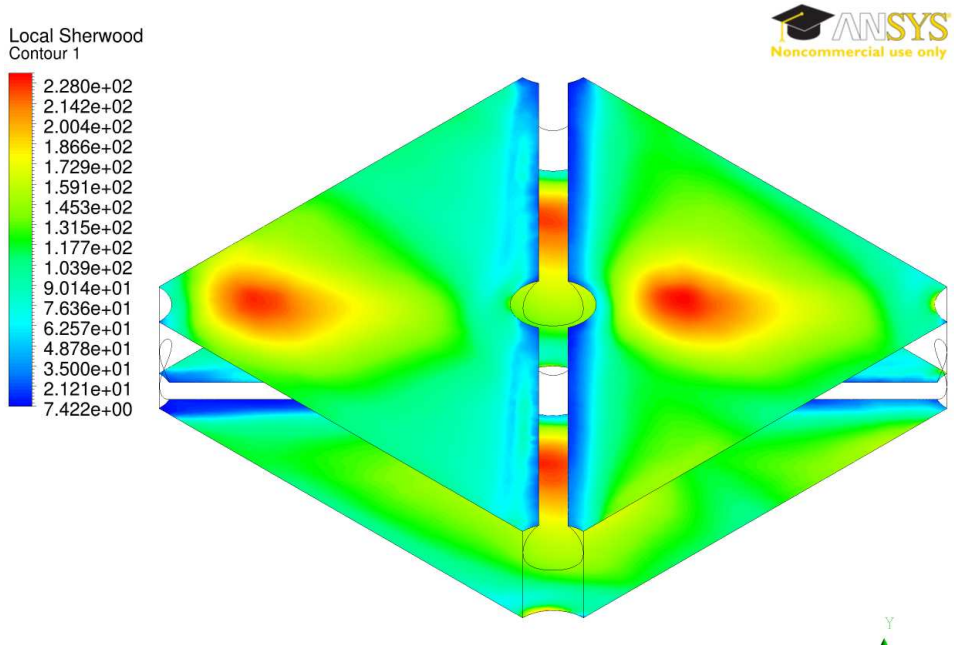

5

Figure 4.21: Distribution of local Sherwood number 25-mil spacer, Re = 92

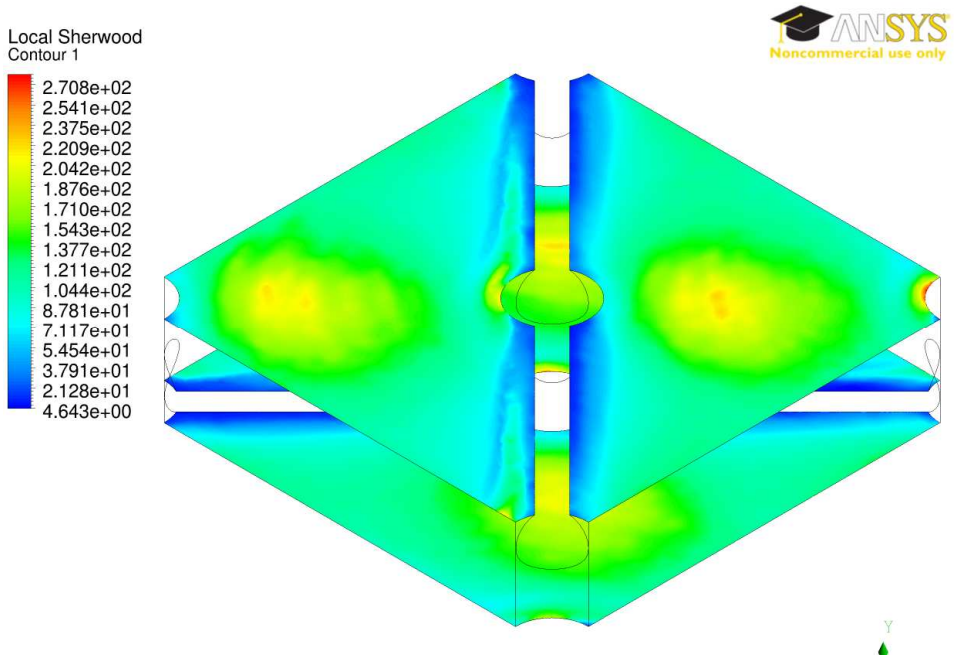

Figure 4.22: Distribution of local Sherwood number 30-mil spacer, Re = 116

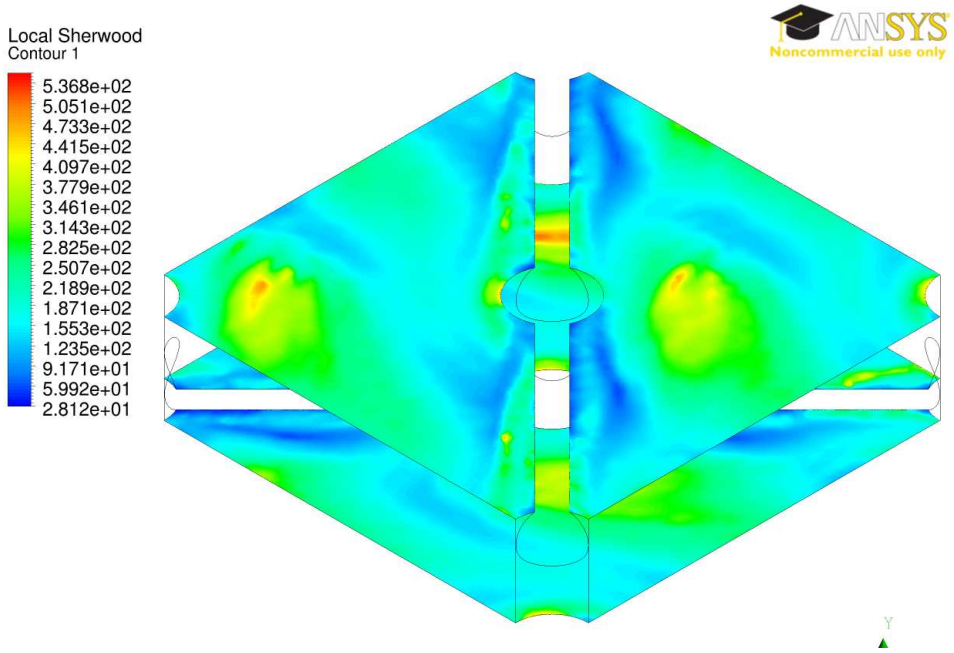

Figure 4.23: Distribution of local Sherwood number 35-mil spacer, Re = 143

4.7 Pressure drop factor and the Sherwood number in simulation

The results from Equation (4.5) and Equation (4.7) are used to calculate pressure drop along the length of the element and the concentration polarization in the feed spacer respectively. The pressure gradient along any point on the feed spacer is calculated by Equation (2.4)

$$|\Delta P| = f.\frac{1}{2}\rho.v_{feed}{}^{2}.\frac{1}{d_h}.|\Delta x| \tag{4.10}$$

The concentration polarization in the feed spacer at any point is calculated from the Sherwood number using the equation (3.59). By substituting the value for salt passage from Equations (2.25) into Equation (3.59), the concentration polarization is given by

$$CP = \frac{1 + \frac{d_h.J.}{Sh.D}}{1 + \frac{d_h.J.B}{Sh.D.(J + B)}} \tag{4.11}$$

where B is the *Membrane B value* at the point of interest.

Chapter 5 : EXPERIMENTS

5.1 Introduction

This chapter discusses the experiments conducted to verify the simulation models. The experimental procedures are described, and the results are compared with those of the simulation correlation equations (Equations (4.5) and (4.7))

5.2 Experiments to measure feed spacer pressure drop

The aim of the experiment is to measure the pressure drop across the feed spacers in an RO element. The layout of the RO system used in the experiments is show in Figure 5.1. The working fluid for the experiments is a synthetic feedwater made by mixing pure water (product water of RO operation is be good example of pure water) and common salt. The amounts of water and salt were specific to the individual experiment.

A schematic diagram of the experiment setup used for the pressure measurements is displayed in Figure 5.1. Although the test facility shown there can be operated to produce product water, this function was disabled because it does not add to the focus of the experiment, which was to determine pressure drop. Pressurized working fluid is delivered by a variable speed pump (a) to a micro-porous filter (b) from which it passes through a feedwater temperature and pH management system (c). The feed pressure of the water entering the RO module (e) is measured by the master feed-water pressure gauge (d). The RO module consists of an assemblage of RO pressure vessels connected in series. Each pressure vessel houses a commercially available 2.5-inch diameter and one-meter-long RO element. Pressures are measured at each end of six pressure vessels by means of pressure transducers (f) whose resolution is 0.01 psi. High-pressure working fluid exiting the RO module (e) is throttled by a pressure-regulating valve (g). The flowrate of the feedwater is measured by an electronic flow-rate measuring device (h) before the feed-water is collected in the feedwater tank for recirculation. The resolution of this flow-rate measuring device is 0.001 GPM.

The protocol of the experiments is to vary the flow-rate of the feedwater passing through the feed spacer and to measure the corresponding pressure drop. The per-element pressure drop is measured by means of an electronic pressure transducer situated at each end of the element. The flowrate

through the RO elements are controlled by varying the speed of the positive displacement pump. The temperature of the system is controlled and maintained at 25°C.

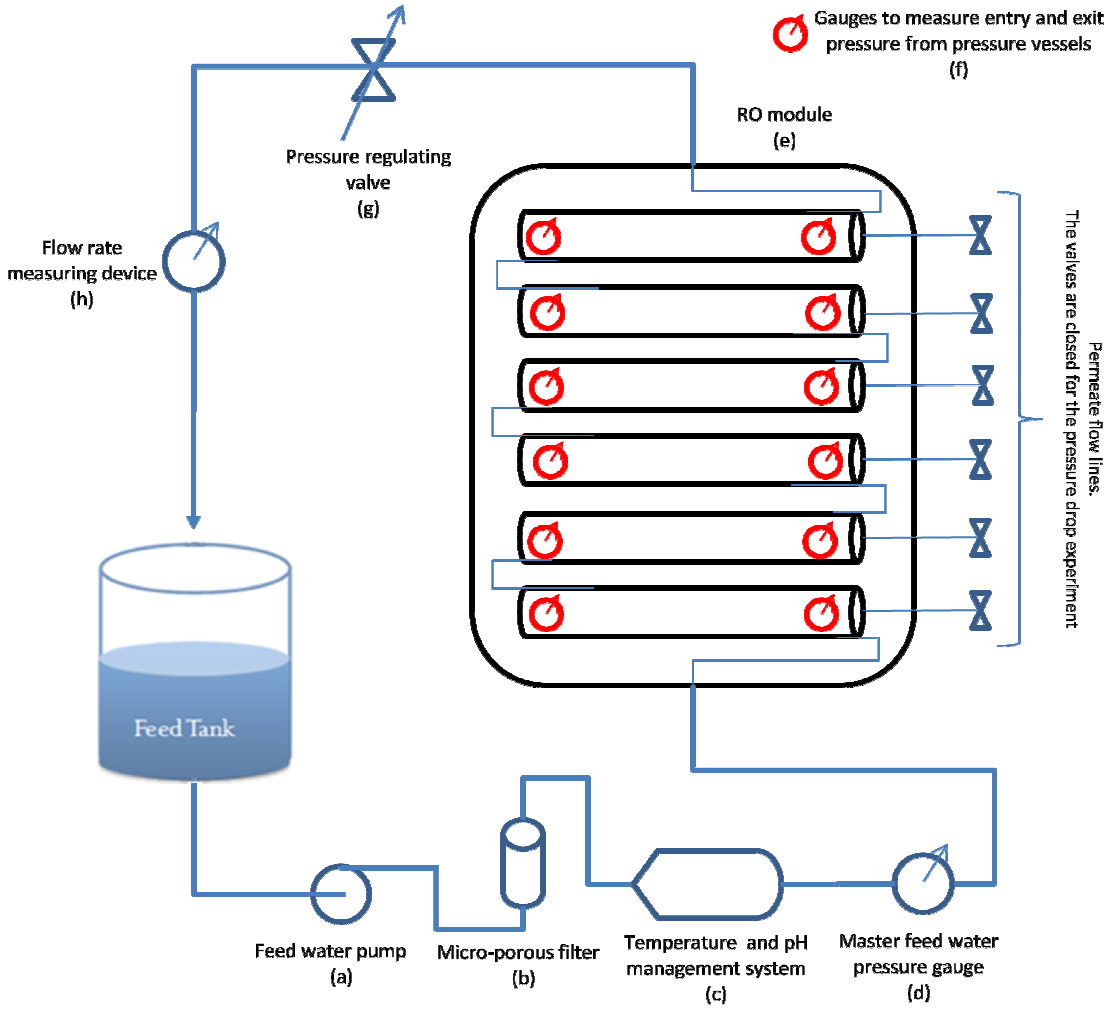

Figure 5.1: Schematic of the RO system used in the experiments

5.2.1 Cleaning

To eliminate fouling, the RO system is cleaned with a bleaching agent- sodium hypochlorite at 100 ppmw. Later, the RO system is cleaned with hydrochloric acid at pH-2 for 30 minutes followed by a sodium hydroxide base cleaning at pH-13 for 30 minutes. The RO system is neutralized and then flushed with RO water maintained at pH-8 for 30 minutes. The flowrate used in the system during the whole cleaning cycle is 5 lpm.

5.2.2 The RO elements and test preparation

Commercially available 2.5-inch diameter and 1 meter long RO elements were used. Feed spacers with 28-mil thickness and 7-strand per inch with 90° strand angle were used in the experiments. The elements built for the RO feed spacer pressure drop experiments were tested for defects, damages, and leaks. The RO elements were loaded in the pressure vessels. After loading the elements, the system is flushed with soft water to remove any preservatives. Preservatives are used in RO elements to improve their shelf life during storage. The flowrate of soft water during this flushing process is 15 liters of feedwater per minute. Later, the system with the elements installed is cleaned with pH-2 HCl for 30 minutes and again with pH-13 NaOH for 30 minutes. The system is flushed with filtered RO water at 8 lpm overnight for experiments to be performed the next day. The foregoing process is performed to ensure that no contaminants that can foul the system alter the pressure drop data. The feedwater line has a micron-filter and a carbon filter to prevent any fouling that may occur from accidental pollutants in the line.

5.2.3 Experiment and data acquisition

The entire RO test is performed without permeate production. To eliminate the production of permeate, the permeate tubes are plugged. Further, to prevent any accidental leaks of feedwater through cracks and seals, caused by the high hydrostatic feed pressure, the feedwater is mixed with 1000 ppmw salt (sodium chloride). This corresponds to 11 psi of osmotic pressure. The feed water's osmotic pressure counteracts the hydrostatic pressure to prevent accidental leaks. The reject flow-controlling valve is completely opened to minimize the hydrostatic feed pressure in the system. The feedwater and the system temperature is maintained at 25°C to ensure that there is no variations brought by the change in viscosity with temperature. The pump speed is gradually increased to enable the system to reach the desired flowrate. The outlet feed pressure of the system is atmospheric as the reject-flow controlling valve is completely open. The pressure drop along the lengths of the RO element add up to contribute to the inlet feed pressure. The system is run until it reaches steady state; it takes the system one to two minutes to reach steady state. Once the steady state is reached, the system's, flowrate and the pressure drop across each element is noted. Six elements were tested in series. The same experiments were repeated over four days with RO elements built from different batches. The results are reported in Table 5-1. Twenty-four elements were tested in the experiments that were conducted over four days.

Table 5-1: Results from feed spacer pressure drop experiment

	Feedwater flowrate in GPM	Feed flow velocity in m/sec	Pressure drop across the element in psi					
			1	2	3	4	5	6
Day 1	1	0.05	0.686	0.42	0.723	0.723	0.7492	0.7375
	1.97	0.10	1.69	1.1	1.7	1.89	1.74	1.54
	3.02	0.16	3.12	2.78	3.14	3.2	3.29	3.22
	4.05	0.21	4.84	4.81	4.98	5.16	5.15	5.02
	5.09	0.27	6.93	7.05	6.99	7.22	7.19	7.00
	6.02	0.31	8.98	9.33	9.04	9.4	9.3	9.09
	7.05	0.37	11.4	12.0	11.5	11.9	11.7	11.6
	7.5	0.39	12.7	13.3	12.7	13.2	12.9	12.7
Day 2	1.01	0.05	0.686	0.6	0.66	0.62	0.63	0.63
	2.04	0.11	1.65	1.67	1.68	1.64	1.68	1.61
	3.02	0.16	2.93	3.02	2.97	2.92	2.9	2.94
	4.05	0.21	4.61	4.84	4.63	4.63	4.55	4.59
	5.05	0.26	6.5	6.83	6.47	6.52	6.42	6.42
	6.09	0.32	8.74	9.18	8.67	8.75	8.58	8.58
	7.07	0.37	11.0	11.6	10.8	11.0	10.7	10.7
	7.53	0.39	12.1	12.8	11.9	12.0	11.7	11.7
Day 3	1.06	0.06	0.73	0.77	0.78	0.75	0.77	0.78
	2.01	0.10	1.66	1.76	1.78	1.76	1.72	1.77
	3.1	0.16	3.13	3.21	3.2	3.24	3.25	3.33
	4.01	0.21	4.63	4.81	4.65	4.76	4.77	4.93
	4.98	0.26	6.5	6.83	6.51	6.75	6.74	6.93
	6	0.31	8.7	9.21	8.68	9.03	9.03	9.26
	7.09	0.37	11.3	12.0	11.2	11.7	11.7	12.0
	8.08	0.42	14.0	14.8	13.8	14.4	14.4	14.8
	9.11	0.47	16.9	17.9	16.7	17.4	17.3	17.7
Day 4	1.06	0.06	0.65	0.68	0.69	0.69	0.69	0.73
	2.06	0.11	1.64	1.67	1.69	1.69	1.68	1.79
	3.16	0.16	3.1	3.22	3.15	3.21	3.21	3.37
	4	0.21	4.47	4.71	4.51	4.65	4.65	4.84
	5.15	0.27	6.4	6.8	6.43	6.68	6.68	6.9
	6.05	0.32	8.68	9.23	8.68	9.03	9.03	9.31
	7	0.36	10.9	11.6	10.9	11.3	11.3	11.7
	8.06	0.42	13.7	14.6	13.6	14.2	14.2	14.6
	9.07	0.47	16.7	17.7	16.5	17.2	17.2	17.6

The raw data are used to calculate the Reynolds number and the *pressure drop factor* f .

The thickness of the feed spacer used in the experiment is 28-mil. Therefore, the Reynolds number is given by Equation (2.2). The hydraulic diameter is twice the feed spacer thickness = 56-mil or 0.01422 m. The density used is 1000 kg/m^3 and the dynamic viscosity is 8.899E-4 Pa-sec. The *pressure drop factor* is calculated by

$$f = \frac{\Delta P . d_h}{\frac{1}{2} \rho v_{feed}{}^2 . L} \tag{5.1}$$

where f is the calculated *pressure drop factor*,

ρ is the density at 1000 kg/m^3

v_{feed} is the bulk velocity of the feed flow in the feed spacer.

d_h is the hydraulic diameter = 0.01422 m

ΔP is the pressure drop across the element. The data in psi is converted to Pascals in the equation.

L is the length of the RO element. The RO element is ~ 40 inches long. It is approximated as one meter.

The *pressure drop factor* is calculated from Equation (4.5) where X is calculated from the strands per inch and the feed spacer thickness. As the feed spacer has 7-strands per inch, the distance between the strands is 142-mil, and the thickness of the spacer is 28-mil, *geometry factor* $X = 0.196$. With the substitution of the value of X in Equation (4.5), the value of the *pressure drop factor* is calculated. The results are plotted in Figures 5.2 and 5.3. Figure 5.3 shows the data on a log-log plot. The curve labeled "The fitted data" shows the expected result based on the numerical simulations.

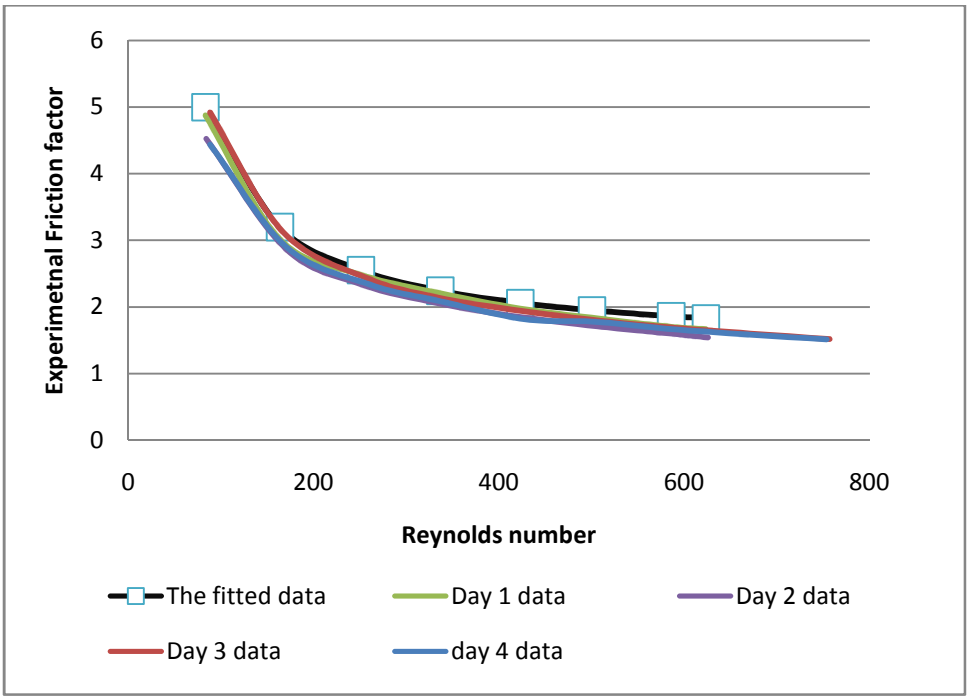

Figure 5.2: Pressure drop factor vs. Reynolds number

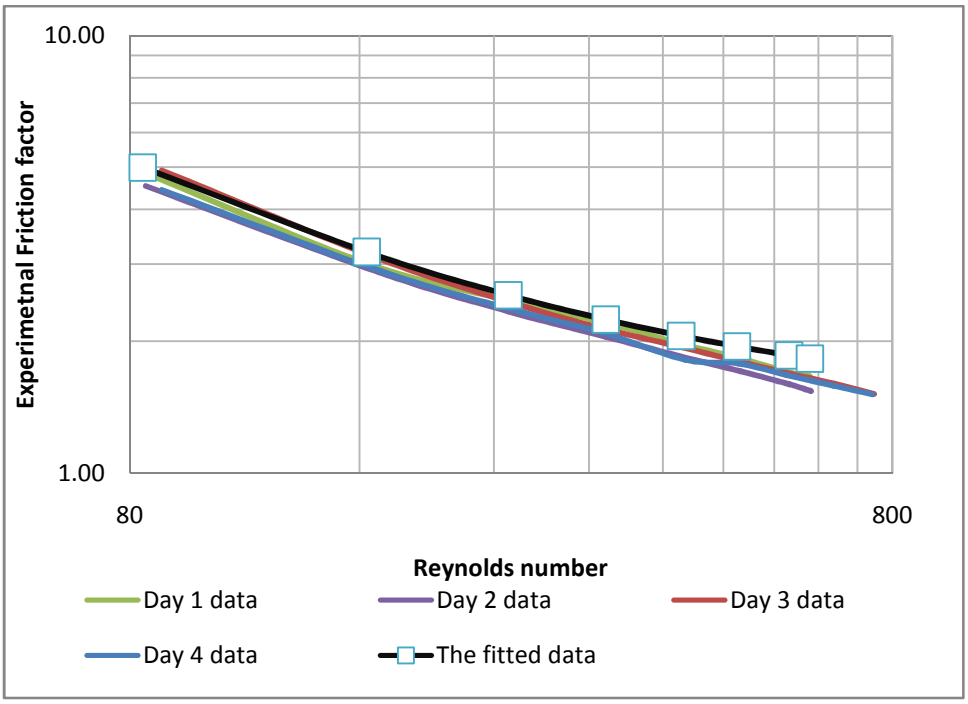

Figure 5.3: Pressure drop factor vs. Reynolds number (log-log graph)

From Figures 5.2 and 5.3, the fit of the *pressure drop factor* based on simulation and experiment seems adequate. The information from the log-log figure shows that the CFX simulation accurately captures the trend. In Figures 5.4 and 5.5, the pressure drop predicted is compared against the pressure drop measured from experiment. Figure 5.4 plots the data from six different elements conducted on Day 1. Figure 5.5 shows the average of the six elements' data plotted over four different days.

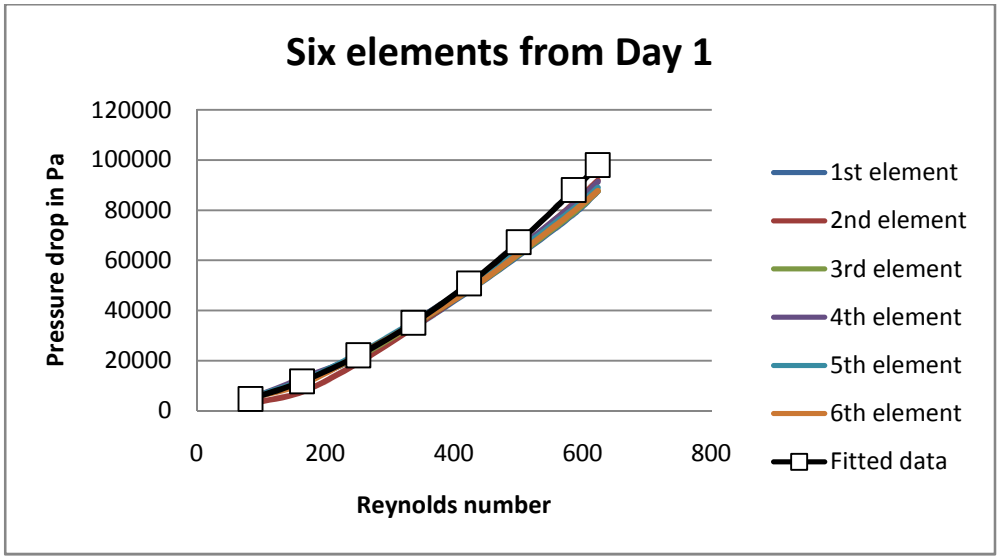

Figure 5.4: Pressure drop v. Reynolds Number from day 1 elements

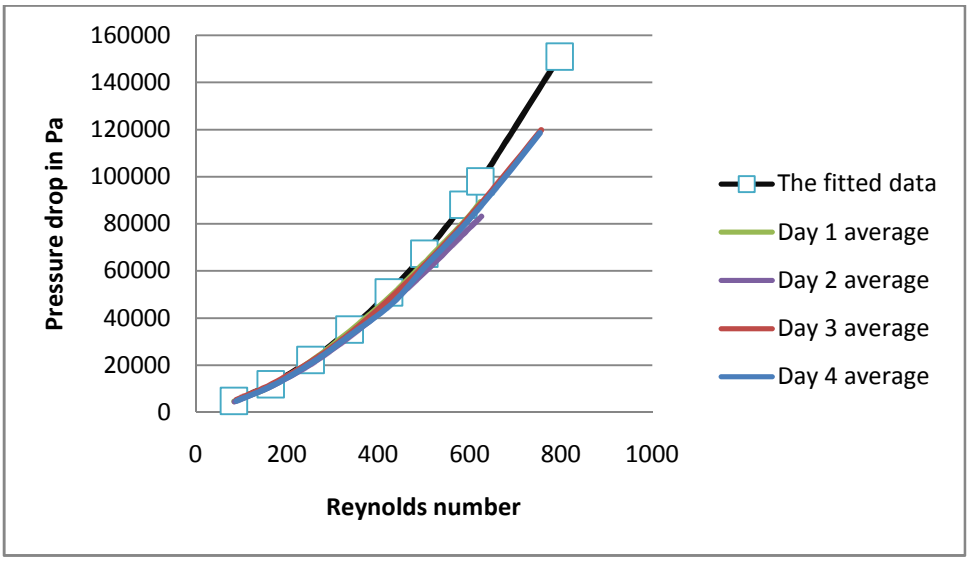

Figure 5.5: Pressure drop v. Reynolds Number from all four day averages

It can be observed from Figures 5.4 and 5.5 (especially in Figure 5.5) that the CFX simulations seem to overestimate the pressure drop across the elements at higher Reynolds number. To analyze this discrepancy further, the elements tested were opened up and the feed spacers were inspected for geometric consistency. Two vital observations were made:

1. The feed spacers were found to be imprinted deep into the RO membrane
2. The feed spacers appeared stretched after being installed in the RO element.

The deep imprinting of the feed spacers into the membrane suggests a narrower passage for feedwater passage through the feed spacer. This observation leads to higher feedwater flow velocities through the feed spacers than the ones calculated based on the feed spacer geometry as a raw material. The increase in velocity is inversely proportional to the decrease in the hydraulic diameter, which leaves the Reynolds number of the feed flow unchanged. The only factor in Equation (4.5) that is altered significantly by the feed spacer imprinting is the *geometry factor*. A reduction in the feed spacer channel height would reduce the value of X from the originally calculated value of 0.196.

The second observation made is that the feed spacers appeared stretched after being installed in the RO element compared to the raw material. Further investigation into the issue revealed that plastic stretching occurs when the feed spacers are inserted in the RO element. The spacers are stretched during manufacturing to keeps the feed spacer taut. The increase in the strand spacing also reduces the value of X from the calculated value of 0.196.

The value of X was reduced iteratively from 0.196 to best fit on the experimental data. The new value of $X = 0.175$. Figure 5.6 shows the fit with the new simulated curve and the experimental data. For the value of X to be 0.175, the actual feed spacer channel thickness should be 25-mil. This amounts to 1.5-mil indentation of the feed spacer into the membrane. This situation was recreated on a bench top to see if the screen indents into the membrane. It was observed that the polypropylene screen and the polysulfone membrane deformed during the element rolling process.

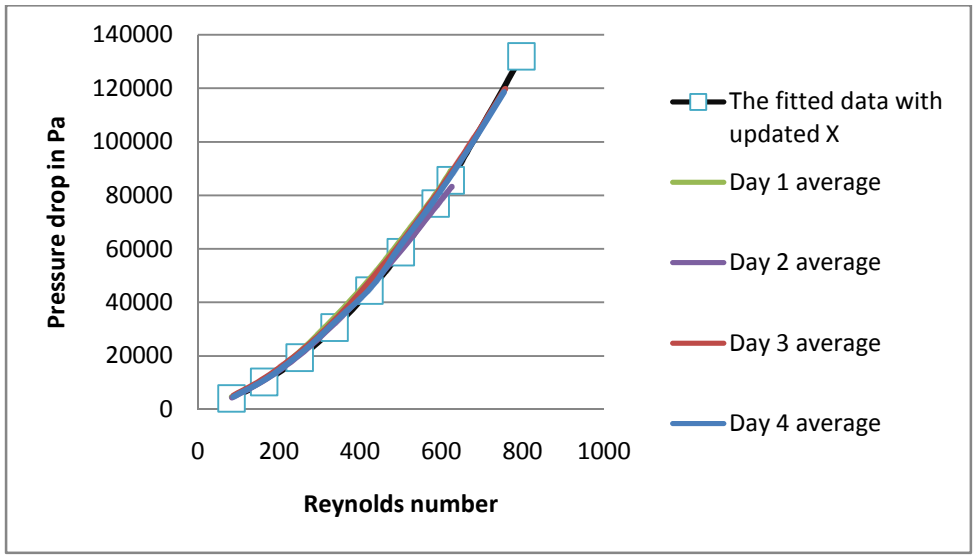

Figure 5.6: Pressure drop vs. Reynolds Number with updated $X = 17.5$

5.2.4 Theory of feed spacer deformation during membrane fabrication

In the previous section, it was observed that the simulation data based on theory does not quite fit the experimental data. A hypothesis set forth was that the feed spacer channel height was reduced from 28-mil (the thickness of the feed spacer as a raw material) to a thickness as low as 25-mil. A deformation of 3-mil in the feed spacer geometry is significant; therefore, to validate this conjuncture, a simple calculation to understand the forces involved to create this deformation is conveyed in the following.

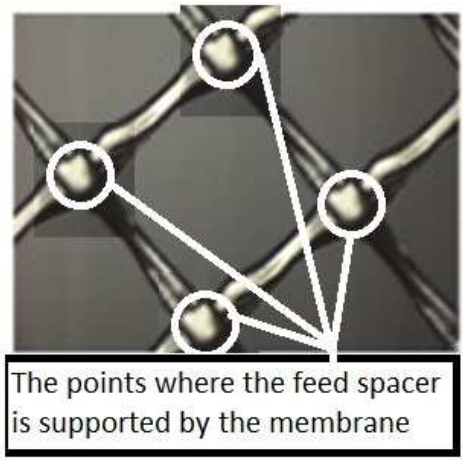

Figure 5.7: Figure of feed spacer and the support points

The feed spacer--membrane contact pressure is not evenly distributed along the length of the feed spacer strand. The force is supported at only those regions where the two strands intersect (as shown in Figure 5.7). This region can be envisioned as two spheres in contact with one another pressed by a flat plane as shown in Figure 5.8. This is a valid assumption because the contact between two crossed cylinders of equal radius is very similar to that between two spheres [79].

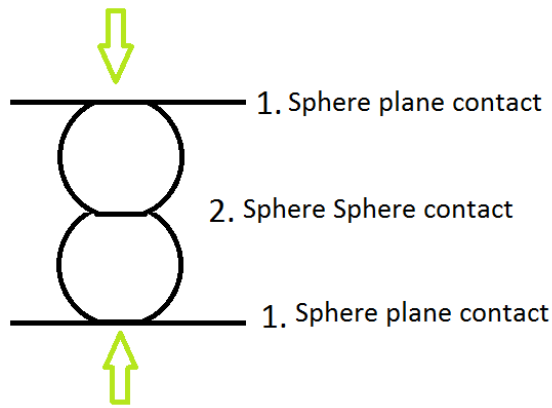

Figure 5.8: Schematic for feed spacer compression estimation

The elastic-plastic deformation of two spheres in contact with one another is given by the works of L. Vu-Cuoc [80]

$$F_{contact} = \frac{4}{3} E^{*} R_{cyl}^{\frac{1}{2}} d_{cyl}^{\frac{3}{2}} \tag{5.2}$$

where E^{*} is given by

$$\frac{1}{E^{*}} = \frac{1-\upsilon_{cyl-1}^{2}}{E_1} + \frac{1-\upsilon_{cyl-2}^{2}}{E_2} \tag{5.3}$$

In these equations, $F_{contact}$ is the force of the contact between the feed spacer and the membrane and R_{cyl} is the cylinder radius of the feed spacer strand. In the experiment portrayed in Table 5-1, the radius of the cylinder is 7-mil (one-half of the feed spacer thickness). The quantity d_{cyl} is the depth of the indentation left by the cylinder. This indentation is caused by the local deformation of the feed spacer and the feed spacer strand. In this case d_{cyl} is equated to 1.5-mil. υ_{cyl-1} and υ_{cyl-2} are the Poisson's ratio of the feed spacer and the membrane, respectively; E_1 and E_2 are the elastic Youngs Moduli of the feed spacer and the membrane respectively.

The Youngs modulus of the polypropylene used as the feed spacer is approximately 1.5 GPa. The membrane is plastically deformable because of the sponge-like properties of the membrane support structure made of polysulfone (refer to Figure 2.2). The measured plastic/elastic modulus of the membrane varies from one membrane type to another. The membranes built for seawater applications have a higher Youngs modulus compared with the membranes built for brackish water application. As some of these membrane properties are considered proprietary, they are not discussed in detail in this section. The calculated Youngs modulus of the membrane used in the RO element testing is valued at 0.5 Mpa.

The Poisson's ratio of the polypropylene feed spacer is 0.45. The membrane is assumed to have zero Poisson's ratio because of its spongy property.

The value of $F_{contact}$ by substituting E^* in Equation (5.2)

$$F_{contact} = \frac{4}{3}\frac{E_1 E_2}{\left(1-\upsilon_{cyl-1}{}^2\right)E_2 + \left(1-\upsilon_{cyl-2}{}^2\right)E_1} R_{cyl}{}^{\frac{1}{2}} d_{cyl}{}^{\frac{3}{2}} \tag{5.4}$$

To create a 1.5-mil deformation in the feed channel, the force calculated at the feed spacer--membrane contact is 0.5 N. A seven strand per inch feed spacer has 49 contact points per square inch. This amounts to a total force of 24.6 N per square inch or 5.5-pounds force per square inch. When the RO element is rolled as spiral wound elements, forces greater than 10-pound force per square inch is applied on the membrane. Finally, when the RO element is taped, the applied force is

locked into the element form. Hence, it is plausible that the feed spacer deforms from its original state as a raw material when it is incorporated into an RO element. Further, the feed spacer gap after membrane indentation in the RO element ultimately defines the *pressure drop factor* across the feed spacer.

5.3 Experiments to measure the mixing created by the feed spacer

The aim of the experiments reported in this section is to quantify experimentally, the concentration polarization occurring in the feed spacer. The direct method to determine the concentration polarization is to measure the quality of the permeate and back-calculate the possible values of concentration polarization. This method of back calculating the concentration polarization works only when the membrane properties remain constant during testing. It is a well-known fact that the properties of the membrane (*Membrane A value* and *Membrane B value*) are variables as a function of membrane operating conditions. Further, this variation with the operating condition is unique to each membrane type. Data on the variation of *Membrane A values* and *B values* as a function of the operation condition is proprietary.

It is know that *Membrane A value*s vary significantly as a function of

1. location on the membrane (membrane variations and occasional defects)
2. feedwater concentration flowing over the membrane
3. temperature of the operation
4. foulants on the membrane

Similarly, *Membrane B value*s vary significantly as a function of

1. pH of the feedwater
2. location on the membrane (membrane variations and occasional defects)
3. feedwater concentration flowing over the membrane
4. feedwater pressure
5. temperature of the operating condition
6. solute contaminants in the feedwater (dissolved carbon dioxide and other gaseous solutes)

There is no known way to determine the concentration polarization occurring in the feed spacer, directly or indirectly, when the *Membrane A* and *B values* are unknown. Of all the above-mentioned variables, factors like feedwater concentration and temperature can be controlled sufficiently. The

factor that is completely not under control is the spatial variation of membrane property (*Membrane A* and *B values*. Even though the membrane production process is a well-controlled one, the spatial membrane property variation is sufficiently significant to induce considerable errors in the concentration polarization calculations. To minimize the effect of spatial membrane variation, a small sample of the RO membrane is used instead of the whole element. The area of the sample is 0.0192 ft^2 as against 28 ft^2 in the RO elements tested. This reduction in area of observation should indeed help to reduce the spatial variations.

Two separate tests were conducted- one to measure the variation of the membrane property with operating conditions, and the other to measure the impact of the feed spacer on membrane concentration polarization. The first test was performed with no feed spacer in the flat cell channel, and the second was done with the feed spacer in the channel. Figure 5.9 shows a representative diagram of the flat cell test setup used for membrane property estimation. The flat cell test setup consists of a variable speed high-pressure pump (a). This pump sends high- pressure synthetic feedwater to the flat cells (b). There are 14 flat cells in series. Each flat cell has a provision to hold an RO membrane. The pressurized feedwater with very high hydrostatic pressure is made to flow on top of the active area of the membrane. The other side of the membrane is maintained at atmospheric pressure. This large pressure difference enables water to permeate through the membrane. This permeate water is collected for further analysis. The feedwater exiting the 14th flat cell still has a very high hydrostatic pressure. This pressure is reduced by the variable pressure-regulating valve. The spent feedwater is returned back to the feed tank for recirculation.

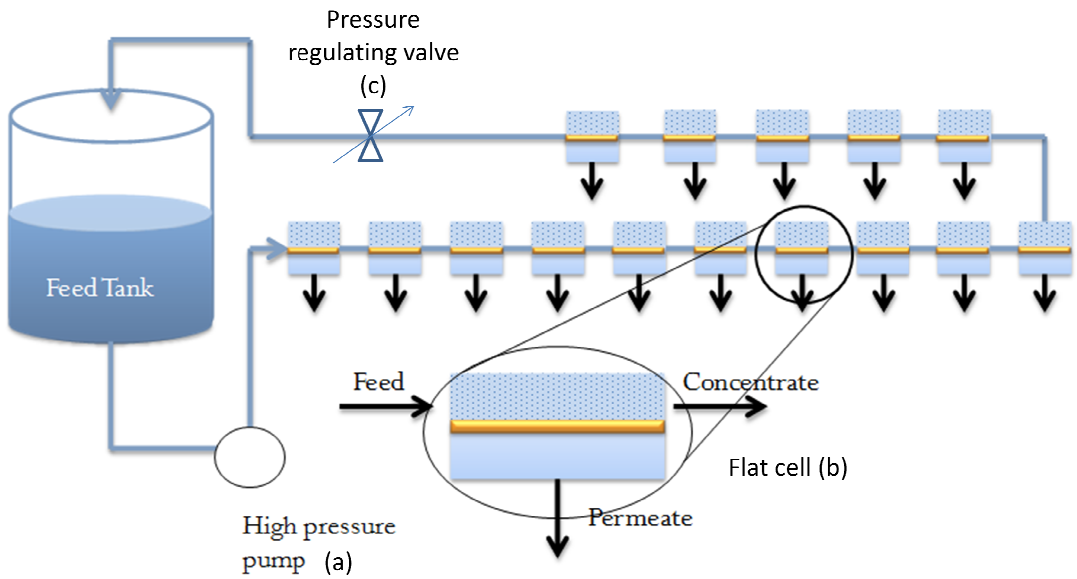

Figure 5.9: Layout of the flat cell apparatus used to measure concentration polarization

The quality of the feedwater was monitored in the tank and if the pH or the concentration were to drift, necessary actions were taken to maintain the feedwater quality entering the flat cells. The whole setup was maintained in a temperature, humidity, and air-quality-controlled environment to prevent any unknown disturbances in the experiments or the observations.

The flat cell experiment was conducted in an ultra-pure test facility. The ultra-pure test facility was chosen to prevent carbon dioxide contamination. Atmospheric carbon dioxide dissolves in water and makes the feedwater acidic. As the membrane performance varies strongly as a function of the pH, prevention of water carbonation was necessary.

5.3.1 Understanding the response of the membrane to the feedwater pH

The membrane's salt passage response is a strong function of the pH of the feedwater. Value of pH is a measure of the activity of the (solvated) hydrogen ion [81]. The pH of naturally occurring water or seawater is around eight. To understand the impact of pH on membranes, the membrane chosen for study was tested in the flat cell apparatus shown in Figure 5.9. The feedwater pH is raised by adding sodium hydroxide and the pH is lowered using hydrochloric acid.

The conditions for testing were:

- Flat cell feed flow velocity is 15 cm/sec
- Feed concentration is 2000 ppmw NaCl
- Temperature is 25°C
- Net driving pressure is 125 psi
- pH range [4 to 9]

Values of pH lower than four and greater than nine were not tested because, such extreme conditions tend to etch the top surface of the membrane. Extreme pH conditions are used to clean the RO membrane and not used as the operating environment.

The estimated *Membrane B value* is calculated from the permeate water salt passage using Equation (2.24). To give a context for these results, they are divided by the *B value* of the membrane at pH = 8. The *Membrane B values* are determined experimentally here.

The variation of *Membrane B value* ratio as a function of the feedwater pH is displayed in Figure 5.10. It can be observed that the membrane B values increase with decreases in pH. Understanding this trend of the membrane is necessary to determine accurately the *Membrane B value* at operation condition. An accurate *Membrane B value* is necessary to determine concentration polarization.

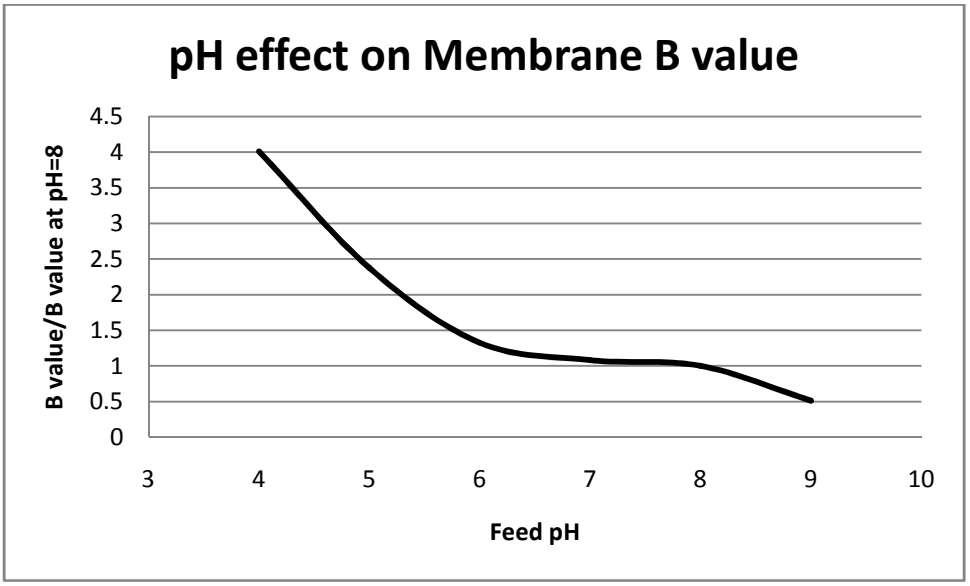

Figure 5.10: Effect of pH on the membrane salt rejection

Atmospheric carbon dioxide at 400 ppm can carbonate water and reduce the pH of the water to five. Therefore, to maintain the feed pH at 8, NaOH is added to the feed water. The presence of NaOH (sodium hydroxide) in the feedwater increases the feedwater's ability to dissolve more carbon dioxide. This addition of sodium hydroxide in feedwater changes the feed composition of the feedwater. The whole process is described in form of chemical equilibrium equations as in the following.

First, the CO2 dissolves in water:

(1) $CO_2\ (g) \Leftrightarrow CO_2\ (l)$

At room temperature, the solubility of carbon dioxide is about 90 cm^3 of CO_2 per 100 ml water.

Later, equilibrium is established between the dissolved CO_2 and H_2CO_3, carbonic acid.

(2) $CO_2\ (l) + H_2O\ (l) \Leftrightarrow H_2CO_3\ (l)$

Carbonic acid is a weak acid that dissociates in two steps.

(3) $H_2CO_3 + H_2O \Leftrightarrow H_3O^+ + HCO_3^-$

(4) $HCO_3^- + H_2O \Leftrightarrow H_3O^+ + CO_3^{2-}$

Note that these carbonate anions CO_3^{2-} can interact with the cations (Like Na, Ca, K, etc.) present in the water

(5) $2\ Na+ +2\ Cl^- + CO32- \Leftrightarrow Na2CO3+ 2\ Cl^-$

When sodium hydroxide is added to the feedwater to maintain the pH, cations are available in plenty to enable copious carbon dioxide dissolution. All the species described in the chemical equilibrium coexist in the solution. Further, the concentration of each element affects the concentrations of the others, and this in turn affects the pH of the solution.

To understand the impact of pH of the feedwater on the RO membrane performance, it is necessary to understand the RO membrane chemistry. Figure 5.11 [82] shows the representative structure of the polyamide barrier layer that constitutes the functional layer of the RO membrane. The 'x' and 'y' seen in the figure show the molecular length of the *repeating unit*s. These lengths are varied to create membranes of different *Membrane A* and *Membrane B value*s.

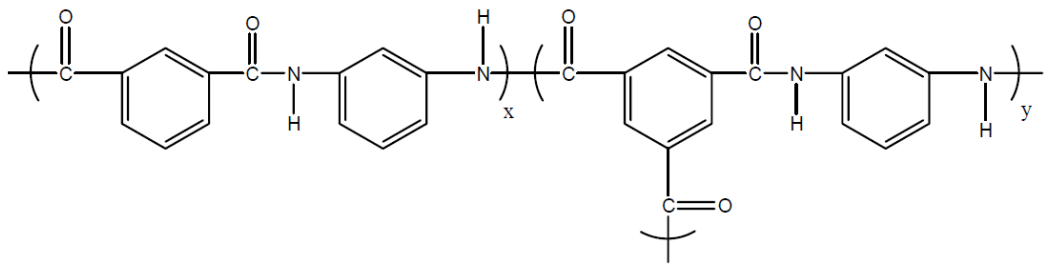

Figure 5.11: Representative chemical structure of commercial polyamide RO membranes

These COOH groups dissociate in water as COO^- and H^+ under basic conditions. The H+ dissolves in the feedwater and the COO- bonded to the polyamide contributes to the negative charge on the membrane. Just as COOH groups contribute to the negative charge on the membrane, the NH_2 groups on the polyamide are capable of hydrolysis and can create a positive charge on the membrane under acidic conditions. Therefore, RO membrane separation is a strong function of the pH of the feedwater.Figure 5.12 describes the phenomenon, which occurs, on the polyamide RO molecule.

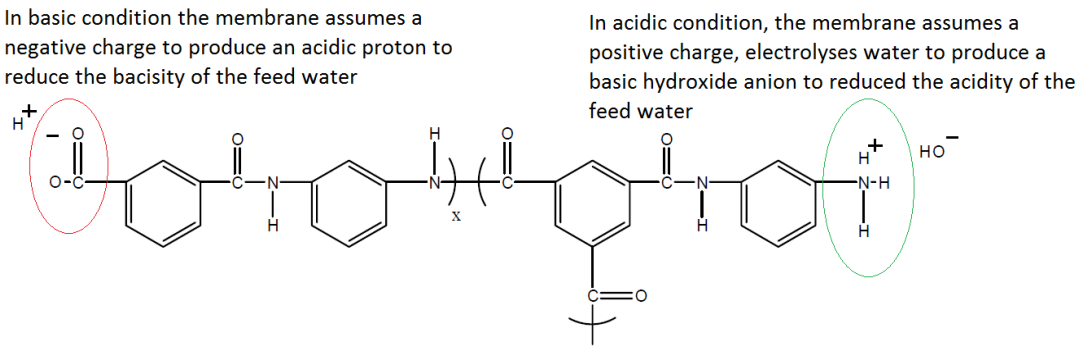

Figure 5.12: Mode of hydrolysis by RO membrane in acidic and basic feedwater conditions

At acidic pH, the membrane is either neutral or positively charged. This leads to better rejection of Na^+ cations in the solution. Similarly, at basic pH, the membrane is negatively charged and leads to better rejection of Cl^- anion in solution. As the hydrodynamic diameter of hydrated sodium cation is smaller than the hydrodynamic diameter of hydrated chloride anion, a negatively charged membrane is more effective in rejecting sodium chloride than is a neutral or a positively charged membrane.

5.3.2 Understanding the response of membrane to feedwater concentration

The RO membranes are selectively permeable membranes. The *Membrane B value* is expressed for NaCl or, to be specific, Na^+ and CL^- ions. When the feedwater is contaminated with carbon dioxide,

sodium carbobonate Na_2CO_3 is formed, and the membrane rejection is artificially decreased. Undissociated Na_2CO_3 is a large molecule, and it has superior rejection throughout the membrane. The same phenomenon tends to increase the *Membrane B value*s at lower feedwater concentration because the lower concentration of sodium carbonate is very stable as sodium cations and carbonate/bicarbonate anions. As most RO membranes are negatively charged, the salt rejection is primarily dictated by the rejection of the corresponding anions. In the case where sodium chloride is the solute, if the membrane is capable of rejecting the chloride anion, then as ions occur in corresponding pairs to maintain electro neutrality, the whole of sodium-chloride ion pairs are rejected.

When there is more than one anion present in the solute, then the salt rejection is determined by the anion that is least rejected by the membrane. In a sodium-chlorine-bicarbonate-carbonate system, the bicarbonate anion has one negative charge and five atoms, making it the least rejectable species throughout the RO membrane due to its smaller hydration ionic diameter. In such cases, more bicarbonates pass through the membrane. Sodium also passes through the membrane as its corresponding conjugate pair. High removal of bicarbonate in the feedwater creates a shift in the chemical equilibrium (especially chemical Equations, 3 and chemical Equations 4). This shift or imbalance in chemical equilibrium creates greater solubility of carbon dioxide in water and further reduces the pH of the feed system. This is phenomenon is documented in literature by Craig Bartels [83].

To understand the variation of *Membrane B value* as a function of the feedwater concentration the flat cell tests were conducted in the ultra-pure test facility, and the feedwater concentration was varied from salt-free ultra-pure water to 10,000 ppmw NaCl. The flat cell is specified to have a Sherwood number for salt in water at 75 for a feed flowrate of 0.3 GPM through the flat cells. This information was provided by the manufacturer of the flat cells. This Sherwood number was used to estimate the concentration polarization in the flat cells. The flat cells are later lined with wetted RO membranes, and the flat cells are sealed. The sealed flat cells are flushed with RO water for five hours. The system is degassed, and the system is fed with ultra-pure water over night to remove any contaminants on the membrane and to remove all trace carbon dioxide. The system is maintained at 25°C, and the feedwater is maintained at pH = 8. This amounts to adding small amounts of sodium hydroxide as the theoretical pH of ultra-pure water is seven. The amount of sodium hydroxide added to the system also helps to get an estimation of carbonate, bicarbonate present in the system due to carbon

dioxide dissolution. Even though sufficient care is taken to conduct the test and prevent carbon dioxide contamination, it is impossible to eliminate the effect.

The presence of trace amounts of sodium hydroxide and the bicarbonates were used for tests containing de-ionized water. The system is bubbled with 5-lpm inert gas continuously to displace even trace amounts of carbon dioxide, sulfates, and nitrates present in the system. The permeate waters produced in the flat cells are collected in containers. The permeate collector system is also flushed with inert gas to prevent contamination from atmospheric carbon dioxides, sulfur dioxides and various compounds of nitrous oxides. The qualities of the feedwater and the permeate water are measured by state of the art ICP-MS. This special instrument is used over electrical conductivity probes to minimize cross contamination of the feedwater or the product water. The quality of the permeate water is divided by the quality of the feedwater to report salt passage. Advanced titration is used to measure the pH of the water. The data from pH titration is inspected to ensure that there is no accidental contamination. During the test, the pH data of the water was well within acceptable limits, and the pH varied within the least count of the measuring instrument.

The conditions tested were

- Flat cell feed flow velocity is 15 cm/sec or 0.3 GPM
- Feed concentration varied from pure water, 20, 40, 80, 200, 250, 500, 1000, 2000, 4000, 8000, and 10,000 ppmw NaCl in water
- Temperature is 25°C
- Net driving pressure of 125 psi
- pH is kept constant at 8

Equation (2.24) is used to calculate the *B value* of the membrane based on the salt passage experimentally observed in each flat cell. To give a sense of perspective, the *B value*s results are divided by the *B value* of the membrane when the feed water concentration was 2000 ppmw NaCl. Figure 5.13 shows the change in *Membrane B value* as a function of the feed water salt concentration.

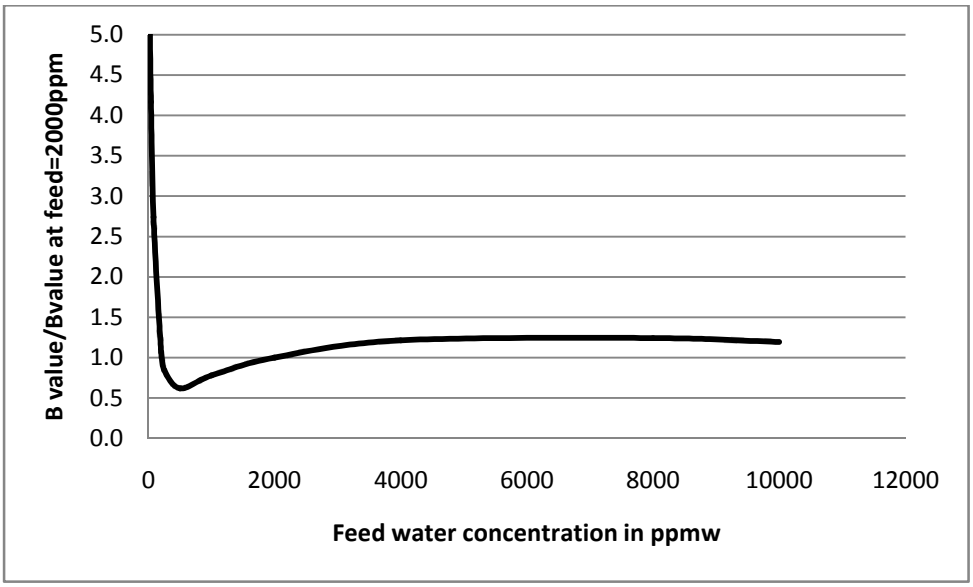

Figure 5.13: Effect of feedwater concentration on *Membrane B value*

The observation that is relevant to Figure 5.13 is similar to the observations made by Craig Bartel [83] for negatively charged membranes. As stated in Bartel's work, the salt passage through a negatively charged membrane is significantly affected by feedwater concentration. At higher feed water concentrations, comes an increase in the cations at the membrane surface, which shields the Donnan potential of the RO membranes thereby increasing the membrane B value. At very low feed concentrations, the solution diffusion salt transport mechanism of the membrane no longer holds and the membrane becomes more pervious to salt.

5.3.3 Understanding the effect of feed spacer on mass transfer

The aforementioned exercises enable a better understanding of the response of the *Membrane B value* to feedwater pH and concentration. The ideal method to estimate the concentration polarization would be to conduct the test at the RO element scale. As the author did not have the facility to conduct the ultra-pure water test at the RO element scale, the tests were conducted on a modified flat cell. In the new test setup (shown in Figure 5.14), the multiple flat cells were replaced by one large flat cell capable of accommodating a feed spacer in it. The large flat cell has a 2 inches x 4 inches active area. The feed channel in the flat cell was lined with a cut out feed spacer strip. This setup was expected to recreate the situation that would have existed inside the RO element feed spacer channel. Appropriate shims were used to prevent feedwater from bypassing the feed spacer.

The concentration polarization is estimated based on the membrane rejection at various feed flow Reynolds numbers. The feed flow Reynolds number was varied by varying the flowrates.

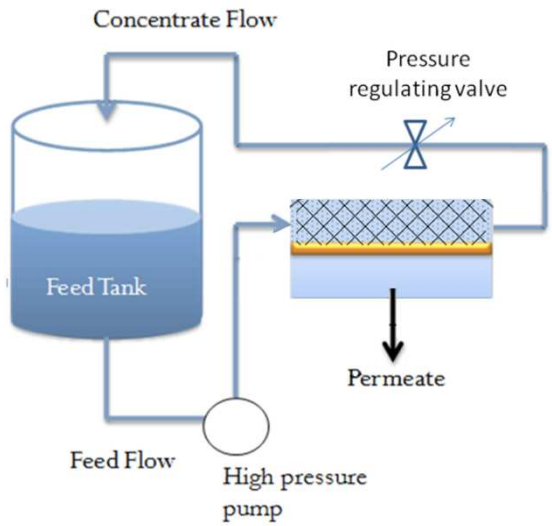

Figure 5.14: Layout of the flat-cell apparatus used to measure concentration polarization with feed spacer

The feed spacer is placed on top of the functional layer side of the membrane and appropriate shims are placed on top of the feed spacer to prevent feedwater bypass. To simulate the flow similar to that of the flat cells, 14 tests were conducted with conditions similar to the flow conditions in each flat cell. The flow conditions here refer to the feed pressure and the feed concentration. The flat cells were operated at cell cross flow velocities of 5, 10, 15, 20, and 25 cm/sec. The flat cell test setup was allowed to equilibrate for 20 minutes before the permeate is collected. The permeate from each test is collected for 10 minutes.

The conditions tested were

- Flat cell feed flow velocity is 5, 10, 15, 20, and 25 cm/sec or 0.1, 0.2, 0.3, 0.4, and 0.5 GPM
- Feed concentration was kept constant at 2000 ppm
- Temperature is 25°C
- Net driving pressure is 225 psi
- pH is kept constant at 8

The tests were repeated 14 times to create a complete dataset.

A proprietary flat-cell normalization algorithm was used to normalize the data acquired from the different tests. Table 5-2 shows the normalized data recorded during the experiment.

Table 5-2: Data from feed spacer concentration polarization experiment

	Feed flowrate (GPM)	0.1	0.2	0.3	0.4	0.5
	Feed velocity (m/sec)	0.05	0.10	0.15	0.20	0.25
	Reynolds Number	80	159	239	319	398
Test Number	Permeate flux J (m/sec)	Salt Passage SP				
Test 1	1.47E-05	0.0031	0.0031	0.0029	0.0029	0.0028
Test 2	1.44E-05	0.0031	0.003	0.003	0.0029	0.0029
Test 3	1.43E-05	0.0036	0.0033	0.0032	0.0031	0.0031
Test 4	1.40E-05	0.0034	0.0031	0.0031	0.003	0.0029
Test 5	1.35E-05	0.0035	0.0034	0.0033	0.0032	0.0032
Test 6	1.34E-05	0.0038	0.0035	0.0034	0.0033	0.0033
Test 7	1.32E-05	0.0034	0.0032	0.0031	0.0031	0.003
Test 8	1.30E-05	0.0034	0.0034	0.0033	0.0032	0.0032
Test 9	1.27E-05	0.0039	0.0036	0.0035	0.0034	0.0034
Test 10	1.25E-05	0.0038	0.0038	0.0037	0.0036	0.0036
Test 11	1.22E-05	0.004	0.0037	0.0037	0.0036	0.0035
Test 12	1.19E-05	0.004	0.0037	0.0036	0.0035	0.0035
Test 13	1.18E-05	0.004	0.0039	0.0038	0.0036	0.0036
Test 14	1.09E-05	0.0041	0.0039	0.0039	0.0038	0.0038

From the previous section, the *Membrane B values* were estimated at 0.085 GFD which corresponds to 3.99E-8 m/sec. Substitution of this value as the assumed *Membrane B value* in Equation (5.5) gives the concentration polarization estimate in each test as

$$CP = \frac{SP(J+B)}{B} \tag{5.5}$$

where CP is the concentration polarization, SP is the salt passage, J is the permeate flux, and B is the M*embrane B value*

In Equation (5.5), the salt passage SP and membrane flux J are shown in Table 5-2 where the *Membrane B value* is assumed as 0.085 GFD. Table 5-3 shows the value of concentration polarization calculated from Equation (5.5).

Table 5-3: Experimentally calculated concentration polarization

	Feed flowrate (GPM)	0.1	0.2	0.3	0.4	0.5
	Feed velocity (m/sec)	0.05	0.10	0.15	0.20	0.25
	Reynolds Number	80	159	239	319	398
Test Number	Permeate flux J (m/sec)	Concentration Polarization				
Test 1	1.47E-05	1.144	1.144	1.070	1.070	1.033
Test 2	1.44E-05	1.120	1.084	1.084	1.048	1.048
Test 3	1.43E-05	1.292	1.184	1.148	1.112	1.112
Test 4	1.40E-05	1.195	1.089	1.089	1.054	1.019
Test 5	1.35E-05	1.186	1.152	1.119	1.085	1.085
Test 6	1.34E-05	1.278	1.177	1.144	1.110	1.110
Test 7	1.32E-05	1.123	1.057	1.024	1.024	0.991
Test 8	1.30E-05	1.110	1.110	1.077	1.044	1.044
Test 9	1.27E-05	1.244	1.148	1.116	1.084	1.084
Test 10	1.25E-05	1.193	1.193	1.162	1.130	1.130
Test 11	1.22E-05	1.226	1.134	1.134	1.103	1.073
Test 12	1.19E-05	1.196	1.106	1.076	1.046	1.046
Test 13	1.18E-05	1.186	1.156	1.126	1.067	1.067
Test 14	1.09E-05	1.123	1.068	1.068	1.041	1.041

A value of concentration polarization less than one can be seen in the results shown in Table 5-3. This error is possible from an incorrect assumption of the *Membrane B value*. The *Membrane B value*s of these membrane were assumed, and not measured.

The Sherwood number is estimated for the flow in the flat cells by rearranging Equation (3.59)

$$Sh = \frac{d_h.J.(1-SP)}{(CP-1).D} \tag{5.6}$$

The d_h of the feedwater channel is 56-mil and the molecular diffusion coefficient of salt in water is set at 1.5E-9 m²/sec. Table 5-4 shows the Sherwood number calculations.

Table 5-4: Experimentally observed Sherwood number

	Reynolds Number	80	159	239	319	398
Test Number	Permeate flux (m/sec)	Sherwood Number				
Test 1	1.47E-05	96.7	96.7	199.0	199.0	422.1
Test 2	1.44E-05	113.0	161.5	161.5	282.9	282.9
Test 3	1.43E-05	46.3	73.3	91.1	120.2	120.2
Test 4	1.40E-05	67.9	148.3	148.3	244.6	698.6
Test 5	1.35E-05	68.4	83.7	107.6	150.7	150.7
Test 6	1.34E-05	45.5	71.4	88.1	115.0	115.0
Test 7	1.32E-05	101.0	218.2	519.0	519.0	-
Test 8	1.30E-05	112.1	112.1	159.7	277.5	277.5
Test 9	1.27E-05	49.2	81.1	103.4	142.7	142.7
Test 10	1.25E-05	61.2	61.2	73.1	90.7	90.7
Test 11	1.22E-05	51.0	86.1	86.1	111.7	158.8
Test 12	1.19E-05	57.4	105.9	147.4	242.4	242.4
Test 13	1.18E-05	60.0	71.5	88.2	166.3	166.3
Test 14	1.09E-05	83.6	150.6	150.6	251.3	251.3

Data from Tests 1, 4 and 7 were considered outliers because those data lie outside the mean plus or minus three sigma. These data were discounted in the plot shown in Figure 5.15, which shows the data shown in Table 5-4 plotted on graph and compares the results with the Sherwood number predicted based on CFX simulations.

The large variation in *Membrane B values* resulted in a large variation in the estimation of the experiment-based Sherwood number of the flow through the feed spacer. In Figure 5.15, the Sherwood number determined by CFX simulation lie within the cloud of experimental data, which suggests a satisfactory, fit.

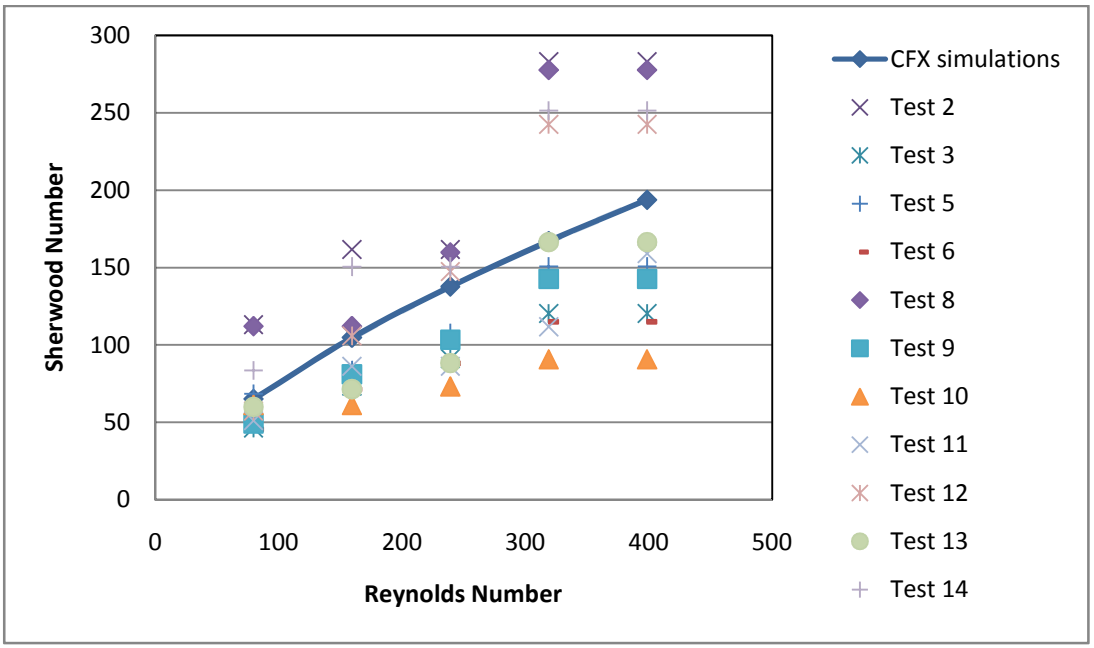

Figure 5.15: Comparison of the Sherwood number between experiment and simulation

5.4 Conclusion

The experimental data show that the correlation equations- Equations (4.5) and (4.7) give a good estimation of the feed spacer pressure drop and the feed spacer Sherwood number. The feed spacer is observed to deform during the RO element manufacturing process. The force applied on the feed spacer--membrane interface is sealed tight when the spiral wound RO element is encapsulated in a fiberglass shell as the final product. The feed spacer is also found to be in a stretched position when inserted in the RO element, thereby creating deformation from the original raw material.

There is no known method to estimate the *Membrane B value* and the concentration polarization simultaneously. In the foregoing exploration, the membrane concentration polarization and the Sherwood number were estimated assuming that the *Membrane B value* was equal to the RO membrane manufacturer's specification. Subtle variations in the *B value*s result in a large variation in the estimation of the Sherwood number. The CFX-based estimation of the Sherwood number falls within the cloud of experimentally deduced Sherwood numbers.

Chapter 6 : ENTRY AND EXIT PRESSURE DROP

6.1 Introduction

In this chapter, the magnitude of the pressure drop that occurs due to feedwater entering and leaving the element is calculated using numerical simulation. Later, the significance of the inlet and the exit feed pressure drop on the entire RO operation is discussed.

6.2 Discussion of the geometry

The geometry used for the numerical simulation is comprised of a pressure vessel and a representative element into which the feedwater flows in or out. An 8-inch element constructed with a 25-mil feed spacer and a 1.5-inch product water tube installed in an 8-inch element pressure vessel is simulated as the geometry. In Figure 6.1, the region of the RO pressure vessel that is chosen for simulation is enclosed in red in the left portion of the figure. A much enlarged view shaded gray in the right portion of the figure provides details relevant to the actual setup of the simulation. The configuration on the left side of Figure 6.1 is a cut section of Figure 2.15. The reader may refer to Figure 2.15 for the diagram of three RO elements inside a pressure vessel.

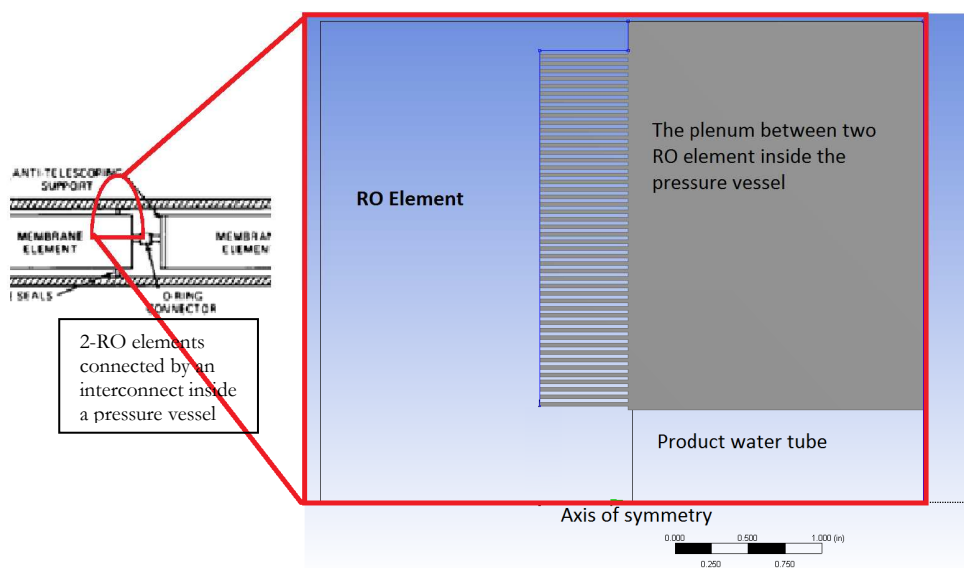

Figure 6.1: Diagram of the CFX simulation domain

The spiral winding of the RO element is simulated by concentric annuli. Figure 6.2 shows the difference between the spiral-wound RO (SPRO) element and the simulated geometry.

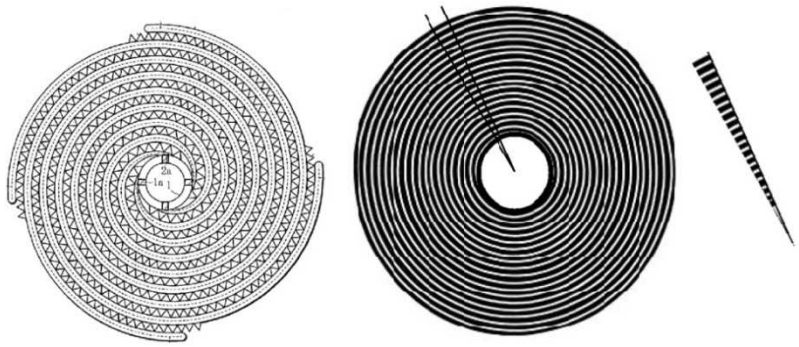

(a) (b) (c)

Figure 6.2: Diagram of a spiral RO element (a), modeled as concentric annuli (b) and simulated as a wedge (c)

In view of axisymmetry, a narrow wedge as show in Figure 6.2 (c) is sufficient for the numerical simulation. Experience has taught that a 3º wedge is suitable. The use of a wedge greatly diminishes the number of nodes required to perform the numerical solution. The center of the wedge is at the axis of the product water tube, and the outer boundaries are the fiberglass shell, the end-caps, and the brine seal. The center of the wedge that constitutes the product water tube also houses the O-ring interconnect. Figure 6.3 shows the mesh used for this simulation. This mesh comprises 455,210 nodes and 222,240 elements. The mesh is rectangular with sufficient care taken to prevent high aspect ratios. The mesh density is increased at the regions that constitute no-slip walls.

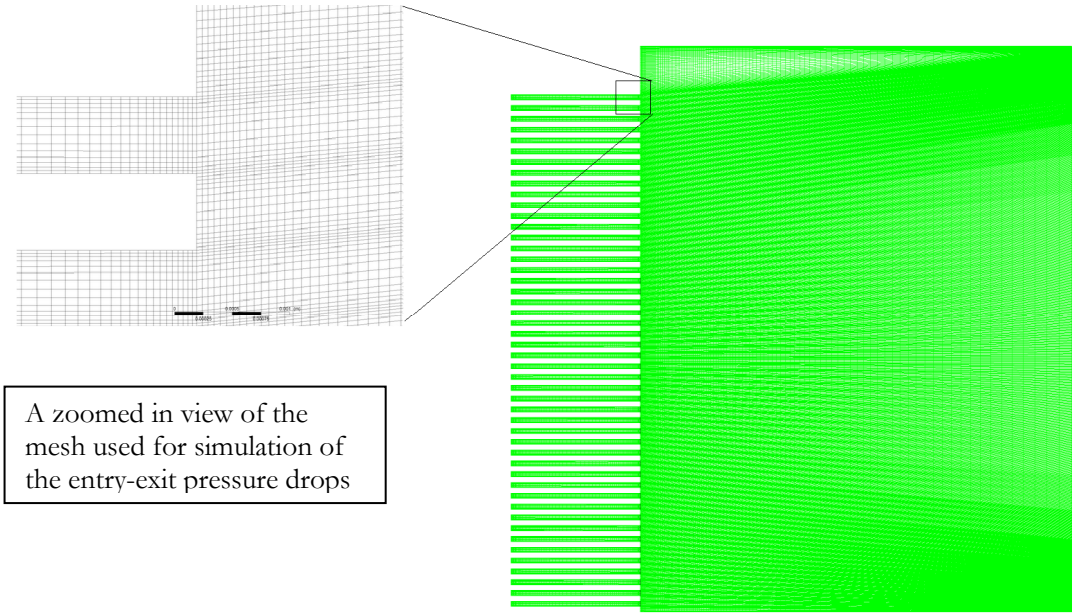

Figure 6.3: Diagram of the mesh used in the simulation

6.3 Boundary conditions

The side view of the wedge used for the simulation is shown in Figure 6.4. The two sides of the simulation domain that constitute the openings (inlet or exit) are shown in green.

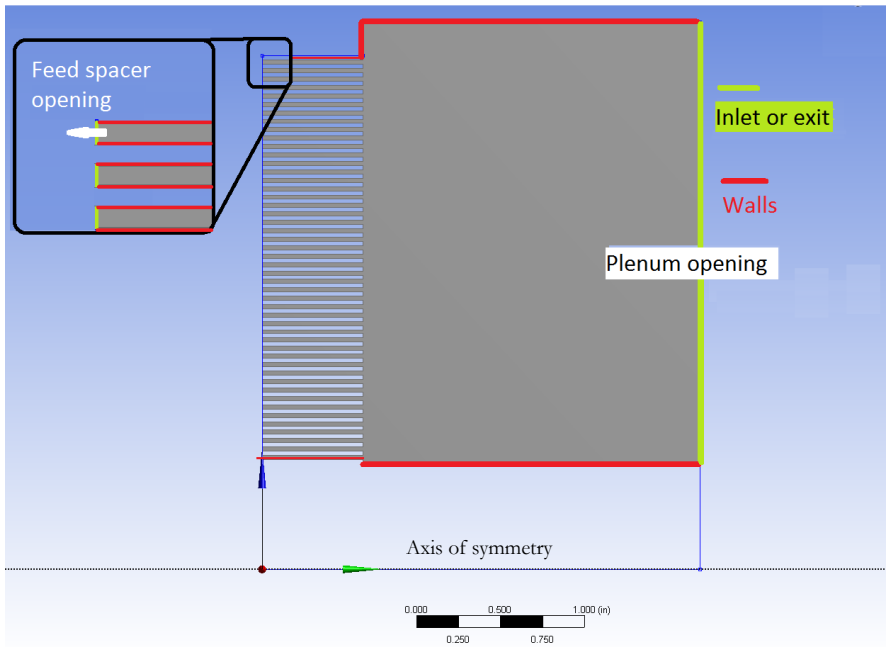

Figure 6.4: Simulation domain and the boundary conditions

When the simulation is run to analyze the entry pressure loss, the plenum opening becomes the inlet, and the feed spacer opening becomes the outlet. Conversely, when the simulation is run to determine the exit pressure drop, the plenum opening becomes the outlet, and the feed spacer opening becomes the inlet. The two sides of the wedge provide symmetric boundary conditions. All the other boundaries are no-slip walls. The boundaries that comprise the walls are shown in red color in Figure 6.4. The no-slip wall condition is attributed to the boundaries that comprise:

- the product water tube,
- the end caps,
- the membranes,
- the glue lines,
- the brine seals, and
- the pressure vessel walls

The fluid flow in the simulation is driven by pressure. Pressure-driven flow simulations calculate a more accurate velocity profile, relative to the standard flat velocity profile at the boundaries. Pressure

differences of 5 to 100 Pa in increments of 10-15 Pa are applied across the openings in either direction to simulate the flow in and out of the RO element.

The shear stress transport- k-ω turbulence model is used in the simulation as the flow is in the transition zone. As discussed earlier, the flow in the feed spacer is laminar whereas the flow in the plenum inside the pressure vessel is turbulent. The velocity of the feedwater flowing inside the plenum is of the order of a few centimeters a second. As the diameter of the pressure vessel is over 20 centimeters. The Reynolds number of the flow inside the plenum is over 3000.

6.4 Results and discussion

6.4.1 Entry pressure drop

In this section, a pressure difference of 5, 10, 20, 30, 40, 50, 75, and 100 Pa are applied, with the plenum opening at a higher pressure than the feed spacer opening. Figure 6.5 show the velocity of the feed flow corresponding to these applied entry pressure differences.

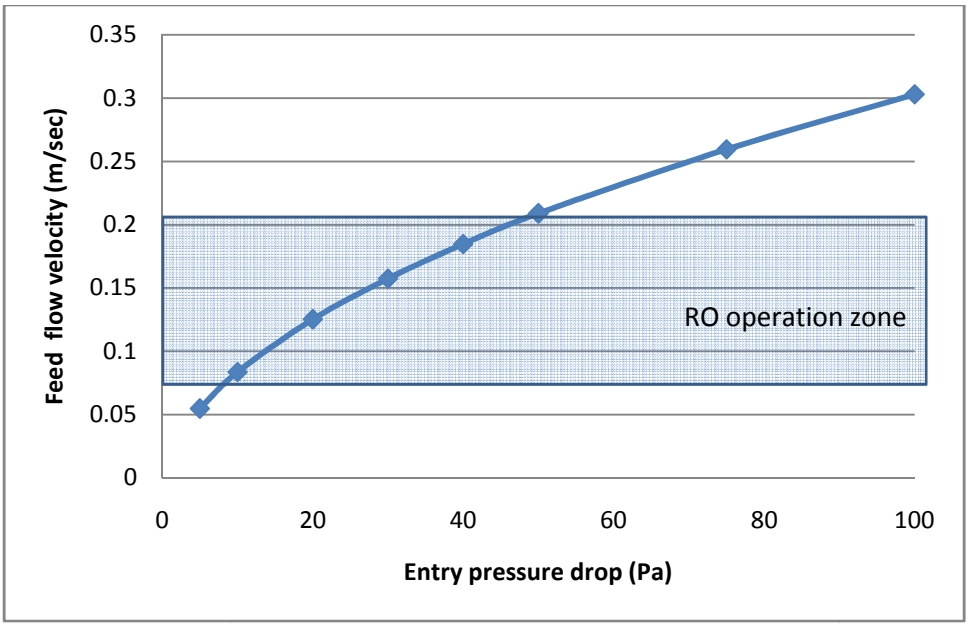

Figure 6.5: Plot of entry pressure drop and the feed flow velocity

The first observation made from Figure 6.5 is that the entry pressure drop is less than 200 Pa or 0.02 psi. A pressure drop of 0.02 psi is insignificant when the operating pressure is of the order of hundreds of pounds per square inch. Further, even in the RO elements at the tail end of the RO system, the net driving pressure is maintained greater than 10 psi to prevent accidental osmosis of

water from the permeate to the feed stream. Variations and disturbances of the order of 0.02 psi are truly negligible.

The pressure contour diagram of the flow for an entry pressure of 50 Pa is shown in Figure 6.6. It may be observed that the pressure increases near the corners where the flow velocity is low.

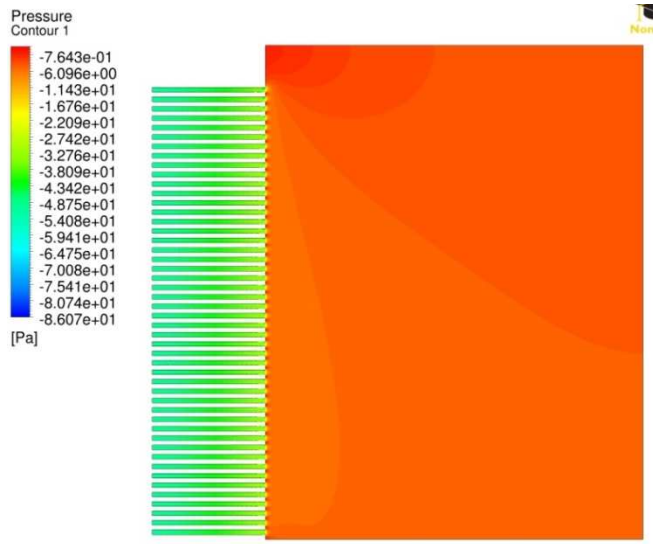

Figure 6.6: Pressure contour diagram of entry pressure drop of 50 Pa

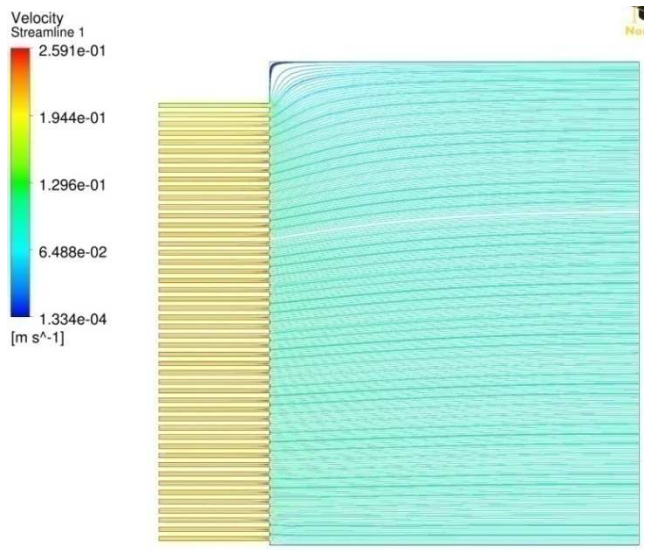

Figure 6.7: Simulated streamlines of the flow entering the RO vessel

Figure 6.7 shows the streamlines for the flow entering the RO element. No large recirculation zones were observed in the simulated flow. The colors of the streamlines represent the velocity of the flow.

In Figure 6.8, the radial variation of the axial flow velocities is shown. The maxima are in the annular spaces that represent the feed spacer and the minima represent the glue line walls between the feed spacer annuli.

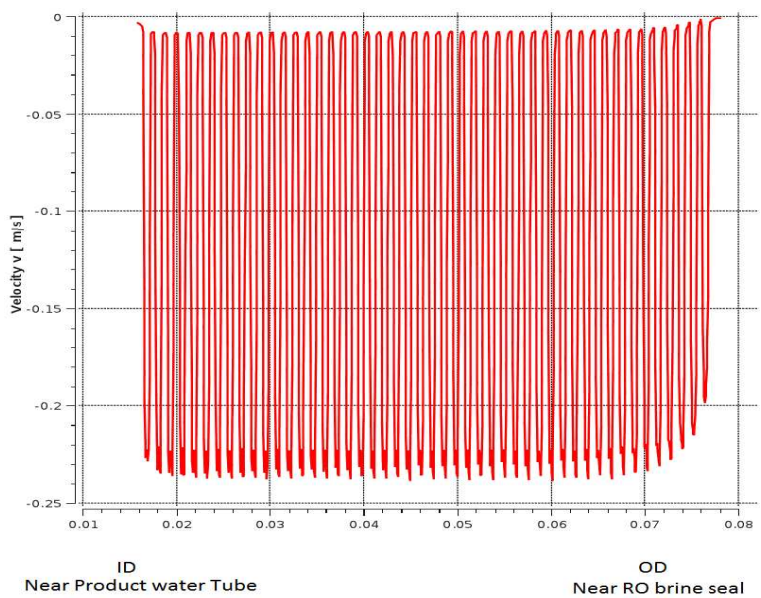

Figure 6.8: Radial variation of feedwater axial velocities in the feed spacers

From Figure 6.8, one may observe that the bulk velocities entering each annular channel are uniform. The magnitude of the velocity entering the annulus adjacent to the OD of the spiral wound element is seen to be somewhat lower than in other regions. This behavior is attributed to the viscous drag caused by the wall of the pressure vessel. Furthermore, when the pressure drop across the whole length of the element is taken into account, this radial variation of the bulk feedwater velocity will be inconsequential, as the effective bulk velocity of the feed flow in each annulus will be determined by the feed spacer *pressure drop factor* and not the entry or the exit pressure drop.

In Figure 6.9, lines 1, 2, and 3 represent the flow into the annulus near the product water tube, the middle and near the brine seal of the element, respectively. The pressure (Figure 6.10) and the velocity (Figure 6.11) variations along lines 1, 2, and 3 are plotted.

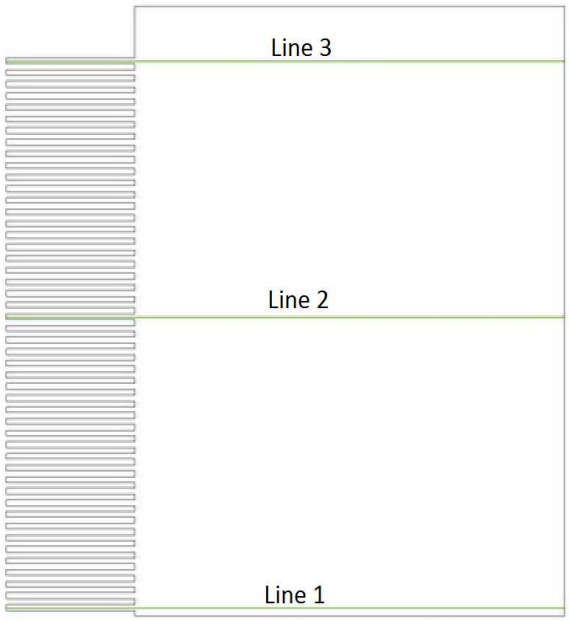

Figure 6.9: Picture showing the location of lines where pressure and velocity changes are plotted

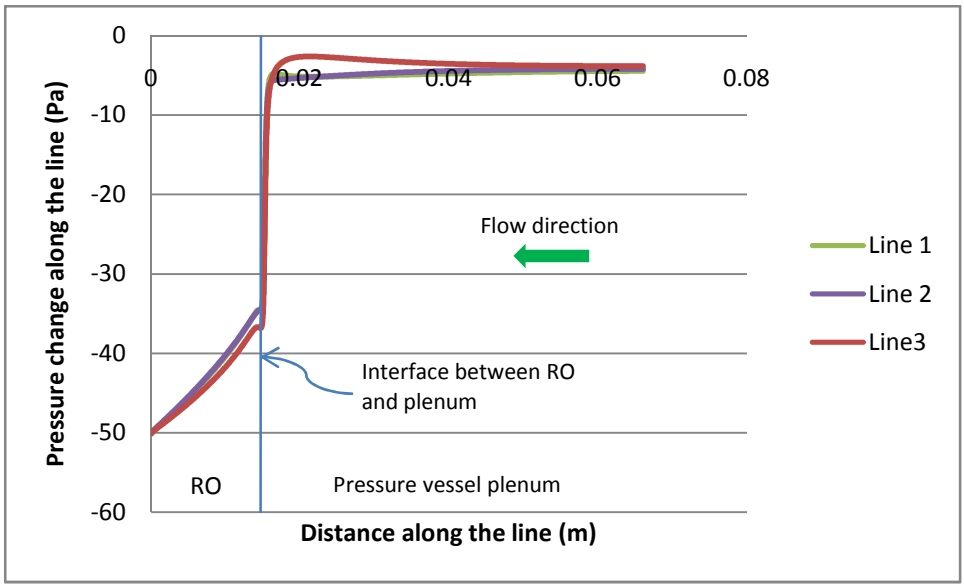

Figure 6.10: Axial pressure variations at different radial positions for flow entering the RO element

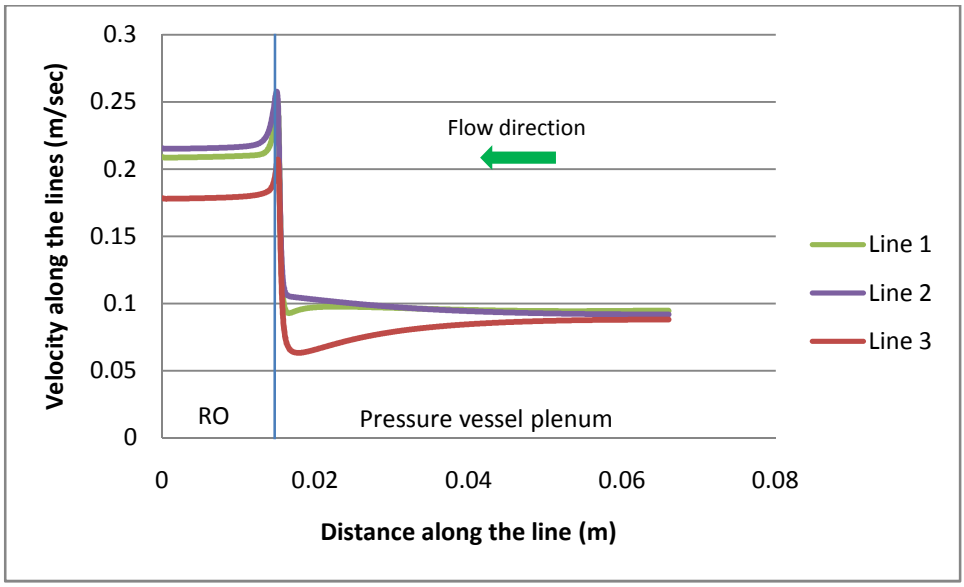

Figure 6.11: Axial velocity variations at different radial positions for flow entering the RO element

From Figure 6.10, a steep drop in static pressure is observed as the feedwater enters the RO element feed spacer. The pressure along *Line 3,* near the OD of the pressure vessel, shows a rise in static pressure before entering the RO element. This is caused by the deceleration of the flow along the streamlines. For corroboration, reference may be made to Figure 6.7; it may be observed that the streamlines slow down significantly near the brine seal before entering the RO element. This slowing down behavior is also observed in the velocity plot shown in Figure 6.11. This concave turning of the fluid is also responsible for lower velocities in the feedwater entering the feed spacer near the brine seal. Similarly, the presence of the product water tube and the sharp turning of the flow are responsible for the relatively lower velocity along *Line 1* compared to *Line 2*.

Further from Figure 6.11, a spike may be observed in the velocity after the fluid enters the feed spacer. This is created because the fluid streams cannot abruptly change direction when they enter the feed spacers. The same phenomenon that creates the Vena Contracta causes the velocities to spike.

6.4.2 Exit pressure drop

In this section a pressure difference of 5, 10, 20, 30, 40, 50, 75, and 100 Pa are applied with the feed spacer opening at a higher pressure than the plenum opening. Figure 6.12 show the CFX simulation results.

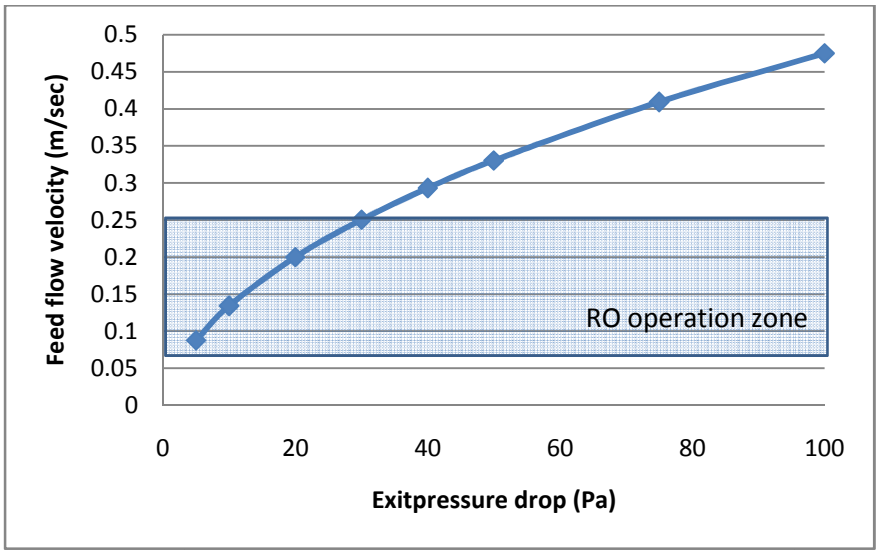

Figure 6.12: Plot of exit pressure drop and the feed flow velocity

Both Figures 6.12 and 6.5 share a similar shape. This shape suggests that the pressure drop is chiefly due to inertial losses because the graph follows $y=\sqrt{x}$ pattern. Another important observation is that the magnitude of the entry pressure drop is greater than that of the exit pressure drop for a given feed velocity. This is shown in Figure 6.13

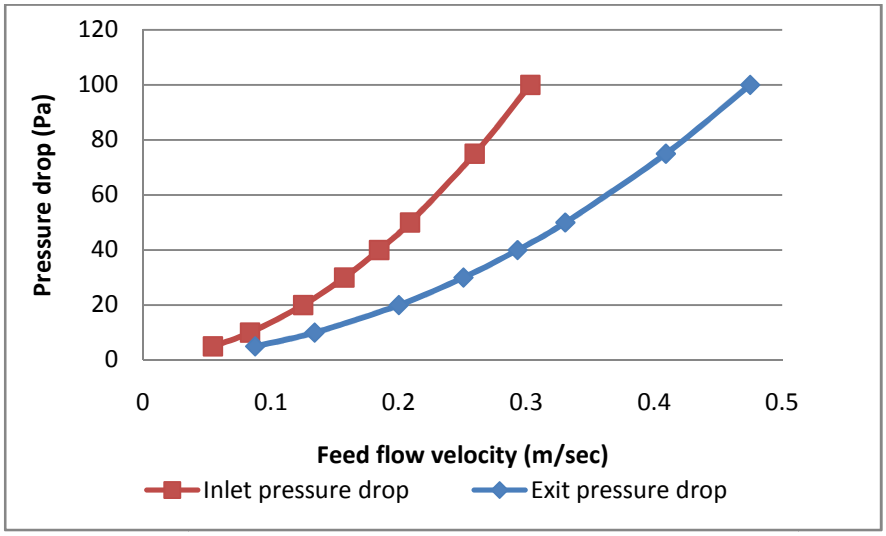

Figure 6.13: Comparing the magnitudes of inlet and exit pressure drops

In a simple potential flow where viscous effects are negligible, the entry pressure drop should be equal and opposite to the exit pressure drop provided the momentum changes are identical. A streamline map of the flow exiting the RO element is plotted to help understand the differences.

From Figure 6.14, the large recirculation zone is evident. Recirculation zones dissipate flow energy. However, the existence of a recirculation zone does not provide the reason for the exit pressure drop to be lower than that of the entry pressure drop.

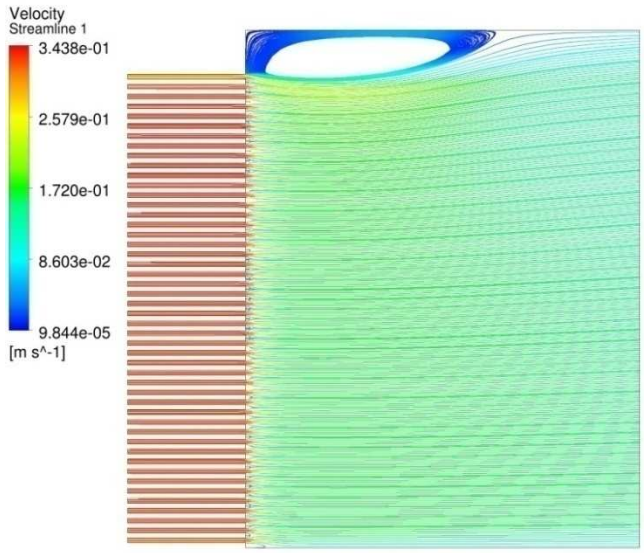

Figure 6.14: Streamlines of the flow exiting the RO element

For further considerations, the pressure (Figure 6.15) and velocity (Figure 6.16) distributions along lines 1, 2 and 3 are analyzed. The location of lines 1, 2, and 3 are shown in Figure 6.9. It may be observed from the pressure and velocity graphs that some pressure is reversibly recovered from momentum. The recovery of pressure from decelerating fluid exiting the feed spacer provides the explanation for the lower exit pressure drop.

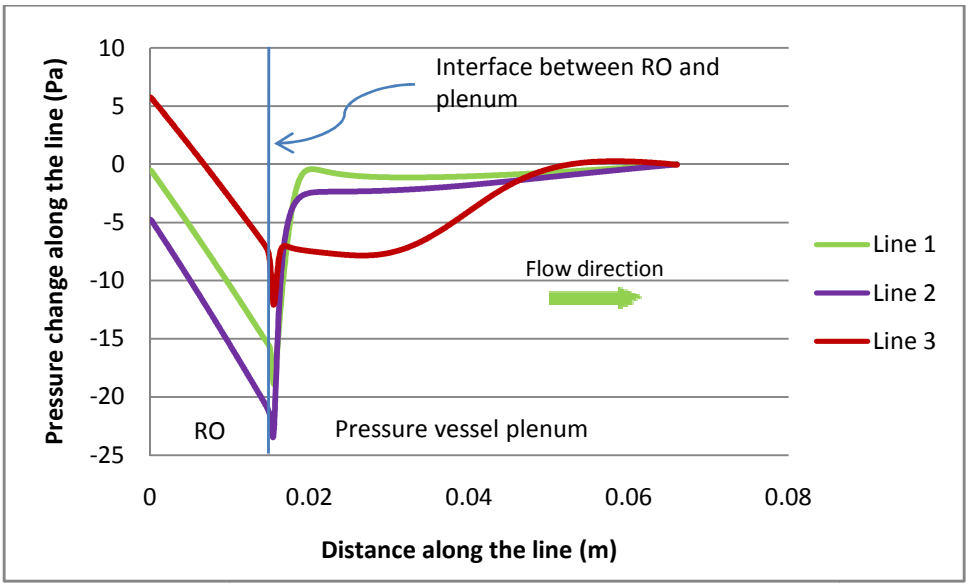

Figure 6.15: Pressure variations at different radial positions for flow exiting the RO element

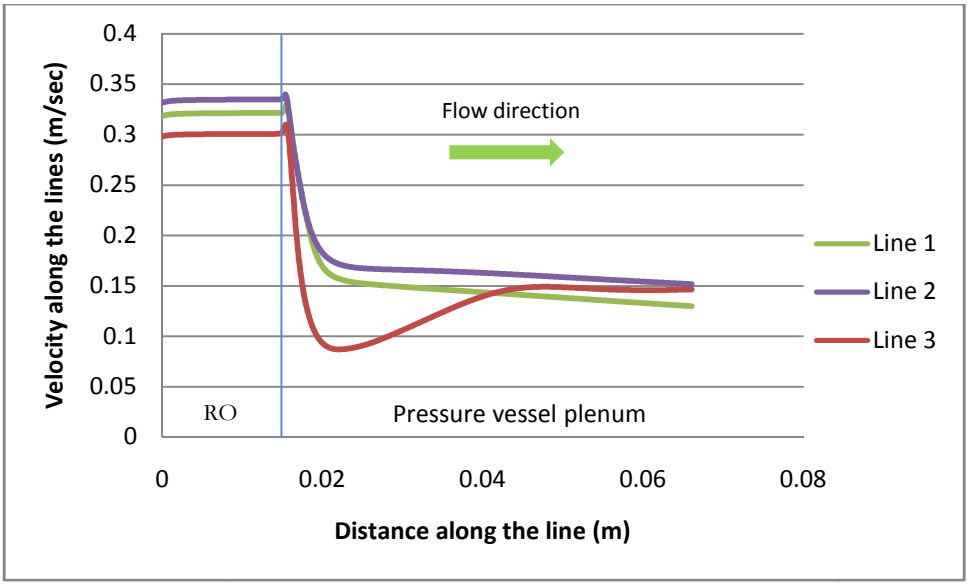

Figure 6.16: Velocity variations at different radial positions for flow exiting the RO element

It may be observed from Figure 6.16 that as the feedwater exits the feed spacers, there is a short spiking in the feedwater velocity. This spiking is caused by the entrainment of fluid. The pockets of fluid behind the glue lines recirculate due to the steep velocity gradient. These micro-eddies constrict the fluid passage and accelerate the flow. The acceleration of flow can also be seen as a momentary

drop in pressure. Later, the feedwater flow area increases, and the flow decelerates. This deceleration of the flow also leads to momentum recovery and a raise in pressure. This behavior is most prominent near the OD of the RO element.

6.5 Conclusion

From the foregoing, it was shown from the CFD simulations that the magnitudes of the inlet and exit pressure drops are insignificant and inconsequential in affecting the RO performance as a whole. The new and improved RO simulation method that will be set forth in the following chapter will not take account of these pressure drops.

Chapter 7 : NEW RO SIMULATION METHOD

7.1 Introduction

In this chapter, a new method to simulate the fluid flow in a RO element is presented. This method reduces the assumptions that are present in current RO simulations. Although this method increases the computational complexity involved in solving RO operations, the accuracy of the calculations outweighs the cost of computation. Ideas described in previous chapters are brought together to make a meaningful and working computer algorithm that can solve the fluid flow in an RO element. The algorithm used to solve the fluid flow in an RO element is shown in Appendix A. The reader is encouraged to refer to the algorithm in Appendix A in conjunction with this chapter. The focus of this chapter is to provide a systematic description of the algorithm. Key implementation routines are discussed in detail to enable better understanding of the overall code.

7.2 Method of RO discretization

The following analysis demonstrates a comprehensive way to simulate the performance of the RO element. In this simulation, one half-leaf of an RO element is modeled. If the RO element has, for example, 25 leaves, then the performance of the RO element is found by scaling up the flow values by 50 times. Readers can refer to Figures 2.4 and 2.5 to see the positioning and the construction of the RO leaf. One half-leaf consists of a single membrane sheet with a feed spacer on the feed side of the membrane and the permeate spacer on the product waterside of the membrane. Figure 7.1 shows a diagram of a typical half-leaf.

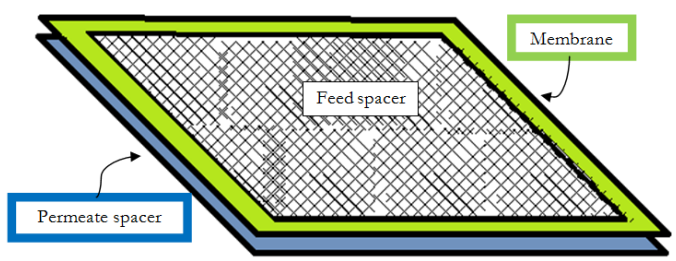

Figure 7.1: Diagram of a typical half of a leaf

The RO membrane sheet is discretized in two directions: (1) along the direction of the feedwater flow in the feed spacer, and (2) along the length of the product water flow in the permeate spacer. Then, the half-leaf is divided into N subdivisions along the direction of the feedwater flow and M subdivisions along the direction of the permeate water flow. Feedwater flow and the permeate water flow directions have been explained in-detail in Chapter 2 in Figures 2.5 and 2.6. Figure 7.2 shows how the discretization is achieved, looking at the face of the membrane.

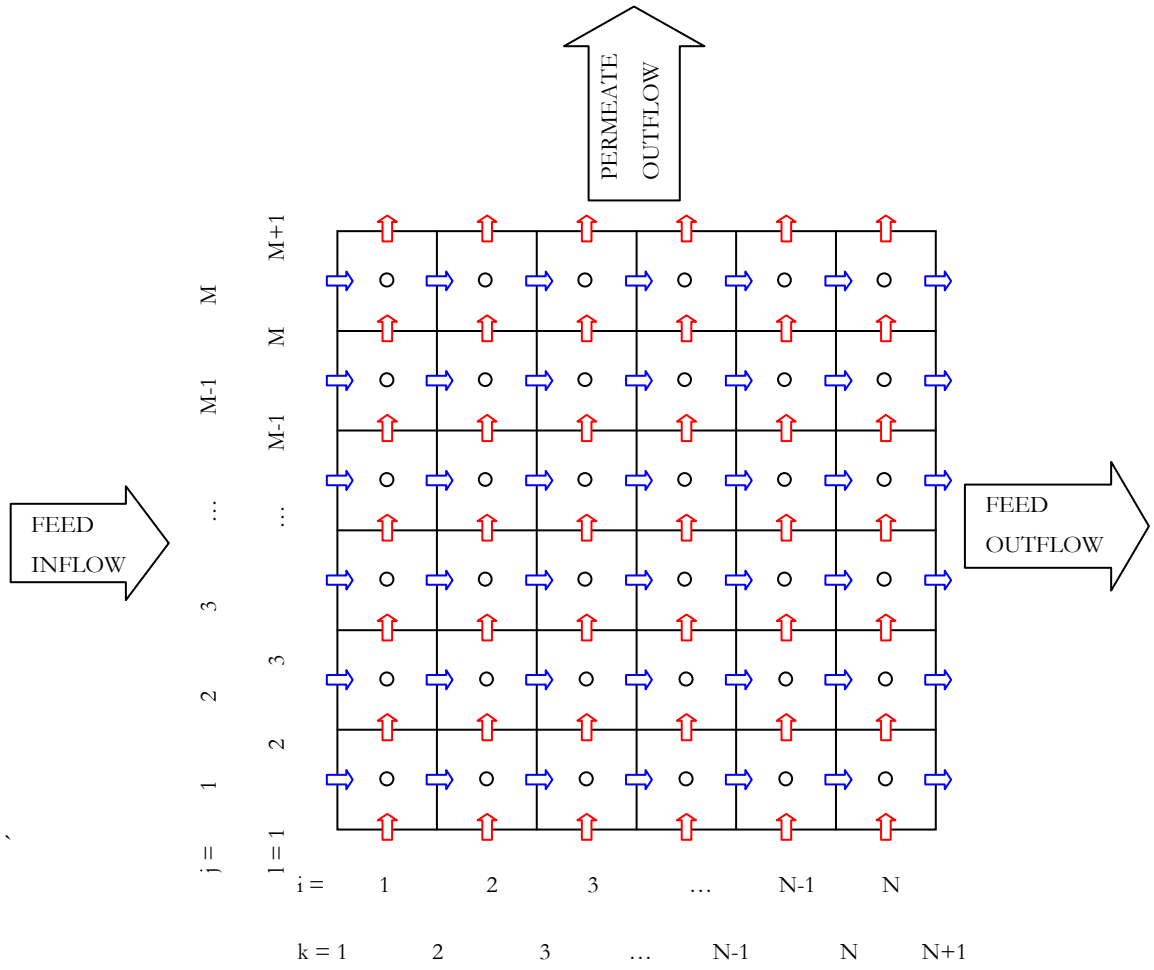

Figure 7.2: Discretization of the membrane sheet in an RO element

From Figure 7.2, it may be observed that the face of the membrane is divided into discrete rectangular *element*s (The word *element* is italicized when it refers to the discrete elements used in modeling in contrast to the reference to an entire RO element). Every rectangular *element* consists of faces and edges. The face of the *element* is represented in Figure 7.2 by the symbol o. The indices *(i, j)*

are used to identify each discrete face. The following properties of the RO operations are described on the faces: feed pressure, permeate pressure, feed concentration, permeate concentration, wall concentration, feed osmotic pressure, permeate osmotic pressure, membrane properties (*A and B values*), net driving pressure, permeate flux, and permeate pressure.

The edges are shown with arrows bisecting to indicate two types of flow directions. The blue arrows ⇨ denote the flow of feed water in the feed spacer. Indices (*k, j*) is used to denote these edges. The feed flow direction is described on the edge shown in blue. The arrows shown in red ⇧ denote the flow of the permeate water in the permeate spacer. The direction of the permeate flow in the permeate spacer is described on the edge by the arrow. Indices (*i, l*) is used to denote these edges.

To provide another visual illustration, the arrows shown in Figure 7.2 have been overlaid onto the diagram of Figure 7.1 and a descriptive picture is presented below in Figure 7.3

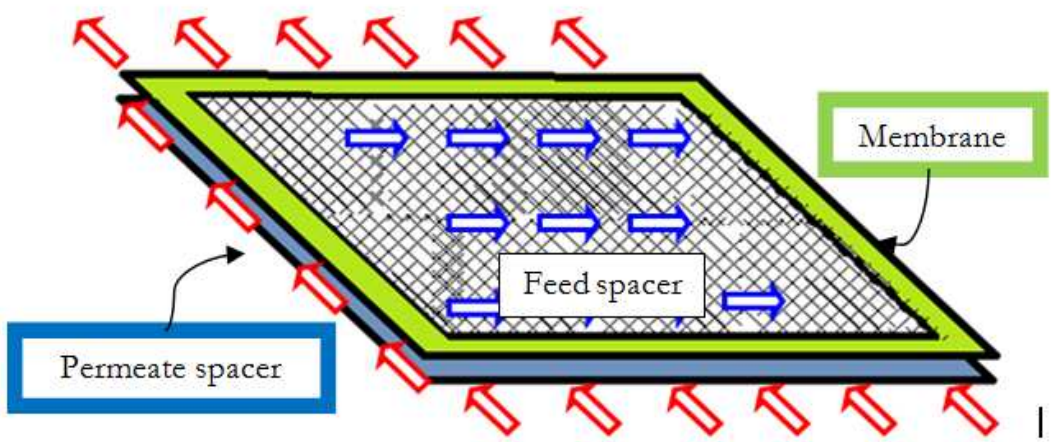

Figure 7.3 : Diagram of the half-leaf with arrows showing feed and permeate flow directions

To reiterate the discretization process,

Figure 7.4 has been prepared to show a small section of Figure 7.2 where the faces and the edges are identified.

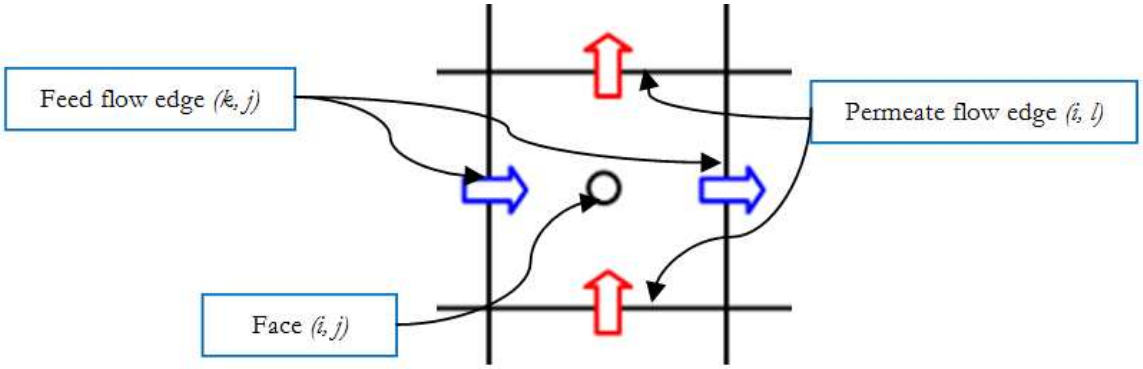

Figure 7.4: Diagram showing the faces and the edges

Figure 7.5 shows an isometric view of the faces and the edges of a single *element* to illustrate the three-dimensional geometry represented in Figure 7.4

.

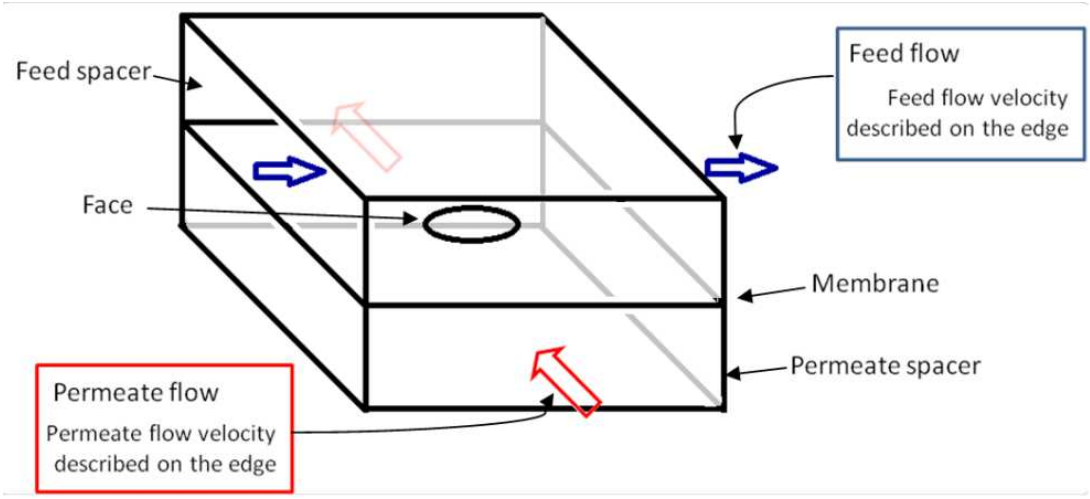

Figure 7.5: Isometric view of the faces and edges

The product water permeates from the feed spacer to the permeate spacer through the face.

7.3 Required user input and its nomenclature

The simulation requires the following user inputs, as shown in Table 7-1

Table 7-1: User input for RO simulations

	Variable name used
1. Property of the membrane	
a. the membrane water permeability (*Membrane A value*)	*A(i, j)*
b. the membrane salt permeability (*Membrane B value*)	*B(i, j)*
2. Property of the RO element	
a. length of the RO element	*L_elem*
b. length of the each leaf in RO element	*L_leaf*
c. number of leaves in the RO element	*Leaf_Num*
d. geometry of the feed spacer	
i. strand angle	*Spcr_ang*
ii. spacer thickness	*Spcr_thick*
iii. strand spacing	*Spcr_spacing*
e. property of the permeate spacer	
i. hydrodynamic resistance	*XP(i, j)*
ii. thickness of the permeate spacer	*d_perm*
3. Pressure of the feedwater entering the RO element	*F_in_press*
4. Flowrate of feedwater	*F_in_flow*
5. Concentration of the feedwater	*F_in_conc*
6. Temperature of the feedwater	*F_in_temp*
7. Permeate back pressure	*P_in_pres*
8. Density of the fluid	*rho*
9. Dynamic viscosity of the fluid	*mu*
10. Molecular diffusion coefficient of solvent (salt) in fluid	*Dab*

It can be observed from the table that the user has the ability to vary *Membrane A* and *B* values spatially. This functionality is useful when the RO membrane manufacturers have greater understanding and control over the spatial variation of *Membrane A* and *Membrane B value*s.

7.4 Identification of notation used in the simulation algorithm

Table 7-2 shows the various terms used in the RO fluid-flow simulation algorithm.

Table 7-2: Table for notation used in simulation algorithm

Property	Variable name used
Feed pressure	*FP(i, j)*
Permeate pressure	*PP(i, j)*
Feed concentration	*FC(i, j)*
Feed wall concentration	*WC(i, j)*
Permeate concentration	*PC(i, j)*
Feed osmotic pressure	*FO(i, j)*
Permeate osmotic pressure	*PO(i, j)*
Net driving pressure	*NDP(i, j)*
Permeate flux flowrate	*P_flux(i, j)*
Permeate flux concentration	*P_Conc(i, j)*
Velocity of feedwater in feed spacer	*VF(k, j)*
Velocity of permeate water in tricot	*VP(i, l)*
Length of the discrete *element*	*dx*
Breadth of the discrete *element*	*dy*
Concentration polarization	*CP(i, j)*
Reynolds number	*Re(i, j)*
Spacer *geometry factor*	*X*
Sherwood number	*Sh(i, j)*
Pressure drop factor	*PRDF(i,j)*
Total permeate produced	*P_out_flow*
Concentration of permeate water	*P_out_conc*
Flowrate of concentrate exiting the RO element	*F_out_flow*
Pressure of concentrate exiting the RO element	*F_out_press*

7.5 Simulation initialization

First, the RO sheet must be discretized in to N × M subdivisions as described previously. Large values of N and M are recommended to improve the resolution of the simulation. In the algorithm shown in Appendix A, the values of M and N are both chosen to be 100. Once the discretization is made, the dimensions of each *element* can be calculated.

The following lines are excerpts from the algorithm shown in Appendix A.

The length of the *element dx* is calculated by dividing the length of the RO element by N.

(#1) $dx = L\_elem / N$

Similarly the breadth of the *element* is calculated by dividing the length of the leaf by M

(#2) $dy = L\_leaf / M$

The inlet velocity of the feedwater in the feed spacer is calculated from the flowrate of the feedwater entering the RO element. The feed flow is assumed to be distributed equally to each leaf in the RO element. The area of the cross section of the feed flow can be calculated from the length of the leaf and the thickness of the feed spacer.

(#3) $VF(k = 1, j) = F\_in\_flow / (Leaf\_Num * Spcr\_thick * L\_leaf)$ for all j

where $VF(k = 1, j)$ is the velocity of the feed water near the inlet of the RO element.

The inlet pressure and concentration are specified from the user input

(#4) $FP(i = 1, j) = F\_in\_press$ for all j

(#5) $FC(i = 1, j) = F\_in\_conc$ for all j

7.6 Simulation algorithm

The first operation is to calculate the permeate water flowing the regions $i = 1$. For the first iteration, the pressure of the permeate water in the permeate spacer is set to the user-defined permeate backpressure. This permeate back pressure is the pressure of the permeate in the product water tube.

(#6) $PP(i = 1, j) = P\_in\_pres$ for all j

The hydraulic diameter is given by twice the feed spacer thickness as shown in Equation (3.47).

(#7) *d_hyd = 2 * Spcr_thick*

The Reynolds number for any *(i, j)* is calculated from the feed flow velocity using Equation (2.2).

(#8) *Re(i, j) = rho * VF(k, j) * d_hyd* where *k = i* (numerically)

The Reynolds number is necessary to predict the Sherwood number, and thereby, the concentration polarization. If the strand angle *Spcr_ang* = 90º, Equation (4.7) can be used to calculate the Sherwood number.

The spacer *geometry factor X* is given by Equation (4.3).

(#9) *X = Spcr_thick / Spcr_spacing*

The Schmidt number for the flow is calculated using the properties of the working fluid from Equation (2.10)

(#10) *Sc = mu / (rho * Dab)*

The Sherwood number is given by Equation (4.7). This Sherwood number is calculated from the parametric Sherwood number equation derived from CFX simulations described in Chapter 4. This equation is represented in the algorithm as

(#11) *Sh(i, j) = (-41 * X^2 + 22.85 * X - 2.52) * ((Re(i, j) / 0.71) ^0.65 - 1.36) * Sc^0.33*

The concentration polarization can be calculated only after the permeate flux *P_flux (i, j)* through the membrane is known. Since the permeate flux is unknown for the first iteration, the concentration polarization is assumed to be one (*CP (i, j) = 1)*.

The feed osmotic pressure is calculated using the Equation (2.14). Specialized and customized osmotic pressure calculations can be used when Equation (2.14) is inadequate.

(# 12) *FO(i, j) = 0.255 * F_in_temp * FC(i, j) * CP (i, j)*

The mass fraction of salt in the permeate is unknown, the concentration of the permeate is assumed to be zero for the first iteration. (*PC (i, j) = 0)*.

The permeate osmotic pressure is always given by

(# 13) *PO(i, j) = 0.255 * F_in_temp * PC(i, j)*

The net driving pressure expression is given by Equation (2.37).

(#14) $NDP(i, j) = FP(i, j) - FO(i, j) + PO(i, j) - PP(i, j)$

The permeate flux seeping through each discrete *element* is given by Equation (2.16).

(#15) $P\_flux\ (i, j) = A(i, j) * NDP(i, j)$

The concentration polarization is given by Equation (4.11).

(#16) $CP(i, j) = (1 + ((d\_hyd * P\_flux\ (i, j)) / (Sh(i, j) * Dab))) / \ldots$
$(1 + ((d\_hyd * P\_flux\ (i, j) * B(i, j)) / (Sh(i, j) * Dab * (P\_flux\ (i, j) + B(i, j))))$

Line numbers (#12) to (#16) are iterated until the value of CP(i, j) does not vary by more than 0.01% between iterations.

With the updated value of $P\_flux\ (i, j)$, the permeate spacer pressure drop is evaluated.

The permeate spacer meets the product water tube at $j = M$. The permeate pressure pressure in the spacer where the permeate spacer meets the tube is equal the the pressure in the product water tube.

(#17) $PP\ (i, j = M) = P\_in\_pres$ for all i

The velocity distribution of the permeate is given by cumulatively adding the permeate flux from every discrete *element*. The velocity of the permeate flow at $l = 1$ is zero as at $l = 1$, since the permeate channel is sealed with glue on the top edge.

(#18) $VP\ (i, l = 1) = 0$ for all i

For inlet conditions where $i = 1$, the velocity of the permeate is given by

(#19) $VP\ (i, l+1) = VP\ (i, l) + 2 * P\_flux\ (i, j) * dx * dy / d\_perm$ for all i and $l = j$

With known values of $VP(i,l)$ for a given i, the permeate pressure $PP(i,j)$ is calculated from Equation (2.31).

(#20) $PP(i, j-1) = PP(i, j) + VP(i, l) * XP(i, j) * d\_perm * dy$

With the updated values for permeate pressures, line numbers (#12) to (#20) are iterated until the value of $PP(i, j)$ does not vary by more than 0.01% between iterations for all values of j.

With updated values of permeate pressure *PP(i, j)*, the permeate concentration is updated iteratively.

The quality of the permeate flux permeating from the membrane is give by Equation (2.18) and Equation (2.25).

(#21) $P\_Conc(i, j) = (B(i, j) * CP(i, j) * FC(i, j)) / (P\_flux (i, j) + B(i, j))$

The concentration of the permeate flow is given by the mass average of the permeate flowing along the permeate spacer and the permeate permeating through the RO membrane. This balance is shown pictorially in Figure 7.6.

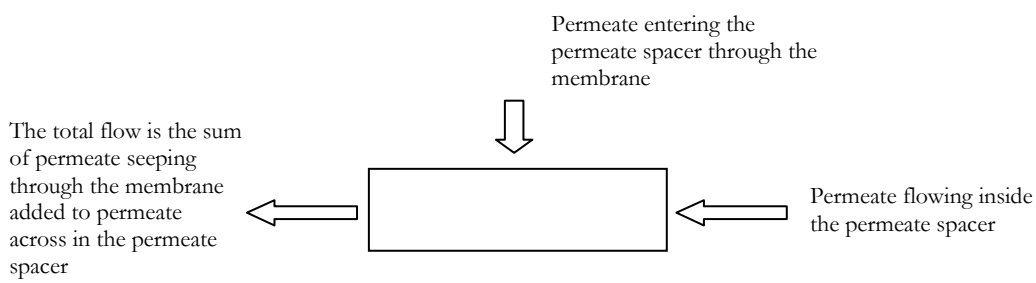

Figure 7.6: Pictorial representation of flow in the permeate spacer in each discrete element

For all positions *i*, the concentration of permeate at $j = 1$ is the concentration of the permeate flowing through the membrane.

(#22) $PC(i, j = 1) = P\_Conc(i, j = 1)$ for all *i*

The concentration of permeate is updated for other locations of *j* as

(#23) $PC(i,j) =(VP(i, l-1) * PP(i, j-1) * d\_perm + 2* P\_conc(i, j) * P\_flux(i, j)) * dy) / VP (i, l)$

With the updated values for permeate concentrations, line numbers (#12) to (#23) are iterated until the value of *PC(i, j)* does not vary by more than 0.01% between iterations for all values of *j*.

It may be observed that the aforementioned technique uses three loops: one is nested inside the other to fine tune the concentration polarization, permeate pressure, and permeate concentration respectively. A single iteration loop can be used; however, under certain extreme conditions, the algorithm has the tendency to become unstable and increase the computational time. Hence, the

simulation loops were tailored to update the most significant variable (concentration polarization) first and placing the least significant variable (permeate concentration) last. Concentration polarization is considered the most significant variable since minor changes in the concentration polarization results in major changes in the final simulation results when compared to the permeate water concentration.

At this point, all of the properties of the fluid flow in the domain $i = 1$ and $k = 1$ have been calculated.

With the discretization of the membrane, the velocity of the feed water for $k = 2$ can be calculated in one of two ways. The most appropriate way to calculate the velocity of the feedwater is

(#~24)[1] $VF(k, j) = (VF(k-1, j) * Spcr\_thick - P\_flux(i, j) * dx) / Spcr\_thick.$

However, an issue that arises is that $VF(k, j)$ is not the same for all values of j. The variation in the value of $VF(k, j)$ across different values of j causes flow of feedwater perpendicular to the pressure gradient. This flow is called the cross feed flow. Experiments have yet to be conducted in order to understand the pressure drop in the feed spacer cause by the cross feed flow.

The cross feed flow is less than 0.01% of the feed flow under standard operating conditions. Therefore, this flow is neglected and the line number (#~24) is modified to be

(#24) $VF(k, j) = (VF(k-1, j) * L\_leaf * Spcr\_thick - VP(i, M+1) * d\_perm * dx) / ...$
$(L\_leaf * Spcr\_thick)$ for all j

The assertion made in the foregoing sentence is represented pictorially in Figure 7.7.

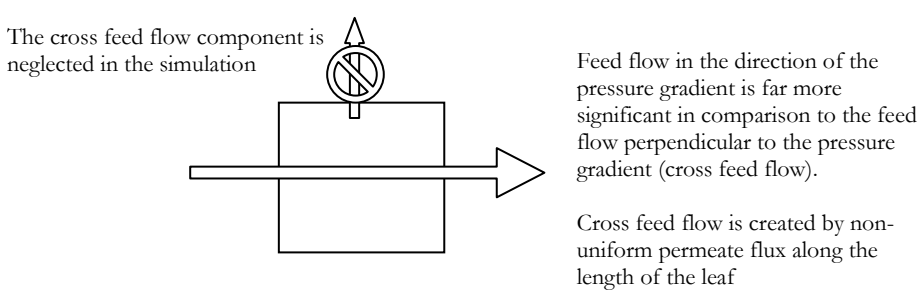

Figure 7.7: Description of the approximation made in the simulation.

[1] A ~ in front of the equation line number means that the cited code in the line number is not used in the simulation algorithm.

The *pressure drop factor* must be estimated from the Reynolds number in order to calculate the pressure drop.

The Reynolds number is calculated by line number (#7)

(#25) $Re(i, j) = rho * VF(k, j) * d\_hyd$ where $k = i$ (numerically)

The Forchheimer equation for the pressure drop factor with the Darcy and the Forchheimer terms is used in this simulation. The derivation of the Forchheimer equation is discussed in detail in Chapter 4. The *pressure drop factor* is given by Equation (4.5).

(#26) $PRDF(i, j) = (1493 / Re(i, j)) * X^{1.19} + 6.60 * X^{1.19}$

The pressure at location $i = 2, 3, \ldots$ is obtained from Equation (4.10).

(#27) $FP(i, j) = FP(i-1, j) - PRDF(i, j) * 0.5 * rho * VF(k, j)^2 * dx / d\_hyd$

The concentration of the feedwater at location $i = 2, 3, \ldots$ is found by simple mass conservation methods.

(#28) $FC(i, j) = (FC(i, j-1) * VF (k-1, j) - [PC(i, M+1) * VP(i, M+1) * d\_perm * dx / \ldots$
$(L\_leaf * Spcr\_thick)]) / VF (k, j)$

With updated values of the feed pressure $FP(i, j)$ and the feed concentration $FC(i, j)$, the operations described in line numbers (#12) to (#28) are repeated for $i = 2$.

Similarly, the simulation of the RO element is carried forward for different values of i, till $i = N$.

After all the values of $i, j, k,$ and l have been utilized, the result is post processed.

7.7 Simulation post processing

The total permeate water produced by the element is calculated by adding the flow from each section.

(#29) $P\_out\_flow = Leaf\_Num * \sum_{i=1}^{N} VP(i, M+1) * d\_perm * dx$

The concentration of salt in the permeate flow is obtained from the mass average.

$$(\#30)\ P\_out\_conc = [\sum_{i=1}^{N} VP(i, M+1) * d\_perm * dx * PC(i, M+1)] / P\_out\_flow$$

The flowrate of the concentrate exiting the RO element is found by using

$$(\#31)\ F\_out\_flow = VF(N+1, j) * (Leaf\_Num * Spcr\_thick * L\_leaf)$$

The pressure of concentrate exiting the RO element is given by

$$(\#32)\ F\_out\_press = FP(N, j) - PRDF(N, j) * 0.5 * rho * VF(N+1, j)^2 * dx / d\_hyd$$

7.8 Multi-element pressure vessel

In a multi-element pressure vessel, the inlet conditions (inlet conditions refers to the flow rate, pressure, and concentration) for the pressure vessel are set as the inlet conditions for the first element in the pressure vessel. The concentrate water exiting the first element is sent as the feedwater to the second element in the row. The product water from each element is collected together to determine the product water from the pressure vessel. In cases where the recovery from the pressure vessel is high or when many elements are placed in series, the flow through the product water tube suffers a pressure loss similar to a pipe-flow pressure loss. This is seen as the permeate backpressure. In specialized cases, permeate back pressure is artificially induced to reduce the recovery and fouling potential. These specialized cases are set by the RO plant designer on a case-by-case basis.

For the RO pressure vessel conditions shown in Table 2-1 and Figure 2.15, the RO element performance is shown in Figure 7.8. The concentrate exits the pressure vessel at 3248 ppmw NaCl, 209 psi and at 5.5 lpm. The quality of permeate exiting the pressure vessel is calculated from the mass average of permeate concentration exiting each element. From the simulations, the quality of permeate exiting elements 1, 2, and 3 are 11.1, 15.7, and 19.0 ppmw NaCl. The flowrate of permeate produced in elements 1, 2, and 3 are 1.45, 1.34, and 1.21 lpm respectively, The quality and flowrate of permeate produced in the pressure vessel is 15.0 ppmw NaCl at 4 lpm.

One can compare this result with the old simulation where the concentrate exits the pressure vessel at 3347 ppmw NaCl, 208.8 psi and 5.7 lpm. The product water exits the pressure vessel at 14.4 ppmw NaCl, at 3.85 lpm.

It is observed from Figure 7.8 that the feed pressure, osmotic pressure and the net driving pressure lines are not straight, but the deviation for the straightline is not significant either. The comparison of the new simulation method and the existing simulation method (Figure 2.18) is shown in Figure 7.9. The difference between the new and the old simulation is clearly observable in this figure.

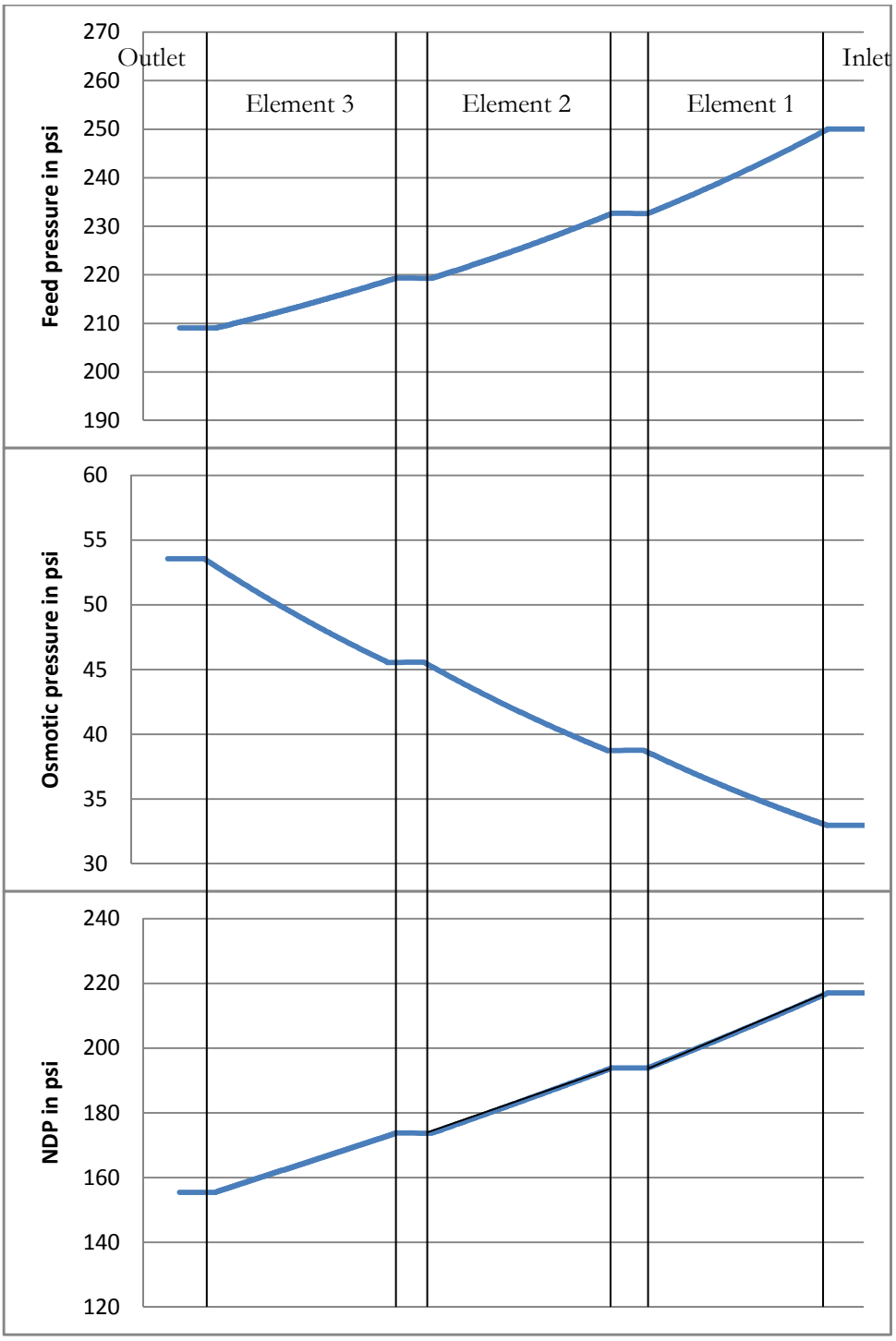

Figure 7.8: Quantitative graph showing element performance in the pressure vessel

7.9 Comparison of results and conclusions

Figure 7.9 superposes the results from the old simulation (shown in Figure 2.16) and the new simulation (shown in Figure 7.8). It may be observed that the differences in the results are small for the first element and begin to become prominent in the second, and the gap further widens in the third element. The deviations are brought about by the incorporation of varying feed water flowrate, feed concentration, and pressure by accounting for the incremental removal of product water along the element. It is important to stress that the lines that depict the results of the new simulation are not straight lines. In conditions where more than three elements are installed in an element, the differences become more pronounced. These differences add up when trying to simulate a large RO water treatment plant comprising of hundreds of RO elements.

It is also important to note that this research work ties to minimize the inaccuracies of RO element simulation alone. However, RO element simulations can only be based on the mean performance of the element. The distribution of element performance is affected by part-to-part variations determined by the quality of the raw materials used namely: feed spacer, RO membranes, manufacturing processes such as forces applied on the RO element while rolling as spiral wound elements and damages to the elements during shipping, handling, and storage. It is important to maintain healthy safety factors to account for RO element to RO element variations.

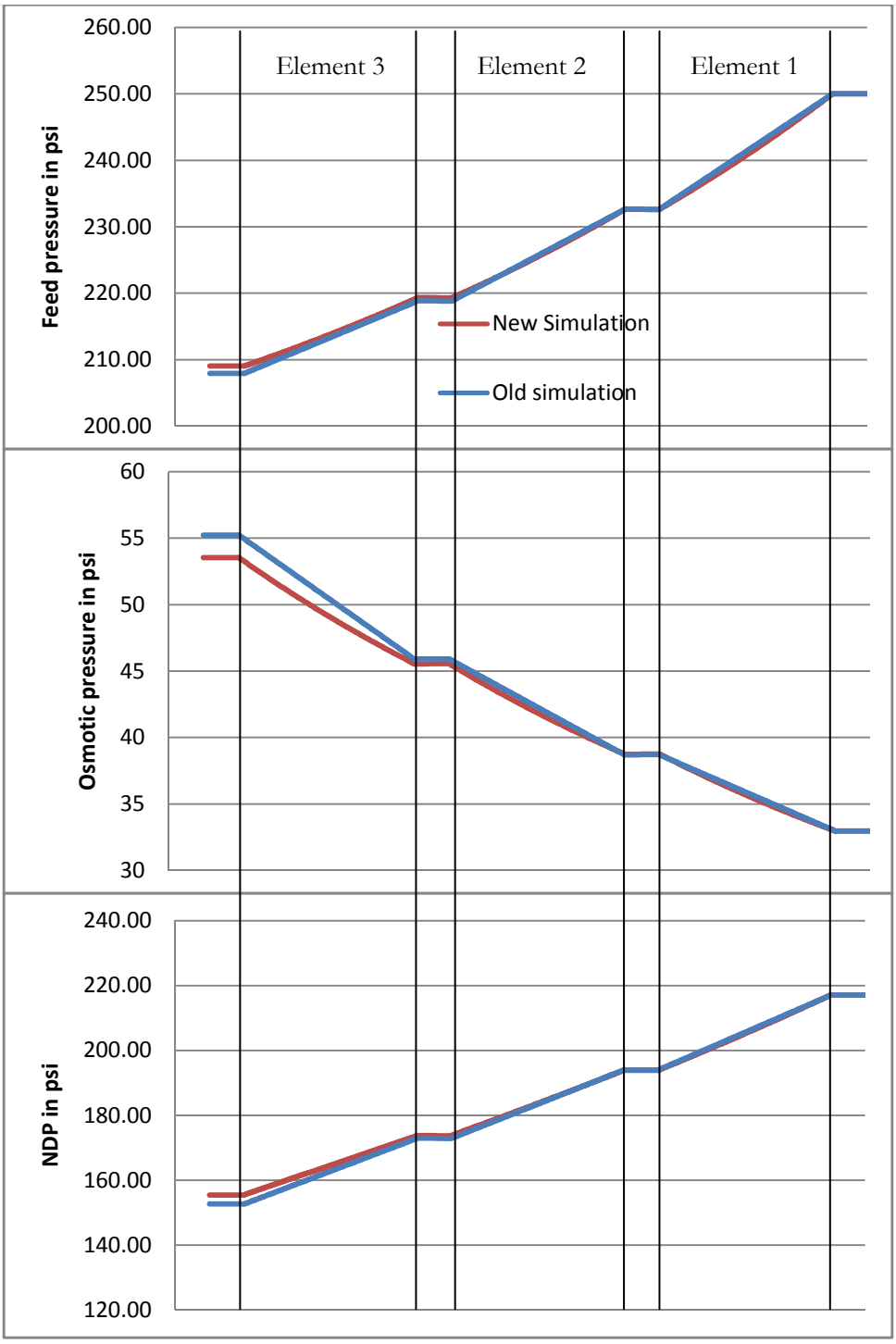

Figure 7.9: Element performance graph that compares the two simulation results

Chapter 8 : SUMMARY AND FUTURE WORK

8.1 Introduction

This section sums up the work set forth in the foregoing chapters, including a new method that is proposed for the calculation of the performance of an RO element. Finally, activities that will be beneficial for further understanding of RO operations are proposed.

8.2 Summary

Chapter 1 of this thesis helps to shine light on the importance of water and water purification. This chapter goes further to explain the importance of removing dissolved solutes from raw water in water purification operations and of the role of reverse osmosis in removing dissolved solutes.

Chapter 2 gives a detailed explanation of an RO plant. It further explains the functioning of the RO module and finally gives an in-depth description of the RO element. It also explains the various terms used in RO industries. Later, it goes into the causes of feedwater pressure drop and gives an in-depth analysis of mass transfer that occurs in the feed channel. The reasons for permeate spacer pressure drop are explained in detail. Finally, the chapter explains the method in which RO elements and RO modules are simulated; the shortcomings of the current model are elaborated; and a new method of RO simulation is proposed.

Chapter 3 deals exclusively with the computational fluid dynamics techniques used to simulate the fluid flow and the mass transport in the feed spacer. It describes the geometries of the feed spacer and the meshing methods. A mesh independency study is conducted to ascertain the reliability of the mesh. The governing equations of mass, momentum, and species conservation used in the CFD (CFX-14.0) simulation are set forth, and the analogy between mass and heat transfer is described. The chapter also examines whether the flow in the feed spacer is laminar or turbulent and steady or transient. The result of the study yields that flow in the feed spacer is laminar and transient. However, the non-steady component in the transient flow is very miniscule in the range of Reynolds numbers in which actual feed spacers operate. Later, the initial conditions and the boundary conditions used for the simulation are described. The geometric periodicity of the feed spacer is used to simulate just one *repeating unit* of the feed spacer. A periodic boundary condition with an assigned flow driving pressure difference is used to simulate the flow through the *repeating unit* and

extrapolated to the entire feed spacer screen. The boundary condition for the membrane is complicated as there is fluid transfer and mass transfer across the boundary. However, for reverse osmosis desalination conditions, the feed water flow velocity in the feed spacer is a few thousand times as that of the permeate water flow velocity through the membrane. Therefore, the velocity of the feedwater flow through the membrane is neglected. Two separate simulations are conducted- one with no flow of water through the RO membrane (no-slip condition) and another with 30 US gallons per square foot per day of product water flow rate. Upon assessment, the difference in the velocity patterns is negligible between the two types of flow and hence a no-slip boundary condition is used to simulate the flow through the feed-spacer *repeating unit*. Finally, the process in which the mass transport of salt in the feedwater is translated into a heat transfer problem in CFX, and the unique implementation of periodic boundary condition is explained in detail.

Chapter 4 displays the results of the fluid flow and the mass transfer simulations. Parametric equations, Equation (4.5) and Equation (4.7), are proposed to predict the *pressure drop factor* and the Sherwood number.

Chapter 5 discusses the experiments conducted to validate the predictions made by the computer simulations in Chapter 4. Three types of experiments were conducted. The first experiment aimed at understanding the feed spacer pressure drop in an RO element. Six elements were tested with 28-mil feed screens. The feed spacer pressure drop determined experimentally is lower than that predicted by CFX simulations. Further investigation revealed that the feed spacer and the membrane deforms under stress imposed during RO element manufacturing. This was verified when the element was opened after the experimentation and deep feed spacer imprinting was found on the membrane. A simple stress-induced deformation calculation was performed to estimate the possible deformation of the feed spacer. The pressure drop predicted by CFX with the revised deformed feed spacer geometry matched well with the experimental observations. The second experiment tried to lend understanding of the variations of the membrane properties with pH, feed pressure, and feed concentration. In that experiment, a flat cell membrane test setup was used as the author did not have the resources to conduct a well-controlled experiment on a large RO element. The observations and results from the second experiment were necessary to understand the results of the third and final experiment. In the third experiment, the feed channel in the flat cell test setup lined with the feed spacer to simulate the flow conditions in an RO element. Then, the concentration polarization in the flat cell was calculated using the *Membrane B value* data acquired from the second experiment. The Sherwood number of the flow through the feed spacer was calculated and compared with that

predicted from the CFX simulations. The possibility of error in the third experiment was significantly high because the concentration polarization was calculated based on the average *Membrane B value*. It was found to be theoretically impossible to measure the *Membrane B value* and the concentration polarization simultaneously. The assumption of a *Membrane B value* based on the claim made by the manufacturer led to large variations in the calculated concentration polarization and Sherwood number values. However, the data sets were repeated, and they were evenly distributed around the Sherwood number predicted by the simulation.

Chapter 6 discusses the results from the simulation of feedwater flow entering and exiting the RO element. The magnitude of pressure drop associated with the feedwater either entering the RO element or leaving the RO element is very insignificant, so that these processes do not affect the overall performance calculations of the RO element in the pressure vessel. The typical pressure drop across the feed spacer is of the order of 30,000 Pa whereas the entry and exit pressure drops are of the order of 50 Pa. The entry or exit pressure drop is about 0.2 % of the pressure drop across the feed spacer; therefore, it is acceptable to neglect the effect in RO element simulation calculations.

Chapter 7 provides an algorithm to use to the correlation equations for *pressure drop factor* and Sherwood number to predict the performance of an element. The new proposed algorithm does not assume linear variations for feedwater pressure drop, feedwater concentration, or the net driving pressure. It is believed that the new algorithm improves the accuracy of the RO predictions.

8.3 Conclusion

Accurate simulation of an RO system is necessary to

- predict the size of the RO plant during the commissioning process
- manage plant expansion when the demand increases
- enable coordinated plant shutdown when the demand drops
- account for the seasonal variation of feedwater quality and quantity
- account for random factors, such as environmental disasters, etc. that affect the plant operations
- maintain water supply during regular maintenance such as
    - Cleaning
    - Element replacements
    - Safety inspections

Many RO establishments try to include a high safety factor and redundancies to cope with such situations. The plant operation efficiency often suffers when high safety factor and redundancies are introduced. The safety factors can be judicially reduced, keeping the same or improving the reliability by means of improving the quality and minimizing errors, assumptions, and variations.

The goal of this dissertation is to improve the accuracy and the reliability of the simulation by minimizing assumptions. The key contributions of this research work are:

a) Investigation of entry and exit pressure drops in an element:

It was observed through CFX simulations that the pressure drops associated with the feedwater entering or exiting the RO element is of the order of 0.01 psi. These pressure drops are very insignificant in the overall simulation of RO elements.

b) Introduction of the Forchheimer model for feed spacer pressure drop:

A new and improved Forchheimer model that includes the viscous losses (Darcy coefficient) and inertial losses (Forchheimer coefficient) helps to capture the variation of the *pressure drop factor* as a function of the Reynolds number more effectively. Readers may recollect that the old model was a power law model. Power law model is generally used to depict a turbulent flow pressure drop. As studies in Chapter 3 have proven that the flow in the feed spacer under standard operating conditions is laminar, the Forchheimer model is more appropriate.

c) The use of a feed spacer geometry factor as a means to incorporate feed spacer deformation:

The term feed spacer deformation is a misnomer. In fact, it is the membrane that deforms more than the feed spacer does, leaving feed spacer imprinting on the membrane. Feed spacer imprinting reduces feed spacer channel width. The reduction of feed spacer channel width and its effect on feedwater pressure drop or the mixing is captured by the geometry factor.

d) Introduction of a parametric equation to estimate the Sherwood number:

Though estimations of the Sherwood number for a fluid flow in a feed spacer have been mentioned by other research groups, the introduction of a quadratic function of the *geometric factor* as a coefficient for the Sherwood number formula is unique to this work. Further, as concentration polarization cannot be estimated directly without knowing the *Membrane B*

value, this parametric equation provides the best estimate of the concentration polarization occurring in a RO element feed spacer.

e) Introduction of a parametric equation to estimate the *pressure drop factor* for various feed spacer geometries.

The work is the first of its kind to introduce a feed-spacer *pressure drop factor* equation that incorporates geometric similarity to predict the pressure drop for any feed spacer with a 90° strand angle.

f) Introduction of element discretization method to simulate the element performance

RO simulations so far have assumed a linear variation of the feed pressure and feed concentration along the length of the element. This assumption deviates from reality and the departure is more pronounced when the recovery of each element is very high. To minimize the error caused by fitting a linear trend from the inlet to the exit of the element, the element is divided into smaller zones and the linear approximation is applied to each zone. This approach accounts for the non-uniform removal of product water from the inlet to the exit.

8.4 Future work

One of the immediate needs that were identified from this work is to understand in detail the RO element fabrication process and the impact that the variations in raw materials have on the performance of the final product. First, a better understanding of the spatial variation of the membrane properties will help to incorporate correct non-uniform values of *Membrane A and B values* in the simulation algorithm.

The RO membrane properties change when they are fabricated as RO elements. Not much work has been done in this regard to understand the variation of membrane properties during element fabrication.

When RO elements are fabricated, the feed spacer indents into the membrane, thereby reducing the effective flow cross-sectional area for the feedwater. This is referred to as feed spacer deformation. In the place of *ex-situ* examination, an *in-situ* examination of the feed spacer will yield valuable and accurate results on the magnitude of the feed spacer deformation.

The feed spacer deformation data proposed in this work is purely qualitative. Useful information can be gleaned by developing a quantitative method for measuring the feed spacer deformation when the feed spacer is still incorporated in the membrane. This measuring method will help to create a model that relates RO manufacturing parameters to feed spacer imprinting. This model will be very useful to promote quality control.

During RO operations, the feedwater hydrostatic pressure pushes the membrane into the permeate spacer and increases the feedwater channel width. A better modeling of the flow through the feed spacer will be possible by incorporating the phenomenon caused by the hydrostatic pressure.

The same hydrostatic pressure also has the potential to compress and deform the permeate spacer. Detailed work on the rigid body deformation of the permeate spacer will yield valuable insight into the variation of the permeate spacer pressure drop constant as a function of the feed pressure.

Similarly, the hydrostatic feed pressure can also deform the membrane surface and the planar assumption of the membrane surface may no longer be valid if the membrane under the huge feedwater pressure indents into the permeate spacer

A parametric equation for pressure drop and Sherwood number for non-90º feed spacer strand angle would be valuable to simulate elements with specialized feed spacer for low pressure drop or high fouling resistance applications

The Sherwood number calculated in this work is for a mono-solute system. If the feed stream water that consists of more than one solute (which is always the case), the present model needs to be upgraded to incorporate that condition. Solving mass transfer for multi-solute feedwater with more than one constitutive Schmidt number will be very useful for industrial and specialized applications.

References

[1] J.P. Holdren, Science and Technology for Sustainable Well-Being, Science, 25 January 2008: Vol. 319 no. 5862 pp. 424-434

[2] http://en.wikipedia.org/wiki/California_Water_Wars, California Water Wars, retrieved March-10-2011

[3] R.A. Sauder, The Lost Frontier: Water Diversion in the Growth and Destruction of Owens Valley Agriculture, University of Arizona, 1994, p. 23 (ISBN 0816513813

[4] Progress in Drinking-water and Sanitation: special focus on sanitation. WHO/UNICEF Joint Monitoring Programme for Water Supply and Sanitation. July 17, 2008. p. 25

[5] Updated Numbers: WHO-UNICEF JMP, Report 2008, www.Unicef.org, retrieved March-10-2011

[6] R.W. Christopherson, Geosystems, 5th edition, Prentice Hall, 2003

[7] W.P. Cunningham, et al., Environmental Science, 7th edition, McGraw-Hill, 2003

[8] N.D. Gulhati, The Indus Waters Treaty: An Exercise in International Mediation, Allied Publishers, Bombay, 1973

[9] Overview of the Hydrology of the Mekong Basin, Mekong River Commission, Vientiane, Lao PDR, 2005

[10] http://en.wikipedia.org/wiki/Water_politics_in_the_Nile_Basin, Water politics in the Nile Basin, retrieved March-10-2011

[11] Progress on Drinking Water and Sanitation: Special Focus on Sanitation. World Health Organization and United Nations Children's Fund Joint Monitoring Programme for Water Supply and Sanitation, UNICEF, New York and WHO, Geneva, 2008. ISBN9789280643138

[12] Comprehensive assessment of water management in agriculture, Insights, International water management (IWMI) report, 2006, p. 8

[13] http://upload.wikimedia.org/wikipedia/commons/thumb/6/67/World_population_density_1994.png/300px-World_population_density_1994.png, Historical Population Density-1994, retrieved March-10-2011

[14] M. Elimelech, et, al., The future of sea water desalination: Energy, Technology, and the environment, Science, 5 August 2011: Vol. 333 no. 6043 pp. 712-717

[15] M. Barlow, Blue Gold, 2001, www.canadians.org, retrieved March-10-2011

[16] http://www.unesco.org/water/wwap /wwdr/index.shtml, United Nations World Water Development Report, WWDR, retrieved March-10-2011

[17] J.E. Miller; Review of water resources and desalination technologies, Sand Report, SAND, March 2003

[18] http://upload.wikimedia.org/wikipedia/commons/2/2c/Sea_salt-e-dp_hg.svg , Composition of sea water, retrieved on March-10-2011

[19] http://en.wikipedia.org/wiki/File:Aquarius_spacecraft_first_global_salinity_map_Aug-Sep_2011.jpg, salinity distribution of seawater, retrieved on March-10-2011

[20] J. Stouffer,et. al., Climate Response to External Sources of Freshwater: North Atlantic versus the Southern Ocean. J. Climate, 20, 436–448

[21] K.S. Spiegler, et. al., A Desalination Primer, Balaban Desalination Publications, Santa Maria Imbaro, Italy, 1994

[22] K.S. Spiegler, et. al., The energetics of desalination processes, Desalination, 134, 2001, p.p. 109–128

[23] Y.M. El-Sayed, Designing desalination systems for higher productivity, Desalination 134, 2001, p.p. 129-158

[24] S.A. Kalogirou, Effect of fuel cost on the price of desalination water: a case for renewable, Desalination 138, 2001, p.p.137-144

[25] G.W.I. Wangnick, Desalination, A quick guide, Worldwide Desalting Plants Inventory. Oxford, England: Global Water Intelligence, 2005

[26] J.E. Miller, Encyclopedia of Desalination and Water Resources, Encyclopedia of life support systems, UNESCO 2004

[27] H. Brüschke, Industrial application of membrane separation processes, Pure and Applied Chemistry, Vol. 67, No. 6, 1995, p. 993-1002

[28] C.J.M. van Rijn, Nano And Micro Engineered Membrane Technology, Elsevier, 2004, ISBN-13: 978-0-444-51489-9

[29] K. Scott, et. al., Industrial Membrane Separation Technology, 1st edition, Chapman Hall, 1996

[30] R.W. Baker, Membrane Technology and Applications, 2nd edition, Wiley, 2004

[31] R.W. Baker et al., Membrane Separation Systems, Noyes Data Corporation, 1991 (ISBN: 0-8155-1270-8)

[32] Y. Yampolskii, et. al., Membrane Gas Separation, Wiley, 2010

[33] T. Sata, Ion Exchange Membranes: Preparation, Characterization, Modification and Application, Royal Society of Chemistry, London, 2004

[34] H. Strathmann, Ion-Exchange Membrane Separation Processes, Elsevier, New York, 2004

[35] A. Galileo, Electrochemical Capacitors For Water Desalination." ScienceDaily, 26 Jan. 2009

[36] Y. Luo, Simulation of osmotic pressure in concentrated aqueous salt solution, The Journal of Physical Chemistry letters, 1, 2010, p. 183-189

[37] A.T.M. Jamaluddin et al., A novel approach for prediction of osmotic pressure for plant design and performance normalization of seawater, 4th Annual workshop on Water Conservation in the Kingdom of Saudi Arabia, 2001

[38] I.S. Al-Mutaz, prediction performance of RO desalination plants, Desalination, 120, 1998, p. 153-160

[39] I. Koyuncu, Effects of operating conditions on the salt rejection of nanofiltration membranes in reactive dye/salt mixtures, Separation and Purification Technology, 33, 2003, p. 283-294

[40] http://www.reverseosmosischemicals.com/reverse-osmosis-guides/reverse-osmosis-glossary-terms/silt-density-index-sdi-reverse-osmosis-systems, Silt Density Index (SDI) - Reverse Osmosis Systems, retrieved on March-10-2011

[41] A.A.F. Al-Dulaimi, Efficiency and reliability of reverse osmosis desalination systems, Iraqi Journal of Chemical and Petroleum Engineering, Vol. 8, No. 4, 2007, p. 59-62

[42] A.S. Kim, Cake structure in dead-end membrane filtration: Monte carlo simulations, Environmental Engineering Science, Vol. 19, No. 6, 2002, p. 373

[43] J.E. Oddo, M.B. Tomson, Scale Control, Prediction and Treatment Or How Companies Evaluate A Scaling Problem and What They Do Wrong, CORROSION/92, Paper No. 34, NACE INTERNATIONAL, Houston, TX, 1992

[44] J.E. Cadotte et al., A new thin film composite seawater reverse osmosis membrane, Desalination, 32, 1980, p. 25-31

[45] http://archive.unu.edu/unupress/unupbooks/80858e/80858E2o.gif, Cross section of a pressure vessel with 3 membrane element, retrieved on March-10-2011

[46] J. Kucera, Reverse Osmosis Industrial Applications and Processes, Scrivener Publishing, Wiley, 2010

[47] A.R. Da Costa, A.G. Fane, C.J.D. Fell, A.C.M. Franken, Optimal channel spacer design for ultra-filtration, Journal of Membrane Science, 62, 1991 p.275–291

[48] S.S. Sablani et al., Influence of spacer thickness on permeate flux in spiral-wound seawater reverse osmosis systems, Desalination, 146, 2002, p. 225-230

[49] W.D. Glatzel, M.C. Tomas, The effect of turbulence promoters on heat transfer and pressure drop in plate heat exchanger, CSIR Special report CHEM 53, 1966

[50] K.K. Lau et al., Feed spacer mesh angle- 3D modeling, simulation and optimization based on unsteady hydrodynamic in spiral wound membrane channel, Journal of Membrane Science, 343, 2009, p. 16-33

[51] C.P. Koutsou et al., Direct numverical simulation of flow in spacer filled channels: Effect of spacer geometry characteristics, Journal of Membrane Science, 291, 2007, p. 53-69

[52] V.V. Rande et al, Fluid Dynamics of Spacer Filled Rectangular and Curvilinear Channels, Journal of Membrane Science, 271, 2006, pp. 1-15

[53] F. Li et al, Novel spacers for mass transfer enhancement in membrane separations Journal of Membrane science 253 2005

[54] V. Geraldes et al., Flow and mass transfer modeling of nanofiltration, Journal of Membrane Science, 191, 2001, p. 109-128

[55] V. Geraldes, The effect of mass transfer on momentum and concentration boundary layers at the entrance region of a slit with a nanofiltration membrane wall, Chemical Engineering Science, 57, 2002, p. 735-748

[56] A.L. Ahmad, K.K. Lau, Modeling, simulation, and experimental validation for aqueous solutions flowing in nanofiltration membrane channel, Industrial & Engineering Chemistry Research, 46, 2007, p. 1316-1325

[57] A.L. Ahmad et al., Integrated CFD simulation of concentration polarization in narrow membrane channel, Computers and Chemical Engineering, 29, 2005, p. 2087-2095

[58] T.K. Sherwood, Industrial and Engineering Chemistry Fundamentals, 4 (2), 1965, p. 113–118

[59] K.K. Lau et al. Effect of feed spacer mesh length ratio on unsteady hydrodynamics in 2D spiral wound membrane channel, Industrial & Engineering Chemistry Research, 49, 2010, p. 5834-5845

[60] A.L. Ahmad, et. al., Impact of different spacer filaments geometries on 2D unsteady hydrodynamics and concentration polarization in spiral wound membrane channel, Journal of Membrane Science, 286, 2006, p. 77-92

[61] L. Song, et. al., Numerical studies on the impact of spacer geometry on concentration polarization in spiral wound membrane modules, Industrial & Engineering Chemistry Research, 44, 2005, p. 7638-7645

[62] V. Geraldes et al., The effect of the ladder-type spacers configuration in NF spiral wound modules on the concentration boundary layers disruption, Desalination, 146, 2002, p. 187-194

[63] S. Ahmad, Heuristic analysis of brackish water treatment by reverse osmosis process, Engineering Journal of Qatar University, Vol. 3, 1990

[64] M. Brusilovsky et al., Prediction of reverse osmosis membrane salt rejection in multi-ionic solution from single salt data, Desalination, 71, 1989, p. 355-366

[65] R. Rangarajan et al., Predictability of reverse osmosis performance of porous cellulose acetate membranes for mixed uni-univalent electrolytes in aqueous solutions, Industrial and Engineering Chemistry, Process Design and Development, Vol. 17, No. 1, 1978

[66] Pitzer, K.S, Activity coefficients in electrolyte solutions (2nd ed.). C.R,C. Press. ISBN 0-8493-5415-3. pp. 75–153

[67] Davies, C.W, Ion Association. London: Butterworths, 1962, pp. 37–53

[68] Y.G. Lee et al., Rapid performance diagnosis of seawater reverse osmosis membranes: simulation approach, Desalination and water treatment, v. 15 i. 1-3, 2010, p. 11-19

[69] A.M. El-Nashar, History and current status of membrane desalination processes, Water and Wastewater Treatment Technologies, 2007

[70] T.D. Hodgson, Selective properties of Cellulose acetate membranes towards ions in aqueous solutions, Desalination, 8, 1970, p. 99-138

[71] F.P. Incopera et al., Fundamentals of Heat and Mass Transfer, John Wiley & Sons, New York, 1985

[72] F. Li, et. al, Optimization of commercial net spacers in spiral wound membrane modules, J. Membrane Sci. 208 (2002) pp. 289-302

[73] G. A. Fimbres et. al. Numerical stydy of mass transfer in three dimensional spacer filled narrow channels with steady flow, Journal of membrane science 306 (2007) 228-243

[74] Menter, F. R. (1993), "Zonal Two Equation k-ω Turbulence Models for Aerodynamic Flows", AIAA Paper 93-2906

[75] Menter, F. R. (1994), "Two-Equation Eddy-Viscosity Turbulence Models for Engineering Applications", AIAA Journal, vol. 32, no 8. pp. 1598-1605

[76] S.A. Orszag, et. al., Numerical simulation of three dimensional homogeneous isotropic turbulence, Phys. Rev. Lett. 28 (1972) 76–79

[77] A.V. Tangborn, S.Q. Zhang, V. Lakshiminarayanan, A three-dimensional instability in mixed advection with streamwise periodic heating, Phys. Fluids 7 (11) (1995) 2648–2658.

[78] E. M Sparrow, et. al., 1977, "Fully-Developed Flow and Heat Transfer in Ducts Having Streamwise-Periodic Variations of Cross-Sectional Area," ASME J. Heat Transfer, 99, pp. 180–186.

[79] A.C. Fischer-Cripps, Introduction to contact Mechanics, Spinger-Verlag, New York, Inc 2000

[80] L. Vu-Cuoc et. al., A Normal Force-Displacement Model for Contacting Spheres Accounting for Plastic Deformation: Force-Driven Formulation. , Journal of Applied Mechanics, June 2000, Volume 67 pp-363 to pp-371

[81] R. G. Bates., Determination of pH: theory and practice. Wiley, 1973

[82] J. E. Cadotte, Materials Science of Synthetic Membranes, 269 ed.; Lloyd, D. R., Ed.; American Chemical Society: Washington D.C., 1985; pp 273-294.

[83] C. Bartels et. al, The Effect of Feed Ionic Strength on Salt Passage Through Reverse Osmosis Membranes, Desalination 184 (2005) 185-195

Appendix A

The simulation code used to generate the results is presented in the following

```
// Srivathsan G University of Minnesota Mechanical Engineering Department PhD
//candidate
//The intent of this code is to simulate the performance of an RO pressure vessel. These
//lines are a product of the research work conducted and described in this thesis
// Notes: commands written after "//" serve as comments to the computer codes.
global double rho mu Dab
// The variables, rho is density, mu is viscosity, and Dab is the molecular diffusion
//coefficient of salt in water.
//The variables rho, mu, and Dab will and do vary as a function of feed water salinity,
//and temperature
// For illustration purposes, these variables are assumed invariant in this simulation.
rho=997;                    //Density
mu=8.899E-4;                //Dynamic Viscosity
Dab=1.5E-9                  //Molecular diffusion coefficient of salt in water
global integer M, N         //The feed spacer is divided M times along the feed flow
                            //direction and N times in the permeate flow direction
M=100
N=100
//The user is requested the feed water flow conditions into the pressure vessel
Structure Flow_conditions   // A data structure to account for flow conditions is
                            //described.
Flow_conditions variables
double F_in_press           //Feed inlet pressure
double F_in_flow            //Feed inlet flow rate in meter cubed per second
double F_in_conc            //Feed inlet concentration in ppmw NaCl
double F_in_temp            //Feed inlet temperature in Kelvin
F_in_Temp = 298             //The feed temperature set at 25°C
end Flow_conditions         //Denotes the end of this structure variable
Flow_conditions IN_FLOW OUT_FLOW     //A variable IN_FLOW and OUT_FLOW is
                            //defined that has the structure of Flow_conditions
                            //IN_FLOW is the property of flow entering the pressure
                            //vessel and
                            //OUT_FLOW is the property of flow exiting the pressure
                            //vessel
Global Integer Number_of_elements //The data structure stores the value for number of
                            //elements in each pressure vessel
Structure  Element_property //A data structure that stores all the variables that
                            //constitute and define the element are stored
//For ease of simulation all the elements inserted in the pressure vessel are considered
//to be of the same type.
```

```
Element_property variables
double A(N,M)               //Membrane A value
double B(N,M)               //Membrane B value
double L_elem               //Length of the RO element
double L_leaf               //Length of the leaf inside the RO element
double Leaf_Num             //Number of leaves in the element
double Spcr_ang             //The spacer angle of the feed spacer
Spcr_ang=90                 //The spacer angle is set at 90°
double Spcr_thick           //The thickness of the spacer in meters
double Spcr_spacing         //The space between two strands in meters
double XP(N,M)              //Hydrodynamic resistance offered by the permeate spacer
double d_perm               //Thickness of the permeate spacer
end Element_property        //Denotes the end of this structure variable
Element_property ELEMENT ELEMENT_VAL //A variable ELEMENT is defined that has
                            the structure of //Element_property
Flow_conditions INLET_FLOW OUTLET_FLOW FLOW_VAL       //Two variables
                            INLET_FLOW and //OUTLET_FLOW are defined
Structure Permeate_property
double perm_flow            // Flow rate of permeate in cubic meters per second
double perm_concentration   //Concentration of permeate
end Permeate_property
Permeate_property PERMEATE PERMEATE_OUT PERMEATE_VAL
//////////////////////////////////////////////////////////////////////////////////////////////////////////////////////////////////////////
Main                        //The simulation starts here
cin<<IN_FLOW                //The user is asked to enter the values of the flow entering
                            //the system
cin<< Number_of_elements    //The user is asked to enter the value for the number of
                            //elements in each pressure vessel
cin<<ELEMENT                //The user is asked to enter the properties of the elements
                            //used in the pressure vessel
integer element_counter     //A counter to keep track of the element that is being
                            //simulated in the pressure vessel. This counter runs from
                            //1 to the user defined total number of elements in the
                            //pressure vessel. This number is inputted by the via the
                            //variable Number_of_elements
INLET_FLOW = IN_FLOW        //The flow condition for the first element in the pressure
                            //vessel is the same as the flow condition of the feed water
                            //entering the pressure vessel
/////////////////////////////////////////////////////////////////////////////
// Initializing permeate flow and concentration
/////////////////////////////////////////////////////////////////////////////
PERMEATE_OUT. perm_flow = 0
PERMEATE_OUT. perm_concentration = 0
for element_counter =1 to Number_of_elements
do      //The following commands are done repeatedly until every element in the
        pressure vessel is simulated
```

```
[PERMEATE OUTLET_FLOW] = Element_model (INLET_FLOW, ELEMENT)
                                        //The function Element_model is evoked.
                              //This function has two inputs namely-
                              //        1. The property of the element
                              //        2. The property of flow entering the element
                              //This function has two outputs namely-
                              //        1. Property of the permeate exiting the element
                              //        2. Property of the concentrate flow exiting the
                              //        element
INLET_FLOW = OUTLET_FLOW
PERMEATE_OUT.perm_flow = PERMEATE.perm_flow+ PERMEATE_OUT.perm_flow
                              //Permeate from each element is added to the stream
                              //flowing out of the pressure vessel
PERMEATE_OUT.perm_concentration = …
( PERMEATE.perm_flow * PERMEATE.perm_concentration + …
PERMEATE_OUT.perm_flow * PERMEATE_OUT.perm_concentration ) / …
PERMEATE_OUT.perm_flow
                              // Mass averaging of the permeate concentration is
                              //performed to evaluate the concentration of the flow
                              //exiting the pressure vessel
end for                       //End of the loop that simulates each element in the
                              //pressure vessel

end Main and Return           //The main function ends and the programs stops here
PERMEATE_OUT                  // Quality of permeate
OUT_FLOW                      //Quality of the concentrate are the output of the simulation
////////////////////////////////////////////////////////////////////////////////////////////////////////////////////////
//The following code defines the function ELEMENT_MODEL
//ELEMENT_MODEL simulates the performance of each element.
//ELEMENT_MODEL has two inputs and two outputs
//The two inputs are
//        1. The property of the element
//        2. The property of flow entering the element
//The two outputs are
//        1. Property of the permeate exiting the element
 //       2. Property of the concentrate flow exiting the element
////////////////////////////////////////////////////////////////////////////////////////////////////////////////////////
function ELEMENT_MODEL (FLOW_VAL, ELEMENT_VAL)
// The following lines define the variables local to the function ELEMENT_MODEL
double A(N,M)                 //Membrane A value
double B(N,M)                 //Membrane B value
double L_elem                 //Length of the RO element
double L_leaf                 //Length of the leaf inside the RO element
double Leaf_Num               //Number of leaves in the element
double Spcr_ang               //The spacer angle of the feed spacer
double Spcr_thick             //The thickness of the spacer in meters
double Spcr_spacing           //The space between two strands in meters
double XP(N,M)                //Hydrodynamic resistance offered by the permeate spacer
```

```
double d_perm            //Thickness of the permeate spacer
double F_in_press        //Feed inlet pressure
double F_in_flow         //Feed inlet flow rate in meter cubed per second
double F_in_conc         //Feed inlet concentration in ppmw NaCl
double F_in_temp         //Feed inlet temperature in Kelvin
double FP(N,M)           // Feed pressure
double PP(N,M)           // Permeate pressure
double FC(N,M)           // Feed concentration
double WC(N,M)           // Feed wall concentration
double PC(N,M)           // Permeate concentration
double FO(N,M)           // Feed osmotic pressure
double PO(N,M)           // Permeate osmotic pressure
double NDP(N,M)          // Net driving pressure
double P_flux(N,M)       // Permeate flux flowrate
double P_Conc(N,M)       // Permeate flux concentration
double VF(N+1,M)         // Velocity of feedwater in feed spacer
double VP(N,M+1)         // Velocity of permeate water in tricot
double CP(N,M)           // Concentration polarization
double Re(N,M)           // Reynolds number
double X                 // Spacer geometry factor
double Sh(N,M)           // Sherwood number
double PRDF(N,M)         // Pressure drop factor
double P_out_flow        // Total permeate produced
double P_out_conc        // Concentration of permeate water
double F_out_flow        // Flowrate of concentrate exiting the RO element
double F_out_press       // Pressure of concentrate exiting the RO element
// Initializing the local variables using the values inputted into the function
A = ELEMENT_VAL.A
B = ELEMENT_VAL.B
L_elem = ELEMENT_VAL.L_elem
L_leaf = ELEMENT_VAL.L_leaf
Leaf_Num = ELEMENT_VAL.Leaf_Num
Spcr_ang = ELEMENT_VAL.Spcr_ang
Spcr_thick = ELEMENT_VAL.Spcr_thick
Spcr_spacing = ELEMENT_VAL.Spcr_spacing
XP= ELEMENT_VAL.XP
d_perm = ELEMENT_VAL.d_perm
F_in_press = FLOW_VAL.F_in_press
F_in_flow = FLOW_VAL.F_in_flow
F_in_conc = FLOW_VAL.F_in_conc
F_in_temp = FLOW_VAL.F_in_temp
double dx dy             //dx and dy are the dimensions of each discrete element
dx = L_elem / N          //Refer to line item (#1) in chapter 7
dy = L_leaf / M          //Refer to line item (#2) in chapter 7
integer i j k l          // the array pointer arguments i,j,k and l are defined
// The variables are initialized
i=1
j=1
```

```
k=1
l=1
//initializing the variables using the user input.
for j=1 to M
do
VF(k, j) = F_in_flow / (Leaf_Num * Spcr_thick * L_leaf)
                                        //Refer to line item (#3) in chapter 7
end for
for j=1 to M
do
FP(1, j) = F_in_press  //Refer to line item (#4) in chapter 7
FC(1, j) = F_in_conc   //Refer to line item (#5) in chapter 7
PP(1, j) = P_in_pres   //Refer to line item (#6) in chapter 7
end for
d_hyd = 2 * Spcr_thick          //Refer to line item (#7) in chapter 7
k=1                             //reinitializing k
for j=1 to M
do
Re(i, j) = rho * VF(k, j) * d_hyd
                                        //Refer to line item (#8) in chapter 7
end for
X =  Spcr_thick / Spcr_spacing
                                        //Refer to line item (#9) in chapter 7
//Reinitializing variables
i = 1
j = 1
k = 1
l = 1
for i = 1 to N
do
// unknown variable initialization
CP = 1
P_conc=0
PP  = P_in_pres
                                        //Refer to line item (#17) in chapter 7
PC(i, 1) = P_Conc(i,1)
                                        //Refer to line item (#22) in chapter 7
PC_last= eps                            //eps is machine epsilon
while (abs((PC_last – PC) ) / PC_last) <0.0001 )
PC_last=PC
do
PP_last = eps                           //eps is machine epsilon
while (abs((PP_last – PP) ) / PP_last) <0.0001 )
do
PP_last=PP
CP_last=eps                             //eps is machine epsilon
while ( abs((CP_last – CP ) / CP_last) <0.0001 )
do
```

```
CP_last=CP(i, j)
Sc = mu / ( rho * Dab )          //Refer to line item (#10) in chapter 7
Sh(i, j) = ( -41 * X^2 + 22.85 * X - 2.52 ) * ( ( Re(i, j) / 0.71 ) ^0.65 - 1.36 ) * Sc^0.33
                                 //Refer to line item (#11) in chapter 7
FO(i, j) = 0.255 * F_in_temp * FC(i, j) * CP (i, j)
                                 //Refer to line item (#12) in chapter 7
 PO(i, j) = 0.255 * F_in_temp * PC(i, j)
                                 //Refer to line item (#13) in chapter 7
NDP(i, j) = FP(i, j) - FO(i, j) + PO(i, j) -PP(i, j)
                                 //Refer to line item (#14) in chapter 7
P_flux (i, j) = A(i, j) * NDP(i, j)
                                 //Refer to line item (#15) in chapter 7
CP(I, j) = ( 1 + ( (d_hyd * P_flux (i, j)) / (Sh(i, j) * Dab) ) ) / ( 1 + ( (d_hyd * P_flux (i, j) …
* B(i, j)) / (Sh(i, j) * Dab * (P_flux (i, j)+ B(i, j)) )
                                 //Refer to line item (#16) in chapter 7
end while

VP (I, 1) = 0
                                 //Refer to line item (#18) in chapter 7
for l = 1 to M
j = l;
VP (i, l+1) = VP (i, l) +2 *  P_flux (i, j) * dx * dy / d_perm
                                 //Refer to line item (#19) in chapter 7
end for
PP(i, M) = P_in_pres
for j = M to 2
do
PP(i, j-1) = PP(i, j) + VP(i, l) * XP(i, j) * d_perm * dy
                                 //Refer to line item (#20) in chapter 7
end while
 P_Conc(i, j) = ( B(i, j) * CP(i, j) * FC(i, j)) /( P_flux (i, j) + B(i, j))
                                 //Refer to line item (#21) in chapter 7

for l = 2 to M+1
j= l - 1
PC(i,j) =( VP(i, l-1) * PP(i, j-1) * d_perm + 2* P_conc(i, j) * P_flux(i, j) ) * dy ) / VP (i, l)
                                 //Refer to line item (#23) in chapter 7
end while
k = i
VF(k, j) = (VF(k-1, j) * L_leaf * Spcr_thick - VP(i, M+1) * d_perm * dx) /...
                            (L_leaf * Spcr_thick)
                                 //Refer to line item (#24) in chapter 7
Re(i, j) = rho * VF(k, j) * d_hyd
                                 //Refer to line item (#25) in chapter 7
PRDF(i, j) = (1493 / Re(i, j) ) * X^1.19 + 6.60 * X^1.19
                                 //Refer to line item (#26) in chapter 7
FP(i, j) = FP(i-1, j) - PRDF(i, j) * 0.5 * rho * VF(k, j)^2 * dx/ d_hyd
                                 //Refer to line item (#27) in chapter 7
```

```
FC(i, j) = ( FC(i, j-1) * VF (k-1, j) - [ PC(i, M+1) *VP(i, M+1) * d_perm * dx /...
                                        (L_leaf * Spcr_thick) ] ) / VF (k, j)
                                        //Refer to line item (#28) in chapter 7
end for
P_out_flow = 0
for i = 1 to N
do
P_out_flow = P_out_flow + Leaf_Num * VP(i, M+1) *  d_perm * dx
                                        //Refer to line item (#29) in chapter 7
end for
double flowmultiple
flowmultiple = 0;
for j = 1 to M
do
flowmultiple = flowmultiple + VP(i, M+1) *  d_perm * dx * PC(i, M+1 )
end for
P_out_conc = flowmultiple / P_out_flow
//Refer to line item (#30) in chapter 7
j=1
F_out_flow = VF(N+1, j) * (Leaf_Num * Spcr_thick * L_leaf)
//Refer to line item (#31) in chapter 7
F_out_press = FP(N, j) - PRDF(N, j) * 0.5 * rho * VF(N+1, j)^2 * dx/ d_hyd
//Refer to line item (#32) in chapter 7
F_out_conc = ( FC(N, M) * VF (N, j) - [ PC(N, M+1) *VP(N, M+1) * d_perm * dx /...
                                        (L_leaf * Spcr_thick) ] ) / VF (N+1, j)
PERMEATE_VAL. perm_flow = P_out_flow
PERMEATE_VAL. perm_concentration = P_out_conc
FLOW_VAL.F_in_press = F_out_press
FLOW_VAL.F_in_flow = F_out_flow
FLOW_VAL.F_in_conc = F_out_conc
F_in_temp = FLOW_VAL.F_in_temp

end ELEMENT_MODEL and return
PERMEATE_VAL FLOW_VAL
//////////////////////////////////////////////////////////////////////////////////////////////////////////////////////////
//End of the code
//////////////////////////////////////////////////////////////////////////////////////////////////////////////////////////
```